Von der Universität Bayreuth

zur Erlangung des Grades eines

Doktors der Naturwissenschaften (Dr. rer. nat.)

genehmigte Abhandlung

From theory to application

3D bioprinting of cells

---

von

Sebastian Johannes Müller, geb. in Naila

1. Gutachter: Prof. Dr. Stephan Gekle
2. Gutachter: Prof. Dr. Michael Wilczek

Tag der Einreichung: 16.02.2023

Tag des Kolloquiums: 13.06.2023

Abstract

Biofabrication comprises all forms of the automated production of living and functional biological tissue, involving methods from medicine, biology, chemistry, engineering, and physics. The efforts are driven by the growing demand of organ and tissue transplants, the need for improved pharmaceutical drug testing models, prosthetics, and cancer research. The broad spectrum of evolving techniques ranges from advances in cell expansion methods to cell specific bioink development, from assembly and controlled self-assembly of organoids to tissue structures of physiological scale. The most popular manufacturing technology is 3D bioprinting, where established fused-deposition techniques have been translated to operate with bioinks that have special material properties; and hence also special demands. For example, the cytocompatibility and permeability with nutrients, or the micromechanical extra-cellular environment provided by the material, have to be tailored to fit the needs of specific cell types. And while negative biochemical interactions can virtually be eliminated through proper biomaterial choice, the hydrodynamic influences during the fabrication process are what inevitably remains to damage the cells. At which stage of the printing process, and in what magnitude it affects the cells, however, is hardly understood so far.

To elucidate the underlying mechanisms, we develop in this thesis a variety of analytical and numerical tools to study the behavior of cells under realistic printing conditions. As a starting point, we investigate the flow of the bioink from the material cartridge through a confined needle and the outlet, which results in elongational and shearing fluid motion acting on the suspended cells. To quantify the major suspect for flow-induced cell damage, the shear stress, we develop a semi-analytical solution of the Navier-Stokes equations for a generalized Newtonian fluid, a class comprising all fluids with strain rate dependent viscosity. A practical Python implementation of our algorithm has become a popular tool among experimentalists of the community. We further propose an analytical method to estimate shear stress induced cell damage during printing, which despite its simplicity accurately reproduces a large experimental data set.
The cell is the second essential ingredient in a bioink for printing. We develop a hyperelastic cell model, which we carefully validate with experiments in both an atomic force microscopy based compression setup and several microfluidic devices. We show that the strain hardening effect of the employed Mooney-Rivlin strain energy functional description strongly depends on the mode of deformation which the cell undergoes in either compression or flow. For our flow-based investigations, we modify the theory of Roscoe and demonstrate that its range of applicability can be extended from the

description of neo-Hookean particles in a linear shear flow to Mooney-Rivlin particles in a Poiseuille flow and, strikingly, still remains valid for shear thinning suspensions. An essential assumption in both micromechanical characterization techniques as well as in large-scale simulations is the homogeneity of the cell's interior. We therefore provide systematic proof of the possibility to substitute any elastic inhomogeneity inside the cell with a homogeneous equivalent, and do so for both compression and flow scenarios. Our knowledge gained from the validation of our flow computations and the cell model is then concentrated into the simulation of the three steps of the extrusion process: the nozzle inlet, the nozzle itself, and its exit at the tip. Single cell simulations are performed to elucidate the role of the particular flow patterns and the bioink rheology. Simulations of dense cell suspensions which resemble desired bioprinting conditions supplement this information. We find that the elongational flows at the inlet of the nozzle have an effect similar in magnitude to the maximum shear stresses present in the nozzle. They are almost independent of the trajectory of the entering cell, however, only act on a very short time span. The shear stresses inside the nozzle, on the other hand, act along its entire length, and the duration is inverse proportional to the flow velocity. Hence, cells flowing closer to the wall experience higher stresses for a longer time span, decreasing their potential to survive during extrusion, or maintain proper functionality post-printing. Elongational flows act on the cells a second time when exiting the nozzle at the tip. We find that here their influence is in general lower than the shear stresses inside the nozzle, and the dominating factor is the relaxation from the sheared deformation into the stress-free shape.

This thesis is a contribution to research regarding the mechanical behavior of cells in different experimental setups and especially bioprinting-related scenarios. The analytical and numerical methods developed herein are capable of explaining various — but not all — features of the cell behavior and identify the major flow-induced damage factors for cells during extrusion, while offering the potential to be extended with further features.

keywords: 3D bioprinting, shear thinning, shear flow, microfluidics, Roscoe theory, hyperelasticity, Mooney-Rivlin, strain hardening, cell mechanics, atomic force microscopy, Lattice-Boltzmann, computational fluid dynamics, biological physics

Zusammenfassung

Unter dem Begriff Biofabrikation fasst man alle Formen der automatisierten Herstellung funktionierenden, lebenden, biologischen Gewebes zusammen, wobei Methoden der Disziplinen Medizin, Biologie, Chemie, Ingenieurswesen und Physik Anwendung finden. Getrieben werden diese Entwicklungen durch den stetig steigenden Bedarf an Spendeorganen und -geweben, der Notwendigkeit verbesserter Gewebemodelle für pharmazeutische Studien, Prothetik und die Krebsforschung. Das breite technologische Spektrum reicht dabei von Methoden der Zellexpansion zur Entwicklung maßgeschneiderter Biotinten, von Selbstorganisation und kontrollierter Selbstorganisation von Organoiden zu Gewebestrukturen physiologischer Längenskala. Die dabei prominenteste Technologie ist der 3D Biodruck, wo die bereits etablierte *fused deposition*-Methode dahingehend erweitert wurde, dass auch Biotinten mit speziellen Materialeigenschaften eingesetzt werden können. Spezielle Anforderungen an die Materialien, etwa die Zellverträglichkeit oder die Permeabilität für Nährstoffe, oder auch die von der Tinte erzeugte mikromechanische Umgebung der Zelle, müssen gemäß der Ansprüche eines jeden Zelltyps angepasst werden. Und selbst wenn die negativen biochemischen Wechselwirkungen durch passende Wahl des Biomaterials im Prinzip ausgeschaltet werden können, bleiben doch unvermeidbar die hydrodynamischen Einflüsse während des Druckprozesses übrig, die die Zellen schädigen können. An welcher Stelle des Druckprozeses und in welcher Stärke diese Einfluss auf die Zellen ausüben, ist bislang nicht vollständig geklärt.

Wir beleuchten die zugrundeliegenden Mechanismen in dieser Arbeit mithilfe mehrerer analytischer und numerischer Werkzeuge, mit denen wir das Verhalten von Zellen unter realistischen Druckbedingungen untersuchen. Als Einstiegspunkt betrachten wir die Strömung der Biotinte von der Materialkartusche beginnend durch die Nadel und die Öffnung am Ende, wobei sowohl Elongations- als auch Scherströmungen auftreten, die auf die suspendierten Zellen wirken. Scherspannungen gelten dabei weitgehend als Hauptursache für Zellschäden. Wir berechnen diese über eine semi-analytische Lösung der Navier-Stokes Gleichungen für generalisierte Newtonsche Fluide, eine Klasse, die jegliche Fluide beschreibt, deren Viskosität von der lokalen Dehnrate abhängt. Unsere anwenderfreundliche Python Implementierung dieses Algorithmus hat sich zu einem beliebten Werkzeug der Experimentalisten entwickelt. Mit einer weitaus simpleren analytischen Methode können wir die von rein durch Scherspannungen verursachte Zellschädigung bereits hervorragend abschätzen, wie wir durch Reproduktion eines großen experimentellen Datensatzes zeigen.
Zellen sind die zweite essentielle Zutat einer Biotinte für den 3D Druck. Wir entwickeln

ein hyperelastisches Zellmodell, welches wir mit Experimenten sowohl aus Rasterkraftmikroskopie als auch Mikrofluidischen Messungen validieren. Dabei zeigen wir, dass die Stärke der Dehnverhärtung der verwendeten Beschreibung durch ein Mooney-Rivlin Dehnenergiefunktional insbesondere von der Deformationsmode abhängt, die die Zelle unter Kompression oder in Fluss annimmt. Zur Betrachtung einer Zelle in der Strömung erweitern wir die Theorie von Roscoe und demonstrieren, dass ihr ursprünglicher Anwendungsbereich deutlich erweitert werden kann: von einem Partikel mit neo-Hookscher Elastizität in einer linearen Newtonschen Strömung hin zu einem Mooney-Rivlin Partikel in einer parabolischen Poiseuille-Strömung und tatsächlich auch für Zellsuspensionen in scherverdünnenden Fluiden in einer nichtlinearen Rohrströmung. In mechanischen Charakterisierungsmethoden von Zellen wie auch in großen Simulationen ist eine häufige Annahme die elastische Homogeneität des Zellinneren. Wir zeigen daher systematische Belege dafür, wie eine Zelle mit beliebig elastisch heterogenem inneren Aufbau grundsätzlich durch eine gleichwertige, homogene Zelle ersetzt werden kann. Diese Betrachtungen führen wir in Kompressions- und in Strömungsszenarien durch. Die Erkenntnisse aus der Validierung des Zellmodells und der Flussberechnungen konzentrieren wir abschließend in unseren Simulationen der wichtigsten Stufen des 3D Biodruckprozesses: (i) dem Eintritt in die Nadel, (ii) der Nadel selbst und (iii) dem Austritt an der Spitze. Simulationen mit einzelnen Zellen klären dabei die Rolle der unterschiedlichen Strömungsmuster und der Rheologie der Biotinte. Unterstützt und erweitert werden diese mit Simulationen von dichten Zellsuspensionen, die realen Biodruck-Bedingungen entsprechen.
Es zeigt sich, dass die Elongationsflüsse am Nadeleintritt einen Einfluss auf die Zellen haben, der vergleichbar ist mit dem der maximalen Scherspannungen innerhalb der Nadel. Der Einfluss ist außerdem annähernd unabhängig von der Trajektorie der Zelle. Er wirkt jedoch nur auf einer kurzen Zeit- und Längenskala, wohingegen die Scherspannungen innerhalb der Nadel auf der gesamten Länge wirken, wobei die Zeitskala invers proportional zur Flussgeschwindigkeit ist. Daher erfahren Zellen, die nahe der Nadelwand fließen, höhere Spannungen und diese zugleich für längere Zeit, was ihr Überlebenspotential nach dem Druck einschränkt. Beim Nadelaustritt wirken ein zweites Mal Elongationsflüsse auf die Zelle ein, hier allerdings im allgemeinen schwächer als am Eintritt. Der dominante Prozess ist die Relaxation vom gescherten in den kräftefreien Zustand.

Diese Arbeit bildet einen Beitrag zur Forschung über Zell- und Strömungsmechanik in verschiedenen experimentellen Aufbauten und im Speziellen für relevante Szenarien des 3D Biodrucks. Die entwickelten analytischen wie auch numerischen Methoden können einige — wenn auch nicht alle — Eigenschaften des Zellverhaltens erklären und die dominierenden Einflüsse strömungsbedinger Zellschädigung während eines Extrusionsprozesses identifizieren. Sie können in Zukunft leicht mit zusätzlichen Funktionen erweitert werden.

Schlüsselwörter: 3D Biodruck, Scherverdünnung, Scherfluss, Mikrofluidik, Roscoe Theorie, Hyperelastizität, Mooney-Rivlin, Dehnverhärtung, Zellmechanik, Rasterkraftmikroskopie, Lattice-Boltzmann, Strömungssimulationen, biologische Physik

Contents

Part I

Extended Abstract

Chapter 1

Introduction

The objectives of the biofabrication research field target developments of high relevance in the medical sector, such as cancer treatment [1–3], wound healing [4, 5, chs. 15, 73], creation of pharmaceutical drug testing models [6–8], or the replacement of dysfunctional tissues and entire organs [9–12]. Being able to produce patient specific biological tissue in an automated manner is one of the major goal of the combined research efforts in the areas of medicine, biology, chemistry, engineering and physics.

Biofabrication, in a basic definition [13, 14], is the production of complex biological components from cells and simple materials or other basic building blocks in a controlled and automated manner, commonly involving computer aided design technologies and additive manufacturing techniques. The tissue types of interest are diverse and comprise — among many others — cartilage [15–19], bone [20–22], muscle [21, 23–28], vascular structures [28–33] and all organs in the human body. Just as diverse are hence the cell types involved: the native types building the aforementioned tissues, but also stem cells as promising candidates for tissue generation due to their controllable ability to differentiate into other cell types [34–38], are harvested via biopsy for patient specific research [39]. The development of scalable cell expansion methods from traditional flat culture plate solutions [34] towards novel bioreactor techniques [34] is one barrier between science and the adoption of the methods in regenerative medicine and tissue engineering products [13]. Another major challenge to be faced in all biofabrication efforts is the maintenance of biological functionality and the prevention of cell damage [40–48], which depends on a suitable biomaterial choice for each individual cell type on the one hand and the technical fabrication process on the other. During the past three decades, a variety of different approaches have been tested, all requiring individually tailored material properties. To name just a few, there are lithography-based biofabrication methods, such as stereolithography [11], digital light processing [20], and 2-photon polymerization [11], drop-on-demand or inkjet techniques [35, 49], and 4D fabrication processes [25, 31] which make use of spatial material compositions that, e. g., allow the construct to fold itself into a tubular shape. Spotlighted in this work is the extrusion-based 3D bioprinting process [41, 43, 50–53], where the bioink is pushed from a material cartridge on the printhead through a fine nozzle onto the substrate in form of a continuous strand. Similar to conventional thermoplast 3D printing, the computer-controlled motion of the printhead along three coordinate axes allows for a

layer-by-layer material deposition in order to build up a three-dimensional construct. A bioink is defined as mixture of cells and other biomaterials [54] — typically hydrogels enriched with biological growth factors [2, 29] and with cross-linking abilities [55, 56]. These biomaterials have to fulfill a variety of requirements to be considered for 3D bioprinting: Starting from the obvious, i. e., the absence of cytotoxic properties [15], they are ranging over process related properties like viscosity and printability [43, 57] up to relevant post-processing properties like shape fidelity and appropriate extra-cellular environment [43, 58]. To name some examples, gelatin and alginate [55, 59–61] and thereof chemically modified derivatives [2, 24, 41, 62] are popular choices of current bioink development efforts. Various protocols and characterization techniques have been and are still being developed to somehow quantify the bioinks' suitability for specific processes [63, 64]. After proper material choice for the fabrication endeavor, another damage source, which is independent of biological or biochemical effects, comes alongside the printing process itself: flow induced mechanical damage, which can arise at different stages of the extrusion process. A major contribution here is the flow of the cell through the fine printing nozzle with its concurrent shear stress [40–48]. But also elongational stresses, as they occur at the inlet and the exit of the nozzle, have been found responsible for a loss of cell functionality and viability after extrusion [65–68].

The goal of this thesis is to first develop a theoretical and numerical framework suited to describe the cell types and the flow of the biomaterials in geometries of interest, and in a second step apply the gained knowledge in order to characterize and predict the cells' behavior during a 3D bioprinting process.
One essential part of a bioink is the shear thinning biomaterial, which flows through different geometries during the bioprinting process. An understanding of the cell-free flow behavior is therefore crucial to monitor the flow-induced effects on the cells. There exist a variety of simulation based methods for simple and complex printer nozzle geometries [40, 55, 57, 69], which take the shear thinning rheology into account. We similarly incorporate an algorithm proposed by [70] for the treatment of non-Newtonian fluids into the software package ESPResSo [71, 72] in [pub1], which we use for all fully three-dimensional simulations in this thesis. However for the sake of simplicity, and especially when including cells into our simulations, we restrict ourselves in most cases to a cylindrical geometry as it is a popular 3D bioprinter nozzle types. This geometry makes it possible to solve the Navier-Stokes equations fully analytical in the case of the power-law viscosity model which is frequently used in literature [40, 43, 55]. We take the well-known solution of the power-law flow one step further and present in this thesis a method which accurately reproduces the large data set of cell viability measurements from Ouyang *et al.* [73] for embryonic stem cells — while it practically depends on only one free parameter. For the more complex, but also more realistic, Carreau-Yasuda description of shear thinning bioinks, we present in our publication [pub1] a semi-analytical solution to the Navier-Stokes equation, which is computationally more efficient than other simulation methods. The handy implementation of this algorithm in Python has become a popular tool for researchers and is used to asses velocity and shear stress profiles in bioprinting experiments [60, 74], as it requires only process parameters which are usually known by the experimentalist — the printing

pressure, the nozzle size, and the bioink rheology.
The other essential part of a bioink are the biological cells. Numerical cell models are no novel development of this thesis; there exist abundant approaches for annucleate, fluid-filled cells, e. g., the human red blood cells [75–79]. As for cells with a complex cytoskeleton, there exist axisymmetric hyperelastic finite-element models [80, 81] in two dimensions, and bead-and-spring based [82] as well as hyperelastic and viscoelastic finite-element models in 3D [83, 84]. While the latter two are partially similar to the cell model used in this thesis, they lack an experimental validation of the mechanical properties of single cells. In our publication [pub2], we perform fluidic force microscopy (FluidFM®) experiments with rat embryonic fibroblasts to validate our model in a compression scenario, a technique which is based on common atomic force microscopy (AFM) for mechanical characterization [85–92]. In addition, we show in this thesis qualitative proof of the correct behavior of this model in flow through comparison with microfluidic experiments of NIH-3T3 cells, by coupling it to our Lattice-Boltzmann simulations via an immersed boundary algorithm. That our description is not limited to only one particular cell type is demonstrated by comparing it to AFM compression and indentation experiments of bovine endothelial cells and hydrogel particles from literature. Our experiments furthermore show that the more complex Mooney-Rivlin description with its additional terms in the strain energy functional is necessary to properly capture the increasingly strain hardening mechanical response, which is not covered by the neo-Hookean description of the models used in [83, 84]. An aged yet accurate analytical approach towards neo-Hookean cells in a linear flow scenario is the Roscoe theory [93], which is an extension to the work of Jeffery for rigid bodies [94]. We find in our publication [pub3], that the Roscoe theory does not only apply to a hyperelastic cell in a simple shear flow, but also correctly predicts the behavior of a cell flowing off-centered in pressure driven flow. We additionally recover that the shear thinning rheology of a bioink does not affect the applicability of the Roscoe theory, although it has been derived strictly for Newtonian liquids. Hence, we extend the analytical formulation of the Roscoe theory [93] from a neo-Hookean to a Mooney-Rivlin description, where we find a decrease of the strain hardening effect compared to the neo-Hookean form, in contrast to our micromechanical investigations with the fluidic force microscope. This seemingly contradictory behavior is uncovered in this thesis through the use of simple mechanical substitute models for the deformation modes of the cells in compression and flow scenario. An arguable attribute that both the numerical and the analytical description of the cell have in common is the isotropy and homogeneity of the elastic properties, as the different constituents of the cell, e. g., the cortex, membrane, and nucleus, all have different mechanical properties [95–98]. Since this assumption is essential for flow-based mechanical cell characterization [74, 99], we propose in [pub4] a homogeneous equivalent of real cells with elastic heterogeneities and provide a systematic numerical investigation to proof its applicability.
The investigation of the behavior of cells in flow is of course one of the driving forces behind the development of the aforementioned numerical models, which have been tested in simple flow scenarios [83, 84]. From experimental side, there exist numerous microfluidic-based high-throughput methods to assess the mechanical properties of cells [97, 99–103], typically by confining the cells in narrow microchannels. Numerical

investigations of cells in these microfluidic setups exist in abundance [78, 104–106]. While the narrow geometry does not affect the cell characterization, the confinement leads to significantly different deformations of the cell which are not present in a 3D bioprinting process. Wider microchannels are used to further characterize the frequency dependent viscoelastic cell response utilizing the tank-treading motion of off-centered flowing cells [74]. Experiments performed by our collaborators under these conditions are used in this thesis for a qualitative experimental validation of our cell model in flow, as we observe the same cell shapes as function of the local shear stress. In the context of a bioprinting process, there exist so far no experimental observations of the cell shapes inside the nozzle and at the exit. Also from numerical side, complex simulations so far disregard the cell and investigate the shear thinning flow alone [40, 57, 69]. In our publication [pub3], we close this gap by providing a systematic analysis of the cell behavior during the passage through the nozzle and the exit. We conduct our simulations explicitly as function of the shear thinning rheology of the fluid. Considering first the cell-free flow, we find that the elongational stresses at the exit gain in significance compared to the shear stresses for shear thinning bioinks. We find this particularly relevant as we also observe a pressure dependent radially inwards-directed migration of the cell, which leads to a focusing of the cell distribution towards the center of the channel, where the elongational stresses have the strongest impact on cells exiting the nozzle. Nevertheless, we do not observe a drastic increase of the cell deformation at the exit even with an increase of the flow velocity of one order of magnitude, since the effect of the large stresses is reduced due to the shorter application time. For off-centered cells it remains the shear stresses which dominate the cell deformation in the entire passage. With this knowledge gained from our fully three-dimensional simulations, we are able to predict the maximum cell stress and strain for the entire process using a much simpler approach utilizing our aforementioned Python tool from [pub1].

Part I of this cumulative thesis provides the basic theoretical background of the publications, followed by individual sections bringing them into context and accompanied by additional, unpublished work. The publications together with a list of the individual author contributions are attached to the thesis in part II.
The remainder of part I has the following structure: Chapter 2 briefly introduces the theories of hydrodynamics and elasticity in the way there are utilized in this thesis. Building up on that, we first describe in section 3.1 analytical approaches to solve or approximate the flow of a bioink in relevant geometries in 3D bioprinting processes, from which we then construct a cell survival prediction method. In section 3.2 a simplified analytical cell model is presented on the basis of which it is possible to understand its strain hardening behavior under loading, and the Roscoe theory for hyperelastic cells in shear flow is introduced. Chapter 4 summarizes our numerical methods for both the simulation of shear thinning bioinks and our hyperelastic cell model used in all simulations. The next chapter 5 explains the application of the developed methods in detail: We start by investigating the relevance of intracellular elastic heterogeneities in section 5.1, reveal the cause of the change in strain hardening behavior of the Mooney-Rivlin model in section 5.2, and propose an approximation method for the elongational stresses during bioprinting in section 5.3, after which we apply our cell survival prediction method

to reproduce a large set of experimental data in section 5.4. Section 5.5 summarizes our investigations of the 3D bioprinting process with numerical methods, followed by conclusions and an outlook in chapter 6.

Chapter 2

Theoretical background

Two theories, the hydrodynamic theory and the theory of elasticity, form the underlying basis for the work in this thesis. The next section reviews the basic principles of both the Navier-Stokes equations and how the properties of shear thinning bioinks can be treated mathematically, followed by a contextualization of how the special conditions employed in this work relate to the general framework. The second section shall provide a brief introduction into the theory of cell elasticity, the hyperelastic description utilized in this work, and relations to other material constitutive models.

2.1 Hydrodynamics

2.1.1 Navier-Stokes equations

Derived from two basic physical principles, respectively the conservation of mass and momentum, the continuity equation and the Navier-Stokes equations describe the dynamics of a fluid. In this work, we consider purely incompressible fluids, since the materials of interest are liquids or hydrogels — which typically do not show the same grade of compressibility as for example gases do.
In vector notation, the Navier-Stokes equations read:

$$\frac{\partial \varrho}{\partial t} + \boldsymbol{\nabla} \cdot (\varrho \vec{u}) = 0 \tag{2.1}$$

$$\varrho \left[\frac{\partial \vec{u}}{\partial t} + (\vec{u} \cdot \boldsymbol{\nabla} \vec{u}) \right] = -\boldsymbol{\nabla} p + \boldsymbol{\nabla} \cdot \underline{\sigma} + \vec{f}_{\text{ext.}} \tag{2.2}$$

The mathematical treatment of this continuum theory considers tiny fluid elements as basic units. The continuity equation (2.1) describes the change of mass density inside such a fluid element: Its mass can only change over time due to the presence of a source or a sink of material inside of it, resulting in a nonzero divergence of the density flux.
The Navier-Stokes equation (2.2) describes the temporal change of the momentum density inside the fluid element, which is possible due to four different mechanisms: (i) The advection of the fluid, (ii) the presence of a spatially changing hydrostatic pressure, (iii) the presence of momentum sinks or sources, e. g., hydrodynamic friction, and (iv) external volume forces, e. g., gravity.

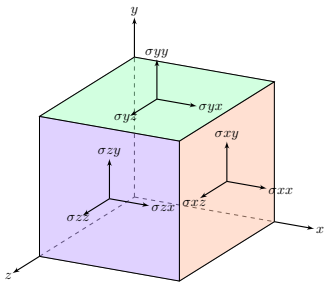

Figure 2.1: Components of the stress tensor at the faces of a cubical fluid element

In a simple picture, hydrodynamic friction is created when adjacent layers of the liquid move with different speed. This happens for example when fluid is being pushed through a static pipe, like — in the context of this thesis — a bioprinter nozzle. The motion can also be imposed onto the fluid by a moving wall, which is what happens in a classical shear rheometer.
In mathematical terms, hydrodynamic friction enters the Navier-Stokes equations through the viscous stress tensor $\underline{\sigma}$. For incompressible fluids it is defined by the constitutive equation

$$\underline{\sigma} = 2\eta\,\underline{\dot{S}}\,, \tag{2.3}$$

with the strain rate tensor

$$\underline{\dot{S}} = \frac{1}{2}\Big[\boldsymbol{\nabla}\vec{u} + (\boldsymbol{\nabla}\vec{u})^{\mathrm{T}}\Big]\,. \tag{2.4}$$

The viscous stress acting on a cubical fluid element can be visualized as in figure 2.1: The tensor element σ_{ij} gives the j-component of the force per area acing on the cube's face in $\vec{e}_i$-direction. In Newton's postulate of viscosity, the dynamic viscosity η would denote the proportionality constant between the viscous stress and the strain rate. Anytime it is referred to Newtonian fluids, we mean a liquid with a viscosity independent of the strain rate. It may however still change with other environmental parameters, e. g., temperature.
In the context of this thesis, however, η will typically not be regarded as a constant, but as a function of the strain rate tensor itself.

2.1.2 Shear thinning fluids

Generally, a fluid is called non-Newtonian when its viscosity changes as function of the applied stress and/or the time of application. One subset of this class exhibits a decrease in viscosity when a shear is applied between neighboring fluid elements, thus becoming "thinner". The viscosity is a function of the strain rate $\dot{S}$,

$$\eta = \eta\Big(\dot{S}\Big)\,, \tag{2.5}$$

which is a scalar quantity obtained from the rate of strain tensor via contraction into its second invariant

$$\dot{S} = \sqrt{2\dot{S}_{ij}\dot{S}_{ij}}\,. \tag{2.6}$$

A variety of empirically driven and also theoretically derived models exist for $\eta\left(\dot{S}\right)$. In this thesis, two of them will receive special attention.

2.1.2.1 The power-law viscosity model

The power-law or Ostwald-de Waele [43, 107, 108] model is a mathematically rather simple formulation of the strain rate dependency of the viscosity, and thus exceptionally practical in analytical derivations. Yet, it does not fall short in reliability when compared to reality [43]. It reads

$$\eta_{\mathrm{pl}}\left(\dot{S}\right) = m\dot{S}^{n-1} \tag{2.7}$$

and its two parameters are the consistency parameter m (in $\mathrm{Pa\,s}^n$) and the flow index $0 < n \leq 1$, which describes the strength of the shear thinning behavior. Setting $n = 1$ yields a Newtonian description with the consistency parameter as viscosity.
The mathematical advantages of the power-law model will be exploited during this thesis in section 3.1.2.1 and section 3.1.2.2.
However, two major shortcomings accompany this model which are of both mathematical and (un-)physical nature: (i) In an entirely stress-free scenario, e. g., a quiescent liquid, the strain rate would vanish and thus the viscosity would tend to infinity. This divergent behavior is also present in any rotationally symmetric flow scenario at the axis of revolution. (ii) The opposite behavior, a vanishing viscosity for increasing strain rates, is similarly unphysical. The first point — while it is surely not promoting the liability of the model — does not cause major difficulties in the solution of the Navier-Stokes equations (2.2) in an actual flow scenario, as described in section 3.1.2.1. Additionally, for materials which exhibit pure power-law behavior in the experimentally accessible range of strain rates, the description remains very accurate as long as the strain rates are not extrapolated too far from that range, as shown in figure 2.4 for Pluronic and Poly-oxazoline (POx). The second point, the vanishing viscosity, is not of mathematical relevance in this thesis, but remains an unphysical representation of what is observed in real liquids, as discussed in the next section.

2.1.2.2 The Cross model

In order to better understand the aforementioned unphysical properties of the power-law model and gain a better description of a realistic shear thinning liquid, the following picture of a simplified polymer solution can be helpful:
In figure 2.2(a) are shown bundles of single polymer strands dissolved in an otherwise quiescent (or low-shear) Newtonian liquid. Since the shear stresses between adjacent fluid elements are not large enough to untangle the polymers, they remain as bundles which are simply advected with the surrounding liquid — the macroscopic Newtonian viscosity unaltered. Upon increasing the shear stresses to the point where the polymers start unfolding, the microscopic composition of the suspension begins to change. The more elongated polymer shapes depicted in figure 2.2(b) allow for better advection and the friction between neighboring bundles decreases — thus reducing the macroscopic viscosity with increasing strain rate. Eventually this extensional process stops due to

Figure 2.2: Schematic of polymer strands in solution untangling due to increasing shearing between the fluid layers: (a) entangled polymer stands at low shear rates, (b) gradually untangling at intermediate shear, and (c) fully stretched polymer strands at high shear rates. Arrows indicate the magnitude and direction of the velocity field.

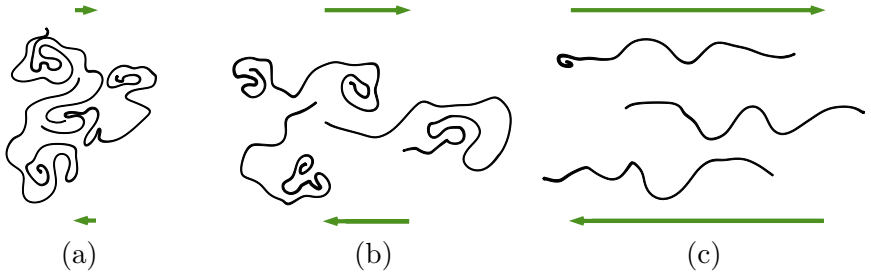

Figure 2.3: Viscosity versus strain rate behavior of the power-law model (2.7) and the four-parameter Cross model (2.8).

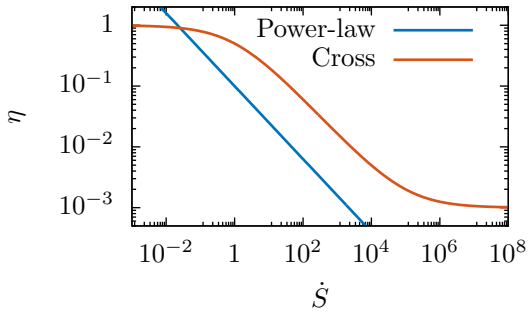

the finite length of the polymers, leaving a suspension of completely elongated polymer strands as in figure 2.2(c) which, again, are simply advected with the surrounding Newtonian liquid. The macroscopic viscosity reaches another limit where it behaves Newtonian.

Mathematically, there are several ways to incorporate the two Newtonian limits — the zero-shear (or low-shear) and the infinite-shear (or high-shear) limit — into the viscosity description in (2.5), one of which is the Cross model [109], which has proven itself quite useful in describing the sorts of materials involved in this thesis. It reads

$$\eta_{\text{Cross},4}\left(\dot{S}\right) = \frac{\eta_0 - \eta_\infty}{1 + (K\dot{S})^\alpha} + \eta_\infty \,, \tag{2.8}$$

with the zero-shear and infinite-shear viscosity, η_0 and η_∞ (both in Pa s), respectively. The exponent α has a similar role as n for the power-law model, with the difference that $\alpha = 0$ describes the Newtonian behavior and increasing shear thinning is obtained for $0 < \alpha < 1$. K (in s) is a time constant; its inverse $\dot{\gamma}_\text{c} = K^{-1}$ is often referred to as "corner shear rate" — when plotted double-logarithmically as in figure 2.3, the transition from the zero-shear Newtonian region into the power-law region happens at $\dot{\gamma}_\text{c}$. It is also the point where the curves of different α intersect.

In accordance with rheological measurements of the materials of interest in this thesis,

Figure 2.4: Rheological measurements of bioinks in the framework of the SFB TRR225 performed by the various subprojects (number in parentheses) show materials with mostly power-law behavior and such with clear low-shear Newtonian plateau.

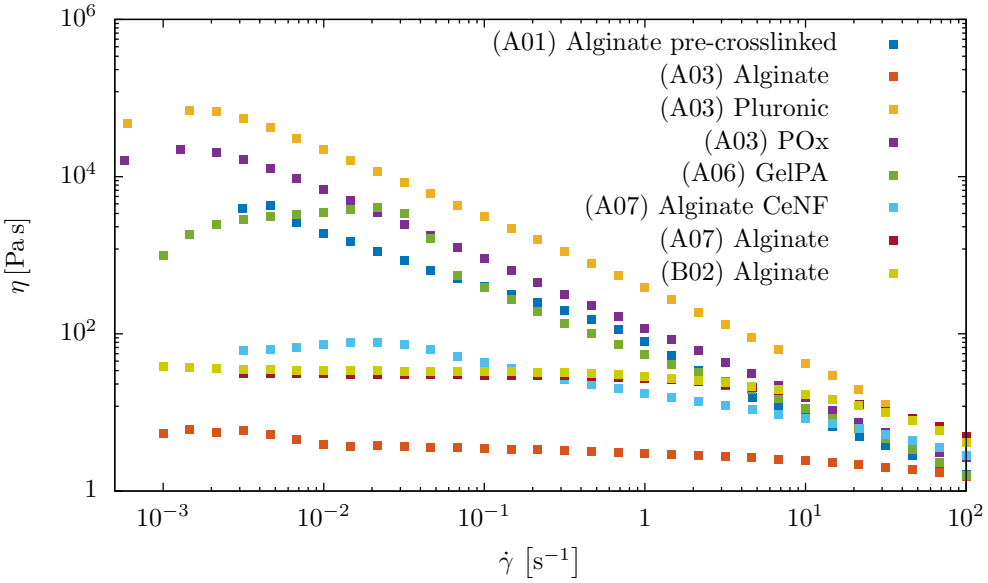

we omit the infinite shear viscosity in (2.8) and effectively reduce it to the following three-parameter model:

$$\eta_{\text{Cross},3}\left(\dot{S}\right) = \frac{\eta_0}{1 + (K\dot{S})^{\alpha}} \tag{2.9}$$

In figure 2.4 we show measurements performed by various contributors to the rheological database of the SFB TRR225 biofabrication. It can be seen very clearly that all bioinks show relevant power-law-like shear thinning behavior in a certain range of strain rates. Some of these materials show purely a power-law dependency in the entire experimentally accessible range, others exhibit the expected low-shear Newtonian plateau in that range. None of the materials show the high-shear Newtonian plateau, which is accounted for by the additional parameter η_∞ in (2.8), thus justifying our simplification in (2.9).
Note, that the power-law description according to (2.7) can be obtained from the parameters of the Cross model (2.9) in the case $(K\dot{S})^{\alpha} \gg 1$ by choosing:

$$m = \eta_0 K^{-\alpha} \tag{2.10}$$

$$n = 1 - \alpha \tag{2.11}$$

2.1.2.3 The Carreau-Yasuda model

The Carreau-Yasuda model [109, 110] is a slightly more generalized formulation of the Cross model of section 2.1.2.2 above. In comes with a total of five parameters, with two

of them being exponents characterizing the shear thinning strength. It reads

$$\eta_{\mathrm{CY}}\left(\dot{S}\right) = \frac{\eta_0 - \eta_\infty}{\left(1 + (K\dot{S})^{a_1}\right)^{\frac{a_2}{a_1}}} + \eta_\infty \,, \tag{2.12}$$

with the zero-shear and infinite shear viscosity, η_0 and η_∞, and the time constant K, as in the Cross model. The additional exponent a_2 tunes the onset behavior of the intermediate power-law region, which eases fitting to experimental data, e. g., for Chitosan hydrogels [111].

2.1.3 Contextualization

Shear thinning liquids are merely one sub-class of non-Newtonian fluids. Another well-known behavior is exhibited by shear thickening fluids, which are materials that seem to solidify under stress. A generalized description of these strain rate dependent viscous properties is achieved by the so-called Reiner-Rivlin model [112], with its constitutive equation

$$\underline{\sigma} = \eta\Big(I_2(\underline{\dot{S}}), I_3(\underline{\dot{S}})\Big)\underline{\dot{S}} + \zeta\Big(I_2(\underline{\dot{S}}), I_3(\underline{\dot{S}})\Big)\underline{\dot{S}}^2 \tag{2.13}$$

relating the viscous stress tensor to multiple orders of the strain rate tensor via coefficients which themselves depend on the second and third invariant of the strain rate tensor.
While steady state material properties are covered by the description (2.13), time-dependent behavior is not accounted for. Such materials with viscosities increasing or decreasing with the duration of an applied stress are called rheopex or thixotropic, respectively.
The last important type of non-Newtonian liquids in the context of bioinks are viscoelastic materials. Viscoelastic fluids show, in addition to Newtonian or strain rate dependent viscous properties, additional elastic behavior, i. e., they can partially store energy in form of reversible shape changes. In the context of biofabrication, the elastic properties of bioinks are often assessed though rheological measurements [43, 50, 59, 113–115].
For simplicity, however, the possible elastic properties of bioinks are purposefully neglected in this thesis.

2.2 Cell elasticity

2.2.1 General principles

The second continuum theory applied in this thesis is that of elasticity. When an elastic body is deformed due to external mechanical influences, e. g., the surrounding flow of a liquid, it can store the energy necessary to revert this deformation in form of so-called strain energy.
Mathematically, the deformation is assessed in terms of the displacement field [116, p. 14]

$$u_i = y_i - x_i \,, \tag{2.14}$$

where y_i and x_i denote the position of a material point of the elastic body in the deformed and undeformed state, respectively. The deformation gradient tensor [116, p. 14]

$$F_{ij} = \frac{\partial y_i}{\partial x_j} \tag{2.15}$$

and the thereof constructed symmetric left Cauchy-Green deformation tensor

$$B_{ij} = F_{ik}F_{kj} \tag{2.16}$$

are used to define measures for the strain of the material. An example showing the similarity in the theoretical description of elastic bodies and liquids is the form of the infinitesimal strain tensor [116, p. 22], which has the same mathematical form as the strain rate tensor (2.4) in fluid dynamics:

$$\varepsilon_{ij} = \frac{1}{2}\left[\frac{\partial u_i}{\partial x_j} + \frac{\partial u_j}{\partial x_i}\right] \tag{2.17}$$

Similar to the constitutive equation in fluid dynamics (2.3), which relates viscous stress to strain rates via the viscosity, constitutive equations in elasticity theory relate the (elastic) stress inside a material to the applied strain via elastic moduli, e. g., the Young's modulus and the Poisson ratio. In an equivalent description, constitutive equations may relate the strain energy density, which is a scalar quantity, directly to the deformation gradient (2.15) via the elastic material parameters [116, p. 97]:

$$U = U(I_1(\underline{F}), I_2(\underline{F}), I_3(\underline{F})) \tag{2.18}$$

Similar to (2.13), I_1, I_2, and I_3 denote invariants of the deformation gradient tensor, i. e., scalar quantities measuring the degree of deformation.
From that, the Cauchy stress as measure for the force per unit area is computed as [116, p. 97]

$$\sigma_{ij} = \frac{1}{\det(\underline{F})} F_{ik} \frac{\partial U}{\partial F_{jk}} \,. \tag{2.19}$$

2.2.2 Neo-Hookean and Mooney-Rivlin materials

In this work, focus lies on material descriptions that prove compatible with properties of biological cells. One major requirement here is the reversibility of even very large deformations, so-called hyperelastic behavior. Further qualities to be fulfilled by the material model are an inclusion of (near) incompressibility and strain-hardening qualities. The neo-Hookean and Mooney-Rivlin constitutive equations both fulfill the aforementioned requirements.
The strain energy density of the neo-Hookean [116, p. 100] and Mooney-Rivlin [116, p. 100f.] description are given by, respectively,

$$U_{\mathrm{NH}} = \frac{\mu}{2}(I - 3) + \frac{\kappa}{2}(J - 1)^2 \tag{2.20}$$

and

$$U_{\mathrm{MR}} = \frac{\mu_1}{2}(I-3) + \frac{\mu_2}{2}(K-3) + \frac{\kappa}{2}(J-1)^2\,. \tag{2.21}$$

Here, μ, μ_1, and μ_2 denote shear moduli, while κ denotes a bulk modulus. For consistency with linear elasticity in the limit of small strains, these material parameters relate to the Young's modulus and the Poisson ratio via [116, p. 74, 100]

$$\mu = \mu_1 + \mu_2 = \frac{E}{2(1+\nu)} \quad \text{and} \quad \kappa = \frac{E}{3(1-2\nu)}\,. \tag{2.22}$$

Sufficiently incompressible materials have very high κ and a Poisson ratio near $\frac{1}{2}$.
The Mooney-Rivlin description (2.21) adds one more term to the neo-Hookean form (2.20) to account for another order of strains, assessed by the invariants J, I, and K [116, p. 96]: [1]

$$J = \det(F) \tag{2.23}$$

$$I = J^{-\frac{2}{3}} B_{kk} \tag{2.24}$$

$$K = \frac{1}{2} J^{-\frac{4}{3}} \left[B_{kk}^2 - B_{nk}B_{kn} \right] \tag{2.25}$$

The additional consideration of terms quadratic in $\underline{B}$ alters the strain hardening behavior compared to the neo-Hookean description. In this thesis, we further choose the shear moduli of the Mooney-Rivlin model as $\mu_1 = w\mu$ and $\mu_2 = (1-w)\mu$, to be able to scan through the influence of the the higher order terms on the deformation behavior. That way the same shear or Young's modulus is found for different w in the case of small deformations. This becomes particularly relevant when the parameters obtained from fits using this model are compared with experimental measurements that employ the traditional Hertz theory for mechanical characterization, as has been done in [pub2].
The Cauchy stress (2.19), from which the *cell stress* will be computed in this thesis, is given as [116, p. 100 f.]

$$\sigma_{ij}^{\mathrm{NH}} = \frac{\mu}{J^{\frac{5}{3}}} \left(B_{ij} - \frac{1}{3} B_{kk}\delta_{ij} \right) + \kappa(J-1)\delta_{ij} \tag{2.26}$$

for the neo-Hookean material and

$$\begin{aligned} \sigma_{ij}^{\mathrm{MR}} =& \frac{w\mu}{J^{\frac{5}{3}}} \left(B_{ij} - \frac{1}{3} B_{kk}\delta_{ij} \right) + \kappa(J-1)\delta_{ij} \\ &+ \frac{(1-w)\mu}{J^{\frac{7}{3}}} \left(B_{kk}B_{ij} - \frac{1}{3} B_{kk}^2\delta_{ij} - B_{ik}B_{kj} + \frac{1}{3} B_{kn}B_{nk}\delta_{ij} \right) \end{aligned} \tag{2.27}$$

for the Mooney-Rivlin material.

[1] $B_{kk} = \mathrm{tr}(B)$ and $B_{nk}B_{kn} = \mathrm{tr}\left(B^2\right)$.

2.2.3 Contextualization

Most hyperelastic material models, and so, too, the neo-Hookean and Mooney-Rivlin description, were originally designed for the characterization and modeling of rubber-like materials, as this group of materials remains highly elastic under very large strains. Empirical approaches exist that generalize the constitutive equation (2.21) using a polynomial series [116, p. 101],

$$U = \sum_{i+j=1}^{N} \mu_{ij}(I-3)^i(K-3)^j + \sum_{i=1}^{N} \frac{\kappa_i}{2}(J-1)^{2i}\,, \tag{2.28}$$

where an appropriate choice of the fit parameters yields the simpler descriptions (2.20) and (2.21).
In this work, we employ these rubber models to describe the mechanical properties of biological cells. Among all possible types of cells that could be considered, we aim to describe cells which have a complex inner structure — like the cytoskeleton or actin cortex — and put less focus on particular membrane mechanics, as it would be necessary for the description of human red blood cells or likewise "simple"-constituted cell types. To name only a few, fibroblasts and muscle cells, but also endothelial cells, fulfill these requirements and are well described with rubber-like models, as we demonstrate in [pub2].
Similar to bioinks, also cells can show viscoelastic behavior due to the presence of protein-laden cytosol and the organelles residing inside of them. In this thesis, however, explicit focus is put on the elastic behavior of the cells, as the viscous properties are attributed to the bioink — thus creating a clear distinction between the two influences for the purpose of abstraction.

Chapter 3

Analytical methods

The analytical approaches presented in this thesis fulfill two purposes. One main goal is to provide useful prediction methods for an actual 3D bioprinting process. The other purpose is to provide a deeper understanding of the behavior of the employed theoretical models and to serve as validation reference to ensure the correctness of the numerical models.
In section 3.1, well-known analytical solutions to the flow in the scenarios of interest are recalled, and our novel method to compute the pipe flow of a Cross fluid from [pub1] is briefly summarized. A prediction method for cell survival is derived from the power-law viscosity model. In section 3.2 thereafter, simplified analytical descriptions for a cell are introduced which elucidate its mechanical behavior. The Roscoe theory [93] is extended to the Mooney-Rivlin description in the end.

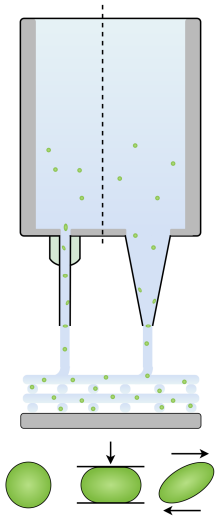

3.1 Flow of a shear thinning bioink

3.1.1 Newtonian fluid in important geometries

Although bioinks and bioink materials do typically not show Newtonian behavior, it is advantageous — and undoubtedly simpler from a mathematical point of view — to first recall the well-known flow behavior of Newtonian fluids in the geometries of interest. During this thesis, it is shown that already the simple pipe flow of a more sophisticated shear thinning fluid creates mathematical difficulties that render an analytical treatment of more complex geometries likely impossible. On the other hand, it is also shown that there exist certain similarities of the flow of Newtonian and shear thinning liquids which are particularly relevant for suspended cells, e. g., the surrounding undisturbed fluid stress.
The introduction introduced the different parts of the printhead: the cartridge, the inlet into the nozzle, the nozzle itself, and its exit. The following sections give an overview over existing analytical solutions of the Navier-Stokes equations (2.2) in these

geometries.

3.1.1.1 Flow inside the cartridge

Prior to any fabrication, the bioink and the cells are contained inside the printer cartridge. This is typically a cylindrical container of roughly 1 cm to 3 cm in diameter (as known from medical syringes) and is attached to the printhead itself. Then, during pneumatically driven extrusion, an air pressure of the order of several 10^5 Pa is applied on the top. Due to the large diameter compared to the fine nozzle, only a negligible portion of the applied pressure drops inside the cartridge.
The main similarity between the flow inside the cartridge and through the nozzle (section 3.1.1.3) is the geometry and, hence, also the flow profile, which has the same radial functional dependency. However, the size difference between the nozzle and the cartridge, which is about two orders of magnitude, causes similarly large differences in the stresses acting in the components. To attain an equal material flow in both parts, the flow velocities in the cartridge are much smaller, and thus is the pressure gradient driving the fluid. Due to the relation between pressure gradient and shear stress (3.5), the latter are also expected to be of negligible magnitude inside the cartridge. As an example, it follows from the formula for the pressure dependent flow rate in a cylinder (3.17) for the ratio between the pressure gradients in cartridge and nozzle:

$$\frac{G_\mathrm{c}}{G_\mathrm{n}} = \left(\frac{R_\mathrm{n}}{R_\mathrm{c}}\right)^4 \tag{3.1}$$

Hence, for a nozzle of radius 100 µm, the pressure gradient and thus the stresses in a cartridge of radius 1 cm are a factor of 10^{-8} smaller than inside the nozzle.

3.1.1.2 Flow through a circular orifice

The inlet of the nozzle is the first stage of the printing process where cells experience flow conditions that are assumed to be strong enough to harm them inside the suspension [65–69, 117]. For cylindrical nozzles the contraction of around two orders of magnitude in diameter takes place very sudden, thus leading to a localized flow acceleration. This mostly elongational flow stretches the cells while they are getting sucked into the nozzle. An analytical solution to the flow profile in this geometry is not available. The velocity field is therefore most easily obtained via numerical simulation of this problem, which has been done extensively in literature [48, 65, 66, 69, 117–120]. In this work, the cell-free flow into the nozzle is thus not investigated in detail. Numerical simulations with cell suspensions entering the constriction are performed in section 5.5.1.

3.1.1.3 Flow through a cylindrical channel

After the quick contraction at the inlet, the cell suspension is pushed through the nozzle itself. The pipe flow of a Newtonian fluid through an infinitely long cylinder, also known as Poiseuille flow, is a classical problem in fluid dynamics, and its solution can be found in every fluid dynamics text book [121, 122]. For convenience, it is briefly summarized in the following. With the assumptions of a stationary, laminar, uniaxial and pressure

driven flow [122, pp. 180 ff.], the velocity field — with the axial component u as only non-zero component — computes as

$$u(r) = u_{\max}\left[1 - \left(\frac{r}{R}\right)^2\right], \tag{3.2}$$

where R is the radius of the cylindrical channel and $u_{\max}$ denotes the maximum velocity at the axis of revolution which relates to the pressure gradient G as follows:

$$u_{\max} = -\frac{G}{4\eta}R^2 \tag{3.3}$$

The pressure gradient $G = \frac{\Delta P}{L}$ is defined as the hydrostatic pressure difference $\Delta P < 0$ along the unit length L. Due to the axisymmetry of the infinitely long channel, the strain rate $\dot{S}$ reduces to the shear rate

$$\dot{\gamma}(r) = \left|\frac{\partial u}{\partial r}\right| = -\frac{G}{2\eta}r\,, \tag{3.4}$$

from which the shear stress follows via multiplication with the viscosity as

$$\sigma(r) = \eta\dot{\gamma}(r) = -\frac{G}{2}r\,. \tag{3.5}$$

This linear radial dependency of the shear stress can easily be understood by considering the force balance of a cylindrical fluid element with radius r concentrically aligned with the channel axis: The forces acting on the cylinder caps are determined by the hydrostatic pressure drop as $P\pi r^2$ and $(P + \Delta P)\pi r^2$, respectively, whereas the force acting on the side face is computed via the viscous shear stress as $2\pi r L\sigma$. The force balance reads

$$P\pi r^2 = (P + \Delta P)\pi r^2 + 2\pi r L\sigma\,, \tag{3.6}$$

which directly yields (3.5) after rearrangement.

3.1.1.4 Flow through a conical channel

In a conical nozzle geometry, the channel is constantly tapering along the axis, requiring a constant displacement of fluid towards the center, thus developing radial flows. The flow problem becomes two-dimensional, but stays rotationally symmetric. It can hence be solved using the stream function approach, as in [121, pp. 138–140], or directly from the Navier-Stokes equations in spherical polar coordinates as done by Raptis *et al.* [123]. When applying these approaches to a conical bioprinter nozzle, entrance and exit effects are neglected similar to the infinitely long cylinder assumption in section 3.1.1.3.
For convenience, the solution of the flow field from [123] is repeated here. Expressed in spherical coordinates (ρ, θ, ϕ) originating from the tip of the cone, the (spherically) radial velocity component reads

$$u_\rho(\rho, \theta) = \frac{1}{\rho^2}\frac{3\Omega}{2\pi}\frac{\cos^2(\theta) - \cos^2(\theta_0)}{(1 + 2\cos(\theta))(1 - \cos(\theta_0))^2}\,, \tag{3.7}$$

with the volumetric flow rate Ω through the conus of half opening angle θ_0. This result is used in section 3.1.2.3 to validate the approximation of the flow of a power-law fluid in the same geometry. The viscous stress tensor

$$\sigma_{ij}(\rho,\theta) = \eta \dot{S}_{ij}(\rho,\theta) \tag{3.8}$$

can be computed from the strain rate. Since the remaining velocity components vanish ($u_\theta(\rho,\theta) = u_\phi(\rho,\theta) = 0$), the components of the rate of strain tensor reduce to:

$$\dot{S}_{\rho\rho}(\rho,\theta) = \frac{\partial u_\rho}{\partial \rho} \tag{3.9}$$

$$\dot{S}_{\theta\theta}(\rho,\theta) = \dot{S}_{\phi\phi} = \frac{u_\rho}{\rho} \tag{3.10}$$

$$\dot{S}_{\rho\theta}(\rho,\theta) = \dot{S}_{\theta\rho} = \frac{1}{2\rho}\frac{\partial u_\rho}{\partial \theta} \tag{3.11}$$

And the rate of strain is obtained using (2.6) as

$$\dot{S}(\rho,\theta) = \frac{3\Omega}{2\pi\rho^3} \frac{\sqrt{12(\cos^2(\theta) - \cos^2(\theta_0))^2 + 4\cos^2(\theta)\sin^2(\theta)}}{(1+2\cos\theta_0)(1-\cos\theta_0)^2}\,. \tag{3.12}$$

3.1.1.5 Flow transition into a free liquid strand

After the transit through the nozzle the bioink experiences the transition from a bounded flow into a free liquid strand, thereby subjecting the flow to a change in boundary conditions. The curved Poiseuille-like flow present inside the nozzle transitions into a plug-flow, where the entire cross-section of the fluid moves with the same velocity. This transition requires a radial redistribution of the axial velocity components: material near the axis is slowed down, while material near the channel wall experiences sudden acceleration. Hence, at the nozzle exit, the bioink itself and the therein suspended cells experience a radial displacement. It is reported for extruded bioinks to produce a widened strand after extrusion, as also shown in our experimental images in [pub3]. Among other parameters, the strand widening is used to characterize the so-called *printability* of the bioink [43].
In this thesis, we assume for simplicity that the free bioink strand maintains the same diameter as inside the nozzle. We therefore prescribe a no-slip boundary condition with vanishing perpendicular and tangential velocity components on the boundary inside the nozzle, and a slip boundary condition outside, allowing for a finite tangential velocity component at the surface. To the knowledge of the author, there is so far no analytical solution available for this problem. An approximative solution using the stream function formalism has been developed by Katharina Gräßel during her Master thesis [124], the main difference to the actual scenario being that her solution does not consider local change of the boundary condition, but solves the intermediate flow between a Poiseuille flow at infinite distance on the one side and a plug flow on the other.
In this thesis, the influence of the special flow conditions at the outlet of the bioprinter nozzle is studied numerically in great detail in [pub3].

3.1.2 Shear thinning fluids in important geometries

3.1.2.1 Power-law fluid in a cylindrical channel

One exception to the aforementioned mathematical difficulties in the treatment of shear thinning liquids is the power-law model introduced in section 2.1.2.1. As demonstrated in the supplementary information to [pub1], it is possible to solve the Navier-Stokes equations (2.2) with the common assumptions of a Poiseuille flow [122, pp. 180 ff.] and to find a solution to the velocity profile in an infinitely long cylinder. For convenience, this section repeats the well-known solution for the velocity profile.
Assuming an incompressible, stationary, laminar, uniaxial, and pressure driven flow in an infinitely long cylinder (cf. 3.1.1.3), the Navier-Stokes equation (2.2) reduces to [pub1]

$$G = \frac{1}{r}\frac{\partial}{\partial r}\left(r\eta(\dot{\gamma})\frac{\partial u}{\partial r}\right), \tag{3.13}$$

with the strain rate given by the shear rate $\dot{\gamma} = -\frac{\partial u}{\partial r}$ as in (3.4). Inserting the power-law formulation for the viscosity (2.7), one obtains the well-known velocity profile:

$$u(r) = \left(-\frac{G}{2m}\right)^{\frac{1}{n}} \frac{n}{n+1} R^{1+\frac{1}{n}} \left[1 - \left(\frac{r}{R}\right)^{1+\frac{1}{n}}\right] \tag{3.14}$$

The maximum velocity is identified by the first three factors as

$$u_{\max} = \left(-\frac{G}{2m}\right)^{\frac{1}{n}} \frac{n}{n+1} R^{1+\frac{1}{n}} \tag{3.15}$$

and the average velocity is found through integration and division by the channel area [pub1] as

$$u_{\text{avg}} = u_{\max}\frac{n+1}{3n+1}\,. \tag{3.16}$$

In practice, the average extrusion velocity is typically chosen similar to the collector plate speed of the 3D bioprinter to provide consistent thickness and hence improve the shape fidelity of the printed strand [43]. From (3.16) and (3.15) the relation between the volumetric flow rate Ω and the pressure gradient is derived:

$$\Omega = \pi R^2 u_{\text{avg}} = \left(-\frac{GR}{2m}\right)^{\frac{1}{n}} R^3 \pi \frac{n}{3n+1} \tag{3.17}$$

The inverse relation is given by

$$G = 2m\left(\frac{3n+1}{n}\frac{\Omega}{R^{3+\frac{1}{n}}}\right)^{n}. \tag{3.18}$$

Since the radial dependency of the shear stress (3.5) remains unchanged when applying power-law rheology [pub1], (3.17) can be expressed in terms of the maximum shear stress $\sigma_{\max}$ as

$$\Omega = \left(\frac{\sigma_{\max}}{m}\right)^{\frac{1}{n}} R^3 \pi \frac{n}{3n+1}\,. \tag{3.19}$$

The velocity also determines the time necessary for a fluid element at position r to transit a nozzle of length L, termed the residence time [43]. It becomes relevant for duration-dependent cell damage considerations [69] and is simply found with (3.14) to be

$$\tau(r) = \frac{L}{u(r)} \,. \tag{3.20}$$

3.1.2.2 Prediction methods from the power-law fluid

With the solution to the Navier-Stokes equation for the power-law viscosity model in section 3.1.2.1, we derive several quantities of interest as monitoring tools for the bioink extrusion process.
One of the major suspects for flow induced cell damage during the extrusion process are the occurring shear stresses [44]. We therefore propose in the following a method to compute the cell survival as function of the maximum stress present in a cylindrical printing nozzle. We consider cells as significantly smaller than the nozzle dimensions, and assume that they remain at their radial position. Therefore, the radial distribution of the cells $c(r)$ does not change along the length of the nozzle. The next step is to determine the fraction of cells that flows inside a cylindrical shell of radius r around the axis from the velocity profile (3.14) via:

$$\omega_C(r) = \frac{\int_0^{2\pi}\int_0^{r} u(r')c(r')r'\,\mathrm{d}r'\,\mathrm{d}\phi}{\int_0^{2\pi}\int_0^{R} u(r')c(r')r'\,\mathrm{d}r'\,\mathrm{d}\phi} \tag{3.21}$$

The simplest form of cell distribution, a uniform one, is described by a constant

$$c(r) = c_0 \,, \tag{3.22}$$

which inserted into (3.21) yields the radial profile of the partial flow rate $\omega(r)$, i. e., the percentage of material that flows inside a cylindrical shell of radius r, divided by the total flow rate (3.17). It yields:

$$\omega(r) = \frac{c_0\int_0^{2\pi}\int_0^{r} u(r')r'\,\mathrm{d}r'\,\mathrm{d}\phi}{c_0\int_0^{2\pi}\int_0^{R} u(r')r'\,\mathrm{d}r'\,\mathrm{d}\phi} = \frac{2\pi r^2 u_{\max}\left[1-\frac{2n}{3n+1}\left(\frac{r}{R}\right)^{1+\frac{1}{n}}\right]}{2\pi R^2 u_{\max}\left[1-\frac{2n}{3n+1}\right]} \tag{3.23}$$

$$= \frac{3n+1}{n+1}\left(\frac{r}{R}\right)^2 - \frac{2n}{n+1}\left(\frac{r}{R}\right)^{3+\frac{1}{n}} \tag{3.24}$$

Note that this equation has become independent of the pressure gradient and the consistency parameter m of the power-law model. Next, we introduce a critical quantity σ_{crit} to denote the shear stress threshold below which a cell stays unharmed and above which it is damaged irreversibly. Using the linear shear stress profile (3.5), the critical

radial position r_{crit}, which separates the safe from the harmful flow regions inside the channel, is determined as

$$r_{\mathrm{crit}} = \frac{\sigma_{\mathrm{crit}}}{\sigma_{\mathrm{max}}} R \,, \tag{3.25}$$

which can be inserted in (3.24). This ultimately yields the percentage of undamaged cells as a function of the maximum applied shear stress during extrusion,

$$\omega(\sigma_{\mathrm{max}}, \sigma_{\mathrm{crit}}) = \frac{3n+1}{n+1}\left(\frac{\sigma_{\mathrm{crit}}}{\sigma_{\mathrm{max}}}\right)^2 - \frac{2n}{n+1}\left(\frac{\sigma_{\mathrm{crit}}}{\sigma_{\mathrm{max}}}\right)^{3+\frac{1}{n}} , \tag{3.26}$$

with the only fluid related parameter being the shear thinning index n and the only cell related parameter being the critical shear stress σ_{crit}. Relation (3.26) is depicted in figure 3.1(a) for a critical cell stress of $\sigma_{\mathrm{crit}} = 400\,\mathrm{Pa}$. Starting at a damage-free plateau while $\sigma_{\mathrm{max}} < \sigma_{\mathrm{crit}}$, the survival percentage rapidly decreases for $\sigma_{\mathrm{max}} > \sigma_{\mathrm{crit}}$. It becomes apparent, that the influence of the shear thinning index n, although present, does not drastically change the shape of the curve.
One modification to this method can be made by introducing the typical variance which is inherent to any biological system. A sample of a large number cells will tend towards a Gaussian distribution of the critical shear stress around the average value of σ_{crit}. The probability of finding a cell with critical stress σ is then given as

$$p(\sigma) = \frac{1}{\sqrt{2\pi\nu^2}} \exp\left(-\frac{(\sigma - \sigma_{\mathrm{crit}})^2}{2\nu^2}\right) , \tag{3.27}$$

with ν^2 denoting the variance here, not the kinematic viscosity. The survival percentage of cell computes as the average of (3.26) weighted with (3.27):

$$\tilde{\omega}(\sigma_{\mathrm{max}}, \sigma_{\mathrm{crit}}) = \int_0^\infty \omega(\sigma_{\mathrm{max}}, \sigma) p(\sigma)\, \mathrm{d}\sigma \tag{3.28}$$

Through numerical integration (3.28) can be evaluated in order to obtain the survival percentage of cells with a certain variance. An example result is plotted in figure 3.1(b) for a distribution of the cells' critical parameter with $\nu = \frac{1}{4}\sigma_{\mathrm{crit}}$. The additional parameter variability clearly smoothens the curve around $\sigma_{\mathrm{max}} = \sigma_{\mathrm{crit}}$. Again, the difference between by a highly shear thinning ($n = 0.1$) and a Newtonian bioink does not exceed 15 %.
In 5.4, we use this method to exactly reproduce literature data for stem cell survival measurements.

3.1.2.3 Flow approximation of a Power-law fluid in a conical channel

Although this thesis does not include a detailed numerical investigation of cells flowing through a conical geometry, it is worth mentioning, as besides cylindrical syringes conical dispenser tips are the other most popular choice for 3D bioprinting nozzles. The main technical motivation behind this is that the gradually flow-focusing geometry is expected

Figure 3.1: Cell survival percentage predicted as function of the maximum shear stress during extrusion for a critical shear stress $\sigma_{\text{crit}} = 400\,\text{Pa}$. (a) Dependency of the cell survival percentage on the shear thinning behavior. (b) Inclusion of a variance of $\nu = 100\,\text{Pa}$ of the critical shear stress softens the sharp edge at σ_{max}, while the influence of the shear thinning behavior stays unaffected.

(a)

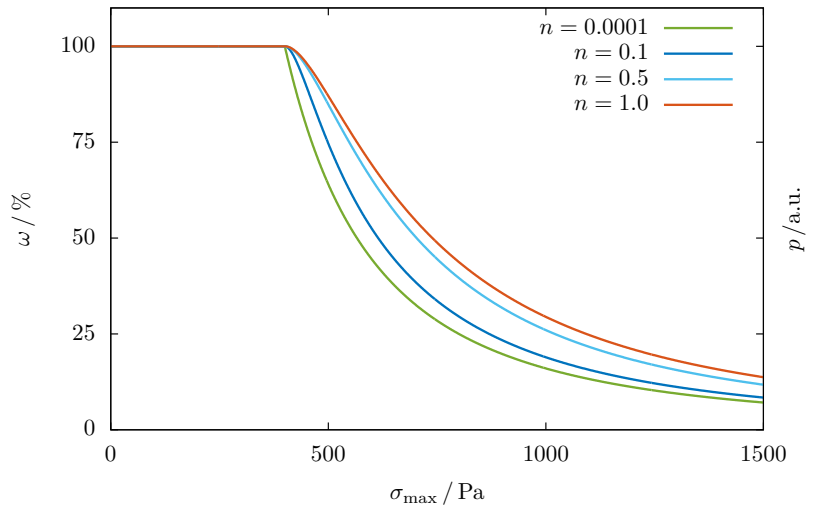

(b)

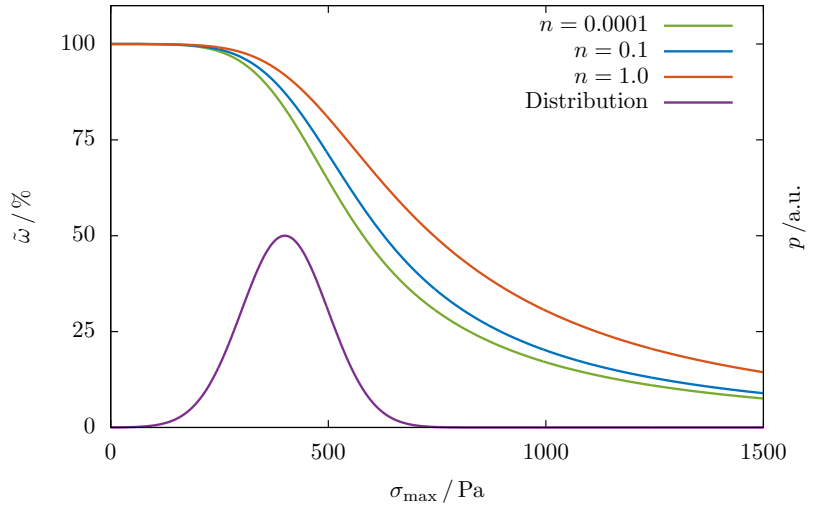

to create less shear stresses inside the nozzle compared to the much more confined cylindrical needles. However, along with the constant tapering come elongational stresses along the entirety of the nozzle, whereas for cylindrical needles these stresses only exist at the inlet and the exit. It is not yet conclusively established which of the two effects are more harmful towards cells [48, 65, 69, 117]. Since — in order to address this topic in future research — knowledge about the undisturbed flow profile will be essential, it is summarized in the following what the major challenges and differences compared to the cylinder are, and an accurate approximation method for typical conical bioprinter nozzles is presented.

As introduced in section 3.1.1.4 for the conical geometry, the strain rate (2.6) does not reduce to the a single term, but has a more complex dependency on the velocity field. Hence, inserting the strain rate into the viscosity model (2.7) introduces many co-dependent terms in the Navier-Stokes equation (2.2), making an analytical solution impossible even for the simple case of the power-law viscosity.

In the course of a bachelor project supervised by the author, an approximation method for the power-law velocity profile inside a conical nozzle has been developed. Clara Gremmelspacher [125] proposes in her thesis a method based on two assumptions: (i) The stream lines are pointing towards the tip of the conus and (ii) the axial velocity profile (in cylindrical coordinates aligned with the conus' axis of revolution) locally has the same form (3.14) as inside an infinite cylinder, but with changing wall radius $R(z)$. Hence it has been termed the wall-variation solution [125]. From that, a local pressure gradient can be derived using (3.18), and the two-dimensional radial velocity field component is obtained via the continuity equation (2.1) to [125]:

$$u_z(z,r) = \frac{3n+1}{n+1}\frac{\Omega}{\pi R^2(z)}\left[1-\left(\frac{r}{R(z)}\right)^{1+\frac{1}{n}}\right] \tag{3.29}$$

$$u_r(z,r) = u_z(z,r)\frac{r}{R(z)}\frac{\partial R(z)}{\partial z} \tag{3.30}$$

To supplement her work, this thesis presents a numerical validation of her method, by simulating a power-law fluid in a conus using the Lattice-Boltzmann method from 4.1. We simulate a funnel with a conical center piece, as schematically illustrated in the inset of figure 3.2(a). The cylindrical inlet and outlet extensions ensure a reasonably well developed Poiseuille flow before and after the conical section. From simulations of a conus with an openening angle of 5.7° with a Newtonian fluid, and a power-law fluid with $n = 0.5$ and $n = 0.1$, we extract slices of the velocity field which we compare to the axial (3.29) and radial (3.30) velocity in figure 3.2. We find that for opening angles $< 20°$ of the conus — which is an assumption that still covers typical bioprinter nozzles with angles of about 6° — the method remains very accurate. Interestingly, the numerical solution shows that the flattening of the axial velocity in the center is less pronounced than in the case of a cylinder. This might be particularly relevant for bioprinting applications, since the flattening of the profile is considered one of the main beneficial effects of shear thinning bioinks. We also find that the magnitude of the radial velocity is almost independent of the shear thinning behavior, whereas the axial velocity changes by a factor of 2.

Figure 3.2: (a) The approximation (black line), the analytical solution (orange dashed line), and the numerical solution (blue squares), agree perfectly in the case of a Newtonian fluid ($n = 1$) for the axial velocity, while the numerical solution slightly underestimates the radial velocity. The approximation compared to the numerical solution for (b) $n = 0.5$ and (c) $n = 0.1$. In both cases we find good agreement. The radial velocity from the numerical solution consistently underestimates the approximation. The inset shows the position, where the velocity slices are taken from the simulation of a funnel with opening angle 5.7°.

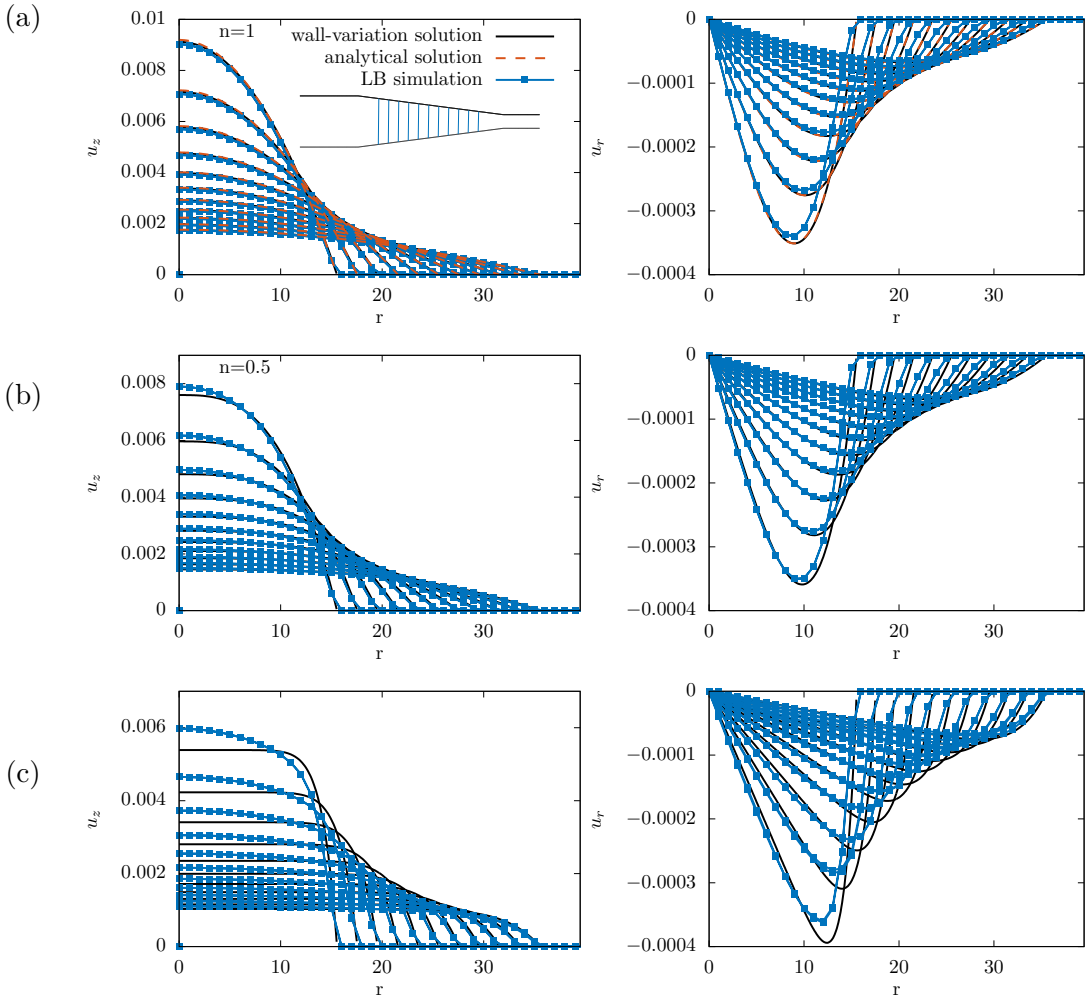

3.1.2.4 Carreau-Yasuda fluid in a cylindrical channel

As mentioned in section 2.1.2, the Cross model (2.9) and the Carreau-Yasuda description (2.12) account for the unrealistic shortcomings of the power-law viscosity model (2.7). However, upon inserting the simpler 3-parameter Cross model (2.9) into the Navier-Stokes equation for the flow in an infinite cylinder (3.13), it becomes apparent that an analytical solution of the resulting differential equation for u is not possible:

$$Gr = \frac{\partial}{\partial r}\left(r\frac{\eta_0}{1+(-K\frac{\partial u}{\partial r})^{\alpha}}\frac{\partial u}{\partial r}\right) \tag{3.31}$$

In our publication [pub1], we therefore present a semi-analytical approach to efficiently solve this equation without the need of computationally expensive simulation tools. In the following, the main idea of the method proposed in [pub1] is summarized.
From 3.1.2.1 we know that the the Navier-Stokes equation can be solved for the power-law viscosity model. Our method therefore utilizes a piecewise definition of the viscosity as function of the strain rate, as illustrated in figure 3.3(a). Each interval between two points of the analytical form of the viscosity $\eta(\dot{S})$ — or data points from a rheological measurement — is then interpolated with a power-law form. The individual parameters m and n for every power-law interval are determined by ensuring continuity at the interval bounds, as demonstrated in the supplementary material of [pub1] for the Carreau-Yasuda model. With the viscosity defined, a piecewise solution of the Navier-Stokes equation is derived, where continuity conditions for the velocity and the strain rate, and the boundary conditions, determine all integration constants. Figure 3.3(b) shows the obtained velocity profile. The accuracy of the method is determined solely by the number (and position) of interpolation intervals, as the remaining computations follow from an analytical form. During her Bachelor thesis [125], Clara Gremmelspacher extended this algorithm with two more viscosity interpolation methods: a piecewise constant (Newtonian) and a piecewise linear interpolation.
In practice, the Python implementation of this algorithm delivered with [pub1] has become a popular tool for other researchers to monitor the flow during experiments [60, 74]. Also, the input parameters for the numerical simulations with shear thinning fluids in this thesis were computed using this method, in order to ensure systematically changing flow conditions. This method's capabilities do not end here, though. In [pub1], the tool has been used to characterize the rheological parameters of a bioink by fitting them to measurements of the pressure versus flow rate dependency in a defined geometry. The parameters obtained were in agreement with classical cone-plane rheometer measurements of the same bioink [pub1].

Figure 3.3: Example computation of our semi-analytical method from [pub1] to compute the flow profile of a bioink with complicated viscosity model: (a) the viscosity versus shear rate function (dashed blue) is interpolated with power-law intervals (solid orange), and (b) the resulting velocity profile is a piecewise solution to the Navier-Stokes equation. Gray vertical lines indicate the 7 interval bounds. Parameters are $\eta_0 = 10\,\mathrm{Pa\,s}$, $K = 0.05$, $\alpha = 0.6$, $R = 50\,\mu\mathrm{m}$, and $G = 5 \times 10^7\,\mathrm{Pa\,m^{-1}}$.

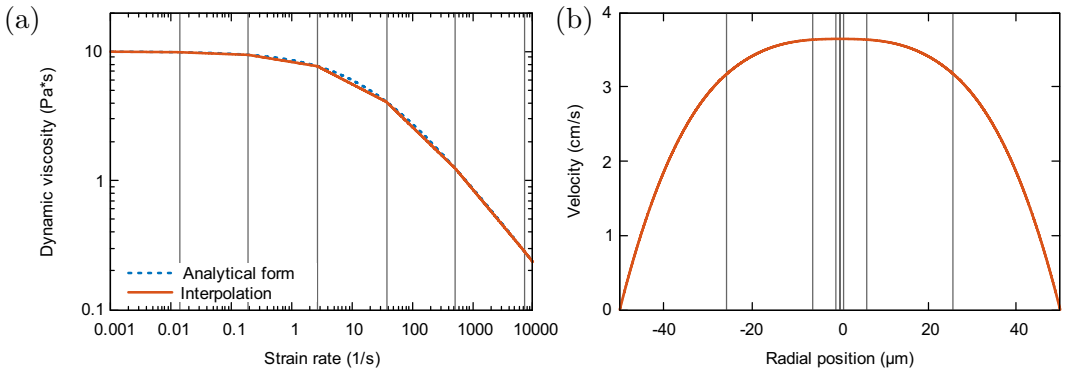

3.2 Deformation modes of cells

In the context of this thesis, one particular deformational mode — a triaxial deformation — of an initially spherical cell plays a major role in both purely elastic analytical computations as well as numerical simulations with flow coupling. When a cell is being compressed between two plates it undergoes an oblate-like deformation, while when it is suspended in a sheared liquid, it exhibits a prolate shearing deformation.
In the following sections, the cell stress is derived as a function of the deformation for the triaxial elongation of an incompressible sphere. The geometry is shown in figure 3.4: A sphere of initial radius a_0 is stretched along all three coordinate axes with their respective stretch factors α_1, α_2, and α_3. This deformation can be described with the linear transformation

$$y_i = \alpha_i x_i \tag{3.32}$$

from the undeformed (reference) coordinates $\vec{x}$ to the deformed coordinates $\vec{y}$. Hence, the deformation gradient tensor (2.15) is a diagonal matrix containing the principal stretches,

$$F_{ij} = \alpha_i \delta_{ij} \tag{3.33}$$

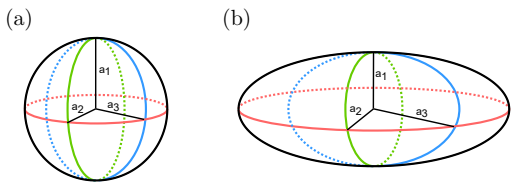

Figure 3.4: Through stretching with factors α_1, α_2, and α_3, along the coordinate axes, (a) a sphere with radius a_0 transforms into (b) a triaxial ellipsoid with semi-axes $a_1 = \alpha_1 a_0$, $a_2 = \alpha_2 a_0$, and $a_3 = \alpha_3 a_0$.

and the left Cauchy-Green deformation tensor (2.16) and its invariants (2.23), (2.24), and (2.25) are obtained as:

$$B_{ij} = \alpha_i^2 \delta_{ij} \tag{3.34}$$

$$J = \alpha_1 \alpha_2 \alpha_3 = 1 \tag{3.35}$$

$$I = \alpha_1^2 + \alpha_2^2 + \alpha_3^2 \tag{3.36}$$

$$K = \frac{1}{\alpha_1^2} + \frac{1}{\alpha_2^2} + \frac{1}{\alpha_3^2} \tag{3.37}$$

To quantify the cell stress, we employ the von Mises effective stress,

$$\sigma_{\mathrm{vM}} = \sqrt{\frac{1}{2}\Big[(\sigma_1 - \sigma_2)^2 + (\sigma_2 - \sigma_3)^2 + (\sigma_3 - \sigma_1)^2\Big]}\,, \tag{3.38}$$

which is computed from the principal stress differences — here the normal stress differences — from the Cauchy stress tensor (2.27) as detailed in [pub3]. As a measure for the cell deformation, we introduce the Taylor deformation parameter

$$D = \frac{a_{\mathrm{major}} - a_{\mathrm{minor}}}{a_{\mathrm{major}} + a_{\mathrm{minor}}}\,, \tag{3.39}$$

which is calculated from the major and minor semi-axes of the ellipsoid, as detailed in [pub2].

3.2.1 Oblate, prolate, and shear deformation

For the Mooney-Rivlin strain energy density [pub2], the normal stress differences, which are equal to the principal stress differences in case of a triaxial deformation, are

$$\sigma_i - \sigma_j = \mu\left[w\Big(\alpha_i^2 - \alpha_j^2\Big) + (1-w)\left(\frac{1}{\alpha_j^2} - \frac{1}{\alpha_i^2}\right)\right], \tag{3.40}$$

and they are further reduced by one variable when incompressibility (3.35) is assumed:

$$\sigma_1 - \sigma_2 = \mu\left[w\Big(\alpha_1^2 - \alpha_2^2\Big) + (1-w)\left(\frac{1}{\alpha_2^2} - \frac{1}{\alpha_1^2}\right)\right] \tag{3.41}$$

$$\sigma_2 - \sigma_3 = \mu\left[w\left(\alpha_2^2 - \frac{1}{\alpha_1^2\alpha_2^2}\right) + (1-w)\left(\alpha_1^2\alpha_2^2 - \frac{1}{\alpha_2^2}\right)\right] \tag{3.42}$$

$$\sigma_3 - \sigma_1 = \mu\left[w\left(\frac{1}{\alpha_1^2\alpha_2^2} - \alpha_1^2\right) + (1-w)\left(\frac{1}{\alpha_1^2} - \alpha_1^2\alpha_2^2\right)\right] \tag{3.43}$$

From these normal stresses, a general expression for the von Mises stress (3.38) of an incompressible sphere is derived:

$$\begin{aligned}\frac{2}{\mu}\sigma_{vM}^2 =&(\sigma_1-\sigma_2)^2+(\sigma_2-\sigma_3)^2+(\sigma_3-\sigma_1)^2 \qquad (3.44)\\ =&\left(\alpha_1^2-\alpha_2^2\right)^2\left[w^2+\frac{1}{\alpha_1^2\alpha_2^2}w(1-w)+\frac{1}{\alpha_1^4\alpha_2^4}(1-w)^2\right]\\ &+\left(\alpha_2^2-\frac{1}{\alpha_1^2\alpha_2^2}\right)^2\left[w^2+\alpha_1^2w(1-w)+\alpha_1^4(1-w)^2\right]\\ &+\left(\alpha_1^2-\frac{1}{\alpha_1^2\alpha_2^2}\right)^2\left[w^2+\alpha_2^2w(1-w)+\alpha_2^4(1-w)^2\right] \qquad (3.45)\end{aligned}$$

This lengthy form (3.45) can be further simplified for the case of an oblate (uniaxial compression) or prolate (uniaxial elongation) deformation. In both cases, two semi-axes are equal, thus $a=\alpha_1=\alpha_2$, and it follows for normal stresses (3.40)

$$\sigma_1-\sigma_2=0 \qquad (3.46)$$

$$\sigma_2-\sigma_3=\mu\left[w\left(a^2-\frac{1}{a^4}\right)+(1-w)\left(a^4-\frac{1}{a^2}\right)\right] \qquad (3.47)$$

$$\sigma_3-\sigma_1=-(\sigma_2-\sigma_3)\,. \qquad (3.48)$$

The cell stress is then given by

$$\sigma_{vM}=\mu\left|w\left(a^2-\frac{1}{a^4}\right)+(1-w)\left(a^4-\frac{1}{a^2}\right)\right|. \qquad (3.49)$$

Alternatively, when a simple shear deformation, described by $a=\alpha_1=\frac{1}{\alpha_2}$ and $\alpha_3=1$, is inserted into the normal stress differences (3.40), they read

$$\sigma_1-\sigma_2=\mu\left(a^2-\frac{1}{a^2}\right) \qquad (3.50)$$

$$\sigma_2-\sigma_3=\mu\left[w\left(\frac{1}{a^2}-1\right)+(1-w)\left(1-\frac{1}{a^2}\right)\right] \qquad (3.51)$$

$$\sigma_3-\sigma_1=\mu\left[w\left(\frac{1}{\alpha_1^2\alpha_2^2}-\alpha_1^2\right)+(1-w)\left(\frac{1}{\alpha_1^2}-\alpha_1^2\alpha_2^2\right)\right] \qquad (3.52)$$

and the corresponding von Mises stress is obtained as:

$$\sigma_{vM}=\mu\sqrt{(1-a^2)^2+\left(\frac{1}{a^2}-1\right)^2+(1-a^2)\left(\frac{1}{a^2}-1\right)-w(1-w)\left(a^2+\frac{1}{a^2}-2\right)^2} \qquad (3.53)$$

Equations (3.49) and (3.53) a are applied in section 5.2 to explain the dependency of the strain hardening behavior of the Mooney-Rivlin model compared to the neo-Hookean model by the influence of the deformational modes.

Figure 3.5: (a) Validation of the Roscoe theory and our numerical cell model in a linear shear flow for the neo-Hookean description. (b) The Mooney-Rivlin model shows stronger strain hardening than the neo-Hookean ($w = 1$) in the range $w = 1.0$ to 0.7; then, it behaves decreasingly strain hardening with decreasing w.

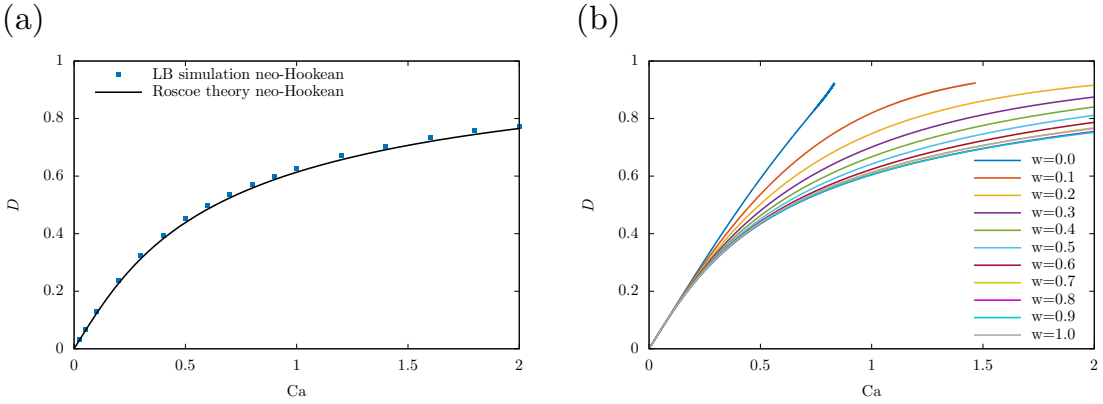

3.2.2 Roscoe theory for cell in flow

In 1922, Jeffery [94] proposed a solution of the Navier-Stokes equations to describe the motion of a rigid ellipsoidal particle in a linear flow. His theory has later been adapted by Roscoe [93] and extended to describe the deformation behavior of a viscoelastic particle with a rotating surface in both a linear shear flow and an elongational flow scenario. The details of the analytical approach are summarized and supplemented with further steps in section A, including a list of corrections of typographical errors in the original works of Jeffery [94] and Roscoe [93], as well as the conversion of important quantities used in both works. For convenience, we also deliver a summary of the theory in the supplementary material of [pub3]. We use a similar approach to adapt Jeffery's method for the computation of the velocity field around a rigid, rotating particle and compute the velocity field inside and outside an elastic, tank-treading, particle according to the Roscoe theory.

One of the key outcomes of the Roscoe theory in the context of this thesis is the quantification of the ellipsoidal deformation as function of the shearing motion of the surrounding fluid, as illustrated in figure 3.5 for a neo-Hookean (2.20) particle in simple shear flow. The neo-Hookean model (2.20) in its incompressible form corresponds to (type A) in [93]. Figure figure 3.5(a) shows the Taylor deformation (3.39) as a function of the Capillary number,

$$\mathrm{Ca} = \frac{\eta\dot{\gamma}}{\mu}\,, \tag{3.54}$$

the dimensionless shear rate, which compares the influence of the fluid stress to the cell stiffness. Roscoe [93] repeats his computations for an elastic model (type B), which corresponds to the second term in (2.21), i. e., the incompressible Mooney-Rivlin description minus the neo-Hookean term. During this thesis, the Mooney-Rivlin description is used in [pub2] to describe the mechanical behavior of fibroblast cells.

Hence, by superposition of type A and type B of [93] we obtain the Mooney-Rivlin hyperelastic description, which we insert into the Roscoe theory to compute the cell deformation in shear flow. Details of the derivation of Roscoe with the Mooney-Rivlin formulation follow in the appendix (section A). In figure 3.5(b) the resulting Ca-D curve is shown: Remarkably, the strain hardening effect compared to the neo-Hookean description ($w = 1$) first increases for decreasing w, up until $w \approx 0.7$. Then, lower w always result in a decreased strain hardening behavior. As discussed in the SI of [pub2], this behavior differs from what is found for a compression scenario: in AFM compression simulations, as in section 4.2.2, decreasing w results in a consistent increase in strain hardening strength compared to the neo-Hookean case.
An approach to understanding this difference is presented in section 5.2 in this thesis, using the analytical approach from section 3.2.1.

Chapter 4

Numerical methods

On the one hand, the complexity of the flow of a shear thinning bioink through different geometries, but especially the coupling between the flowing bioink and a suspended cell, on the other, render the exact analytical treatment of these scenarios impossible. Numerical methods are necessary to look more closely at the time-dependent dynamics of these systems.
The following sections introduce the lattice Boltzmann method as flow solver for non-Newtonian fluids, which is coupled via an immersed boundary algorithm to the hyperelastic cell model. Our AFM compression and indentation setup for the cell is explained thereafter.

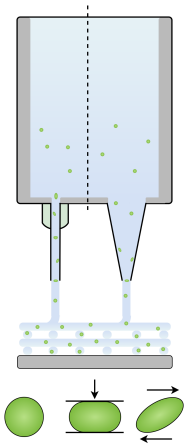

4.1 Shear thinning Lattice Boltzmann flow simulations

Complex flow scenarios — created by complicated geometries, boundary conditions, special fluid material properties, or the inclusion of soft elastic particles — often make an analytical solution of the Navier-Stokes equations (2.2) impossible. Therefore, a diverse set of numerical methods has been developed in the field of computational fluid dynamics to assess these complicated systems, each with their individual advantages and disadvantages. During this thesis, the Lattice Boltzmann method is used in all fully three-dimensional flow simulations; the coupling between bioink flow and cell is achieved with an immersed boundary algorithm. Both methods are briefly outlined in the following section.

4.1.1 Lattice Boltzmann method

The major difference of the Lattice Boltzmann method, when compared to other conventional computational fluid dynamics solvers, is that the Navier-Stokes equations are solved indirectly. Instead of solving the differential equation with numerical methods in discretized space and time like it is done in finite element or finite volume methods,

the evolution equation of a phase space distribution function $f(\vec{x}, \vec{v}, t)$ according to Boltzmann's kinetic theory is solved on a regular lattice. Fluid dynamics are obtained in a second step by identifying several statistical moments of the distribution function with hydrodynamic quantities via the Chapman-Enskog analysis [126, 127].
For the numerical implementation, the phase space is discretized by fixing a set of discrete velocities $\vec{c}_i$, which constrain the motion of the particles described through f to the spatial Eulerian grid denoted by its vertices at position $\vec{x}_j$. The temporal evolution of the velocity components f_i of the distribution function (or short: population) on the lattice is described by the Lattice Boltzmann equation

$$f_i(\vec{x} + \vec{c}_i \Delta t, t + \Delta t) = f_i(\vec{x}, t) + \Omega_i(\vec{x}, t)\Delta t \,, \tag{4.1}$$

with the time increment for the Euler integration step Δt. The collision operator Ω_i comprises all physical interactions that alter the distribution function, e. g., the microscopic collision or viscous relaxation, but also force coupling with the cell. During one time step, the population is further advected into i-direction.
In this thesis, the multiple relaxation time (MRT) scheme with the D3Q19 velocity set of the software package ESPResSo [71, 72] is used. It allows, in particular, for a stable implementation of the shear thinning rheological properties of the bioinks introduced in section 2.1.2 via the inclusion of strain rate dependent relaxation times as discussed in S-4 of the SI of [pub1] or explained in great detail in the author's Master thesis on this topic [128]. For the simulation of any no-slip boundary, a simple bounce-back algorithm is used [127]. To simulate the plug flow of the free bioink strand, we use an extended bounce-back algorithm, which allows for a finite tangential velocity component at the boundary [104]. While, in principle, a moving object like a cell could also be described using the fluid's Eulerian grid, an implementation with more flexible, moving boundaries using an immersed boundary approach is advantageous.

4.1.2 Immersed boundary algorithm

Two-way coupling between cell and bioink is realized according to the following procedure: The Lagrangian points of the cell, which are immersed in the Eulerian grid of the fluid, are advected with the corresponding, interpolated velocity of the fluid at their position. As detailed in the next section 4.2, this displacement results in elastic forces according to the elastic model of the cell. In the second step, these forces are redistributed from the current cell vertex onto the adjacent fluid vertices, by entering into the collision operator in (4.1). As further elaborated in [pub2], this algorithm essentially gives the cell viscoelastic properties, where the viscosity inside the particle resembles that of the surrounding fluid.

4.2 Hyperelastic cell model

The hyperelastic model for the simulation of cells has been one of the main developments during this thesis. In [pub2], we first introduce the model and provide extensive numerical and experimental validation to prove the applicability of this rather simplified picture of a biological cell. Later improvements lead to the application of the model in [pub3] to construct prediction methods for cell deformations during bioprinting. For convenience, the main idea and computational procedure are briefly summarized in the following. Further details can be found in [pub2].

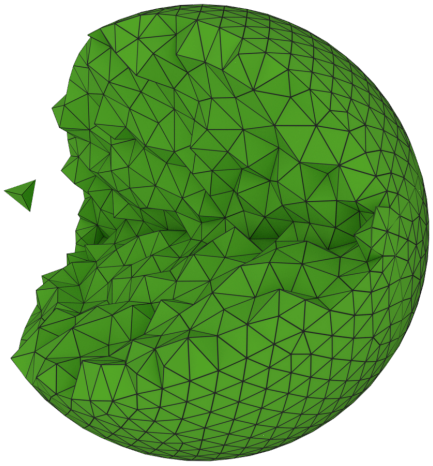

Figure 4.1: Cut-through view of the spherical cell model revealing its inner tetrahedralized mesh.

The cells in this thesis are modeled as a homogeneous, isotropically elastic body with spherical reference shape. Using the software Gmsh [129], a uniform inner tetrahedral mesh is created, as it is shown in figure 4.1. As described in detail in [pub2] and [pub3], the following relations are used on every tetrahedron to compute the forces and stress distribution from the strain energy density (2.20) and (2.21) and the displacement (2.14) inside the cell during the simulation: The vertex forces are computed through the derivative of the strain energy density U with respect to the vertex displacement, multiplied with the reference volume of the tetrahedron as

$$f_i^\beta = -V_0 \frac{\partial U}{\partial u_i^\beta} \,, \tag{4.2}$$

where the index i denotes the Cartesian component and the superscript $\beta = 0, 1, 2, 3$ indicates the index of the vertex inside one tetrahedron. The forces on vertices shared by multiple tetrahedra are summed up. As stress measure, we use the Cauchy stress tensor [116, pp. 43 ff.], which is obtained from U via

$$\sigma_{ij} = J^{-1} F_{ik} \frac{\partial U}{\partial F_{jk}} \,, \tag{4.3}$$

with the Jacobian determinant J (2.23) and the deformation gradient tensor F_{ij} (2.15). As detailed in [pub3], the scalar von Mises stress is a handy quantity to measure the stress acting on the cell in flow. We define the cell stress as in [pub3] via

$$\sigma_{\mathrm{vM}} = V_{\mathrm{cell}}^{-1} \sum_{t=0}^{N_{\mathrm{tetra}}} V^{(t)} \sigma_{\mathrm{vM}}^{(t)} \,, \tag{4.4}$$

which is the von Mises stress in every tetrahedron $\sigma_{\mathrm{vM}}^{(t)}$, given by

$$\sigma_{\mathrm{vM}}^{(t)} = \sqrt{\frac{1}{2}\left[\left(\sigma_1^{(t)} - \sigma_2^{(t)}\right)^2 + \left(\sigma_2^{(t)} - \sigma_3^{(t)}\right)^2 + \left(\sigma_3^{(t)} - \sigma_1^{(t)}\right)^2\right]} \,, \tag{4.5}$$

averaged over all tetrahedra and weighted with the tetrahedron volume $V^{(t)}$.

Figure 4.2: (a) Micrographs of NIH-3T3 cells flowing in a microchannel at different positions and different pressures (modified from [74]) in good visual agreement to (b) our simulations of the same setup with a cell with a shear modulus of $\mu = 270\,\mathrm{Pa}$.

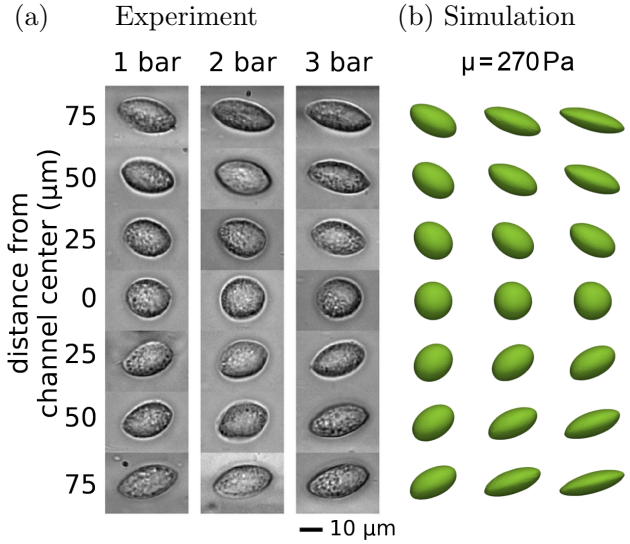

4.2.1 Microfluidic validation

We use the experiments performed by our collaborators in [74] to provide further experimental validation to our cell model — in an actual flow scenario. In figure 4.2(a) bright-field micrographs of NIH-3T3 cells flowing at different positions in a 200 µm × 200 µm microchannel at pressures 1, 2, and 3 bar, suspended in a 2 % alginate solution are shown. While centered flowing cells remain almost spherical, they assume an increasingly elongated ellipsoidal shape further away from the center. When simulating the same setup (alginate parameters from [pub1]) with cells at different lateral positions in the channel with a shear modulus of 270 Pa, we find in figure 4.2(b) an excellent visual agreement between experiment and simulation.

4.2.2 Compression simulations

During this thesis, a simulation program has been developed that mimics different experimental atomic force microscopy (AFM) setups. The first one is the compression of a cell between two parallel plates, as illustrated in the simulation snapshots in figure 4.3(a,b), which is similar to the fluidic force microscopy (FluidFM®) measurements as they were performed for [pub2]. The second setup is the cell indentation with a colloidal probe [130], shown in figure 4.3(c,d), which is another common tip geometry for AFM cantilevers. The method, as detailed in the Supplementary Information of [pub2] (section S-3), computes the relaxation of the cell between a fixed plate at the bottom and a second plate, or a spherical indenter, which is moving downwards to compress the cell.
The method does explicitly not treat any fluid motion inside or outside the particle

Figure 4.3: Simulation snapshots of (a,b) the AFM compression and (c,d) the AFM colloidal probe indentation simulations.

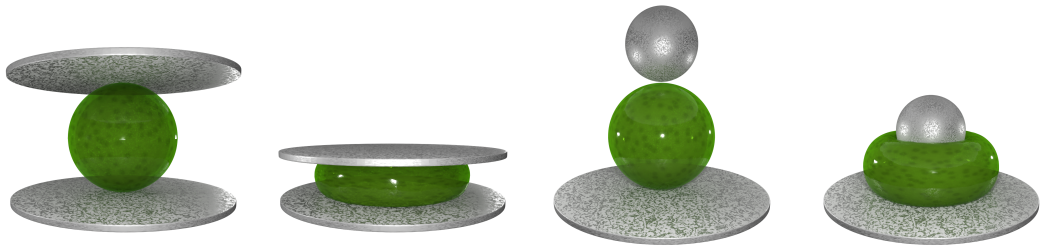

(a) (b) (c) (d)

and thus computes the purely elastic response of the cell to an externally imposed deformation.

4.2.3 Extensibility, diversity in applications

While in the course of this thesis the cell model is mostly applied to single, or multiple, suspended cells flowing in a bioink, the descriptive power of the hyperelastic description goes further: As also shown in [pub2], the compressive mechanics of hydrogel particles of about 80 µm diameter, which are several times larger than the typical cell considered in this work, are well described by our model. The scalability should not be limited there, though. Considering the effectively homogeneous behavior of cells as discussed in section 5.1, an aggregate of multiple cells may likely exhibit similar elastic properties which can be described with knowledge of the single cell mechanics. It is therefore well imaginable to apply our model also to large clusters of cells, cell spheroids, or organoids, and for it to be of use in numerical investigations of these systems. All simulations and analytical computations presented in this thesis assume a cell with a spherical equilibrium shape due to the desired simplicity of the system. The model is of course not limited to this particular case and can easily be extended to describe objects with a different equilibrium geometry.

Chapter 5

Application of the developed methods

In this chapter, our analytical methods from chapter 3 and our numerical methods from chapter 4 are applied to specific problems. In section 5.1, we elucidate the importance of intracellular heterogeneities and present a mechanically equivalent, homogeneous, cell model. Section 5.2 explains how second term in the strain energy functional of the Mooney-Rivlin model results in an increase of the strain hardening behavior compared to the neo-Hookean description when the cell is experiencing compression, while a decrease is predicted by the extended Roscoe theory for a Mooney-Rivlin particle in linear shear flow. Then, we present in section 5.3 our method from [pub3] for the prediction of the average elongational stresses present at the exit of a 3D bioprinter nozzle, supplemented by corresponding analytical calculations to assess this quantity directly using the power-law viscosity model. From the power-law model we also developed a method to predict the cell survival in a printing process, which we apply in section 5.4 to reproduce a large experimental data set. Finally, in section 5.5 we present an analysis of the entire 3D bioprinting process for a single cell and a dense cell suspension using our developed numerical methods.

5.1 The role of intracellular heterogeneities

One of the major simplifications of the cell model used in this work is given by its homogeneous and isotropic elasticity. On the one hand, this assumption is commonly used in numerical cell models [83, 84], for the sake of simplicity and computational efficiency. On the other hand, also experimental techniques for the mechanical characterization of cells [80] implicitly assume a mechanically homogeneous cell interior. Real biological cells, however, have internal structures as complex as they are diverse.
In [pub4], we address the question of how big the deviations introduced by the homogeneity assumption are compared to an actual heterogeneous internal cell structure. We investigate three different cell models, as shown in figure 5.1: First, a well-defined inhomogeneity is used to study the influence of its stiffness, size, shape, and position, on the cell behavior. Then, we employ a randomly inhomogeneous model, where we assign a random stiffness to every tetrahedron of the mesh, to combine all factors at once. Both models we compare with a homogeneous equivalent cell, that we obtain by using

Figure 5.1: The reference shape of our three cell models investigated in [pub4], revealing the inner structure: (a) Our homogeneous equivalent cell, with an effective stiffness obtained as volume weighted average from the constituents', (b) a well-defined inhomogeneity inside the cell volume with various size, stiffness, shape, and position, (c) a randomly inhomogeneous cell with a different stiffness assigned to each tetrahedron of the mesh.

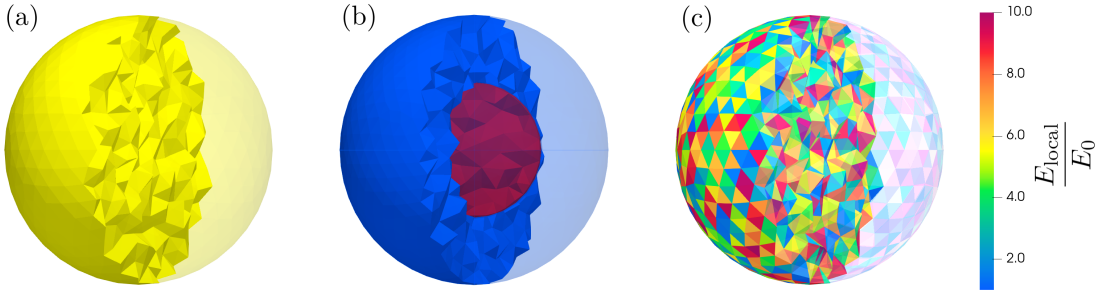

the same stiffness — obtained from a volume weighted average of the heterogeneous structure's constituents — in the entire mesh. In our publication [pub4], we combine our mechanical characterization systems from both [pub2], [pub3], and [74], i. e., the cell under compression and in flow, and systematically investigate the possibility to substitute an inhomogeneous cell with our homogeneous equivalent.
Strikingly, in all cases, the stationary and quasi-static force versus deformation behavior are in perfect agreement with that of the homogeneous equivalent cell. Even for an inhomogeneity that is 50 times, i. e., unrealistically, stiffer than the rest of the cell, we observe practically the same results. Only the dynamic shape of a cell in flow alters, since the tank-treading motion of the material forces a stiffer part at surface to produce a bump that periodically moves along. Nevertheless, while the influence of these bumps is visible in the time evolution of the deformation parameter, its time averaged value exactly represents the one obtained from the homogeneous equivalent cell.

5.2 Explanation of the change in strain hardening behavior of the Mooney-Rivlin model

As was shown before in section 3.2.2 and [pub2] for the Mooney-Rivlin model, the strain hardening effect depends on the mode of deformation. In case of a compression, the higher order terms lead to an increase of the strain hardening when compared to the neo-Hookean model. In the linear shear flow scenario solved by the Roscoe theory [93], on the other hand, the strain hardening effect decreases or increases, depending on the ratio between the shear moduli μ_1 and μ_2 from (2.21). First, using the simple analytical approach developed in section 3.2.1, this general difference is explained by a change of roles of the first and second order deformation terms for oblate and prolate deformations. The turn of the strain hardening effect in shear flow for $w \approx 0.7$ is explained using the shear model from section 3.2.1 at the end of this section.

5.2.1 Role of oblate and prolate deformation

The Taylor deformation (3.39) is calculated from the major and minor semi-axes of the triaxial ellipsoid. Choosing the two equal semi-axes $a = \alpha_1 = \alpha_2$, we for set the oblate spheroidal deformation

$$a_{\text{major}}^{\text{oblate}} = \alpha_1 = \alpha_2 = a \tag{5.1}$$
$$a_{\text{minor}}^{\text{oblate}} = \alpha_3 = a^{-2}\,. \tag{5.2}$$

This yields the Taylor deformation and its inverted form, which gives the distinct semi-axis as function of the Taylor deformation:

$$D^{\text{oblate}} = \frac{a^3-1}{a^3+1} \quad \Leftrightarrow \quad a = \left(\frac{1+D}{1-D}\right)^{\frac{1}{3}} = f(D)^{\frac{1}{3}} \tag{5.3}$$

For the prolate spheroid we have accordingly

$$a_{\text{major}}^{\text{prolate}} = \alpha_3 = a^{-2} \tag{5.4}$$
$$a_{\text{minor}}^{\text{prolate}} = \alpha_1 = \alpha_2 = a\,, \tag{5.5}$$

and obtain for the dependency of a on the Taylor deformation

$$D^{\text{prolate}} = \frac{1-a^3}{1+a^3} \quad \Leftrightarrow \quad a = \left(\frac{1-D}{1+D}\right)^{\frac{1}{3}} = f(D)^{-\frac{1}{3}}\,. \tag{5.6}$$

The functional relation between the cell stress and deformation is then recovered by inserting a from (5.3) and (5.6) into (3.49) as:

$$\sigma_{\text{vM}}^{\text{oblate}} = \mu\Big|w\Big(f^{\frac{2}{3}} - f^{-\frac{4}{3}}\Big) + (1-w)\Big(f^{\frac{4}{3}} - f^{-\frac{2}{3}}\Big)\Big| \tag{5.7}$$
$$\begin{aligned}\sigma_{\text{vM}}^{\text{prolate}} &= \mu\Big|w\Big(f^{-\frac{2}{3}} - f^{\frac{4}{3}}\Big) + (1-w)\Big(f^{-\frac{4}{3}} - f^{\frac{2}{3}}\Big)\Big| \\ &= \mu\Big|(1-w)\Big(f^{\frac{2}{3}} - f^{-\frac{4}{3}}\Big) + w\Big(f^{\frac{4}{3}} - f^{-\frac{2}{3}}\Big)\Big|\end{aligned} \tag{5.8}$$

These relations are depicted in figure 5.2(a,b) for $w \in [0,1]$. When writing (5.7) and (5.8) in terms of the elastic moduli μ_1 and μ_2,

$$\sigma_{\text{vM}}^{\text{oblate}} = \Big|\mu_1\Big(f^{\frac{2}{3}} - f^{-\frac{4}{3}}\Big) + \mu_2\Big(f^{\frac{4}{3}} - f^{-\frac{2}{3}}\Big)\Big| \tag{5.9}$$
$$\sigma_{\text{vM}}^{\text{prolate}} = \Big|\mu_2\Big(f^{\frac{2}{3}} - f^{-\frac{4}{3}}\Big) + \mu_1\Big(f^{\frac{4}{3}} - f^{-\frac{2}{3}}\Big)\Big|\,, \tag{5.10}$$

it becomes clear that the roles of the two moduli switch between oblate and prolate deformations. Thus, as depicted in figure 5.2(a), decreasing w increases the strain hardening effect compared to the neo-Hookean case ($w = 1$), while in figure 5.2(b) decreasing w decreases the strain hardening effect.
A comparison between this analytical approximation for the oblate deformation (5.7) and our cell compression simulations is shown in figure 5.3. Surprisingly, the neo-Hookean case ($w = 1$) is fairly well described by the approximative model; then, the deviations increase to roughly 1.5 times the cell stress obtained from the simulation for $w = 0$.

Figure 5.2: Dimensionless cell stress σ_{vM}/μ versus Taylor deformation D as function of the parameter w for (a) an oblate and (b) a prolate deformation. The strain hardening effect compared to the neo-Hookean formulation ($w = 1$) consistently increases for oblate and decreases for prolate deformations.

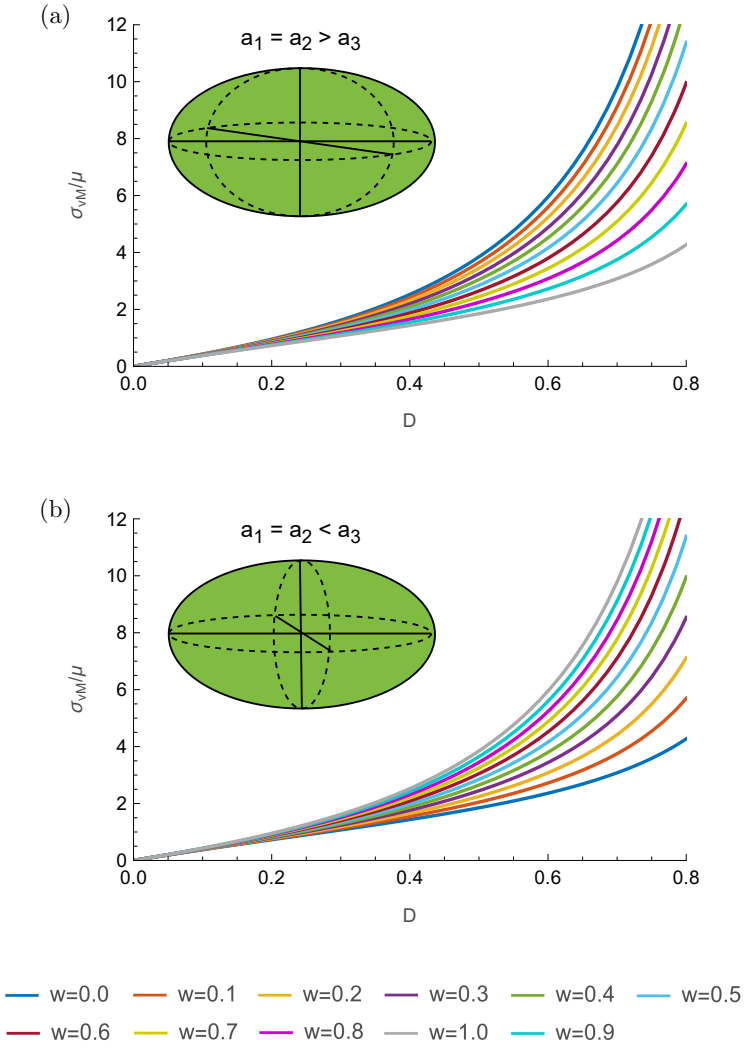

Figure 5.3: Dimensionless cell stress from our AFM simulations in [pub2] compared to the oblate spheroid approximation from figure 5.2(a). Colors refer to the same w as in figure 5.2.

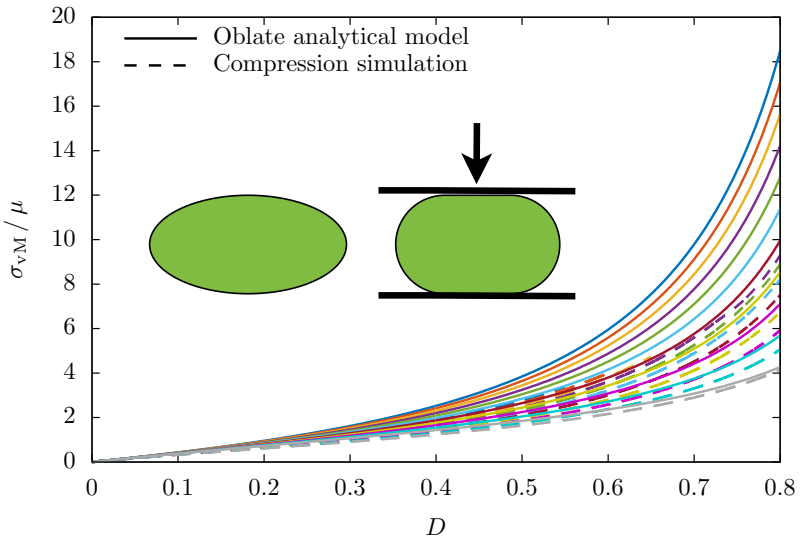

The model consistently overestimates the realistic compression from the simulation due to the geometrical differences: Being compressed between two plates, the cell in the simulation develops two flat circular contact faces increasing in size, while the oblate spheroid has a continuously curved surface. The former, disc-like, geometry is not as well represented through the Taylor deformation.
A slightly different result is obtained when comparing the analytical approximation of (5.8) with data from the Roscoe theory (section 3.2.2), shown in figure 5.4. Since the ellipsoidal deformation of the cell in shear flow computed from the Roscoe theory is quite similar to the prolate spheroid, the Taylor deformation is a good deformation measure for both scenarios. Starting with the same slope for small D, the limiting cases $w = 0$ and $w = 1$ under- and overestimate the behavior predicted by the Roscoe theory. The stress approximation using a prolate spheroid also consistently increases with w. In the data from the Roscoe theory, a turn is observed at $w \approx 0.7$, beyond which the strain hardening effect becomes less. An explanation for that phenomenon is approached in the following, by considering the pure shear deformation for the cell stress calculations instead of a prolate (uniaxially elongated) spheroid.

5.2.2 Effect of shear deformation

In an actual shear flow, the Roscoe theory shows the strain hardening behavior for a neo-Hookean material ($w = 1$). With decreasing w, first an increase of the strain hardening effect is observed until $w \approx 0.7$, below that the effect continuously decreases again. This change in behavior is not captured by the uniaxial description in section 5.2.1; it can, however, be approached using a simple shear deformation — which is not to be confused

Figure 5.4: Dimensionless cell stress from the Roscoe theory [93] compared to the prolate spheroid approximation from figure 5.2(b). Colors refer to the same w as in figure 5.2.

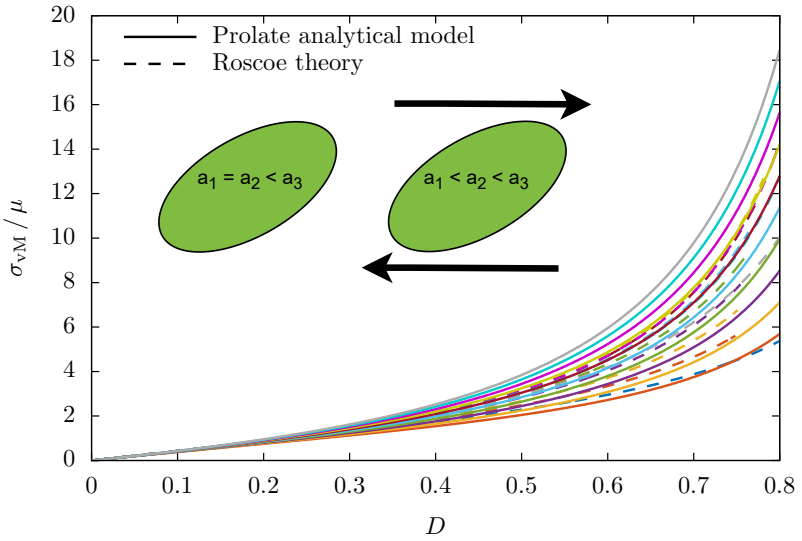

with the deformation inside a shear flow. In shear flow, the incompressible spherical cell assumes the shape of a triaxial ellipsoid with $\alpha_3 = \frac{1}{\alpha_1\alpha_2} \neq 1$, whereas the ideal shearing deformation fixes $\alpha_3 = 1$.
Choosing the major semi-axis as $a = \alpha_1$ we for set the oblate spheroidal deformation

$$a_{\text{major}}^{\text{oblate}} = \alpha_1 = \frac{1}{\alpha_2} = a \tag{5.11}$$

$$a_{\text{minor}}^{\text{oblate}} = \alpha_3 = a^{-2}\,, \tag{5.12}$$

from which the Taylor deformation and its inversion are derived as:

$$D^{\text{oblate}} = \frac{a^2-1}{a^2+1} \quad \Leftrightarrow \quad a = \left(\frac{1+D}{1-D}\right)^{\frac{1}{2}} = f(D)^{\frac{1}{2}} \tag{5.13}$$

Inserting this result into the cell stress equation (3.53), one obtains

$$\sigma_{vM} = \mu\sqrt{(1-\alpha_1^2)^2 + \left(\frac{1}{\alpha_1^2}-1\right)^2 + (1-\alpha_1^2)\left(\frac{1}{\alpha_1^2}-1\right) - w(1-w)(\alpha_1^2+\frac{1}{\alpha_1^2}-2)^2}\,, \tag{5.14}$$

which is symmetric around $w = \frac{1}{2}$, implying that the strain hardening effect changes at this point.
Figure 5.5 shows the cell stress versus deformation data for the shear model in comparison to the Roscoe theory. For small deformations, the approximation describes the data from the Roscoe theory quite well, however, the stress differences covered by the variation of w are comparably small, and the ideal shear approximation mostly underestimates the

Roscoe theory. This does come not surprising, since the actual cell geometry according to the Roscoe theory lies somewhere between the prolate spheroid and the sheared sphere. Additionally, the turning point of the strain hardening effect at $w = 0.5$ is below the value of $w \approx 0.7$ observed for the Roscoe theory. Since the prolate spheroid approximation does not show this behavior, the Roscoe theory lies between the two approximations also in this matter.

Figure 5.5: (a) Dimensionless cells stress from the sheared spheroid approximation with change of shear thinning behavior at $w = 0.5$. (b) Dimensionless cell stress from the Roscoe theory [93] compared to the sheared spheroid approximation from (a).

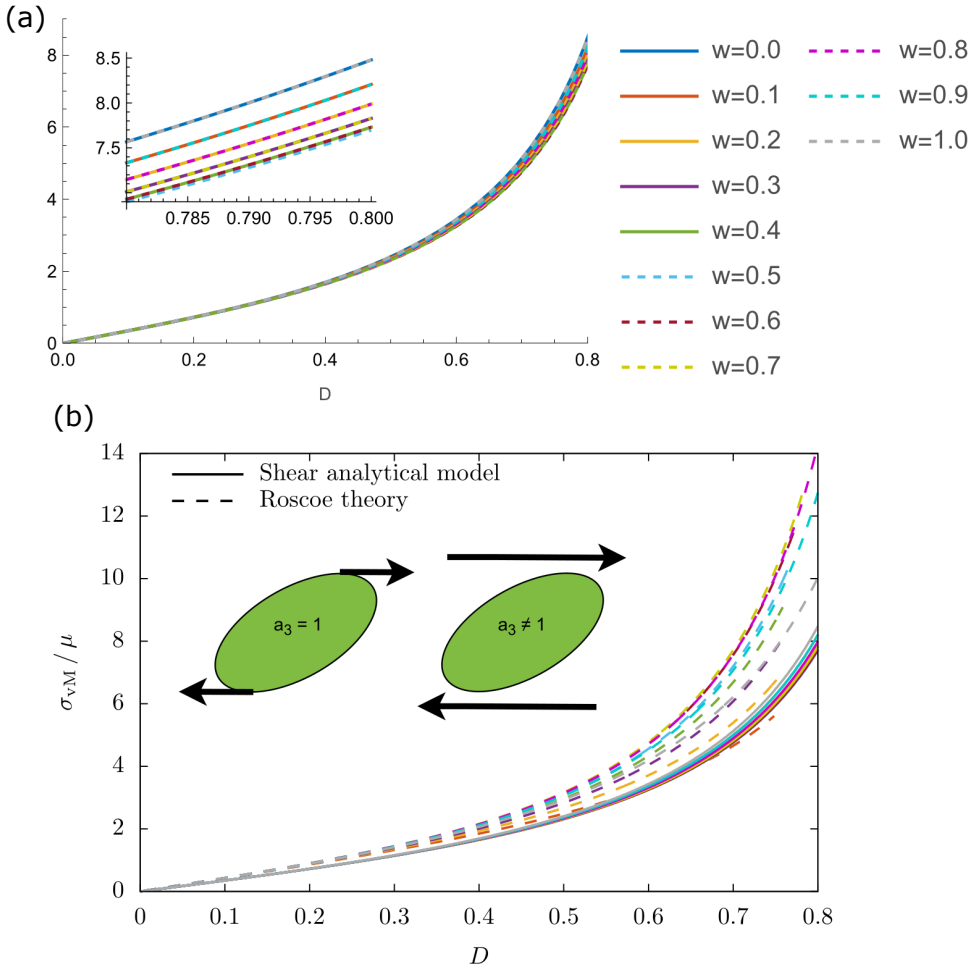

5.3 Estimating the elongational stress at the nozzle exit

As introduced in section 3.1.1.5, the change of the flow conditions from inside the nozzle to the free bioink strand come along with radial flow components at the nozzle exit, which cause the cells passing the transition to be stretched in radial direction, when flowing close to the center.
In [pub3] we provide a detailed numerical analysis of this effect in dependency of the shear thinning rheology of the bioink. Our relevant key findings in [pub3] for this part can be summarized as follows: First of all — inside the nozzle — there is a pressure dependent migration of the cells towards the center, which will focus the cell distribution at the nozzle exit towards the center. The effect of the elongational flow present there will therefore have an effect on a larger portion of the cells than it would have on a uniform radial cell distribution. We conduct a series of simulations of cell-free bioinks at the exit to determine the length scale at which these flow components take effect. Interestingly, the width of the transition is found practically independent of the rheology and has a length scale of two times the channel radius. This finding we use to deduce an accurate approximation for the elongation rate $\dot{\varepsilon}$ at the nozzle exit which only utilizes flow quantities known from the flow inside the nozzle, i. e., the maximum and average velocity of the infinite cylinder computations. The relation ([pub3] equation (15))

$$\dot{\varepsilon} \approx \frac{u_{\max} - u_{\text{avg}}}{2R} \tag{5.15}$$

accurately predicts the average elongational rate, and thus the average elongational stress, acting on cells at the center of the nozzle exit.
This estimate can be applied to the computations using the simple power-law viscosity from section 3.1.2.1 as well. We obtain

$$\dot{\varepsilon} \approx \frac{u_{\text{avg}} - u_{\max}}{2R} = \frac{n^2}{(n+1)(3n+1)} \left(\frac{\sigma_{\max}}{m} \right)^{\frac{1}{n}} \tag{5.16}$$

for the elongation rate as function of the maximum shear stress inside the nozzle. Using the strain rate [pub3]

$$\dot{S} = \sqrt{3} |\dot{\varepsilon}| \,, \tag{5.17}$$

the estimated elongational stress at the exit is found as

$$\sigma^{\text{elong}} = \sigma_{\max} \left[\sqrt{3} \frac{n^2}{(n+1)(3n+1)} \right]^n \,, \tag{5.18}$$

which depends on the shear thinning exponent n as only material parameter. The ratio $\frac{\sigma^{\text{elong}}}{\sigma_{\max}}$ is shown in figure 5.6, revealing the following insights: Similar to our numerical observations in [pub3], the importance of the elongational stress at the nozzle exit relative to the shear stress inside the nozzle increases with increasing shear thinning strength; however, the magnitude never exceeds that of the maximum shear stress.

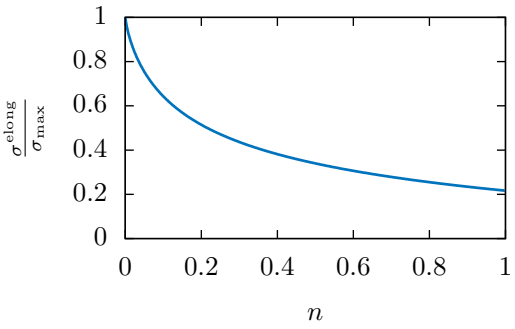

Figure 5.6: The ratio between our estimate for the elongational stress σ^{elong} at the nozzle exit (5.18) and the maximum shear stress $\sigma_{\max}$ inside the nozzle as function of the power-law exponent n, showing how the elongational stress becomes increasingly relevant — relative to the shear stress — for shear thinning fluids.

5.4 Predicting cell survival percentage from critical cell stress

Using the method explained in section 3.1.2.2, we can practically predict the cell survival as function of the maximum printing shear stress from only one material parameter: the critical shear stress σ_{crit} that a cell can endure. Inversely, the procedure can also be applied to determine this critical quantity from experimental cell survival measurements. Through extensive experimental efforts Ouyang *et al.* [73, fig. 8] provided a large data set of cell viability measurements of embryonic stem cells. They used bioinks based on gelatine-alginate mixtures with different concentration compositions at various temperatures between 22.5 °C to 30 °C — therefore varying the viscosity and the shear thinning properties [73]. They report an inverse exponential dependency of the cell survival on the maximum shear stress present in the printing needle.
We use our method (3.28) to reproduce the data from Ouyang [73] via fitting (by eye) the critical shear stress and the corresponding variance. In figure 5.7 the result is presented for $\sigma_{\text{crit}} = 150\,\text{Pa}$ and $\nu = 80\,\text{Pa}$. As can be seen, our prediction perfectly fits the experimental data in the entire range of experimentally assessed shear stresses. The range covered between the highly shear thinning and the Newtonian prediction is similar to the experimentally found error bars, suggesting again that the shear thinning behavior is — practically — irrelevant for the accuracy of this prediction. Finally, in contrast to the empirically proposed exponential dependency [47, 73], our prediction correctly predicts the shoulder for low shear stresses, where the cell viability is close to 100 %.
However, this model is not capable of explaining every experimental data set found in literature; for two — not solely process related — reasons: First of all, research efforts in the field of bioprinting aim to produce printed constructs with high cell viability, meaning that only the report of high cell survival in literature is regarded as success, while a low cell viability deems the entire process useless. Hence, systematically assessed data showing the gradual decrease of cell viability with the change of process relevant parameters is sparse, and most investigations show a merely handful of data points to cover the wide range of process parameters [45, 47, 69]. Another reason is the obvious dependency on the type of cell used. Cells of the various tissue types (of different species) have different mechanical properties, and they also react entirely different to stress. This behavior can further be tuned chemically to alter the cells stiffness [74], which introduces another variable in the aforementioned literature data. Han *et al.* [48]

Figure 5.7: Our cell survival percentage prediction (3.28) from section 3.1.2.2 perfectly reproduces the large experimental data set of Ouyang *et al.* [73, fig. 8] for embryonic stem cells and correctly captures the exponential-like decrease and the low-stress plateau. The probability distribution (3.27) for the critical cell stress is scaled for better visibility.

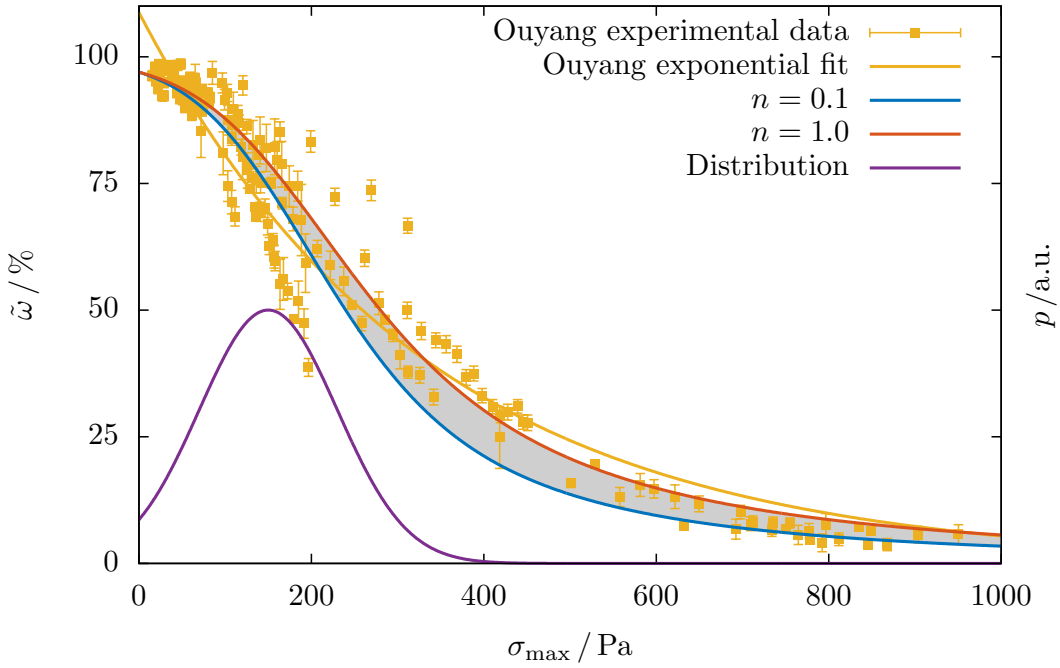

conducted a systematic investigation of fibroblasts in alginate solution with different concentrations, printed at different pressures, with different nozzle diameter and different nozzle length. They observe — in terms of figure 5.7 — a cell viability between 50 % and 90 % in a range of maximum shear stresses up to 2 kPa [48], which may suggest an independence of the fibroblast viability of the shear stress.

5.5 Cells during the bioprinting process

In the following, a numerical analysis of the cell behavior during the 3D bioprinting extrusion process is presented. We build simulation setups of the three main stages — the inlet, the nozzle, and the exit — using our numerical tools developed in section 4.1 and section 4.2. Our interest lies in a quantification of the cell stresses and strains during these stages, especially considering differences of the bioink rheology. In this thesis, we further supplement our detailed single-cell investigation from [pub3] with simulations of a cell suspension passing through the entire printhead.
In section 5.5.1, simulations of the inlet part are presented. The following two sections summarize the work of [pub3] and provide additional simulations with a cell suspension.

5.5.1 Cells entering the nozzle

A part of the printing process not yet considered in the publications for this thesis is the inlet of the nozzle, where the bioink flows from the larger cartridge (typically a cylindrical container with radius of a few cm in diameter) into the fine nozzle. As the fluid is approximately uniformly pushed into the nozzle, an elongational flow pattern is created that stretches the cells on their way approaching the inlet orifice.
We build a simulation setup that approximately resembles this scenario by simulating the flow from a large slit with $533\,\mu m \times 107\,\mu m$ cross-section into a square microchannel with $107\,\mu m$ side length which resembles the nozzle. Cells are placed at random positions in the cartridge and the flow is driven by inflow an outflow planes with constant normal velocities. Figure 5.8(a,c) shows the simulation setup in comparison to the flow through the cylindrical nozzle and its exit. Since the flow is accelerated towards the orifice, cells are elongated in this direction and their deformations appear to be the same at equal radial distances from the orifice. Interestingly, when looking at the Taylor deformation of the cells entering the nozzle in figure 5.8(b), it becomes apparent that the peak deformation caused by the elongational flow pattern is almost equal for all cells entering the orifice. For cells flowing at the center, we observe a clear peak of the deformation only upon entering the nozzle, which quickly relaxes towards the almost negligible deformation inside the nozzle (cf. section 5.5.2). Cells entering from an angle exhibit two further features: first, when flowing close to the sharp edge of the inlet, they deform into a kidney-like shape while bending around the edge. Second, the elongational deformation shortly decreases, but is then superseded by the ellipsoidal deformation caused by the shearing motion of the fluid inside the nozzle, discussed in section 5.5.2. This is also shown in the close-up view in figure 5.9(a,b), together with the internal cell stress distribution. As the similar peak in the cell deformation indicates, also the cell stress distribution is uniform and equal for cells flowing both centered and off-centered upon entering the inlet. The corresponding results for a shear thinning bioink with $\alpha = 0.6$ are shown in figure 5.8(c,d) and figure 5.9(c,d): Cells suspended in a shear thinning bioink show the overall same characteristics as in a Newtonian fluid, however, due to our assumption of equal volume flux, the hydrostatic pressure gradient and hence the hydrodynamic stresses are reduced, resulting in similarly reduced cell deformations during the entrance.

5.5.2 Cells flowing through the nozzle

When cells flow through the cylindrical nozzle, they experience the shear stresses caused by the pressure drop along the channel. We provide a detailed analysis of the behavior of a single cell flowing through the nozzle in [pub3]. The following part summarizes the key findings therein:
When a cells flows along the center axis of the nozzle, it experiences an axisymmetric fluid stress around it, hence deforming into an axisymmetric, bullet-like shape. The inner distribution of the cell stress reflects the linear radial dependency of the undisturbed surrounding fluid stress (3.5). For a increasingly shear thinning bioink, the pressure needed to push it through the needle at equal flow rate, decreases, thus leading to less cell pronounced cell deformation at the center. In fact we find in [pub3], that the

Figure 5.8: Cell suspension during the printing process for (a,b) $\alpha = 0$ and (c,d) $\alpha = 0.6$. The gray vertical lines in the deformation plots indicate the position of the nozzle inlet and exit.

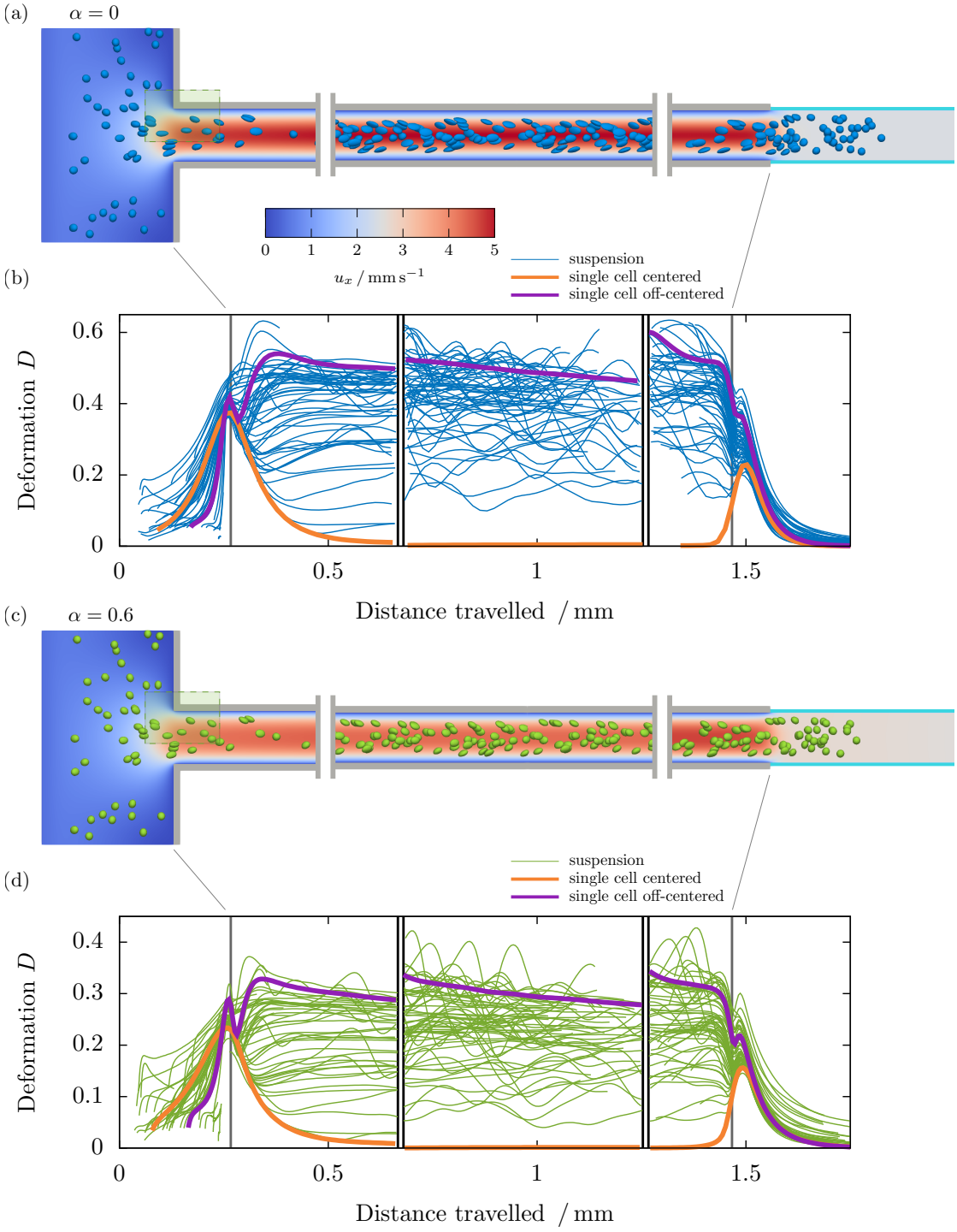

Figure 5.9: Internal cell stress upon entering the nozzle inlet for (a) $\alpha = 0$ and (b) $\alpha = 0.6$ showing a close-up view of the shaded area in figure 5.8(a,c). For both centered and off-centered flowing cells, the stress increases uniformly and with the same magnitude during the passage through the inlet. Then, the centered flowing cell assumes an almost stress-free bullet-like shape, whereas the off-centered flowing cell assumes an ellipsoidal shape which is subject to larger stresses. (c,d) Cells flowing very close to the corner exhibit a kidney-like shape with higher, localized stresses. Flow velocity scale is the same as in figure 5.8.

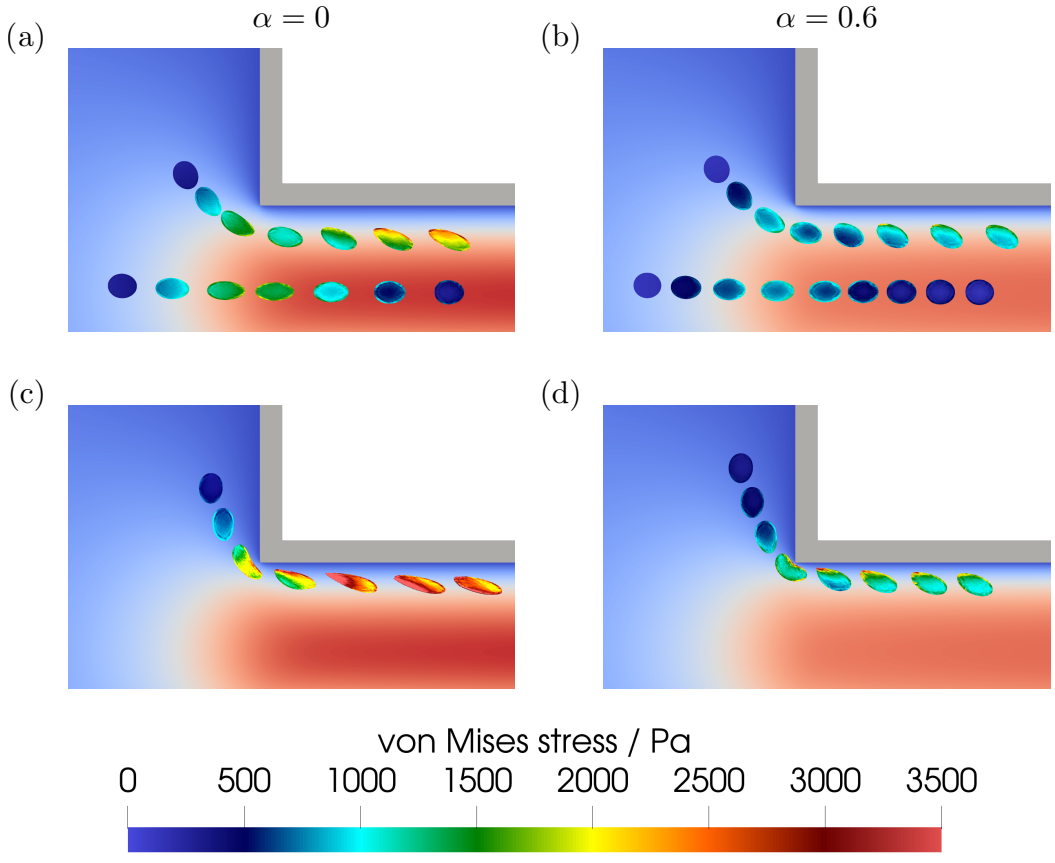

Figure 5.10: Cell deformation of cells in a dense suspension in the nozzle compared to the Roscoe theory [93] for $\alpha = 0$ and $\alpha = 0.6$. Besides noise introduced by cell-cell interactions, the data excellently matches the Roscoe theory.

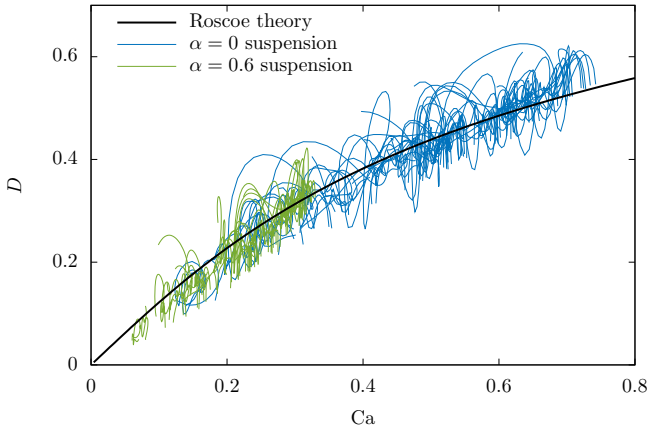

cell strains for centered flowing cells are negligibly small. Cells that flow off-centered and near the wall assume an approximately ellipsoidal shape, with a tank-treading motion followed by the entire cell. The cell migrates radially towards the axis, and while it experiences decreasing fluid stress, it undergoes a series of ellipsoidal shapes until it reaches close (≈ 1 cell radius distance) to the center, where it transitions into the bullet-like or almost undeformed shape. We employ the theory of Roscoe, as detailed in 3.2.2 and the SI of [pub3], which is a theory originally designed to describe the cell motion in a Newtonian fluid in a linear flow. By approximating the local environment of the cell in the nozzle as linear shear flow, we find an excellent agreement between the cell stress and deformation with the prediction of the Roscoe theory. In addition, we show that it is equally accurate for the description of cells in a shear thinning bioink, demonstrating that the shear stresses dominate the cell deformation.
We supplement these single-cell investigations in this thesis with further data obtained from simulations with a dense cell suspension. We place 60 cells in our 400 µm long, periodic channel with 50 µm radius, which corresponds to a cell concentration of approx. 19×10^6 cells/mL or a volume fraction of 4.1 %. As can be seen in figure 5.8 in the middle portion, individual cells assume ellipsoidal shapes while flowing off-center, and bullet-like shapes at the center, similar to our single-cell observations. Hence, we can compare the deformation data to the Roscoe theory in figure 5.10. While the observed time development of each individual cell is occasionally disturbed when it comes in contact with another cell, we still find an excellent agreement of the overall cell deformation with the theoretical prediction as function of the local undisturbed fluid stress. This shows how the Roscoe theory is practically not limited to only single cells or very dilute suspensions, but can also reasonably well describe more dense particle suspensions.
The deformation pattern in figure 5.8(b,d) of cells from inside the nozzle then continues in the nozzle exit portion.

5.5.3 Cells exiting the nozzle

When cells pass through the orifice at the tip of the nozzle, they experience the elongational flows discussed in section 5.3. For a single cell, this scenario has been investigated in detail in [pub3]. Our relevant findings therein are summarized in the following:
When a single cell is flowing at the center, the symmetric flow conditions radially stretch and axially compress it, causing the bullet-like shape from inside the nozzle to assume an oblate-like shape. During this deformation, the internal stress distribution increases uniformly in the whole cell. After the transition, the cell quickly relaxes towards its spherical equilibrium shape. We found in section 5.5.2 that an increasingly shear thinning bioink reduces the cell stress significantly inside the nozzle for cells flowing near the center. However, this effect increases the importance of the elongational cell stress at the nozzle, which inevitable act on the cell. The cell stress peak observed at the exit hence becomes increasingly relevant compared to the shear stress when the shear thinning strength of the bioink increases. Ultimately, cell damage is determined by the strain exhibited by the cell, and the strain depends not only on the stress, but also the time that the cell experiences it. In a simulation series with extrusion velocities increased by more than one order of magnitude, we find that the peak cell strains remain almost unchanged, since the higher elongational fluid stresses are balanced by the short application time. A single cell flowing near the channel wall on the inside experiences the elongational and the shear flow at the same time, which leads to a radial displacement of the entire cell at the exit. We report that in that case the relaxation from the shear deformation from inside the nozzle towards the equilibrium shape remains the dominant effect. We characterize this with the relaxation time scale, which becomes longer for increasing shear thinning, due to the larger viscosity at low shear rates.
To supplement these findings, we conduct simulations of the same flow setup with a suspension of 60 cells passing through the nozzle, as illustrated in figure 5.8 on the right. The suspension (with a cell concentration of approx. 19×10^6 cells/mL) shares the overall same characteristics as the single cell observations: Smoothly continuing the deformation curves from inside the nozzle in figure 5.8(b), the most dominant effect for off-centered flowing cells clearly remains the relaxation from the shear deformation into the stress free shape, while centered flowing cells experience solely the peak of the elongational flows.

Chapter 6

Conclusion and outlook

This thesis explored two pathways from theory to application, which were eventually combined in order to make practical predictions about a real 3D bioprinting process. On the one hand, the independence of cellular behavior on intracellular elastic heterogeneity, and its dependence on the mode of deformation and the rheology of the liquid environment, elucidated the roles of purely passive physical aspects of cell mechanics. On the other, the cell-free flow of shear thinning liquids in important geometries built the basis for efficient prediction methods for bioprinting applications. In combination, we used our analytical tools and numerical investigations to identify the major hydrodynamic influences on cells during a 3D bioprinting process.

Starting with purely fluid-based investigations, we developed in [pub1] a semi-analytical method to compute the exact pressure-driven flow profile of a generalized Newtonian fluid in a pipe, which can easily be implemented for complex viscosity models like the Carreau-Yasuda description, or be applied to rheological measurement data directly. We also showed how this method can be inverted in order to assess the shear thinning properties of a bioink on-line during the printing process via capillary rheometry. Based on the power-law viscosity description, we developed an analytical method to compute the shear-induced cell damage during bioprinting that only requires one critical cell quantity and is practically independent of the bioink rheology. The predictive power of this simple model was demonstrated by accurately reproducing a large experimental data set of cell survival from literature, proving the importance of hydrodynamic shear stresses for cell damage during bioprinting. Due to its simplicity, this method offers a number of opportunities for extensions for future research. For example, time dependent cell damage can be assessed by further taking into account the flow speed of the cells in a nozzle of known length, or a non-uniform cell distribution inside the nozzle can be employed.

Next, in order to build a framework for the simulation of the entire 3D bioprinting process, we developed a suitable numerical model for cells in [pub2]. We provided extensive experimental validation using AFM-based compression and indentation measurements as well as microfluidic flow experiments. By extending the neo-Hookean strain energy density description to the Mooney-Rivlin form, we found an increasingly strain hardening behavior, which was necessary to properly describe our FluidFM compression experiments of rat embryonic fibroblasts in [pub2]. In addition, we showed that the

hyperelastic properties accurately describe also bovine endothelial cells, NIH-3T3 cells, and artificial hydrogel particles. In future research, the applicability of our model to other cell types of interest, entire cell clusters or organoids can be explored.
To supplement our numerical cell model, the theory of Roscoe [93] was extended from the purely neo-Hookean to the Mooney-Rivlin description as well, which revealed a different strain hardening behavior in a linear shear flow scenario compared to the compression. This opposite behavior was explained with a simplified analytical model of a triaxially elongated sphere. In [pub3], we further proved the applicability of the Roscoe theory to cells in a non-linear pipe flow, as well as cells suspended in a shear thinning bioink. On the one hand, this widely expanded the range of applicability of this theory. On the other, it showed that the cell behavior in flow is mostly shear stress driven and does not directly depend on the rheological properties of the surrounding liquid or the flow curvature.
A major simplification in our investigations was the homogeneity of the cell's elastic interior. And while the excellent agreement of our numerical model with experimental studies in [pub2] and [pub3] had already suggested reasonable trust in the assumption, we provided systematic numerical proof in [pub4]. By using one well-defined as well as one randomly inhomogeneous cell, we showed that, in both micromechanical compression scenarios and in microfluidic applications, the heterogeneous cell could be effectively replaced by a homogeneous one. The effective stiffness of our homogeneous equivalent cell was simply obtained as the volume weighted average of the constituents' stiffness.
A detailed investigation of single cells and dense cell suspensions during a realistic 3D bioprinting process combined the usage of all previously calibrated models. The first stage where cells experienced a notable deformation was the inlet from the cartridge into the nozzle. The purely elongational flow produced the same cell deformation almost independent of the direction from which the cell was coming, as the flow pattern pulls radially inwards. This elongational deformation peak was of comparable magnitude as the shear deformation that the cells experience when flowing near the wall inside the nozzle. Due to the radial migration, the cell distribution shifted towards the center of the channel along the length of the nozzle. Therefore, the elongational flow at the exit, although smaller in magnitude than that at the inlet, became relevant. Taking into account increasingly shear thinning fluid properties, the overall cell deformation decreased significantly in all three stages, when considering the same volume flux. We identified the shear stress inside the nozzle as the most significant influence, especially since the time span during which it acted on the cells was the longest. Finally, for this scenario, we proved the applicability of the Roscoe theory [93] for single cells and a dense cell suspension flowing in a shear thinning bioink in a non-linear flow pattern.

Bibliography

[1] Shuangshuang Mao, Jianyu He, Yu Zhao, Tiankun Liu, Feihu Xie, Huayu Yang, Yilei Mao, Yuan Pang, and Wei Sun. Bioprinting of patient-derived *in vitro* intrahepatic cholangiocarcinoma tumor model: Establishment, evaluation and anti-cancer drug testing. *Biofabrication*, 12(4):045014, July 2020. ISSN 1758-5090. doi: 10.1088/1758-5090/aba0c3.

[2] Rafael Schmid, Sonja K. Schmidt, Jonas Hazur, Rainer Detsch, Evelyn Maurer, Aldo R. Boccaccini, Julia Hauptstein, Jörg Teßmar, Torsten Blunk, Stefan Schrüfer, Dirk W. Schubert, Raymund E. Horch, Anja K. Bosserhoff, Andreas Arkudas, and Annika Kengelbach-Weigand. Comparison of Hydrogels for the Development of Well-Defined 3D Cancer Models of Breast Cancer and Melanoma. *Cancers*, 12 (8):2320, August 2020. ISSN 2072-6694. doi: 10.3390/cancers12082320.

[3] Sonja K. Schmidt, Rafael Schmid, Andreas Arkudas, Annika Kengelbach-Weigand, and Anja K. Bosserhoff. Tumor Cells Develop Defined Cellular Phenotypes After 3D-Bioprinting in Different Bioinks. *Cells*, 8(10):1295, October 2019. ISSN 2073-4409. doi: 10.3390/cells8101295.

[4] Mohammad Z. Albanna and James H. Holmes, editors. *Skin Tissue Engineering and Regenerative Medicine*. Elsevier/AP, Academic Press is an imprint of Elsevier, London, UK ; San Diego, CA, USA, 2016. ISBN 978-0-12-801654-1.

[5] Fiona M. Wood. Therapeutic Applications. In *Principles of Regenerative Medicine*, pages 1281–1295. Elsevier, 2019. ISBN 978-0-12-809880-6. doi: 10.1016/B978-0-12-809880-6.00073-4.

[6] Judith Hagenbuchner, Daniel Nothdurfter, and Michael J. Ausserlechner. 3D bioprinting: Novel approaches for engineering complex human tissue equivalents and drug testing. *Essays in Biochemistry*, 65(3):417–427, August 2021. ISSN 0071-1365, 1744-1358. doi: 10.1042/EBC20200153.

[7] Weijie Peng, Derya Unutmaz, and Ibrahim T. Ozbolat. Bioprinting towards Physiologically Relevant Tissue Models for Pharmaceutics. *Trends in Biotechnology*, 34 (9):722–732, September 2016. ISSN 01677799. doi: 10.1016/j.tibtech.2016.05.013.

[8] Weijie Peng, Pallab Datta, Bugra Ayan, Veli Ozbolat, Donna Sosnoski, and Ibrahim T. Ozbolat. 3D bioprinting for drug discovery and development in

pharmaceutics. *Acta Biomaterialia*, 57:26–46, July 2017. ISSN 17427061. doi: 10.1016/j.actbio.2017.05.025.

[9] Madhuri Dey and Ibrahim T. Ozbolat. 3D bioprinting of cells, tissues and organs. *Scientific Reports*, 10(1):14023, s41598–020–70086–y, December 2020. ISSN 2045-2322. doi: 10.1038/s41598-020-70086-y.

[10] Guifang Gao, Ying Huang, Arndt F. Schilling, Karen Hubbell, and Xiaofeng Cui. Organ Bioprinting: Are We There Yet? *Advanced Healthcare Materials*, 7(1): 1701018, January 2018. ISSN 21922640. doi: 10.1002/adhm.201701018.

[11] Lorenzo Moroni, Jason A. Burdick, Christopher Highley, Sang Jin Lee, Yuya Morimoto, Shoji Takeuchi, and James J. Yoo. Biofabrication strategies for 3D in vitro models and regenerative medicine. *Nature Reviews. Materials*, 3(5):21–37, May 2018. ISSN 2058-8437. doi: 10.1038/s41578-018-0006-y.

[12] Sean V Murphy and Anthony Atala. 3D bioprinting of tissues and organs. *Nature Biotechnology*, 32(8):773–785, August 2014. ISSN 1087-0156, 1546-1696. doi: 10.1038/nbt.2958.

[13] Wei Sun, Binil Starly, Andrew C Daly, Jason A Burdick, Jürgen Groll, Gregor Skeldon, Wenmiao Shu, Yasuyuki Sakai, Marie Shinohara, Masaki Nishikawa, Jinah Jang, Dong-Woo Cho, Minghao Nie, Shoji Takeuchi, Serge Ostrovidov, Ali Khademhosseini, Roger D Kamm, Vladimir Mironov, Lorenzo Moroni, and Ibrahim T Ozbolat. The bioprinting roadmap. *Biofabrication*, 12(2):022002, February 2020. ISSN 1758-5090. doi: 10.1088/1758-5090/ab5158.

[14] Jürgen Groll, Thomas Boland, Torsten Blunk, Jason A Burdick, Dong-Woo Cho, Paul D Dalton, Brian Derby, Gabor Forgacs, Qing Li, Vladimir A Mironov, Lorenzo Moroni, Makoto Nakamura, Wenmiao Shu, Shoji Takeuchi, Giovanni Vozzi, Tim B F Woodfield, Tao Xu, James J Yoo, and Jos Malda. Biofabrication: Reappraising the definition of an evolving field. *Biofabrication*, 8(1):013001, January 2016. ISSN 1758-5090. doi: 10.1088/1758-5090/8/1/013001.

[15] Kajsa Markstedt, Athanasios Mantas, Ivan Tournier, Héctor Martínez Ávila, Daniel Hägg, and Paul Gatenholm. 3D Bioprinting Human Chondrocytes with Nanocellulose–Alginate Bioink for Cartilage Tissue Engineering Applications. *Biomacromolecules*, 16(5):1489–1496, May 2015. ISSN 1525-7797, 1526-4602. doi: 10.1021/acs.biomac.5b00188.

[16] I A D Mancini, S Schmidt, H Brommer, B Pouran, S Schäfer, J Tessmar, A Mensinga, M H P van Rijen, J Groll, T Blunk, R Levato, J Malda, and P R van Weeren. A composite hydrogel-3D printed thermoplast osteochondral anchor as example for a zonal approach to cartilage repair: *In Vivo* performance in a long-term equine model. *Biofabrication*, 12(3):035028, July 2020. ISSN 1758-5090. doi: 10.1088/1758-5090/ab94ce.

[17] A. Weizel, T. Distler, D. Schneidereit, O. Friedrich, L. Bräuer, F. Paulsen, R. Detsch, A.R. Boccaccini, S. Budday, and H. Seitz. Complex mechanical behavior

of human articular cartilage and hydrogels for cartilage repair. *Acta Biomaterialia*, 118:113–128, December 2020. ISSN 17427061. doi: 10.1016/j.actbio.2020.10.025.

[18] Stefanie Schmidt, Florencia Abinzano, Anneloes Mensinga, Jörg Teßmar, Jürgen Groll, Jos Malda, Riccardo Levato, and Torsten Blunk. Differential Production of Cartilage ECM in 3D Agarose Constructs by Equine Articular Cartilage Progenitor Cells and Mesenchymal Stromal Cells. *International Journal of Molecular Sciences*, 21(19):7071, September 2020. ISSN 1422-0067. doi: 10.3390/ijms21197071.

[19] Zeynab Mirzaei, Soheila S. Kordestani, Sonja Kuth, Dirk W. Schubert, Rainer Detsch, Judith A. Roether, Torsten Blunk, and Aldo R. Boccaccini. Preparation and Characterization of Electrospun Blend Fibrous Polyethylene Oxide:Polycaprolactone Scaffolds to Promote Cartilage Regeneration. *Advanced Engineering Materials*, 22(9):2000131, September 2020. ISSN 1438-1656, 1527-2648. doi: 10.1002/adem.202000131.

[20] Khoon S. Lim, Riccardo Levato, Pedro F. Costa, Miguel D. Castilho, Cesar R. Alcala-Orozco, Kim M. A. van Dorenmalen, Ferry P. W. Melchels, Debby Gawlitta, Gary J. Hooper, Jos Malda, and Tim B. F. Woodfield. Bio-resin for high resolution lithography-based biofabrication of complex cell-laden constructs. *Biofabrication*, 10(3):034101, May 2018. ISSN 1758-5090. doi: 10.1088/1758-5090/aac00c.

[21] Marietta Herrmann, Klaus Engelke, Regina Ebert, Sigrid Müller-Deubert, Maximilian Rudert, Fani Ziouti, Franziska Jundt, Dieter Felsenberg, and Franz Jakob. Interactions between Muscle and Bone—Where Physics Meets Biology. *Biomolecules*, 10(3):432, March 2020. ISSN 2218-273X. doi: 10.3390/biom10030432.

[22] Sigrid Müller-Deubert, Carolin Ege, Melanie Krug, Jutta Meißner-Weigl, Maximilian Rudert, Oliver Bischof, Franz Jakob, and Regina Ebert. Phosphodiesterase 10A Is a Mediator of Osteogenic Differentiation and Mechanotransduction in Bone Marrow-Derived Mesenchymal Stromal Cells. *Stem Cells International*, 2020:1–11, June 2020. ISSN 1687-966X, 1687-9678. doi: 10.1155/2020/7865484.

[23] Jinah Jang, Hun-Jun Park, Seok-Won Kim, Heejin Kim, Ju Young Park, Soo Jin Na, Hyeon Ji Kim, Moon Nyeo Park, Seung Hyun Choi, Sun Hwa Park, Sung Won Kim, Sang-Mo Kwon, Pum-Joon Kim, and Dong-Woo Cho. 3D printed complex tissue construct using stem cell-laden decellularized extracellular matrix bioinks for cardiac repair. *Biomaterials*, 112:264–274, January 2017. ISSN 1878-5905. doi: 10.1016/j.biomaterials.2016.10.026.

[24] Thomas Distler, Aditya A Solisito, Dominik Schneidereit, Oliver Friedrich, Rainer Detsch, and Aldo R Boccaccini. 3D printed oxidized alginate-gelatin bioink provides guidance for C2C12 muscle precursor cell orientation and differentiation via shear stress during bioprinting. *Biofabrication*, 12(4):045005, July 2020. ISSN 1758-5090. doi: 10.1088/1758-5090/ab98e4.

[25] Indra Apsite, Juan Manuel Uribe, Andrés Fernando Posada, Sabine Rosenfeldt, Sahar Salehi, and Leonid Ionov. 4D biofabrication of skeletal muscle microtissues.

Biofabrication, 12(1):015016, December 2019. ISSN 1758-5090. doi: 10.1088/1758-5090/ab4cc4.

[26] Claudia Mueller, Mairon Trujillo-Miranda, Michael Maier, Daniel E. Heath, Andrea J. O'Connor, and Sahar Salehi. Effects of External Stimulators on Engineered Skeletal Muscle Tissue Maturation. *Advanced Materials Interfaces*, 8(1):2001167, January 2021. ISSN 2196-7350, 2196-7350. doi: 10.1002/admi.202001167.

[27] Carina S. Russell, Azadeh Mostafavi, Jacob P. Quint, Adriana C. Panayi, Kodi Baldino, Tyrell J. Williams, Jocelyn G. Daubendiek, Victor Hugo Sánchez, Zack Bonick, Mairon Trujillo-Miranda, Su Ryon Shin, Olivier Pourquie, Sahar Salehi, Indranil Sinha, and Ali Tamayol. *In Situ* Printing of Adhesive Hydrogel Scaffolds for the Treatment of Skeletal Muscle Injuries. *ACS Applied Bio Materials*, 3 (3):1568–1579, March 2020. ISSN 2576-6422, 2576-6422. doi: 10.1021/acsabm.9b01176.

[28] Johannes P. M. Kramer, Tamara B. Aigner, Jana Petzold, Kaveh Roshanbinfar, Thomas Scheibel, and Felix B. Engel. Recombinant spider silk protein eADF4(C16)-RGD coatings are suitable for cardiac tissue engineering. *Scientific Reports*, 10 (1):8789, December 2020. ISSN 2045-2322. doi: 10.1038/s41598-020-65786-4.

[29] Byoung Soo Kim, Yang Woo Kwon, Jeong-Sik Kong, Gyu Tae Park, Ge Gao, Wonil Han, Moon-Bum Kim, Hyungseok Lee, Jae Ho Kim, and Dong-Woo Cho. 3D cell printing of in vitro stabilized skin model and in vivo pre-vascularized skin patch using tissue-specific extracellular matrix bioink: A step towards advanced skin tissue engineering. *Biomaterials*, 168:38–53, June 2018. ISSN 1878-5905. doi: 10.1016/j.biomaterials.2018.03.040.

[30] Dominik Steiner, Lara Lingens, Laura Fischer, Katrin Köhn, Rainer Detsch, Aldo R. Boccaccini, Tobias Fey, Peter Greil, Christian Weis, Justus P. Beier, Raymund E. Horch, and Andreas Arkudas. Encapsulation of Mesenchymal Stem Cells Improves Vascularization of Alginate-Based Scaffolds. *Tissue Engineering Part A*, 24(17-18):1320–1331, September 2018. ISSN 1937-3341, 1937-335X. doi: 10.1089/ten.tea.2017.0496.

[31] Christopher K. Arakawa, Barry A. Badeau, Ying Zheng, and Cole A. DeForest. Multicellular Vascularized Engineered Tissues through User-Programmable Biomaterial Photodegradation. *Advanced Materials (Deerfield Beach, Fla.)*, 29(37), October 2017. ISSN 1521-4095. doi: 10.1002/adma.201703156.

[32] Tilman U. Esser, Kaveh Roshanbinfar, and Felix B. Engel. Promoting vascularization for tissue engineering constructs: Current strategies focusing on HIF-regulating scaffolds. *Expert Opinion on Biological Therapy*, 19(2):105–118, February 2019. ISSN 1471-2598, 1744-7682. doi: 10.1080/14712598.2019.1561855.

[33] Ge Gao, Jun Hee Lee, Jinah Jang, Dong Han Lee, Jeong-Sik Kong, Byoung Soo Kim, Yeong-Jin Choi, Woong Bi Jang, Young Joon Hong, Sang-Mo Kwon, and

Dong-Woo Cho. Tissue engineered bio-blood-vessels constructed using a tissue-specific bioink and 3D coaxial cell printing technique: A novel therapy for ischemic disease. *Advanced Functional Materials*, 27(33):1700798, 2017. doi: 10.1002/adfm.201700798.

[34] Timothy R. Olsen, Kelvin S. Ng, Lye T. Lock, Tabassum Ahsan, and Jon A. Rowley. Peak MSC—Are we there yet? *Frontiers in Medicine*, 5, 2018. ISSN 2296-858X. doi: 10.3389/fmed.2018.00178.

[35] Alan Faulkner-Jones, Catherine Fyfe, Dirk-Jan Cornelissen, John Gardner, Jason King, Aidan Courtney, and Wenmiao Shu. Bioprinting of human pluripotent stem cells and their directed differentiation into hepatocyte-like cells for the generation of mini-livers in 3D. *Biofabrication*, 7(4):044102, October 2015. ISSN 1758-5090. doi: 10.1088/1758-5090/7/4/044102.

[36] Qi Gu, Eva Tomaskovic-Crook, Rodrigo Lozano, Yu Chen, Robert M. Kapsa, Qi Zhou, Gordon G. Wallace, and Jeremy M. Crook. Functional 3D Neural Mini-Tissues from Printed Gel-Based Bioink and Human Neural Stem Cells. *Advanced Healthcare Materials*, 5(12):1429–1438, June 2016. ISSN 2192-2659. doi: 10.1002/adhm.201600095.

[37] Lothar Koch, Andrea Deiwick, Annika Franke, Kristin Schwanke, Axel Haverich, Robert Zweigerdt, and Boris Chichkov. Laser bioprinting of human induced pluripotent stem cells-the effect of printing and biomaterials on cell survival, pluripotency, and differentiation. *Biofabrication*, 10(3):035005, April 2018. ISSN 1758-5090. doi: 10.1088/1758-5090/aab981.

[38] Constantin Berger, Yngvild Bjørlykke, Lukas Hahn, Markus Mühlemann, Sebastian Kress, Heike Walles, Robert Luxenhofer, Helge Ræder, Marco Metzger, and Daniela Zdzieblo. Matrix decoded – A pancreatic extracellular matrix with organ specific cues guiding human iPSC differentiation. *Biomaterials*, 244:119766, June 2020. ISSN 01429612. doi: 10.1016/j.biomaterials.2020.119766.

[39] Joshua G. Hunsberger, Thomas Shupe, and Anthony Atala. An Industry-Driven Roadmap for Manufacturing in Regenerative Medicine. *Stem Cells Translational Medicine*, 7(8):564–568, August 2018. ISSN 2157-6564. doi: 10.1002/sctm.18-0060.

[40] Julia Emmermacher, David Spura, Jasmina Cziommer, David Kilian, Tobias Wollborn, Udo Fritsching, Juliane Steingroewer, Thomas Walther, Michael Gelinsky, and Anja Lode. Engineering considerations on extrusion-based bioprinting: Interactions of material behavior, mechanical forces and cells in the printing needle. *Biofabrication*, 12(2):025022, March 2020. ISSN 1758-5090. doi: 10.1088/1758-5090/ab7553.

[41] F. Ruther, T. Distler, A. R. Boccaccini, and R. Detsch. Biofabrication of vessel-like structures with alginate di-aldehyde—gelatin (ADA-GEL) bioink. *Journal of Materials Science: Materials in Medicine*, 30(1):8, January 2019. ISSN 0957-4530, 1573-4838. doi: 10.1007/s10856-018-6205-7.

[42] Jia Shi, Bin Wu, Shihao Li, Jinchun Song, Bin Song, and Wen F Lu. Shear stress analysis and its effects on cell viability and cell proliferation in drop-on-demand bioprinting. *Biomedical Physics & Engineering Express*, 4(4):045028, June 2018. ISSN 2057-1976. doi: 10.1088/2057-1976/aac946.

[43] Naomi Paxton, Willi Smolan, Thomas Böck, Ferry Melchels, Jürgen Groll, and Tomasz Jungst. Proposal to assess printability of bioinks for extrusion-based bioprinting and evaluation of rheological properties governing bioprintability. *Biofabrication*, 9(4):044107, November 2017. ISSN 1758-5090. doi: 10.1088/1758-5090/aa8dd8.

[44] Andreas Blaeser, Daniela Filipa Duarte Campos, Uta Puster, Walter Richtering, Molly M. Stevens, and Horst Fischer. Controlling Shear Stress in 3D Bioprinting is a Key Factor to Balance Printing Resolution and Stem Cell Integrity. *Advanced Healthcare Materials*, 5(3):326–333, February 2016. ISSN 21922640. doi: 10.1002/adhm.201500677.

[45] Jessica Snyder, Ae Rin Son, Qudus Hamid, Chengyang Wang, Yigong Lui, and Wei Sun. Mesenchymal stem cell printing and process regulated cell properties. *Biofabrication*, 7(4):044106, December 2015. ISSN 1758-5090. doi: 10.1088/1758-5090/7/4/044106.

[46] Yu Zhao, Yang Li, Shuangshuang Mao, Wei Sun, and Rui Yao. The influence of printing parameters on cell survival rate and printability in microextrusion-based 3D cell printing technology. *Biofabrication*, 7(4):045002, November 2015. ISSN 1758-5090. doi: 10.1088/1758-5090/7/4/045002.

[47] Kalyani Nair, Milind Gandhi, Saif Khalil, Karen Chang Yan, Michele Marcolongo, Kenneth Barbee, and Wei Sun. Characterization of cell viability during bioprinting processes. *Biotechnology Journal*, 4(8):1168–1177, August 2009. ISSN 1860-6768. doi: 10.1002/biot.200900004.

[48] Seungsu Han, Chul Min Kim, Songwan Jin, and Taig Young Kim. Study of the process-induced cell damage in forced extrusion bioprinting. *Biofabrication*, 13(3):035048, July 2021. ISSN 1758-5082, 1758-5090. doi: 10.1088/1758-5090/ac0415.

[49] Alan Faulkner-Jones, Sebastian Greenhough, Jason A. King, John Gardner, Aidan Courtney, and Wenmiao Shu. Development of a valve-based cell printer for the formation of human embryonic stem cell spheroid aggregates. *Biofabrication*, 5(1):015013, March 2013. ISSN 1758-5090. doi: 10.1088/1758-5082/5/1/015013.

[50] Malik Salman Haider, Taufiq Ahmad, Mengshi Yang, Chen Hu, Lukas Hahn, Philipp Stahlhut, Jürgen Groll, and Robert Luxenhofer. Tuning the Thermogelation and Rheology of Poly(2-Oxazoline)/Poly(2-Oxazine)s Based Thermosensitive Hydrogels for 3D Bioprinting. *Gels*, 7(3):78, June 2021. ISSN 2310-2861. doi: 10.3390/gels7030078.

[51] Chen Hu, Lukas Hahn, Mengshi Yang, Alexander Altmann, Philipp Stahlhut, Jürgen Groll, and Robert Luxenhofer. Improving printability of a thermoresponsive hydrogel biomaterial ink by nanoclay addition. *Journal of Materials Science*, 56(1):691–705, January 2021. ISSN 0022-2461, 1573-4803. doi: 10.1007/s10853-020-05190-5.

[52] Cristina Colosi, Su Ryon Shin, Vijayan Manoharan, Solange Massa, Marco Costantini, Andrea Barbetta, Mehmet Remzi Dokmeci, Mariella Dentini, and Ali Khademhosseini. Microfluidic Bioprinting of Heterogeneous 3D Tissue Constructs Using Low-Viscosity Bioink. *Advanced Materials (Deerfield Beach, Fla.)*, 28(4): 677–684, January 2016. ISSN 1521-4095. doi: 10.1002/adma.201503310.

[53] Liliang Ouyang, Rui Yao, Shuangshuang Mao, Xi Chen, Jie Na, and Wei Sun. Three-dimensional bioprinting of embryonic stem cells directs highly uniform embryoid body formation. *Biofabrication*, 7(4):044101, November 2015. ISSN 1758-5090. doi: 10.1088/1758-5090/7/4/044101.

[54] J Groll, J A Burdick, D-W Cho, B Derby, M Gelinsky, S C Heilshorn, T Jüngst, J Malda, V A Mironov, K Nakayama, A Ovsianikov, W Sun, S Takeuchi, J J Yoo, and T B F Woodfield. A definition of bioinks and their distinction from biomaterial inks. *Biofabrication*, 11(1):013001, November 2018. ISSN 1758-5090. doi: 10.1088/1758-5090/aaec52.

[55] Jenni Leppiniemi, Panu Lahtinen, Antti Paajanen, Riitta Mahlberg, Sini Metsä-Kortelainen, Tatu Pinomaa, Heikki Pajari, Inger Vikholm-Lundin, Pekka Pursula, and Vesa P. Hytönen. 3D-Printable Bioactivated Nanocellulose–Alginate Hydrogels. *ACS Applied Materials & Interfaces*, 9(26):21959–21970, July 2017. ISSN 1944-8244, 1944-8252. doi: 10.1021/acsami.7b02756.

[56] Bapi Sarker, Julia Rompf, Raquel Silva, Nadine Lang, Rainer Detsch, Joachim Kaschta, Ben Fabry, and Aldo R. Boccaccini. Alginate-based hydrogels with improved adhesive properties for cell encapsulation. *International Journal of Biological Macromolecules*, 78:72–78, July 2015. ISSN 01418130. doi: 10.1016/j.ijbiomac.2015.03.061.

[57] Ali Malekpour and Xiongbiao Chen. Printability and Cell Viability in Extrusion-Based Bioprinting from Experimental, Computational, and Machine Learning Views. *Journal of Functional Biomaterials*, 13(2):40, April 2022. ISSN 2079-4983. doi: 10.3390/jfb13020040.

[58] Jos Malda, Jetze Visser, Ferry P. Melchels, Tomasz Jüngst, Wim E. Hennink, Wouter J. A. Dhert, Jürgen Groll, and Dietmar W. Hutmacher. 25th Anniversary Article: Engineering Hydrogels for Biofabrication. *Advanced Materials*, 25(36): 5011–5028, September 2013. ISSN 09359648. doi: 10.1002/adma.201302042.

[59] Thomas Lorson, Matthias Ruopp, Ali Nadernezhad, Julia Eiber, Ulrich Vogel, Tomasz Jungst, and Tessa Lühmann. Sterilization Methods and Their Influence on Physicochemical Properties and Bioprinting of Alginate as a Bioink Component.

ACS Omega, 5(12):6481–6486, March 2020. ISSN 2470-1343, 2470-1343. doi: 10.1021/acsomega.9b04096.

[60] Jonas Hazur, Rainer Detsch, Emine Karakaya, Joachim Kaschta, Jörg Teßmar, Dominik Schneidereit, Oliver Friedrich, Dirk W Schubert, and Aldo R Boccaccini. Improving alginate printability for biofabrication: Establishment of a universal and homogeneous pre-crosslinking technique. *Biofabrication*, 12(4):045004, July 2020. ISSN 1758-5090. doi: 10.1088/1758-5090/ab98e5.

[61] Jon A. Rowley, Gerard Madlambayan, and David J. Mooney. Alginate hydrogels as synthetic extracellular matrix materials. *Biomaterials*, 20(1):45–53, January 1999. ISSN 0142-9612. doi: 10.1016/s0142-9612(98)00107-0.

[62] Dalia Dranseikiene, Stefan Schrüfer, Dirk W. Schubert, Supachai Reakasame, and Aldo R. Boccaccini. Cell-laden alginate dialdehyde–gelatin hydrogels formed in 3D printed sacrificial gel. *Journal of Materials Science: Materials in Medicine*, 31 (3):31, March 2020. ISSN 0957-4530, 1573-4838. doi: 10.1007/s10856-020-06369-7.

[63] Jonathan M. Zuidema, Christopher J. Rivet, Ryan J. Gilbert, and Faith A. Morrison. A protocol for rheological characterization of hydrogels for tissue engineering strategies. *Journal of Biomedical Materials Research Part B: Applied Biomaterials*, 102(5):1063–1073, December 2013. ISSN 1552-4973. doi: 10.1002/jbm.b.33088.

[64] X Y Tian, M G Li, N Cao, J W Li, and X B Chen. Characterization of the flow behavior of alginate/hydroxyapatite mixtures for tissue scaffold fabrication. *Biofabrication*, 1(4):045005, December 2009. ISSN 1758-5082. doi: 10.1088/1758-5082/1/4/045005.

[65] Thomas Billiet, Elien Gevaert, Thomas De Schryver, Maria Cornelissen, and Peter Dubruel. The 3D printing of gelatin methacrylamide cell-laden tissue-engineered constructs with high cell viability. *Biomaterials*, 35(1):49–62, January 2014. ISSN 01429612. doi: 10.1016/j.biomaterials.2013.09.078.

[66] Young Bok Bae, Hye Kyeong Jang, Tae Hwan Shin, Geetika Phukan, Thanh Tinh Tran, Gwang Lee, Wook Ryol Hwang, and Ju Min Kim. Microfluidic assessment of mechanical cell damage by extensional stress. *Lab on a Chip*, 16(1):96–103, 2016. ISSN 1473-0197, 1473-0189. doi: 10.1039/C5LC01006C.

[67] Robert Chang, Jae Nam, and Wei Sun. Effects of Dispensing Pressure and Nozzle Diameter on Cell Survival from Solid Freeform Fabrication–Based Direct Cell Writing. *Tissue Engineering Part A*, 14(1):41–48, January 2008. ISSN 1937-3341, 1937-335X. doi: 10.1089/ten.a.2007.0004.

[68] Khalida Fakhruddin, Mohd Syahir Anwar Hamzah, and Saiful Izwan Abd Razak. Effects of extrusion pressure and printing speed of 3D bioprinted construct on the fibroblast cells viability. *IOP Conference Series: Materials Science and Engineering*, 440:012042, October 2018. ISSN 1757-899X. doi: 10.1088/1757-899X/440/1/012042.

[69] Liqun Ning, Nicholas Betancourt, David J. Schreyer, and Xiongbiao Chen. Characterization of Cell Damage and Proliferative Ability during and after Bioprinting. *ACS Biomaterials Science & Engineering*, 4(11):3906–3918, November 2018. ISSN 2373-9878, 2373-9878. doi: 10.1021/acsbiomaterials.8b00714.

[70] Zhenhua Chai, Baochang Shi, Zhaoli Guo, and Fumei Rong. Multiple-relaxation-time lattice Boltzmann model for generalized Newtonian fluid flows. *Journal of Non-Newtonian Fluid Mechanics*, 166(5-6):332–342, March 2011. ISSN 03770257. doi: 10.1016/j.jnnfm.2011.01.002.

[71] D. Roehm and A. Arnold. Lattice Boltzmann simulations on GPUs with ESPResSo. *The European Physical Journal Special Topics*, 210(1):89–100, August 2012. ISSN 1951-6355, 1951-6401. doi: 10.1140/epjst/e2012-01639-6.

[72] H.J. Limbach, A. Arnold, B.A. Mann, and C. Holm. ESPResSo—an extensible simulation package for research on soft matter systems. *Computer Physics Communications*, 174(9):704–727, May 2006. ISSN 00104655. doi: 10.1016/j.cpc.2005.10.005.

[73] Liliang Ouyang, Rui Yao, Yu Zhao, and Wei Sun. Effect of bioink properties on printability and cell viability for 3D bioplotting of embryonic stem cells. *Biofabrication*, 8(3):035020, September 2016. ISSN 1758-5090. doi: 10.1088/1758-5090/8/3/035020.

[74] Richard Gerum, Elham Mirzahossein, Mar Eroles, Jennifer Elsterer, Astrid Mainka, Andreas Bauer, Selina Sonntag, Alexander Winterl, Johannes Bartl, Lena Fischer, Shada Abuhattum, Ruchi Goswami, Salvatore Girardo, Jochen Guck, Stefan Schrüfer, Nadine Ströhlein, Mojtaba Nosratlo, Harald Herrmann, Dorothea Schultheis, Felix Rico, Sebastian Müller, Stephan Gekle, and Ben Fabry. Viscoelastic properties of suspended cells measured with shear flow deformation cytometry. Preprint, Biophysics, January 2022.

[75] Jonathan B. Freund. Numerical Simulation of Flowing Blood Cells. *Annual Review of Fluid Mechanics*, 46(1):67–95, January 2014. ISSN 0066-4189, 1545-4479. doi: 10.1146/annurev-fluid-010313-141349.

[76] Gábor Závodszky, Britt van Rooij, Victor Azizi, and Alfons Hoekstra. Cellular Level In-silico Modeling of Blood Rheology with An Improved Material Model for Red Blood Cells. *Frontiers in Physiology*, 8:563, August 2017. ISSN 1664-042X. doi: 10.3389/fphys.2017.00563.

[77] Johannes Mauer, Simon Mendez, Luca Lanotte, Franck Nicoud, Manouk Abkarian, Gerhard Gompper, and Dmitry A. Fedosov. Flow-Induced Transitions of Red Blood Cell Shapes under Shear. *Physical Review Letters*, 121(11):118103, September 2018. ISSN 0031-9007, 1079-7114. doi: 10.1103/PhysRevLett.121.118103.

[78] Achim Guckenberger, Alexander Kihm, Thomas John, Christian Wagner, and Stephan Gekle. Numerical–experimental observation of shape bistability of red blood cells flowing in a microchannel. *Soft Matter*, 14(11):2032–2043, 2018. ISSN 1744-683X, 1744-6848. doi: 10.1039/C7SM02272G.

[79] Christos Kotsalos, Jonas Latt, and Bastien Chopard. Bridging the computational gap between mesoscopic and continuum modeling of red blood cells for fully resolved blood flow. *Journal of Computational Physics*, 398:108905, December 2019. ISSN 00219991. doi: 10.1016/j.jcp.2019.108905.

[80] Nathalie Caille, Olivier Thoumine, Yanik Tardy, and Jean-Jacques Meister. Contribution of the nucleus to the mechanical properties of endothelial cells. *Journal of Biomechanics*, 35(2):177–187, February 2002. ISSN 0021-9290.

[81] M. Mokbel, D. Mokbel, A. Mietke, N. Träber, S. Girardo, O. Otto, J. Guck, and S. Aland. Numerical Simulation of Real-Time Deformability Cytometry To Extract Cell Mechanical Properties. *ACS Biomaterials Science & Engineering*, 3(11):2962–2973, November 2017. ISSN 2373-9878, 2373-9878. doi: 10.1021/acsbiomaterials.6b00558.

[82] Kirill Lykov, Yasaman Nematbakhsh, Menglin Shang, Chwee Teck Lim, and Igor V. Pivkin. Probing eukaryotic cell mechanics via mesoscopic simulations. *PLOS Computational Biology*, 13(9):e1005726, September 2017. ISSN 1553-7358. doi: 10.1371/journal.pcbi.1005726.

[83] Marco E. Rosti, Luca Brandt, and Dhrubaditya Mitra. Rheology of suspensions of viscoelastic spheres: Deformability as an effective volume fraction. *Physical Review Fluids*, 3(1):012301, January 2018. ISSN 2469-990X. doi: 10.1103/PhysRevFluids.3.012301.

[84] Amir Saadat, Christopher J. Guido, Gianluca Iaccarino, and Eric S. G. Shaqfeh. Immersed-finite-element method for deformable particle suspensions in viscous and viscoelastic media. *Physical Review E*, 98(6):063316, December 2018. ISSN 2470-0045, 2470-0053. doi: 10.1103/PhysRevE.98.063316.

[85] Elisabeth Fischer-Friedrich, Anthony A. Hyman, Frank Jülicher, Daniel J. Müller, and Jonne Helenius. Quantification of surface tension and internal pressure generated by single mitotic cells. *Scientific Reports*, 4(1):6213, May 2015. ISSN 2045-2322. doi: 10.1038/srep06213.

[86] Valentin Lulevich, Tiffany Zink, Huan-Yuan Chen, Fu-Tong Liu, and Gang-yu Liu. Cell Mechanics Using Atomic Force Microscopy-Based Single-Cell Compression. *Langmuir*, 22(19):8151–8155, September 2006. ISSN 0743-7463, 1520-5827. doi: 10.1021/la060561p.

[87] V. V. Lulevich, I. L. Radtchenko, G. B. Sukhorukov, and O. I. Vinogradova. Deformation Properties of Nonadhesive Polyelectrolyte Microcapsules Studied with the Atomic Force Microscope. *The Journal of Physical Chemistry B*, 107 (12):2735–2740, March 2003. ISSN 1520-6106, 1520-5207. doi: 10.1021/jp026927y.

[88] Hamid Ladjal, Jean-Luc Hanus, Anand Pillarisetti, Carol Keefer, Antoine Ferreira, and Jaydev P. Desai. Atomic force microscopy-based single-cell indentation: Experimentation and finite element simulation. In *2009 IEEE/RSJ International*

Conference on Intelligent Robots and Systems, pages 1326–1332, St. Louis, MO, USA, October 2009. IEEE. ISBN 978-1-4244-3803-7. doi: 10.1109/IROS.2009.5354351.

[89] Robert Kiss. Elasticity of Human Embryonic Stem Cells as Determined by Atomic Force Microscopy. *Journal of Biomechanical Engineering*, 133(10):101009, November 2011. ISSN 0148-0731. doi: 10.1115/1.4005286.

[90] Fabian M. Hecht, Johannes Rheinlaender, Nicolas Schierbaum, Wolfgang H. Goldmann, Ben Fabry, and Tilman E. Schäffer. Imaging viscoelastic properties of live cells by AFM: Power-law rheology on the nanoscale. *Soft Matter*, 11(23): 4584–4591, 2015. ISSN 1744-683X, 1744-6848. doi: 10.1039/C4SM02718C.

[91] Ali Ghaemi, Alexandra Philipp, Andreas Bauer, Klaus Last, Andreas Fery, and Stephan Gekle. Mechanical behaviour of micro-capsules and their rupture under compression. *Chemical Engineering Science*, 142:236–243, March 2016. ISSN 00092509. doi: 10.1016/j.ces.2015.11.002.

[92] Ana Sancho, Ine Vandersmissen, Sander Craps, Aernout Luttun, and Jürgen Groll. A new strategy to measure intercellular adhesion forces in mature cell-cell contacts. *Scientific Reports*, 7(1):46152, May 2017. ISSN 2045-2322. doi: 10.1038/srep46152.

[93] R. Roscoe. On the rheology of a suspension of viscoelastic spheres in a viscous liquid. *Journal of Fluid Mechanics*, 28(02):273, May 1967. ISSN 0022-1120, 1469-7645. doi: 10.1017/S002211206700206X.

[94] George Barker Jeffery. The motion of ellipsoidal particles immersed in a viscous fluid. *Proceedings of the Royal Society of London. Series A, Containing Papers of a Mathematical and Physical Character*, 102(715):161–179, November 1922. ISSN 0950-1207, 2053-9150. doi: 10.1098/rspa.1922.0078.

[95] Andrea Cordes, Hannes Witt, Aina Gallemí-Pérez, Bastian Brückner, Florian Grimm, Marian Vache, Tabea Oswald, Jonathan Bodenschatz, Daniel Flormann, Franziska Lautenschläger, Marco Tarantola, and Andreas Janshoff. Prestress and Area Compressibility of Actin Cortices Determine the Viscoelastic Response of Living Cells. *Physical Review Letters*, 125(6):068101, August 2020. ISSN 0031-9007, 1079-7114. doi: 10.1103/PhysRevLett.125.068101.

[96] D.V. Zhelev, D. Needham, and R.M. Hochmuth. Role of the membrane cortex in neutrophil deformation in small pipets. *Biophysical Journal*, 67(2):696–705, August 1994. ISSN 00063495. doi: 10.1016/S0006-3495(94)80529-6.

[97] Janina R. Lange, Claus Metzner, Sebastian Richter, Werner Schneider, Monika Spermann, Thorsten Kolb, Graeme Whyte, and Ben Fabry. Unbiased High-Precision Cell Mechanical Measurements with Microconstrictions. *Biophysical Journal*, 112(7):1472–1480, April 2017. ISSN 00063495. doi: 10.1016/j.bpj.2017.02.018.

[98] Alexander Mietke, Oliver Otto, Salvatore Girardo, Philipp Rosendahl, Anna Taubenberger, Stefan Golfier, Elke Ulbricht, Sebastian Aland, Jochen Guck, and Elisabeth Fischer-Friedrich. Extracting Cell Stiffness from Real-Time Deformability Cytometry: Theory and Experiment. *Biophysical Journal*, 109(10):2023–2036, November 2015. ISSN 00063495. doi: 10.1016/j.bpj.2015.09.006.

[99] Oliver Otto, Philipp Rosendahl, Alexander Mietke, Stefan Golfier, Christoph Herold, Daniel Klaue, Salvatore Girardo, Stefano Pagliara, Andrew Ekpenyong, Angela Jacobi, Manja Wobus, Nicole Töpfner, Ulrich F Keyser, Jörg Mansfeld, Elisabeth Fischer-Friedrich, and Jochen Guck. Real-time deformability cytometry: On-the-fly cell mechanical phenotyping. *Nature Methods*, 12(3):199–202, March 2015. ISSN 1548-7091, 1548-7105. doi: 10.1038/nmeth.3281.

[100] Marta Urbanska, Hector E. Muñoz, Josephine Shaw Bagnall, Oliver Otto, Scott R. Manalis, Dino Di Carlo, and Jochen Guck. A comparison of microfluidic methods for high-throughput cell deformability measurements. *Nature Methods*, 17(6): 587–593, June 2020. ISSN 1548-7091, 1548-7105. doi: 10.1038/s41592-020-0818-8.

[101] Bob Fregin, Fabian Czerwinski, Doreen Biedenweg, Salvatore Girardo, Stefan Gross, Konstanze Aurich, and Oliver Otto. High-throughput single-cell rheology in complex samples by dynamic real-time deformability cytometry. *Nature Communications*, 10(1):415, December 2019. ISSN 2041-1723. doi: 10.1038/s41467-019-08370-3.

[102] Amy C. Rowat, Diana E. Jaalouk, Monika Zwerger, W.Lloyd Ung, Irwin A. Eydelnant, Don E. Olins, Ada L. Olins, Harald Herrmann, David A. Weitz, and Jan Lammerding. Nuclear Envelope Composition Determines the Ability of Neutrophil-type Cells to Passage through Micron-scale Constrictions. *Journal of Biological Chemistry*, 288(12):8610–8618, March 2013. ISSN 00219258. doi: 10.1074/jbc.M112.441535.

[103] Janina R. Lange, Julian Steinwachs, Thorsten Kolb, Lena A. Lautscham, Irina Harder, Graeme Whyte, and Ben Fabry. Microconstriction Arrays for High-Throughput Quantitative Measurements of Cell Mechanical Properties. *Biophysical Journal*, 109(1):26–34, July 2015. ISSN 00063495. doi: 10.1016/j.bpj.2015.05.029.

[104] Mathias Schlenk, Eddie Hofmann, Susanne Seibt, Sabine Rosenfeldt, Lukas Schrack, Markus Drechsler, Andre Rothkirch, Wiebke Ohm, Josef Breu, Stephan Gekle, and Stephan Förster. Parallel and Perpendicular Alignment of Anisotropic Particles in Free Liquid Microjets and Emerging Microdroplets. *Langmuir*, 34(16): 4843–4851, April 2018. ISSN 0743-7463, 1520-5827. doi: 10.1021/acs.langmuir.8b00062.

[105] Christian Bächer, Lukas Schrack, and Stephan Gekle. Clustering of microscopic particles in constricted blood flow. *Physical Review Fluids*, 2(1):013102, January 2017. ISSN 2469-990X. doi: 10.1103/PhysRevFluids.2.013102.

[106] Christian Bächer and Stephan Gekle. Computational modeling of active deformable membranes embedded in three-dimensional flows. *Physical Review E*, 99(6):062418, June 2019. ISSN 2470-0045, 2470-0053. doi: 10.1103/PhysRevE.99.062418.

[107] Wolfgang Ostwald. Ueber die rechnerische Darstellung des Strukturgebietes der Viskosität. *Kolloid-Zeitschrift*, 47(2):176–187, February 1929. ISSN 0303-402X, 1435-1536. doi: 10.1007/BF01496959.

[108] G. W. Scott. Blair, J. C. Hening, and A. Wagstaff. The Flow of Cream through Narrow Glass Tubes. *The Journal of Physical Chemistry*, 43(7):853–864, July 1939. ISSN 0092-7325, 1541-5740. doi: 10.1021/j150394a004.

[109] Taha Sochi. Analytical solutions for the flow of Carreau and Cross fluids in circular pipes and thin slits. *Rheologica Acta*, 54(8):745–756, August 2015. ISSN 0035-4511, 1435-1528. doi: 10.1007/s00397-015-0863-x.

[110] D. A. Cruz, P. M. Coelho, and M. A. Alves. A Simplified Method for Calculating Heat Transfer Coefficients and Friction Factors in Laminar Pipe Flow of Non-Newtonian Fluids. *Journal of Heat Transfer*, 134(9):091703, 2012. ISSN 00221481. doi: 10.1115/1.4006288.

[111] Qinghua Wu, Daniel Therriault, and Marie-Claude Heuzey. Processing and Properties of Chitosan Inks for 3D Printing of Hydrogel Microstructures. *ACS Biomaterials Science & Engineering*, 4(7):2643–2652, July 2018. ISSN 2373-9878, 2373-9878. doi: 10.1021/acsbiomaterials.8b00415.

[112] Howard A. Barnes, J. F. Hutton, and Kenneth Walters. *An Introduction to Rheology*. Number vol. 3 in Rheology Series. Elsevier : Distributors for the U.S. and Canada, Elsevier Science Pub. Co, Amsterdam ; New York, 1989. ISBN 978-0-444-87140-4.

[113] Lübtow, Mrlik, Hahn, Altmann, Beudert, Lühmann, and Luxenhofer. Temperature-Dependent Rheological and Viscoelastic Investigation of a Poly(2-methyl-2-oxazoline)-b-poly(2-iso-butyl-2-oxazoline)-b-poly(2-methyl-2-oxazoline)-Based Thermogelling Hydrogel. *Journal of Functional Biomaterials*, 10 (3):36, August 2019. ISSN 2079-4983. doi: 10.3390/jfb10030036.

[114] Ali Nadernezhad, Leonard Forster, Francesca Netti, Lihi Adler-Abramovich, Jörg Teßmar, and Jürgen Groll. Rheological analysis of the interplay between the molecular weight and concentration of hyaluronic acid in formulations of supramolecular HA/FmocFF hybrid hydrogels. *Polymer Journal*, 52(8):1007–1012, August 2020. ISSN 0032-3896, 1349-0540. doi: 10.1038/s41428-020-0358-1.

[115] Matthias Weis, Junwen Shan, Matthias Kuhlmann, Tomasz Jungst, Jörg Tessmar, and Jürgen Groll. Evaluation of Hydrogels Based on Oxidized Hyaluronic Acid for Bioprinting. *Gels*, 4(4):82, October 2018. ISSN 2310-2861. doi: 10.3390/gels4040082.

[116] Allan F. Bower. *Applied Mechanics of Solids*. CRC Press, Boca Raton, 2010. ISBN 978-1-4398-0247-2.

[117] Brian A. Aguado, Widya Mulyasasmita, James Su, Kyle J. Lampe, and Sarah C. Heilshorn. Improving Viability of Stem Cells During Syringe Needle Flow Through the Design of Hydrogel Cell Carriers. *Tissue Engineering Part A*, 18(7-8):806–815, April 2012. ISSN 1937-3341, 1937-335X. doi: 10.1089/ten.tea.2011.0391.

[118] Evan Mitsoulis. Numerical simulation of entry flow of fluid S1. *Journal of Non-Newtonian Fluid Mechanics*, 78(2-3):187–201, August 1998. ISSN 03770257. doi: 10.1016/S0377-0257(98)00073-1.

[119] Jonathan P. Rothstein and Gareth H. McKinley. Extensional flow of a polystyrene Boger fluid through a 4 : 1 : 4 axisymmetric contraction/expansion. *Journal of Non-Newtonian Fluid Mechanics*, 86(1-2):61–88, September 1999. ISSN 03770257. doi: 10.1016/S0377-0257(98)00202-X.

[120] D V Boger. Viscoelastic Flows Through Contractions. *Annual Review of Fluid Mechanics*, 19(1):157–182, January 1987. ISSN 0066-4189, 1545-4479. doi: 10.1146/annurev.fl.19.010187.001105.

[121] John Happel and Howard Brenner. *Low Reynolds Number Hydrodynamics*, volume 1 of *Mechanics of Fluids and Transport Processes*. Springer Netherlands, Dordrecht, 1981. ISBN 978-90-247-2877-0 978-94-009-8352-6. doi: 10.1007/978-94-009-8352-6.

[122] G. K. Batchelor. *An Introduction to Fluid Dynamics*. Cambridge University Press, Cambridge, 2000. ISBN 978-0-511-80095-5. doi: 10.1017/CBO9780511800955.

[123] A. Raptis, C. Massalas, and N. Kafousias. An exact solution of navier-stokes equations for conical tubes. *Journal of the Chinese Institute of Engineers*, 3(2):129–131, March 1980. ISSN 0253-3839, 2158-7299. doi: 10.1080/02533839.1980.9676657.

[124] Katharina Gräßel. Analytical and numerical description of liquid micro jets in the context of biological applications. Master's thesis, University of Bayreuth, Bayreuth, 2019.

[125] Clara Gremmelspacher. *Flow Profiles of Shearthinning Fluids in Typical Bioprint-ernozzels*. Bachelor thesis, University of Bayreuth, Bayreuth, 2021.

[126] Wenhuan Zhang, Changsheng Huang, Yihang Wang, Baochang Shi, Shibo Kuang, and Zhenhua Chai. The computation of strain rate tensor in multiple-relaxation-time lattice Boltzmann model. *Computers & Mathematics with Applications*, 75 (8):2888–2902, April 2018. ISSN 08981221. doi: 10.1016/j.camwa.2018.01.019.

[127] Timm Krüger, Halim Kusumaatmaja, Alexandr Kuzmin, Orest Shardt, Goncalo Silva, and Erlend Magnus Viggen. *The Lattice Boltzmann Method*. Graduate Texts in Physics. Springer International Publishing, Cham, 2017. ISBN 978-3-319-44647-9 978-3-319-44649-3. doi: 10.1007/978-3-319-44649-3.

[128] Sebastian Johannes Müller. Simulation of Stem Cells in Shear Thinning Bioinks. Master's thesis, University of Bayreuth, Bayreuth, 2018.

[129] Christophe Geuzaine and Jean-François Remacle. Gmsh: A 3-D finite element mesh generator with built-in pre- and post-processing facilities. *International Journal for Numerical Methods in Engineering*, 79(11):1309–1331, September 2009. ISSN 00295981, 10970207. doi: 10.1002/nme.2579.

[130] Jens W. Neubauer, Nicolas Hauck, Max J. Männel, Maximilian Seuss, Andreas Fery, and Julian Thiele. Mechanoresponsive Hydrogel Particles as a Platform for Three-Dimensional Force Sensing. *ACS Applied Materials & Interfaces*, 11(29): 26307–26313, July 2019. ISSN 1944-8244, 1944-8252. doi: 10.1021/acsami.9b04312.

Appendix A

Details of the derivation of the Roscoe theory

In this section, the mathematical derivations of the works of Roscoe [93] and Jeffery [94] are repeated for convenience and supplemented with additional details and explanations. For comparability, we will use the notation employed by Roscoe where possible and introduce new symbols where necessary. Hence, important equations which appear in both works will be references with the equation number according to Roscoe, who usually references the respective equation in Jeffery's work. Primed quantities always denote those of the fluid, such without prime belong to the particle. Quantities with a bar are the respective quantities averaged over the particle volume, which are equal to the value at the particle surface.
In a liquid of undisturbed (linear) fluid motion defined by [93, eq. (22)]

$$v_i' = e_{ij}'^{(1)} x_j + \zeta_{ij}' x_j \,, \tag{A.1}$$

with local strain [93, eq. (13)] and vorticity

$$e_{ij}'^{(1)} = \frac{1}{2}\left(\frac{\partial v_i'}{\partial x_j} + \frac{\partial v_j'}{\partial x_i}\right) \quad \text{and} \quad \zeta_{ij}' = \frac{1}{2}\left(\frac{\partial v_i'}{\partial x_j} - \frac{\partial v_j'}{\partial x_i}\right), \tag{A.2}$$

the fluid stress is given by [93, eq. (8)]

$$p_{ij}' = -p''\delta ij + 2\eta_0 e_{ij}'^{(1)} \,. \tag{A.3}$$

Here, p'' is a hydrostatic pressure and η_0 denotes the dynamic viscosity of the fluid. The second term is identical to the viscous stress defined previously in (2.3). The force per unit area at the particle surface (normals pointing outwards) at any point is given by [93, eq. (10)]

$$T_i = p_{ij} n_j \,, \tag{A.4}$$

where p_{ij} is the stress tensor inside the particle, which is assumed to fulfill

$$\frac{\partial p_{ik}}{\partial x_k} = 0 \,, \tag{A.5}$$

i. e., there is no variation of the stress inside the particle, and hence [93, eq. (11)]

$$p_{ij} = \frac{\partial(p_{ik}x_j)}{\partial x_k} \,. \tag{A.6}$$

Therefore, the average stress in the particle volume V (enclosed by the surface S) can be derived using the divergence theorem (‡) as follows:

$$\bar{p}_{ij} = \frac{1}{V}\int_V p_{ij}\,\mathrm{d}V \tag{A.7}$$

$$\overset{(A.6)}{=} \frac{1}{V}\int_V \frac{\partial(p_{ik}x_j)}{\partial x_k}\,\mathrm{d}V \tag{A.8}$$

$$\overset{‡}{=} \frac{1}{V}\int_S (p_{ik}x_j)n_k\,\mathrm{d}S \tag{A.9}$$

$$= \frac{1}{V}\int_S (p_{ik}n_k)x_j\,\mathrm{d}S \tag{A.10}$$

$$\overset{(A.4)}{=} \frac{1}{V}\int_S T_i x_j\,\mathrm{d}S \tag{A.11}$$

Note that the condition (A.5) for the stress in the particle is also assumed for the fluid,

$$\frac{\partial p'_{ik}}{\partial x_k} = \frac{1}{2}\left(\frac{\partial^2 v'_i}{\partial x_k^2} + \frac{\partial}{\partial x_k}\frac{\partial v'_k}{\partial x_i}\right) = 0\,, \tag{A.12}$$

and is known as slow-motion assumption.

The disturbed velocity field around the particle has to fulfill three conditions: (i) It has to approach the undisturbed velocity (A.1) for large distances from the particle, (ii) it has to be continuous across the particle surface, and (iii) fulfills a stress balance between fluid stresses (A.3) and particle stresses (A.11) [93].

This problem has been solved by Jeffery [94] for a rigid, ellipsoidal particle. His solution (using the notation of Roscoe [93]) for the force per unit area exerted by the liquid on the particle (A.4) is [93, eq. (15)]

$$T_i = -p'' n_i + \eta_0 A_{ij} n_j \,, \tag{A.13}$$

where A_{ij} is a certain deviatoric tensor (cf. eqs. (A.27)–(A.35) and description) with components that depend on the shape of the ellipsoidal particle and the undisturbed surrounding fluid motion (A.1). The shape of the ellipsoid is defined by its principal stretches α_1, α_2, and α_3, with

$$\alpha_1\alpha_2\alpha_3 = 1 \quad \text{and} \quad V = \frac{4\pi}{3}\alpha_1\alpha_2\alpha_3 a_0^3 \,. \tag{A.14}$$

Upon identifying the undisturbed fluid stress (A.3) in (A.13), it can be rewritten as

$$T_i = -p'' n_i + 2\eta_0 e'^{(1)}_{ij} n_j + \eta_0 A_{ij} n_j - 2\eta_0 e'^{(1)}_{ij} n_j \tag{A.15}$$

$$= \underbrace{-p'' n_i}_{\text{(i)}} + \underbrace{2\eta_0 e'^{(1)}_{ij} n_j}_{\text{(ii)}} + \underbrace{\eta_0 A_{ij} n_j}_{\text{(iii)}} + \underbrace{2\eta_0 \Delta e'^{(1)}_{ij} n_j}_{\text{(iv)}} = p_{ij} n_j \,. \tag{A.16}$$

With (A.4), one can identify four contributions to the particle stress: (i) The hydrostatic pressure, (ii) the fluid stress of the real undisturbed flow (A.1) in large distance of the particle, (iii) the stress exerted by the actual flow around the particle at its surface (A.13), and (iv) the stress caused by the disturbance $\Delta v_i'$ of the real undisturbed flow due to the particle presence at its surface. The last term [93, eq. (24)] contains the strain part of

$$\Delta v_i' = v_i - v_i' \,, \tag{A.17}$$

the difference between the real undisturbed fluid motion (A.1) and the particle motion at the surface, which is of similar form [93, eq. (23)]

$$v_i = \bar{e}_{ij}^{(1)} x_j - \bar{\zeta}_{ij} x_j \,, \tag{A.18}$$

and vanishes for a rigid particle, $v_i^{\text{rigid}} = 0$. Hence

$$\Delta v_i' = -v_i' = \Delta e_{ij}'^{(1)} x_j - \Delta \zeta_{ij}' x_j = -e_{ij}'^{(1)} x_j + \zeta_{ij}' x_j \,. \tag{A.19}$$

Roscoe applies the solution of Jeffery (A.16) to the case of a particle with internal and surface motion, i. e., $v_i \neq 0$. To be able to use the same formula as for the rigid particle, the disturbance (A.17) has to be equal to (A.19), which can be achieved via replacing the undisturbed flow by [93, eq. (25)]

$$v_i'' = e_{ij}''^{(1)} x_j - \zeta_{ij}'' x_j = v_i' - v_i \tag{A.20}$$

$$= \left(e_{ij}'^{(1)} - \bar{e}_{ij}^{(1)}\right) x_j - \left(\zeta_{ij}' - \bar{\zeta}_{ij}\right) x_j \,, \tag{A.21}$$

which yields

$$\Delta v_i' = \underbrace{0}_{\text{rigid}} - v_i'' \overset{\text{(A.17)}}{=} \underbrace{v_i}_{\text{moving}} - v_i' \,. \tag{A.22}$$

The surface force acting on a particle with surface motion v_i in an undisturbed flow v_i' is therefore:

$$T_i = \underbrace{-p'' n_i}_{\text{(i)}} + \underbrace{2\eta_0 e_{ij}'^{(1)} n_j}_{\text{(ii)}} + \underbrace{\eta_0 A_{ij}' n_j}_{\text{(iii)}} + \underbrace{2\eta_0 \Delta e_{ij}'^{(1)} n_j}_{\text{(iv)}} \tag{A.23}$$

The terms (i) and (ii) of (A.23) are equal to those of (A.16). A_{ij}' in (iii) denotes the deviatoric tensor A_{ij}, but computed for the replaced undisturbed fluid motion v_i'' (A.20) instead of v_i' (A.1). For the last term (iv), we insert the strain part of the disturbance (A.19) or (A.22) and obtain [93, eq. (26)]:

$$T_i = -p'' n_i + 2\eta_0 e_{ij}'^{(1)} n_j + \eta_0 A_{ij}' n_j - 2\eta_0 e_{ij}''^{(1)} n_j \tag{A.24}$$

$$= -p'' n_i + 2\eta_0 e_{ij}'^{(1)} n_j + \eta_0 A_{ij}' n_j - 2\eta_0 \left(e_{ij}'^{(1)} - \bar{e}_{ij}^{(1)}\right) n_j \tag{A.25}$$

$$= -p'' n_i + \eta_0 A_{ij}' n_j + 2\eta_0 \bar{e}_{ij}^{(1)}) n_j \tag{A.26}$$

The deviatoric tensor A_{ij} is found during the derivation of the velocity field around the rigid particle in the work of Jeffery [94] by applying the boundary condition to the flow field at the particle surface, and is defined by [93, eqs. (17),(19)] (or [94, eqs. (25),(26)] in the original work):

$$A_{11} = \frac{4}{3}\frac{2g_1'' e_{11}'^{(1)} - g_2'' e_{22}'^{(1)} - g_3'' e_{33}'^{(1)}}{g_2'' g_3'' + g_3'' g_1'' + g_1'' g_2''} \tag{A.27}$$

$$A_{22} = \frac{4}{3}\frac{2g_2'' e_{22}'^{(1)} - g_3'' e_{33}'^{(1)} - g_1'' e_{11}'^{(1)}}{g_2'' g_3'' + g_3'' g_1'' + g_1'' g_2''} \tag{A.28}$$

$$A_{33} = \frac{4}{3}\frac{2g_3'' e_{33}'^{(1)} - g_1'' e_{11}'^{(1)} - g_2'' e_{22}'^{(1)}}{g_2'' g_3'' + g_3'' g_1'' + g_1'' g_2''} \tag{A.29}$$

$$A_{12} = 4\frac{g_1 e_{12}'^{(1)} - \alpha_2^2 g_3' \zeta_{12}'}{g_3'(\alpha_1^2 g_1 + \alpha_2^2 g_2)} \tag{A.30}$$

$$A_{13} = 4\frac{g_1 e_{13}'^{(1)} - \alpha_3^2 g_2' \zeta_{13}'}{g_2'(\alpha_1^2 g_1 + \alpha_3^2 g_3)} \tag{A.31}$$

$$A_{23} = 4\frac{g_2 e_{23}'^{(1)} - \alpha_3^2 g_1' \zeta_{23}'}{g_1'(\alpha_2^2 g_2 + \alpha_3^2 g_3)} \tag{A.32}$$

Due to the symmetry of the tensors $e_{ij}'^{(1)} = e_{ji}'^{(1)}$ and $\zeta_{ij}' = -\zeta_{ji}'$, it follows for the lower off-diagonal elements of A_{ij}:

$$A_{21} = \frac{g_2 e_{21}'^{(1)} - \alpha_1^2 g_3' \zeta_{21}'}{2g_3'(\alpha_1^2 g_1 + \alpha_2^2 g_2)} = \frac{g_2 e_{12}'^{(1)} + \alpha_1^2 g_3' \zeta_{12}'}{2g_3'(\alpha_1^2 g_1 + \alpha_2^2 g_2)} \tag{A.33}$$

$$A_{31} = \frac{g_3 e_{31}'^{(1)} - \alpha_1^2 g_2' \zeta_{31}'}{2g_2'(\alpha_1^2 g_1 + \alpha_3^2 g_3)} = \frac{g_3 e_{13}'^{(1)} + \alpha_1^2 g_2' \zeta_{13}'}{2g_2'(\alpha_1^2 g_1 + \alpha_3^2 g_3)} \tag{A.34}$$

$$A_{32} = \frac{g_3 e_{32}'^{(1)} - \alpha_2^2 g_1' \zeta_{32}'}{2g_1'(\alpha_2^2 g_2 + \alpha_3^2 g_3)} = \frac{g_3 e_{23}'^{(1)} + \alpha_2^2 g_1' \zeta_{23}'}{2g_1'(\alpha_2^2 g_2 + \alpha_3^2 g_3)} \tag{A.35}$$

Note that Jeffery's solution [94, eq. (26)] is derived for a rotating particle and its rotation frequencies ω_i appear in the off-diagonal components, which is omitted here. The quantities g_i, g_i', and g_i'', are given with $\Delta' = \sqrt{(\alpha_1^2+\lambda')(\alpha_2^2+\lambda')(\alpha_3^2+\lambda')}$ by the following integrals [93, eq. (20)][94, eq. (11)]:

$$g_1 = \int_0^\infty \frac{\mathrm{d}\lambda'}{(\alpha_1^2+\lambda')\Delta'} \tag{A.36}$$

$$g_2 = \int_0^\infty \frac{\mathrm{d}\lambda'}{(\alpha_2^2+\lambda')\Delta'} \tag{A.37}$$

$$g_3 = \int_0^\infty \frac{\mathrm{d}\lambda'}{(\alpha_3^2+\lambda')\Delta'} \tag{A.38}$$

$$g_1' = \int_0^\infty \frac{\mathrm{d}\lambda'}{(\alpha_2^2+\lambda')(\alpha_3^2+\lambda')\Delta'} = \frac{g_3-g_2}{\alpha_2^2-\alpha_3^2} \tag{A.39}$$

$$g_2' = \int_0^\infty \frac{\mathrm{d}\lambda'}{(\alpha_3^2+\lambda')(\alpha_1^2+\lambda')\Delta'} = \frac{g_1-g_3}{\alpha_3^2-\alpha_1^2} \tag{A.40}$$

$$g_3' = \int_0^\infty \frac{\mathrm{d}\lambda'}{(\alpha_1^2+\lambda')(\alpha_2^2+\lambda')\Delta'} = \frac{g_2-g_1}{\alpha_1^2-\alpha_2^2} \tag{A.41}$$

$$g_1'' = \int_0^\infty \frac{\lambda'\,\mathrm{d}\lambda'}{(\alpha_2^2+\lambda')(\alpha_3^2+\lambda')\Delta'} = \frac{\alpha_2^2 g_2-\alpha_3^2 g_3}{\alpha_2^2-\alpha_3^2} \tag{A.42}$$

$$g_2'' = \int_0^\infty \frac{\lambda'\,\mathrm{d}\lambda'}{(\alpha_3^2+\lambda')(\alpha_1^2+\lambda')\Delta'} = \frac{\alpha_3^2 g_3-\alpha_1^2 g_1}{\alpha_3^2-\alpha_1^2} \tag{A.43}$$

$$g_3'' = \int_0^\infty \frac{\lambda'\,\mathrm{d}\lambda'}{(\alpha_1^2+\lambda')(\alpha_2^2+\lambda')\Delta'} = \frac{\alpha_1^2 g_1-\alpha_2^2 g_2}{\alpha_1^2-\alpha_2^2} \tag{A.44}$$

Note that we use the symbol λ' to denote the difference between Roscoe's dimensionless quantity λ [93, eq. (18)] (which we use here) and Jeffery's notation [94, eq. (7)]. Shall the fluid stress be symmetric, the same will apply to A_{ij}, which leads to the following relations between the undisturbed fluids rate of strain and vorticity and the shape of the ellipsoid:

$$A_{12} = A_{21} \tag{A.45}$$

$$\Rightarrow \quad \frac{\zeta_{12}'}{e_{12}'^{(1)}} = -\frac{\alpha_1^2-\alpha_2^2}{\alpha_1^2+\alpha_2^2} \tag{A.46}$$

Inserted into (A.30)–(A.32) simplifies the off-diagonal components of A and yields [94, eq. (39)]

$$A_{12} \overset{(A.30)}{=} 4\frac{g_1 e'^{(1)}_{12} - \alpha_2^2 g'_3 \zeta'_{12}}{g'_3(\alpha_1^2 g_1 + \alpha_2^2 g_2)} \tag{A.47}$$

$$\overset{(A.46)}{=} 4e'^{(1)}_{12} \frac{g_1 + \alpha_2^2 \frac{\alpha_1^2-\alpha_2^2}{\alpha_1^2+\alpha_2^2} g'_3}{g'_3(\alpha_1^2 g_1 + \alpha_2^2 g_2)} \tag{A.48}$$

$$\overset{(A.41)}{=} 4e'^{(1)}_{12} \frac{g_1 + \alpha_2^2 \frac{\alpha_1^2-\alpha_2^2}{\alpha_1^2+\alpha_2^2} \frac{g_2-g_1}{\alpha_1^2-\alpha_2^2}}{g'_3(\alpha_1^2 g_1 + \alpha_2^2 g_2)} \tag{A.49}$$

$$= \frac{4e'^{(1)}_{12}}{g'_3(\alpha_1^2+\alpha_2^2)} \left(\alpha_1^2+\alpha_2^2\right) \frac{g_1 + \alpha_2^2 \frac{\alpha_1^2-\alpha_2^2}{\alpha_1^2+\alpha_2^2} \frac{g_2-g_1}{\alpha_1^2-\alpha_2^2}}{(\alpha_1^2 g_1 + \alpha_2^2 g_2)} \tag{A.50}$$

$$= \frac{4e'^{(1)}_{12}}{g'_3(\alpha_1^2+\alpha_2^2)} \frac{g_1\alpha_1^2 + g_1\alpha_2^2 + g_2\alpha_2^2 - g_1\alpha_2^2}{(\alpha_1^2 g_1 + \alpha_2^2 g_2)} \tag{A.51}$$

$$= \frac{4e'^{(1)}_{12}}{g'_3(\alpha_1^2+\alpha_2^2)} \,, \tag{A.52}$$

as well as

$$A_{13} = \frac{4e'^{(1)}_{13}}{g'_2(\alpha_3^2+\alpha_1^2)} \tag{A.53}$$

$$A_{23} = \frac{4e'^{(1)}_{23}}{g'_1(\alpha_2^2+\alpha_3^2)} \,. \tag{A.54}$$

Roscoe [93, ch. 4] applies the computations above to a viscoelastic ellipsoidal particle with a moving boundary (tank-treading behavior) in linear shear flow as follows: The coordinates of a material point of the particle starting at position $(\tilde{x}_1, \tilde{x}_2, \tilde{x}_3)$ are following an elliptical trajectory and are given by [93, eq. (29a)]

$$x_1 = \alpha_1(\tilde{x}_1 \cos(\nu t) - \tilde{x}_2 \sin(\nu t)) \tag{A.55}$$

$$x_2 = \alpha_2(\tilde{x}_1 \sin(\nu t) + \tilde{x}_2 \cos(\nu t)) \tag{A.56}$$

$$x_3 = \alpha_3 \tilde{x}_3 \,, \tag{A.57}$$

where x_1, x_2, and x_3, align with the ellipsoid's semi-axes, thus yielding the surface velocity [93, eq. (29b)]

$$v_1 = -\frac{\alpha_1}{\alpha_2} \nu x_2 \tag{A.58}$$

$$v_2 = \frac{\alpha_2}{\alpha_1} \nu x_1 \tag{A.59}$$

$$v_3 = 0 \,. \tag{A.60}$$

The surface velocity defines the rate of strain and vorticity from (A.18). A linear shear flow — commonly described in the global coordinate system as $v'_1 = \kappa x_2$, $v'_2 = v'_3 = 0$

[93, eq. (27)] with a shear rate κ — written in terms of a coordinate system aligned with the ellipsoid's semi-axes through rotation by an angle θ is given by [93, eq. (32)]

$$v_1' = \kappa\Big(x_1 \sin\theta\cos\theta + x_2 \cos^2(\theta)\Big) \tag{A.61}$$

$$v_2' = -\kappa\Big(x_1 \sin^2(\theta) + x_2 \sin\theta\cos\theta\Big) \tag{A.62}$$

$$v_3' = 0\,. \tag{A.63}$$

From that, the only non-zero components of the replaced undisturbed fluid's rate of strain and vorticity from (A.2) follow as [93, eqs. (33)–(35)]

$$e_{11}'^{(1)} - \bar{e}_{11}^{(1)} = -\Big(e_{22}'^{(1)} - \bar{e}_{22}^{(1)}\Big) = \frac{\kappa}{2}\sin(2\theta) \tag{A.64}$$

$$e_{12}'^{(1)} - \bar{e}_{12}^{(1)} = e_{21}'^{(1)} - \bar{e}_{21}^{(1)} = \frac{\kappa}{2}\cos(2\theta) + \nu\frac{\alpha_1^2 - \alpha_2^2}{2\alpha_1\alpha_2} \tag{A.65}$$

$$\zeta_{12}' - \bar{\zeta}_{12} = -\Big(\zeta_{21}' - \bar{\zeta}_{21}\Big) = -\frac{\kappa}{2} - \nu\frac{\alpha_1^2 + \alpha_2^2}{2\alpha_1\alpha_2}\,, \tag{A.66}$$

and, together with (A.18), the fluid stress at the particle surface from (A.24) can be computed as [93, eq. (36)]:

$$p_{11}' = -p'' + \eta_0 A_{11}' \tag{A.67}$$

$$p_{22}' = -p'' + \eta_0 A_{22}' \tag{A.68}$$

$$p_{33}' = -p'' + \eta_0 A_{33}' \tag{A.69}$$

$$p_{12}' = \eta_0 A_{12}' - \eta_0\nu\frac{\alpha_1^2 - \alpha_2^2}{\alpha_1\alpha_2} \tag{A.70}$$

$$p_{21}' = \eta_0 A_{21}' - \eta_0\nu\frac{\alpha_1^2 - \alpha_2^2}{\alpha_1\alpha_2} \tag{A.71}$$

Differences of the normal stresses can be used to eliminate the hydrostatic pressure p''. One obtains [93, eqs. (37),(38)][1]

$$p_{11}' - p_{22}' = 2\eta_0\kappa\sin(2\theta)\frac{g_1'' + g_2''}{g_2''g_3'' + g_3''g_1'' + g_1''g_2''} = 5\eta_0\kappa\sin(2\theta)I \tag{A.72}$$

$$p_{11}' + p_{22}' - 2p_{33}' = 2\eta_0\kappa\sin(2\theta)\frac{g_1'' - g_2''}{g_2''g_3'' + g_3''g_1'' + g_1''g_2''} = 5\eta_0\kappa\sin(2\theta)J\,. \tag{A.73}$$

Due to the symmetry of the stress tensor, $p_{12}' = p_{21}'$, it follows with (A.46) the relation between the shear rate of the undisturbed liquid κ and the tank-treading frequency of

[1] The parameters I and J correspond to the notation used by Roscoe and do not refer to the strain invariants of the elastic cell model.

the particle ν [93, eq. (41)]:

$$-\frac{\zeta'_{12}}{e'^{(1)}_{12}} = \frac{\alpha_1^2-\alpha_2^2}{\alpha_1^2+\alpha_2^2} \tag{A.74}$$

$$\frac{\frac{\kappa}{2}+\nu\frac{\alpha_1^2+\alpha_2^2}{2\alpha_1\alpha_2}}{\frac{\kappa}{2}\cos(2\theta)+\nu\frac{\alpha_1^2-\alpha_2^2}{2\alpha_1\alpha_2}} = \frac{\alpha_1^2-\alpha_2^2}{\alpha_1^2+\alpha_2^2} \tag{A.75}$$

$$\nu\left(\frac{\alpha_1^2-\alpha_2^2}{\alpha_1^2+\alpha_2^2}\frac{\alpha_1^2-\alpha_2^2}{2\alpha_1\alpha_2}-\frac{\alpha_1^2+\alpha_2^2}{2\alpha_1\alpha_2}\right) = \frac{\kappa}{2}\left(1-\frac{\alpha_1^2-\alpha_2^2}{\alpha_1^2+\alpha_2^2}\cos(2\theta)\right) \tag{A.76}$$

$$-\frac{2\alpha_1\alpha_2}{\alpha_1^2+\alpha_2^2}\nu = \frac{\kappa}{2}\left(1-\frac{\alpha_1^2-\alpha_2^2}{\alpha_1^2+\alpha_2^2}\cos(2\theta)\right) \tag{A.77}$$

$$\Rightarrow \quad \nu = -\frac{\alpha_1^2+\alpha_2^2}{2\alpha_1\alpha_2}\frac{\kappa}{2}\left(1-\frac{\alpha_1^2-\alpha_2^2}{\alpha_1^2+\alpha_2^2}\cos(2\theta)\right) \tag{A.78}$$

Inserting the obtained results into (A.70), one obtains

$$p'_{12} = \eta_0 A'_{12} - \eta_0\nu\frac{\alpha_1^2-\alpha_2^2}{\alpha_1\alpha_2} \tag{A.79}$$

$$\overset{(A.52)}{=} \eta_0\frac{4e'^{(1)}_{12}}{g'_3(\alpha_1^2+\alpha_2^2)} - \eta_0\nu\frac{\alpha_1^2-\alpha_2^2}{\alpha_1\alpha_2} \tag{A.80}$$

$$\overset{(A.65)}{=} \eta_0\frac{4}{g'_3(\alpha_1^2+\alpha_2^2)}\left(\frac{\kappa}{2}\cos(2\theta)+\nu\frac{\alpha_1^2-\alpha_2^2}{2\alpha_1\alpha_2}\right) - \eta_0\nu\frac{\alpha_1^2-\alpha_2^2}{\alpha_1\alpha_2} \tag{A.81}$$

$$\begin{aligned}\overset{(A.78)}{=} \eta_0\frac{4}{g'_3(\alpha_1^2+\alpha_2^2)}&\left(\frac{\kappa}{2}\cos(2\theta)-\frac{\alpha_1^2+\alpha_2^2}{2\alpha_1\alpha_2}\frac{\kappa}{2}\left(1-\frac{\alpha_1^2-\alpha_2^2}{\alpha_1^2+\alpha_2^2}\cos(2\theta)\right)\frac{\alpha_1^2-\alpha_2^2}{2\alpha_1\alpha_2}\right)\\ &- \eta_0\nu\frac{\alpha_1^2-\alpha_2^2}{\alpha_1\alpha_2}\,,\end{aligned} \tag{A.82}$$

which simplifies to [93, eqs. (42),(43)]

$$= \eta_0\frac{4\kappa}{2g'_3}\left[\frac{\cos(2\theta)}{(\alpha_1^2+\alpha_2^2)}-\frac{1}{2\alpha_1\alpha_2}\left(1-\frac{\alpha_1^2-\alpha_2^2}{\alpha_1^2+\alpha_2^2}\cos(2\theta)\right)\frac{\alpha_1^2-\alpha_2^2}{2\alpha_1\alpha_2}\right] - \eta_0\nu\frac{\alpha_1^2-\alpha_2^2}{\alpha_1\alpha_2} \tag{A.83}$$

$$= \eta_0\frac{\kappa}{2g'_3}\left[\cos(2\theta)\left(\frac{4}{(\alpha_1^2+\alpha_2^2)}+\frac{(\alpha_1^2-\alpha_2^2)^2}{\alpha_1^2\alpha_2^2(\alpha_1^2+\alpha_2^2)}\right)-\frac{(\alpha_1^2-\alpha_2^2)}{\alpha_1^2\alpha_2^2}\right] - \eta_0\nu\frac{\alpha_1^2-\alpha_2^2}{\alpha_1\alpha_2} \tag{A.84}$$

$$= \eta_0\frac{\kappa}{2g'_3}\left[\cos(2\theta)\frac{\alpha_1^2+\alpha_2^2}{\alpha_1^2\alpha_2^2}-\frac{(\alpha_1^2-\alpha_2^2)}{\alpha_1^2\alpha_2^2}\right] - \eta_0\nu\frac{\alpha_1^2-\alpha_2^2}{\alpha_1\alpha_2} \tag{A.85}$$

$$= \eta_0\frac{\kappa}{2g'_3}\frac{\alpha_1^2+\alpha_2^2}{\alpha_1^2\alpha_2^2}\left[\cos(2\theta)-\frac{\alpha_1^2-\alpha_2^2}{\alpha_1^2+\alpha_2^2}\right] - \eta_0\nu\frac{\alpha_1^2-\alpha_2^2}{\alpha_1\alpha_2} \tag{A.86}$$

$$= \frac{5}{2}\kappa\eta_0 K\left[\cos(2\theta)-\frac{\alpha_1^2-\alpha_2^2}{\alpha_1^2+\alpha_2^2}\right] - \eta_0\nu\frac{\alpha_1^2-\alpha_2^2}{\alpha_1\alpha_2}\,. \tag{A.87}$$

With the equations above, the viscous stress exerted by the fluid on the particle surface is determined by the ellipsoid's shape, the shear rate of the undisturbed flow in infinite distance, and the inclination angle between the flow axis and the ellipsoid's major semi-axis. The shape of the ellipsoid depends on the constitutive law of its material, which defines how much elastic stress the particle exerts on the fluid at its surface given a certain deformation and the material properties. For the triaxial ellipsoidal deformation defined by (A.55) and introduced the beginning of section 3.2, the normal stress differences at the particle surface using the Mooney-Rivlin description (2.21) can be computed from (3.40):

$$p_{11} - p_{22} = \mu\left[w\left(\alpha_1^2 - \alpha_2^2\right) + (1-w)\left(\frac{1}{\alpha_2^2} - \frac{1}{\alpha_1^2}\right)\right] \tag{A.88}$$

$$p_{11} + p_{22} - 2p_{33} = \mu\left[w\left(\alpha_1^2 + \alpha_2^2 - \frac{2}{\alpha_1^2\alpha_2^2}\right) + (1-w)\left(\frac{1}{\alpha_2^2} + \frac{1}{\alpha_1^2} - 2\alpha_1^2\alpha_2^2\right)\right] \tag{A.89}$$

In a stationary state, the fluid stress must be balanced by the cell stress at the particle surface [93], i. e., the normal stress differences of the fluid (A.72) and (A.73) must balance the elastic particle stress from (A.88) and (A.88), respectively. Since the off-diagonal components are zero for a triaxial deformation, the fluid stress p'_{12} must be balanced by the viscous stress caused by the material motion inside the particle (A.58)–(A.60) [93, eq. (54)]

$$p_{12} = -\eta_1 \bar{e}_{12}^{(1)} = -\eta_1 \nu \frac{\alpha_1^2 - \alpha_2^2}{\alpha_1 \alpha_2}\,, \tag{A.90}$$

where viscosity of the particle material is denoted by η_1. The obtained system of equations for the coupled viscoelastic motion is:

$$p'_{11} - p'_{22} = p_{11} - p_{22} \tag{A.91}$$

$$p'_{11} + p'_{22} - 2p'_{33} = p_{11} + p_{22} - 2p_{33} \tag{A.92}$$

$$p'_{12} = p_{12} \tag{A.93}$$

From the equality of the (purely viscous) shear stress (A.93), the inclination angle θ can be derived [93, eq. (80)] as follows:

$$0 = p'_{12} - p_{12} \tag{A.94}$$

$$\overset{(A.87),(A.90)}{=} \frac{5}{2}\kappa\eta_0 K\left[\cos(2\theta) - \frac{\alpha_1^2-\alpha_2^2}{\alpha_1^2+\alpha_2^2}\right] - \eta_0\nu\frac{\alpha_1^2-\alpha_2^2}{\alpha_1\alpha_2} + \eta_1\nu\frac{\alpha_1^2-\alpha_2^2}{\alpha_1\alpha_2} \tag{A.95}$$

$$= \frac{5}{2}\kappa\eta_0 K\left[\cos(2\theta) - \frac{\alpha_1^2-\alpha_2^2}{\alpha_1^2+\alpha_2^2}\right] - \nu\frac{\alpha_1^2-\alpha_2^2}{\alpha_1\alpha_2}(\eta_0-\eta_1) \tag{A.96}$$

$$\overset{(A.78)}{=} 5\frac{\kappa}{2}\eta_0 K\left[\cos(2\theta) - \frac{\alpha_1^2-\alpha_2^2}{\alpha_1^2+\alpha_2^2}\right] + \frac{\alpha_1^2+\alpha_2^2}{2\alpha_1\alpha_2}\frac{\kappa}{2}\left[1 - \frac{\alpha_1^2-\alpha_2^2}{\alpha_1^2+\alpha_2^2}\cos(2\theta)\right]\frac{\alpha_1^2-\alpha_2^2}{\alpha_1\alpha_2}(\eta_0-\eta_1) \tag{A.97}$$

$$\overset{\times\frac{2}{5\kappa\eta_0 K}}{\Leftrightarrow} 0 = \cos(2\theta) - \frac{\alpha_1^2-\alpha_2^2}{\alpha_1^2+\alpha_2^2} + \frac{\alpha_1^2+\alpha_2^2}{2\alpha_1\alpha_2}\left[1 - \frac{\alpha_1^2-\alpha_2^2}{\alpha_1^2+\alpha_2^2}\cos(2\theta)\right]\frac{\alpha_1^2-\alpha_2^2}{\alpha_1\alpha_2}\frac{\eta_0-\eta_1}{5K\eta_0} \tag{A.98}$$

$$= \cos(2\theta)\left[1 - \frac{\alpha_1^2+\alpha_2^2}{2\alpha_1\alpha_2}\frac{\alpha_1^2-\alpha_2^2}{\alpha_1^2+\alpha_2^2}\frac{\alpha_1^2-\alpha_2^2}{\alpha_1\alpha_2}\frac{\eta_0-\eta_1}{5K\eta_0}\right] - \frac{\alpha_1^2-\alpha_2^2}{\alpha_1^2+\alpha_2^2} + \frac{\alpha_1^2+\alpha_2^2}{2\alpha_1\alpha_2}\frac{\alpha_1^2-\alpha_2^2}{\alpha_1\alpha_2}\frac{\eta_0-\eta_1}{5K\eta_0} \tag{A.99}$$

$$= \cos(2\theta)\left[1 - \frac{\left(\alpha_1^2-\alpha_2^2\right)^2}{2\alpha_1^2\alpha_2^2}\frac{\eta_0-\eta_1}{5K\eta_0}\right] - \frac{\alpha_1^2-\alpha_2^2}{\alpha_1^2+\alpha_2^2}\left[1 - \frac{\left(\alpha_1^2+\alpha_2^2\right)^2}{2\alpha_1^2\alpha_2^2}\frac{\eta_0-\eta_1}{5K\eta_0}\right] \tag{A.100}$$

$$\Leftrightarrow \cos(2\theta) = \left(\frac{\alpha_1^2-\alpha_2^2}{\alpha_1^2+\alpha_2^2}\right)\frac{1 - \frac{2}{5K}\frac{\eta_0-\eta_1}{\eta_0}\left(\frac{\alpha_1^2+\alpha_2^2}{2\alpha_1\alpha_2}\right)^2}{1 - \frac{2}{5K}\frac{\eta_0-\eta_1}{\eta_0}\left(\frac{\alpha_1^2-\alpha_2^2}{2\alpha_1\alpha_2}\right)^2} \tag{A.101}$$

Using the parameter definition in [93, eq. (62)], i. e.,

$$\tau = \frac{3\eta_0+2\eta_1}{2\mu}, \quad \sigma = \frac{5\eta_0}{2\mu} \quad \text{and} \quad \frac{\tau-\sigma}{K\sigma} = -\frac{2}{5K}\frac{\eta_0-\eta_1}{\eta_0}, \tag{A.102}$$

(A.101) can be written as [93, eq. (80)]

$$\cos(2\theta) = \left(\frac{\alpha_1^2-\alpha_2^2}{\alpha_1^2+\alpha_2^2}\right)\frac{1 + \frac{\tau-\sigma}{K\sigma}\left(\frac{\alpha_1^2+\alpha_2^2}{2\alpha_1\alpha_2}\right)^2}{1 + \frac{\tau-\sigma}{K\sigma}\left(\frac{\alpha_1^2-\alpha_2^2}{2\alpha_1\alpha_2}\right)^2}. \tag{A.103}$$

Numerical solution of the Roscoe theory

One of the key results of the Roscoe theory used in the present thesis is the knowledge of stationary cell deformation as function of the Capillary number. The following section

describes one approach to obtain it from the coupled problem from the previous section step by step. The relevant equations are repeated here for convenience.

1. Set the viscous and elastic parameters η_0, η_1, and μ.

2. Choose a value of α_1 for which the rest of the parameters is to be determined.

3. Divide (A.92) by (A.91) to obtain an equation that can be solved (numerically) for α_2 [93, eq. (78)]:

$$\frac{p_{11}+p_{22}-2p_{33}}{p_{11}-p_{22}} = \frac{J}{I} \tag{A.104}$$

$$\frac{w\left(\alpha_1^2+\alpha_2^2-\frac{2}{\alpha_1^2\alpha_2^2}\right)+(1-w)\left(\frac{1}{\alpha_2^2}+\frac{1}{\alpha_1^2}-2\alpha_1^2\alpha_2^2\right)}{w(\alpha_1^2-\alpha_2^2)+(1-w)\left(\frac{1}{\alpha_2^2}-\frac{1}{\alpha_1^2}\right)} = \frac{g_1''-g_2''}{g_1''+g_2''} \tag{A.105}$$

4. The incompressibility condition yields the last semi-axis

$$\alpha_3 = \frac{1}{\alpha_1\alpha_2} \tag{A.106}$$

   and the cell deformation is completely determined.

5. With the particle shape fully defined, its inclination angle with the flow axis can be computed with (A.101)

$$\cos(2\theta) = \left(\frac{\alpha_1^2-\alpha_2^2}{\alpha_1^2+\alpha_2^2}\right)\frac{1-\frac{2}{5K}(1-\phi)\left(\frac{\alpha_1^2+\alpha_2^2}{2\alpha_1\alpha_2}\right)^2}{1-\frac{2}{5K}(1-\phi)\left(\frac{\alpha_1^2-\alpha_2^2}{2\alpha_1\alpha_2}\right)^2}\,, \tag{A.107}$$

   where $\phi = \frac{\eta_1}{\eta_0}$ denotes the viscosity ratio between the liquid inside and outside of the particle.

6. Solving (A.91) for κ yields

$$\kappa = \frac{\mu}{2\eta_0\sin(2\theta)}\frac{g_2''g_3''+g_3''g_1''+g_1''g_2''}{g_1''+g_2''}\left[w\left(\alpha_1^2-\alpha_2^2\right)+(1-w)\left(\frac{1}{\alpha_2^2}-\frac{1}{\alpha_1^2}\right)\right]. \tag{A.108}$$

7. Finally, the tank-treading frequency follows from (A.78) from the computed flow parameters:

$$\nu = -\frac{\kappa}{2}\frac{\alpha_1^2+\alpha_2^2}{2\alpha_1\alpha_2}\left(1-\frac{\alpha_1^2-\alpha_2^2}{\alpha_1^2+\alpha_2^2}\cos(2\theta)\right) \tag{A.109}$$

Roscoe theory in the limits of low and high Capillary number

Ca $\to$ 0: In the limit of very low Capillary number, the cell remains essentially spherical thus greatly simplifying the theoretical computations of Roscoe. The integrals in (A.36)–(A.44) reduce to

$$g_1 = g_2 = g_3 = \frac{2}{3} \tag{A.110}$$

$$g_1' = g_2' = g_3' = \frac{2}{5} \tag{A.111}$$

$$g_1'' = g_2'' = g_3'' = \frac{4}{15}\,. \tag{A.112}$$

Since $\lim\limits_{\mathrm{Ca}\to 0} \alpha_1 = \lim\limits_{\mathrm{Ca}\to 0} \alpha_2 = \lim\limits_{\mathrm{Ca}\to 0} \alpha_3 = 1$, the inclination angle (A.101) is found as $\theta = 45°$. The tank-treading frequency (A.78) is therefore $\nu = -\frac{\kappa}{2}$, the shear stress (A.71) vanishes, and the diagonal stresses (A.67)–(A.70) give $\sigma_{11} = -\sigma_{22} = \frac{5}{2}\kappa\eta_0$.

Ca $\to \infty$: In the limit of very high Capillary number, the cell becomes an infinitley stretched ellipsoid, with semi axes

$$\lim_{\mathrm{Ca}\to\infty} \alpha_1 = \infty \tag{A.113}$$

$$\lim_{\mathrm{Ca}\to\infty} \alpha_2 = 0 \tag{A.114}$$

$$1 < \alpha_3 \ll \alpha_1 \tag{A.115}$$

aligned with the global coordinate axes. The alignment $\theta = 0$ again follows from (A.101) (using $\eta_0 = \eta_1$):

$$\lim_{\mathrm{Ca}\to\infty} \cos(2\theta) = \lim_{\mathrm{Ca}\to\infty} \frac{\alpha_1^2 - \alpha_2^2}{\alpha_1^2 + \alpha_2^2} = 1\,, \tag{A.116}$$

hence $\theta = 0$. Similarly, it follows

$$\lim_{\mathrm{Ca}\to\infty} \nu = -\frac{\kappa}{2} \lim_{\mathrm{Ca}\to\infty} \frac{\alpha_1^2 + \alpha_2^2}{2\alpha_1\alpha_2} \left(1 - \frac{\alpha_1^2 - \alpha_2^2}{\alpha_1^2 + \alpha_2^2} \cos(2\theta)\right) \tag{A.117}$$

$$= -\frac{\kappa}{2} \lim_{\mathrm{Ca}\to\infty} \frac{1}{2\alpha_1\alpha_2} \frac{\left(\alpha_1^2 + \alpha_2^2\right)^2 - \left(\alpha_1^2 - \alpha_2^2\right)^2}{\alpha_1^2 + \alpha_2^2}$$

$$= -\frac{\kappa}{2} \lim_{\mathrm{Ca}\to\infty} \frac{2\alpha_1\alpha_2}{\alpha_1^2 + \alpha_2^2} = 0^{(-)} \tag{A.118}$$

for the tank-treading frequency. Note however, that, while ν asymptotically approaches zero, the velocity of a point at the particle surface does not vanish. In fact, for a point

on the α_2-axis inside the cell, one obtains for the velocity (A.58)

$$\lim_{\mathrm{Ca}\to\infty} v_1 = -\lim_{\mathrm{Ca}\to\infty} \frac{\alpha_1}{\alpha_2} x_2 \left(-\frac{\kappa}{2}\right) \frac{\alpha_1^2+\alpha_2^2}{2\alpha_1\alpha_2} \left(1 - \frac{\alpha_1^2-\alpha_2^2}{\alpha_1^2+\alpha_2^2}\cos(2\theta)\right) \tag{A.119}$$

$$= \kappa x_2 \lim_{\mathrm{Ca}\to\infty} \frac{1}{4}\left(\frac{\alpha_1^2+\alpha_2^2}{\alpha_2} - \frac{(\alpha_1^2-\alpha_2^2)^2}{\alpha_2^2(\alpha_1^2+\alpha_2^2)}\right) \tag{A.120}$$

$$= \kappa x_2 \lim_{\mathrm{Ca}\to\infty} \frac{\alpha_1^2}{\alpha_1^2+\alpha_2^2)} = \kappa x_2 \,, \tag{A.121}$$

which is equal to the motion of the surrounding undisturbed fluid. This behavior is also clearly visible in the viscous shear stress of the cell which approaches that of the surrounding undisturbed flow for high Ca, as we investigate more detailed in [pub3].

Computing the velocity field around a tank-treading particle

The velocity field around the particle is not explicitly given by Roscoe, but derived by Jeffery [94, eqs. (22)–(24)] for a rotating, rigid, particle. However, for its calculation in the vicinity of an elastic, tank-treading, particle, we can use the same reasoning as used in (A.24) for the computation of the surface stress distribution. I. e., for the real undisturbed velocity in infinite distance of the particle we use (A.1), while we use the replaced undisturbed motion (A.21) for the computation of the velocity field disturbance near the particle. Inside the particle, the velocity is given by (A.18). For the computation of the velocity field u_i, the following additional quantities are needed: Similar to g_1, g_2', etc., Jeffery defines [94, eqs. (8)–(10)]

$$\tilde{g}_1 = \int_{a_0^2\lambda'}^{\infty} \frac{\mathrm{d}\lambda}{(\alpha_1^2+\lambda)\Delta'(\lambda)} = a_0^3\alpha \tag{A.122}$$

$$\tilde{g}_1' = \int_{a_0^2\lambda'}^{\infty} \frac{\mathrm{d}\lambda'}{(\alpha_2^2+\lambda')(\alpha_3^2+\lambda')\Delta'} = a_0^5\alpha' \tag{A.123}$$

$$\tilde{g}_1'' = \int_{a_0^2\lambda'}^{\infty} \frac{\lambda'\,\mathrm{d}\lambda'}{(\alpha_2^2+\lambda')(\alpha_3^2+\lambda')\Delta'} = a_0^5\alpha'' \tag{A.124}$$

which are the integrals in (A.36)–(A.44), but with $a_0^2\lambda'$ instead of 0 at the lower integration limit, and in this thesis denoted with a tilde. The rightmost equalities in (A.122) and the following equations give the corresponding relation with the symbols

used by Jeffery [94]. Furthermore, we define analogously to [94, eqs. (15),(27),(28)]

$$\frac{1}{P'^2} = \left[\frac{x_1^2}{\left(\alpha_1^2+\lambda'\right)^2} + \frac{x_2^2}{\left(\alpha_2^2+\lambda'\right)^2} + \frac{x_3^2}{\left(\alpha_3^2+\lambda'\right)^2}\right] = a_0^4 \frac{1}{P^2} \tag{A.125}$$

$$B_1' = -\frac{e_{23}''}{g_1'} = a_0^{-5} R \tag{A.126}$$

$$B_2' = -\frac{e_{31}''}{g_2'} = a_0^{-5} S \tag{A.127}$$

$$B_3' = -\frac{e_{12}''}{g_3'} = a_0^{-5} T \tag{A.128}$$

$$C_1' = 2\alpha_2^2 A_{22}' - 2\alpha_3^2 A_{33}' = 8 a_0^{-5} U \tag{A.129}$$

$$C_2' = 2\alpha_3^2 A_{33}' - 2\alpha_1^2 A_{11}' = 8 a_0^{-5} V \tag{A.130}$$

$$C_3' = 2\alpha_1^2 A_{11}' - 2\alpha_2^2 A_{22}' = 8 a_0^{-5} W\,. \tag{A.131}$$

As before x_1, x_2, and x_3, are aligned with the particles semi-axes. Due to the dependency on x_i, the dimension of P' is L, the dimensions of A_{ij}, B_i', and C_i', is T^{-1}. Then, with the convenient substitution

$$\begin{aligned} Q' \coloneqq &+ \frac{x_2 x_3}{\left(\alpha_2^2+\lambda'\right)\left(\alpha_3^2+\lambda'\right)}\left[B_1' + \frac{1}{4}\left(\alpha_2^2+\lambda'\right)A_{23}' + \frac{1}{4}\left(\alpha_3^2+\lambda'\right)A_{32}'\right] \\ &+ \frac{x_3 x_1}{\left(\alpha_3^2+\lambda'\right)\left(\alpha_1^2+\lambda'\right)}\left[B_2' + \frac{1}{4}\left(\alpha_3^2+\lambda'\right)A_{13}' + \frac{1}{4}\left(\alpha_1^2+\lambda'\right)A_{13}'\right] \\ &+ \frac{x_1 x_2}{\left(\alpha_1^2+\lambda'\right)\left(\alpha_2^2+\lambda'\right)}\left[B_3' + \frac{1}{4}\left(\alpha_1^2+\lambda'\right)A_{12}' + \frac{1}{4}\left(\alpha_2^2+\lambda'\right)A_{21}'\right], \end{aligned} \tag{A.132}$$

the disturbed velocity field u_i outside the particle can be expressed analogously to [94, eq. (22)–(24)] as

$$\begin{aligned} u_1 = &+ x_1\left[e_{11}'^{(1)} - \zeta_{11}' + \frac{1}{8}\tilde{g}_3' C_3' - \frac{1}{8}\tilde{g}_2' C_2' - \frac{1}{4}(\tilde{g}_1+\tilde{g}_2+\tilde{g}_3)A_{11}'\right] \\ &+ x_2\left[e_{12}'^{(1)} - \zeta_{12}' + \tilde{g}_3' B_3' - \frac{1}{4}\tilde{g}_2 A_{12}' + \frac{1}{4}\tilde{g}_1 A_{21}'\right] \\ &+ x_3\left[e_{13}'^{(1)} - \zeta_{13}' + \tilde{g}_2' B_2' - \frac{1}{4}\tilde{g}_3 A_{13}' + \frac{1}{4}\tilde{g}_1 A_{13}'\right] \\ &- \frac{2x_1 P'^2}{\left(\alpha_1^2+\lambda'\right)\Delta'}\Bigg\{Q' + x_2^2/\left(\alpha_2^2+\lambda'\right)^2\left[\frac{1}{8}C_3' - \frac{1}{4}\left(\alpha_1^2+\lambda'\right)A_{11}' + \frac{1}{4}\left(\alpha_2^2+\lambda'\right)A_{22}'\right] \\ &\qquad - x_3^2/\left(\alpha_3^2+\lambda'\right)^2\left[\frac{1}{8}C_2' - \frac{1}{4}\left(\alpha_3^2+\lambda'\right)A_{33}' + \frac{1}{4}\left(\alpha_1^2+\lambda'\right)A_{11}'\right]\Bigg\}, \end{aligned} \tag{A.133}$$

$$
\begin{aligned}
u_2 = &+ x_1\left[e_{21}^{\prime(1)} - \zeta_{21}' + \tilde{g}_3' B_3' + \frac{1}{4}\tilde{g}_2 A_{12}' - \frac{1}{4}\tilde{g}_1 A_{21}'\right] \\
&+ x_2\left[e_{22}^{\prime(1)} - \zeta_{22}' + \frac{1}{8}\tilde{g}_1' C_1' - \frac{1}{8}\tilde{g}_3' C_3' - \frac{1}{4}(\tilde{g}_1 + \tilde{g}_2 + \tilde{g}_3) A_{22}'\right] \\
&+ x_3\left[e_{23}^{\prime(1)} - \zeta_{23}' + \tilde{g}_1' B_1' - \frac{1}{4}\tilde{g}_3 A_{23}' + \frac{1}{4}\tilde{g}_2 A_{32}'\right] \\
&- \frac{2x_2 P'^2}{(\alpha_2^2 + \lambda')\Delta'}\Bigg\{Q' + x_3^2/(\alpha_3^2 + \lambda')^2\left[\frac{1}{8}C_1' - \frac{1}{4}\Big(\alpha_2^2 + \lambda'\Big)A_{22}' + \frac{1}{4}\Big(\alpha_3^2 + \lambda'\Big)A_{33}'\right] \\
&\qquad - x_1^2/(\alpha_1^2 + \lambda')^2\left[\frac{1}{8}C_3' - \frac{1}{4}\Big(\alpha_1^2 + \lambda'\Big)A_{11}' + \frac{1}{4}\Big(\alpha_2^2 + \lambda'\Big)A_{22}'\right]\Bigg\},
\end{aligned}
\tag{A.134}
$$

and

$$
\begin{aligned}
u_3 = &+ x_1\left[e_{31}^{\prime(1)} - \zeta_{13}' + \tilde{g}_2' B_2' - \frac{1}{4}\tilde{g}_1 A_{13}' + \frac{1}{4}\tilde{g}_3 A_{31}'\right] \\
&+ x_2\left[e_{32}^{\prime(1)} - \zeta_{32}' + \tilde{g}_1' B_1' + \frac{1}{4}\tilde{g}_3 A_{23}' - \frac{1}{4}\tilde{g}_2 A_{32}'\right] \\
&+ x_3\left[e_{33}^{\prime(1)} - \zeta_{33}' + \frac{1}{8}\tilde{g}_2' C_2' - \frac{1}{8}\tilde{g}_1' C_1' - \frac{1}{4}(\tilde{g}_1 + \tilde{g}_2 + \tilde{g}_3) A_{33}'\right] \\
&- \frac{2x_3 P'^2}{(\alpha_3^2 + \lambda')\Delta'}\Bigg\{Q' + x_1^2/(\alpha_1^2 + \lambda')^2\left[\frac{1}{8}C_2' - \frac{1}{4}\Big(\alpha_3^2 + \lambda'\Big)A_{33}' + \frac{1}{4}\Big(\alpha_1^2 + \lambda'\Big)A_{11}'\right] \\
&\qquad - x_2^2/(\alpha_2^2 + \lambda')^2\left[\frac{1}{8}C_1' - \frac{1}{4}\Big(\alpha_2^2 + \lambda'\Big)A_{22}' + \frac{1}{4}\Big(\alpha_3^2 + \lambda'\Big)A_{33}'\right]\Bigg\}.
\end{aligned}
\tag{A.135}
$$

In the equations (A.133)–(A.135), the first two terms in the first three lines can be identified with the undisturbed flow surrounding the particle (A.1). In figure A.1, the velocity vectors of the flow inside and outside the particle at the central plane ($x_3 = 0$) are shown for different Capillary numbers.

Figure A.1: Velocity field disturbance according to (A.17) inside and around an elastic, tank-treading particle suspended in linear shear flow at increasing Capillary numbers. The arrow length and coloring indicate the magnitude of the disturbance, which is normalized using the respective shear rate of the fluid and a constant distance.

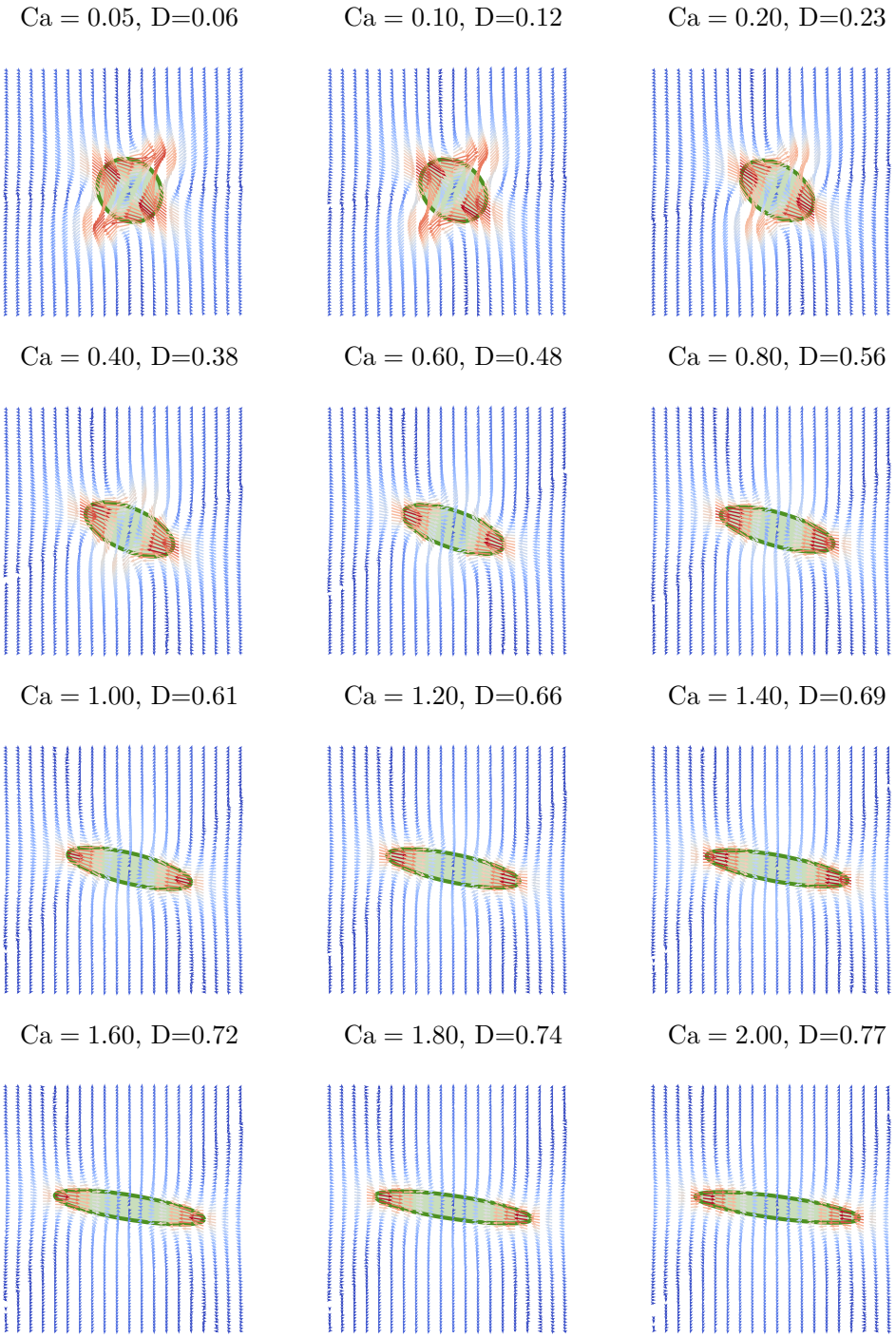

Conversion between Jeffery and Roscoe (and present work) notation For future reference, the relations between the quantities used by Jeffery [94] on the left side and the ones used by Roscoe [93] on the right side are given in the following. Note that λ' defined below corresponds to Roscoe's λ, while λ below denotes that used by Jeffery.

$$\lambda = a_0^2 \lambda' \qquad \Delta = a_0^3 \Delta' \tag{A.136}$$

$$\begin{pmatrix} A & H & G' \\ H' & B & F \\ G & F' & C \end{pmatrix} = \frac{1}{8} a_0^3 A_{ij} = \frac{1}{8} a_0^3 \begin{pmatrix} A_{11} & A_{12} & A_{13} \\ A_{21} & A_{22} & A_{23} \\ A_{31} & A_{32} & A_{33} \end{pmatrix} \tag{A.137}$$

$$\begin{pmatrix} U \\ V \\ W \end{pmatrix} = \frac{1}{8} a_0^5 \begin{pmatrix} C_1' \\ C_2' \\ C_3' \end{pmatrix} \qquad \begin{pmatrix} R \\ S \\ T \end{pmatrix} = a_0^5 \begin{pmatrix} B_1' \\ B_2' \\ B_3' \end{pmatrix} \tag{A.138}$$

$$P = a_0^4 P' \tag{A.139}$$

$$\begin{pmatrix} \mathbf{a} & \mathbf{h} & \mathbf{g} \\ \mathbf{h} & \mathbf{b} & \mathbf{f} \\ \mathbf{g} & \mathbf{f} & \mathbf{c} \end{pmatrix} = e_{ij}'^{(1)} = \begin{pmatrix} e_{11}'^{(1)} & e_{12}'^{(1)} & e_{13}'^{(1)} \\ e_{21}'^{(1)} & e_{22}'^{(1)} & e_{23}'^{(1)} \\ e_{31}'^{(1)} & e_{32}'^{(1)} & e_{33}'^{(1)} \end{pmatrix} \tag{A.140}$$

$$\begin{pmatrix} 0 & \zeta & -\eta \\ -\zeta & 0 & \xi \\ \eta & -\xi & 0 \end{pmatrix} = \zeta_{ij}' = \begin{pmatrix} \zeta_{11}' & \zeta_{12}' & \zeta_{13}' \\ \zeta_{21}' & \zeta_{22}' & \zeta_{23}' \\ \zeta_{31}' & \zeta_{32}' & \zeta_{33}' \end{pmatrix} \tag{A.141}$$

$$\begin{pmatrix} a \\ b \\ c \end{pmatrix} = a_0 \begin{pmatrix} \alpha_1 \\ \alpha_2 \\ \alpha_3 \end{pmatrix} \tag{A.142}$$

$$\begin{pmatrix} \alpha_0 \\ \beta_0 \\ \gamma_0 \end{pmatrix} = a_0^{-3} \begin{pmatrix} g_1 \\ g_2 \\ g_3 \end{pmatrix} \qquad \begin{pmatrix} \alpha \\ \beta \\ \gamma \end{pmatrix} = a_0^{-3} \begin{pmatrix} \tilde{g}_1 \\ \tilde{g}_2 \\ \tilde{g}_3 \end{pmatrix} \tag{A.143}$$

$$\begin{pmatrix} \alpha_0' \\ \beta_0' \\ \gamma_0' \end{pmatrix} = a_0^{-5} \begin{pmatrix} g_1' \\ g_2' \\ g_3' \end{pmatrix} \qquad \begin{pmatrix} \alpha' \\ \beta' \\ \gamma' \end{pmatrix} = a_0^{-5} \begin{pmatrix} \tilde{g}_1' \\ \tilde{g}_2' \\ \tilde{g}_3' \end{pmatrix} \tag{A.144}$$

$$\begin{pmatrix} \alpha_0'' \\ \beta_0'' \\ \gamma_0'' \end{pmatrix} = a_0^{-3} \begin{pmatrix} g_1'' \\ g_2'' \\ g_3'' \end{pmatrix} \qquad \begin{pmatrix} \alpha'' \\ \beta'' \\ \gamma'' \end{pmatrix} = a_0^{-3} \begin{pmatrix} \tilde{g}_1'' \\ \tilde{g}_2'' \\ \tilde{g}_3'' \end{pmatrix} \tag{A.145}$$

Notes and corrections in Jeffery's and Roscoe's original work

- In [94, eq. (26)], all equations miss a "prime" on the right-hand side of the equation in the second term of the numerator, e. g.

$$F = \frac{\beta_0 \boldsymbol{f} - c^2\alpha_0(\xi - \omega_1)}{2\alpha_0'(b^2\beta_0 + c^2\gamma_0)} \quad \text{should be} \quad F = \frac{\beta_0 \boldsymbol{f} - c^2\alpha_0'(\xi - \omega_1)}{2\alpha_0'(b^2\beta_0 + c^2\gamma_0)} \,. \tag{A.146}$$

- The prefactor $\frac{1}{8}a_0^3$ in [93, eq. (16)] belongs on the other side of the equation: Roscoe non-dimensionalizes the ellipsoids semi-axes, hence the quantities g_1, g_2', etc., are dimensionless and the tensor A_{ij} has the dimension T^{-1} of a strain rate. In Jeffery's work the dimension of α_1, β', etc., is L^{-3}, and that of the tensor components A, B, etc., is L^3T^{-1}. This is merely a typographic error in [93, eq. (16)] which does not affect the rest of the derivation.

- A factor of 8 is missing in [93, eq. (19)] in order to be consistent with the definition of A_{ij} of [93, eq. (16)]. This is a typographic error only and Roscoe uses the correct form for later calculations, as can be seen from the derivation of the fluid shear stress in (A.79), which gives the same result as [93, eq. (42)].

- The plus sign in [93, eq. (79)] should be a minus sign: This equation is the first normal stress difference [93, eqs. (37),(76)], the minus follows directly from [93, eq. (76)].

Part II

Publications

The author's contributions

Contributions to the publications for this thesis

[pub1] S. J. Müller, E. Mirzahossein, E. N. Iftekhar, C. Bächer, S. Schrüfer, D. W. Schubert, B. Fabry , and S. Gekle. Flow and hydrodynamic shear stress inside a printing needle during biofabrication. *PLOS ONE* **15**(7): e0236371. DOI: 10.1371/journal.pone.0236371
Individual contributions:

Sebastian Johannes Müller during this thesis

- designed the research
- designed, developed, and implemented the algorithm and the method
- designed, performed, and analyzed the computations and simulations
- analyzed the experimental data for flow profile error computation
- wrote the article.

E. Mirzahossein conducted the microchannel flow experiments and contributed to the design and implementation of the capillary rheometer setup.

E. N. Iftekhar conducted the microchannel flow experiments and contributed to the design and implementation of the capillary rheometer setup.

C. Bächer helped developing the global solution of section 2.1 and helped writing the article.

S. Schrüfer conducted the cone-plate rheometer measurements.

D. W. Schubert supervised the research and helped writing the article.

B. Fabry designed and implemented the capillary rheometer and microchannel setup, supervised the research, and helped writing the article.

S. Gekle supervised the research and helped writing the article.

[pub2] S. J. Müller, F. Weigl, C. Bezold, C. Bächer, K. Albrecht, and S. Gekle (2021). A hyperelastic model for simulating cells in flow. *Biomechanics and Modeling in Mechanobiology* **20**, p. 509–520. DOI: 10.1007/s10237-020-01397-2

Individual contributions:

Sebastian Johannes Müller during this thesis

- designed the research
- improved the numerical model and provided further validation
- designed, performed, and analyzed the simulations
- analyzed the experimental data for plotting
- wrote the article.

F. Weigl conducted the fluidic force microscopy experiments and helped writing the article.

C. Bezold developed and validated the neo-Hookean cell model during her Master thesis.

A. Sancho designed, implemented, and supervised the fluidic force microscopy experiments.[a]

C. Bächer supervised the work of C. Bezold and helped writing the article.

K. Albrecht supervised the research and helped writing the article.

S. Gekle supervised the research and helped writing the article.

[a] Erroneously, A. Sancho is not stated as author in the journal version. The correct author list is the one given in the preprint available at arxiv.org/abs/2003.03130

[pub3] S. J. Müller, B. Fabry , and S. Gekle (2022). Predicting cell stress and strain during extrusion 3D bioprinting. *(submitted)*. Preprint DOI: 10.1101/2022.09.28.509836
Individual contributions:

Sebastian Johannes Müller during this thesis

- designed the research
- designed, developed, and implemented the algorithm and the prediction methods
- designed, performed, and analyzed the computations and simulations
- wrote the article

B. Fabry designed and implemented the imaging setup, conducted the experiment, and helped writing the article.

S. Gekle supervised the research and helped writing the article.

[pub4] S. Wohlrab*, S. J. Müller*, and S. Gekle (2022). A mechanically homogeneous equivalent of real cells. *(draft)*.
Individual contributions:

Sebastian Johannes Müller during this thesis

- designed and supervised the research
- implemented the compression and indentation simulation method of the inhomogeneous cell model
- performed simulations and analysis of the random inhomogeneous cell
- helped creating the figures
- wrote the article

S. Wohlrab

- implemented the inhomogeneous cell model in the flow simulations
- performed simulations and analysis of the inhomogeneous cell with nucleus
- created the figures
- helped writing the article.

S. Gekle helped writing the article and supervising the research.

*S. J. Müller during this thesis and S. Wohlrab contributed equally.

Further publications

During his doctorate, the author of the present thesis also contributed to the following publications:

M. Lehmann, S. J. Müller, and S. Gekle (2020). Efficient viscosity contrast calculation for blood flow simulations using the lattice Boltzmann method: Efficient viscosity contrast calculation for blood flow simulations using the lattice Boltzmann method. *International Journal for Numerical Methods in Fluids* **92**, p. 1463–1477. DOI: 10.1002/fld.4835

R. Gerum, E. Mirzahossein, M. Eroles, J. Elsterer, A. Mainka, A. Bauer, S. Sonntag, A. Winterl, J. Bartl, L. Fischer, S. Abuhattum, R. Goswami, S. Girardo, J. Guck, S. Schrüfer, N. Ströhlein, M. Nosratlo, H. Herrmann, D. Schultheis, F. Rico, S. J. Müller, S. Gekle, and B. Fabry (2022). Viscoelastic properties of suspended cells measured with shear flow deformation cytometry. *eLife* **11**, e788233. DOI: 10.7554/eLife.78823.

S. Pantawane, S. J. Müller, and S. Gekle (2022). Effect of particle insertion on Poly(3-hexylthiopene) brush's π–π stacking. *Submitted to Computational Materials Science*.

Contributions to conferences and symposia

Various parts of the present thesis have been presented by the author at the following conferences and symposia during his doctorate:

Talks:

- 2nd SFB TRR225 retreat 2018, Kloster Banz, Germany
- 3nd SFB TRR225 retreat 2019, Kloster Banz, Germany
- 4th SFB TRR225 retreat 2019, Kloster Banz, Germany
- 6th SFB TRR225 retreat 2020, Kloster Banz, Germany
- 7th SFB TRR225 retreat 2020, Kloster Banz, Germany
- 8th SFB TRR225 retreat 2021, Kloster Banz, Germany
- DPG Frühjahrstagung 2021, Berlin (virtual), Germany
- Living fluids workshop 2021, Saarbrücken (virtual), Germany
- Biofabrication Australia 2021, Wollongong (virtual), Australia

Poster contributions:

- 2nd SFB TRR225 retreat 2018, Kloster Banz, Germany
- 3nd SFB TRR225 retreat 2019, Kloster Banz, Germany
- DPG Frühjahrstagung 2019, Regensburg, Germany
- Living fluids workshop 2019, Bayreuth, Germany

Publication 1

Flow and hydrodynamic shear stress inside a printing needle during biofabrication

---

S. J. Müller, E. Mirzahossein, E. N. Iftekhar, C. Bächer, S. Schrüfer, D. W. Schubert, B. Fabry , and S. Gekle

PLOS ONE **15**(7), 2020

DOI: 10.1371/journal.pone.0236371

PLOS ONE

RESEARCH ARTICLE

Flow and hydrodynamic shear stress inside a printing needle during biofabrication

Sebastian J. Müller[1], Elham Mirzahossein[2], Emil N. Iftekhar[2], Christian Bächer[1], Stefan Schrüfer[3,4], Dirk W. Schubert[3,4], Ben Fabry[2], Stephan Gekle[1]*

1 Biofluid Simulation and Modeling, Universität Bayreuth, Bayreuth, Germany, **2** Department of Phyiscs, Friedrich-Alexander Universität Erlangen-Nürnberg, Erlangen, Germany, **3** Institute of Polymer Materials, Friedrich-Alexander Universität Erlangen-Nürnberg, Erlangen, Germany, **4** KeyLab Advanced Fiber Technology, Bavarian Polymer Institute, Fürth, Germany

* stephan.gekle@uni-bayreuth.de

Citation: Müller SJ, Mirzahossein E, Iftekhar EN, Bächer C, Schrüfer S, Schubert DW, et al. (2020) Flow and hydrodynamic shear stress inside a printing needle during biofabrication. PLoS ONE 15(7): e0236371. https://doi.org/10.1371/journal.pone.0236371

Editor: Fang-Bao Tian, University of New South Wales, AUSTRALIA

Received: March 31, 2020

Accepted: July 2, 2020

Published: July 24, 2020

Data Availability Statement: All relevant data are within the manuscript and its Supporting Information files. The Python tool is available at https://github.com/sjmuellerbt/CYprofiles.

Funding: This work was funded by the Deutsche Forschungsgemeinschaft (SFB-TRR 225, project number 326998133, subprojects A01, A07 and B07) (to SJM, EM, SS, DWS, BF and SG). This work was partly funded by the National Institutes of Health grant HL120839 (to BF). Christian Bächer thanks the Studienstiftung des deutschen Volkes

Abstract

We present a simple but accurate algorithm to calculate the flow and shear rate profile of shear thinning fluids, as typically used in biofabrication applications, with an arbitrary viscosity-shear rate relationship in a cylindrical nozzle. By interpolating the viscosity with a set of power-law functions, we obtain a mathematically exact piecewise solution to the incompressible Navier-Stokes equation. The algorithm is validated with known solutions for a simplified Carreau-Yasuda fluid, full numerical simulations for a realistic chitosan hydrogel as well as experimental velocity profiles of alginate and chitosan solutions in a microfluidic channel. We implement the algorithm in an easy-to-use Python tool, included as Supplementary Material, to calculate the velocity and shear rate profile during the printing process, depending on the shear thinning behavior of the bioink and printing parameters such as pressure and nozzle size. We confirm that the shear stress varies in an exactly linear fashion, starting from zero at the nozzle center to the maximum shear stress at the wall, independent of the shear thinning properties of the bioink. Finally, we demonstrate how our method can be inverted to obtain rheological bioink parameters *in-situ* directly before or even during printing from experimentally measured flow rate versus pressure data.

Introduction

Biofabrication, or bioprinting, is a novel technology aimed at applying common 3D printing techniques to fabricate living tissues. In extrusion-based biofabrication, the survival and functionality of printed cells strongly depend on the hydrodynamic stresses that the cells experience during printing [1–5]. These stresses arise mainly from viscous shear forces in the printer nozzle and are thus directly related to the flow profile and the viscosity of the bioink [6–11] in which the cells are suspended. In an effort to reduce hydrodynamics stresses, shear thinning bioinks have been designed that exhibit a nearly flat velocity profile and correspondingly low shear rates in the nozzle center, in contrast to purely Newtonian liquids that develop a parabolic flow profile with higher shear rates throughout most of the nozzle [12–19]. Consequently,

for financial support. Stephan Gekle thanks the Volkswagen Foundation. The funders had no role in study design, data collection and analysis, decision to publish, or preparation of the manuscript.

Competing interests: The authors have declared that no competing interests exist.

cells suspended in shear thinning bioinks can be expected to show increased survival rate and better functionality after printing [4, 16, 20, 21].

To describe the rheology of inelastic, time-independent, shear thinning materials, a variety of viscosity models exists, which are collectively labeled as generalized Newtonian fluids [22]. One of the simplest models assumes a power-law, also known as Ostwald-de Waele relationship [4, 23, 24]. Real shear thinning materials, however, show power-law behavior only in a limited range of shear rates, while Newtonian behavior is observed above and below this range. The latter is particularly relevant for bioprinting applications and prevails in the central region of the printing nozzle where the velocity approaches a constant value and thus a vanishing shear rate. To properly model this behavior, a widely used description is the Carreau-Yasuda (CY) [22, 25] model, which features a central power-law region that smoothly transitions into two Newtonian plateaus in the limits of low and high shear rates. Many commonly used hydrogel materials for bioprinting [26] but also polymer melts or solutions [27] can be accurately characterized with the CY model. Existing methods to calculate theoretically the velocity profile in the printing nozzle for a CY fluid [28, 29] require the shear rate at the nozzle wall as an input parameter. Experimentally, however, this quantity is usually not known. Instead either the pressure difference or the volume flux serve as control parameter.

In this work, we present an algorithm to compute the full velocity, shear rate, and viscosity profile in a printing nozzle for generalized Newtonian fluids such as shear thinning bioinks. Our algorithm is based on interpolating an arbitrary viscosity-shear rate relation by piecewise continuous power-law functions, and requires only the experimentally imposed printing parameters such as the channel radius and the driving pressure difference or flow rate as input values. To allow for an efficient application of our method in everyday laboratory work, we provide a user-friendly implementation of our algorithm for CY fluids as a Python tool included as S1 File. This tool is much simpler to use than typical computational fluid dynamics software and at the same time can provide higher accuracy at much less computational load. The calculated shear stresses are a measure for the mechanical load experienced by cells embedded in the bioink and can thus directly be correlated to post-printing cell viability measurements [1, 11]. We confirm that the well-known linear shear stress distribution found in Newtonian pipe flow is also valid for shear thinning fluids. We validate our algorithm by comparing it to the exact solution for a simplified Carreau-Yasuda fluid, to full numerical Lattice Boltzmann simulations for a realistic chitosan hydrogel under typical printing conditions, and to experimental velocity profiles of a shear thinning alginate solution in a microfluidic channel. Furthermore, we show how our method can be inverted to construct a capillary rheometer, which allows users to determine the rheological parameters of a given bioink using only a bioprinter and a standard laboratory scale without the need of a sophisticated rheometer. Such *in-situ* measurements of bioink rheology combined with the calculation of expected shear rates will help users to optimize the printing process and to achieve the desired printing results especially when bioprinting shear stress-sensitive living cells.

1 Theory and results

1.1 Viscosity model

Our algorithm starts from an experimentally known viscosity-shear rate relation $\eta(\dot{\gamma})$ and interpolates it by a series of power-law functions. The viscosity-shear rate relationship of the bioink, e. g. a cell-laden hydrogel, or any other generalized Newtonian fluid, can be approximated by a continuous, piecewise function as given in (S-1) and depicted in Fig 1a. In every interval, the viscosity-shear rate relation is described by a power-law model $\eta_i(\dot{\gamma}) = K_i\dot{\gamma}^{n_i-1}$

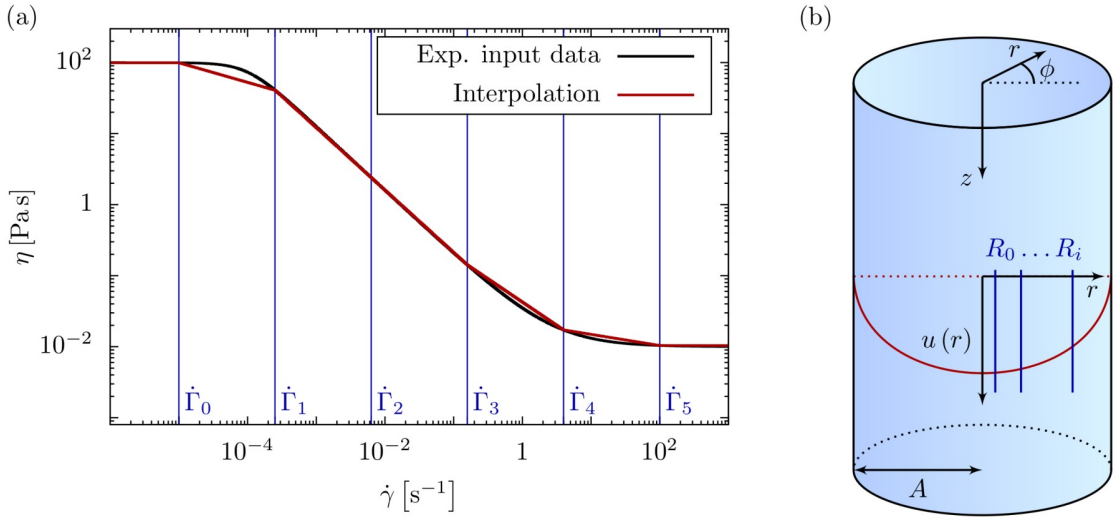

Fig 1. Viscosity and flow profile interpolation. (a) The viscosity-shear rate relationship of an arbitrary shear thinning fluid obtained e. g. from a rheometer measurement is interpolated by power-law intervals. The bounds of the intervals (vertical lines) are given by the intermediate shear rates, $\dot{\Gamma}_i$. By using a large number of intervals, any arbitrary viscosity-shear rate relationship can be approximated as closely as desired. (b) A long cylinder with uniaxial, stationary flow is used as a model for the flow of a bioink through a printer nozzle. The flow profile is split into radial intervals R_i determined implicitly via the intermediate shear rates $\dot{\Gamma}_i$.

https://doi.org/10.1371/journal.pone.0236371.g001

with a consistency parameter K_i and a dimensionless exponent n_i. The i^{th} interval is bounded by the shear rates $\dot{\Gamma}_{i-1}$ and $\dot{\Gamma}_i$, and we demand $\eta(\dot{\gamma})$ to be continuous at these bounds.

This continuity condition together with a set of $\dot{\Gamma}_i$ uniquely determines the power-law parameters K_i and n_i in every interpolation interval, as detailed in section S-1.2.

We note that this approach can be applied to any material described in terms of generalized Newtonian fluids, including yield stress fluids. Furthermore, our method includes cell-laden bioinks, as, on the one hand, the presence of cells has been shown to only slightly alter the materials' rheological behavior [5, 30]. On the other hand, the macroscopic rheology of a cell suspension, determined e. g. via shear rheometry or our capillary rheometry method presented in section 3, can be used as input for our method.

1.2 Governing equations

Analogously to the well-known Poiseuille flow of a Newtonian fluid [31, pp. 180 ff.], we assume a stationary, laminar, and pressure driven flow, with the velocity having only an axial component u depending on the radial position r. We consider a cylindrical channel and neglect entrance and exit effects. Applying these flow conditions, the incompressible Navier-Stokes equations reduce to the ordinary differential equation as shown in section S-1.3:

$$G = \frac{1}{r}\frac{\partial}{\partial r}\left(r\eta(\dot{\gamma})\frac{\partial u}{\partial r}\right) \tag{1}$$

Here, the constant pressure gradient $G := \frac{\partial p}{\partial z} = \frac{\Delta p}{L}$ is defined by the pressure drop $\Delta p = p_0 - p_L < 0$ over a channel segment of length L. For a Newtonian fluid, i. e. $\eta(\dot{\gamma}) = \eta$, integration of Eq (1) directly yields the well-known linear radial dependency of the shear stress:

$$\sigma(r) = \eta\dot{\gamma} = -\frac{G}{2}r \tag{2}$$

Similar to the piecewise viscosity model in Fig 1a, we decompose the axial velocity $u(r)$ and the shear rate $\dot{\gamma}(r)$ into radial intervals R_i as given in (S-29) and (S-32) and illustrated in Fig 1b for the velocity.

Inserting these piecewise profiles into the Navier-Stokes equation Eq (1) yields the following system of equations where i denotes the intervals as above:

$$G = \frac{1}{r}\frac{\partial}{\partial r}[-rK_i(\dot{\gamma}_i(r))^{n_i}] \tag{3}$$

$$\dot{\gamma}_i(r) = -\frac{\partial u_i(r)}{\partial r} \tag{4}$$

In order to solve this system of equations we assume the axial velocity to be continuously differentiable and the shear rate to be continuous. The flow shall further fulfill a no-slip boundary condition at the channel wall and have its maximum at the channel center. The mathematical solution to the system of equations Eqs (3) and (4) is detailed in section S-1.4 and section S-1.5 and can be summarized as follows: the shear rate profile is obtained by integrating Eq (3) over the radial position once. Inserting this solution into Eq (4) yields the velocity profile after another integration over r. Both integrations come along with integration constants that are determined employing the boundary conditions of the flow and the continuity conditions as stated above.

1.3 Results

The first equation Eq (3) can be rearranged and integrated once to obtain the shear rate profile in the i^{th} interval:

$$\dot{\gamma}_i(r) = \left(-\frac{G}{2K_i}r\right)^{\frac{1}{n_i}} \tag{5}$$

From this, the velocity profile is obtained by integrating over r, which ultimately yields (cf. (S-58)):

$$\begin{aligned} u_i(r) = & -\left(-\frac{G}{2K_i}\right)^{\frac{1}{n_i}}\frac{n_i}{n_i+1}r^{1+\frac{1}{n_i}} \\ & +\left(-\frac{G}{2K_k}\right)^{\frac{1}{n_k}}\frac{n_k}{n_k+1}A^{1+\frac{1}{n_k}} \\ & -\sum_{j=i}^{k-1}R_j\dot{\Gamma}_j\left(\frac{n_{j+1}}{n_{j+1}+1}-\frac{n_j}{n_j+1}\right) \end{aligned} \tag{6}$$

Here, the newly introduced index k denotes the radial interval that contains the physical boundary of the channel, i. e. $R_{k-1} \leq A \leq R_k$ with the channel radius A.

The radial shear stress profile can, similarly to the Newtonian case, be derived from Eq (1), yielding the same linear behavior:

$$\sigma(r) = -\eta(\dot{\gamma})\frac{\partial u}{\partial r} = -\frac{G}{2}r \tag{7}$$

This shows that the shear stress profile in a cylindrical channel is independent of the shear thinning properties of the material.

Using the solutions for the shear rate (5) and the velocity (6), we derive mathematical expressions for the flow rate as well as the average velocity, shear rate, viscosity, and shear

stress. Details of the derivation and the corresponding solutions can be found in (S-63), (S-66), (S-71) and (S-74), respectively (cf. section S-1.6). The flow rate or, equivalently, the average flow velocity determines the printing speed in 3D bioprinting processes. The average shear rate and shear stress can be used to estimate cell damage during printing [2, 4] as detailed in section S-1.8 of the S1 File. We discuss the inclusion of possible wall-slip effects [35] in section S-1.9 of the S1 File.

2 Validation

To validate our method, we implement the presented algorithm in a Python [32] tool, included as S1 File together with an explanatory tutorial in section S-3 and available at https://github.com/sjmuellerbt/CYprofiles. Our tool performs the viscosity interpolation according to section 1.1 for a five-parameter Carreau-Yasuda fluid, given in Eq (9). The radial profiles for velocity, shear rate, viscosity, and shear stress and their respective averaged quantities are calculated after providing the printing parameters, i. e. the nozzle radius and the pressure gradient or an imposed flow rate.

We first validate our algorithm using an exact global mathematical solution for a simplified CY model. Next, we compare our algorithm with Lattice Boltzmann simulations for a general CY model using the open source software package ESPResSo [33, 34], for which we extended both the CPU and GPU implementation with several inelastic viscosity models, including the CY model. We finally perform experimental velocity profile measurements in a microfluidic channel and confirm the theoretical prediction of our Lattice Boltzmann simulations.

2.1 Validation with global solution

We consider a simplified Carreau-Yassuda (CY) model of the following form

$$\tilde{\eta}(\dot{\gamma}) = \frac{\tilde{\eta}_0}{1 + K\dot{\gamma}} \tag{8}$$

where $\tilde{\eta}_0$ is the viscosity in the limit of zero shear rate and K is a time constant. For this model, an exact global solution to the NSE Eq (1) can be found as described in(S-79) and (S-81) (cf. section S-1.7). As shown in Fig 2, we find excellent agreement between this exact solution and the calculated profiles using our Python tool.

2.2 Validation with Lattice Boltzmann simulations

The general CY model [25] is given by

$$\tilde{\eta}(\dot{\gamma}) = \tilde{\eta}_\infty + \frac{\tilde{\eta}_0 - \tilde{\eta}_\infty}{[1 + (K\dot{\gamma})^{a_1}]^{\frac{a_2}{a_1}}}\,, \tag{9}$$

where $\tilde{\eta}_\infty$ is the viscosity in the limit of infinite shear rates and the exponents a_1 and a_2 determine the shape of the transition between the zero-shear Newtonian plateau and the power-law region as well as the power-law behavior. For this general CY fluid a global mathematical solution to the NSE does not exist. We therefore compare our algorithm to Lattice-Boltzmann simulations using realistic bioink and printing parameters for a chitosan hydrogel taken from [26] with the following rheological parameters: $\tilde{\eta}_0 = 5807$ Pas, $K = 5.33$ s, $a_1 = 1.35$ and $a_2 = 0.87$. The simulation setup consists of a $5 \times 400 \times 400$ ($x \times y \times z$) box with a cylindrical boundary along the x-axis corresponding to a physical radius of $A = 100$ μm. The flow is periodic in x-direction thus leading to an effectively infinitely long channel. Further details of the Lattice-Boltzmann simulations are given in the S1 File.

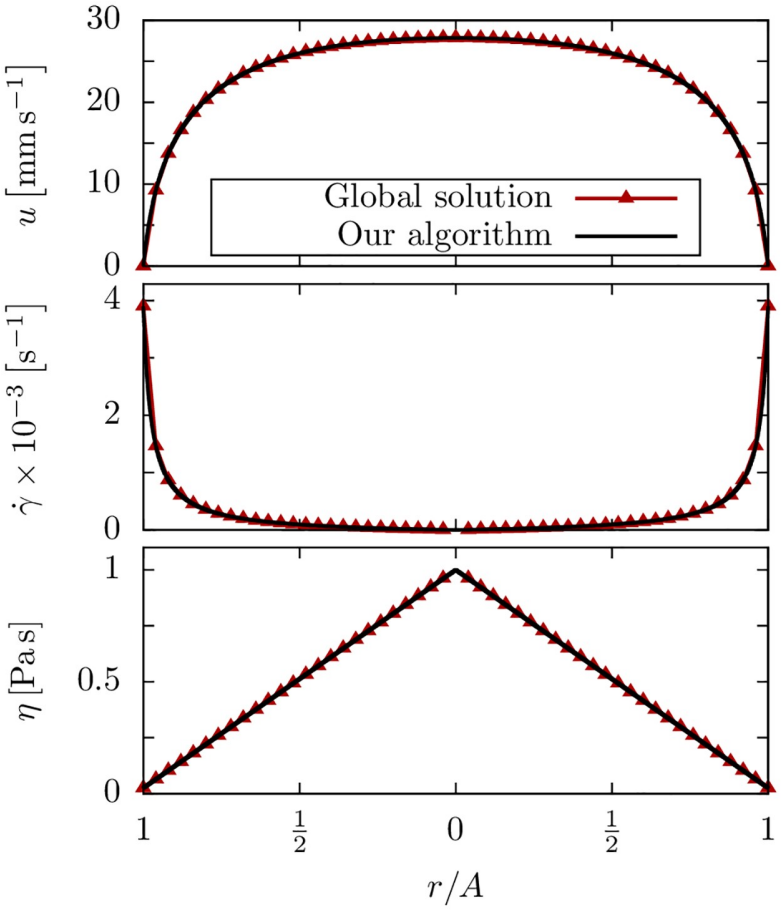

Fig 2. Validation with a mathematical solution. Flow profiles for the simplified CY model: the global mathematical solution and the prediction by our algorithm agree very well. The parameters are $N = 1000$, $\eta_0 = 100$ Pa s, $K = 1.0$ s and $G = -1.95 \times 10^6$ Pa m^{-1}.

https://doi.org/10.1371/journal.pone.0236371.g002

The calculated and simulated flow profiles are in excellent agreement (Fig 3) thus validating our algorithm for a general CY fluid.

2.3 Validation with experimental flow profile measurements

As experimental proof, we measure the flow profile of an alginate solution along the centerline of a microchannel and compare our findings to Lattice Boltzmann simulations of the same geometry.

We prepare a 2.0% alginate solution by mixing 800 mg of alginate (Grindsted PH 176, Dupont, USA) in 50 ml Dulbecco's phosphate buffered saline under constant stirring overnight at room temperature together with yellow-green fluorescent beads (FluoroSphere carboxylated beads, Invitrogen, diameter: 0.5 μm). The alginate solution is injected under defined pressure into a polymethylmetacrylate microfluidic channel equipped with male mini Luer lock connectors (Darwin Microfluidics, France, internal volume: 8 μl) via a 15 cm long silicon tube (inner diameter: 1 mm). The channel has a length of 58 mm and a quadratic cross section of 190 μm × 190 μm, similar in size to the cross section of a typical printing needle. A square cross section of the channel was chosen to avoid optical distortions that would arise from the

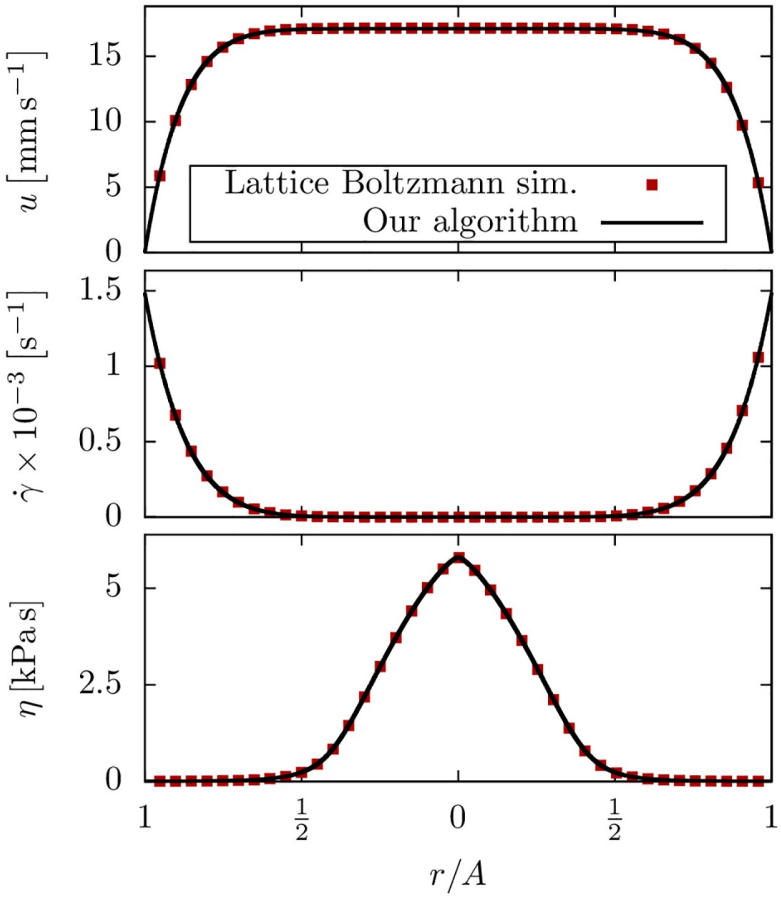

Fig 3. Validation with Lattice Boltzmann calculations. Flow profiles of a chitosan hydrogel with a pressure gradient of $G = -7.0 \times 10^7$ Pa m^{-1} and $N = 1000$.

https://doi.org/10.1371/journal.pone.0236371.g003

curvature of a cylindrical glass capillary in combination with the refractive index differences between glass and alginate. We visualize the flow of alginate using an epifluorescence microscope (DM4, Leica Microsystems, Germany) equipped with a CCD camera (frame rate: 100 Hz, Prosilica GE680, Allied Vision, Germany) and a 100 mW laser diode (473 nm). The microscope is focussed at the mid-section of the channel (height: 95 μm).

We perform measurements at a pressure of 300 kPa, close to actual printing conditions. The maximum flow speed in the center of the channel is around 2 cm s^{-1}, which is too fast to track the beads between successive frames. Instead, the velocity is estimated from the length of the linear streaks of the beads during exposure, as shown in Fig 4a, divided by the exposure time of 7 ms.

We perform Lattice Boltzmann simulations of the pressure driven flow of the alginate solution in a square microchannel. The simulation setup consists of a $5 \times 400 \times 400$ ($x \times y \times z$) box with plane boundaries in y- and z-direction forming a square channel that corresponds to the 190 μm × 190 μm microfluidic channel used in the experiment. The viscosity parameters were obtained using our capillary rheometry method described in section 3 as $\tilde{\eta}_0 = 3.65$ Pas, $\dot{\gamma}_c = 21.71$ s^{-1} and $\alpha = 0.67$, according to equation Eq (10) below. Since we do not know the pressure drop across the mini Luer-lock connectors and tubings, we estimate the pressure gradient from the maximum flow speed measured at the center of the channel. Accordingly, we

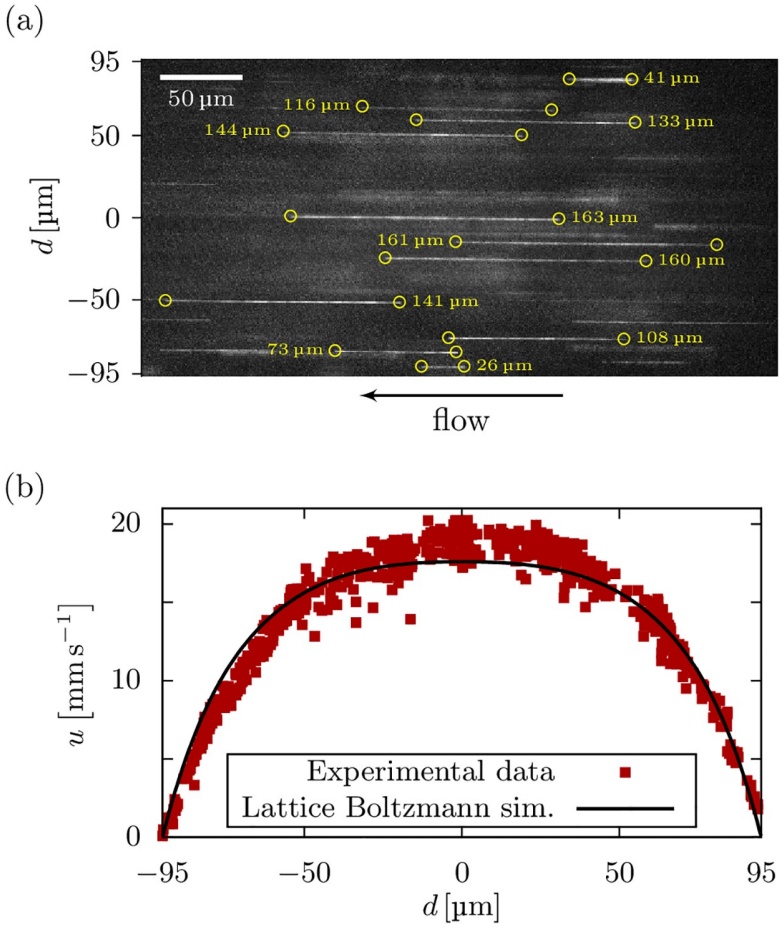

Fig 4. Validation with experimental flow measurements. Experimental measurement of the flow profile of a 2% alginate solution in a 190 µm × 190 µm microchannel. (a) Example micrograph of the bead tracking procedure. The velocity with respect to the lateral position is obtained as the length (yellow circles and labels) of the streaks divided by the exposure time. (b) The measured flow profile is in excellent agreement with our Lattice Boltzmann simulations.

https://doi.org/10.1371/journal.pone.0236371.g004

find that 79% of the total pressure drop of 300 kPa occurs across the 58 mm long channel, while the mini Luer-lock connectors and tubings account for the remaining 21%.

Fig 4b depicts the measured flow profile in comparison to our Lattice Boltzmann simulations. We see excellent agreement of the measured velocity profile and our numerical prediction. Further measurements of alginate hydrogels with different concentrations, as well as a chitosan hydrogel, at various printing pressures and in different channel geometries are included as S1 File.

3 Inverse application for a capillary rheometer

Not all laboratories working in bioprinting may have access to sophisticated rheometers for measuring the non-linear viscosity of their bioinks. Moreover, bioinks are often highly sensitive fluids with a large batch-to-batch variation, and the sample used for rheometer measurements may not behave in the same way as the sample used for the actual printing process. In this section, we show how our method can be inverted to perform *in-situ* capillary rheometry measurements using only a bioprinter and a standard laboratory scale. For this, we measure

the pressure versus flow rate relationship [35] for a range of discrete pressure values. Using our Python tool, we then extract from this data the non-linear viscosity parameters of the bioink.

3.1 Experimental setup

We prepare a 2.5% alginate solution using the protocol described in section 2.3 without the addition of fluorescent beads. We measure the viscosity of the alginate solution at a temperature of 25˚C at shear rates between 0.01 s^{-1} and 100 s^{-1} using a cone-plate rheometer (DHR-3, TA-Instruments, USA). Alternatively, we measure the viscosity with a custom-made bioprinter that we use here as a capillary rheometer. A schematic of the experimental setup is shown in Fig 5. The alginate solution is driven with a defined pressure (K8P electronic pressure regulator, Camozzi Automation, Italy) through a steel needle (21G blunt cannula #9180109-02, B-Braun, Germany, 28 mm length, 551 μm inner diameter). The pressure is increased stepwise from 20 kPa to 200 kPa in steps of 20 kPa. The driving pressure is measured with a pressure

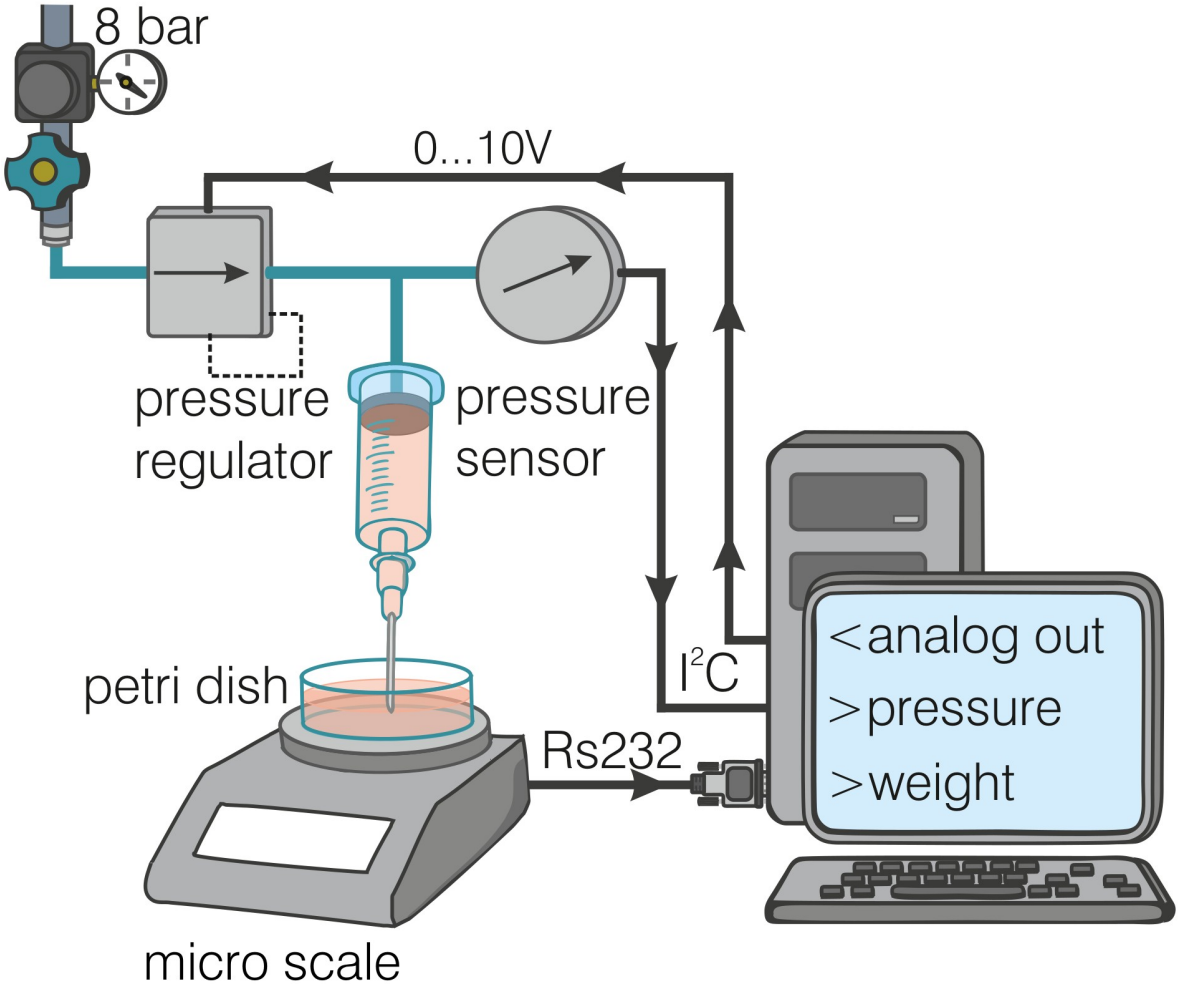

Fig 5. Experimental capillary rheometer setup. Schematic of the experimental setup using a custom-made bioprinter as capillary rheometer: the bioink is driven through a syringe under defined pressure, and the flow rate of the extruded alginate is measured with a precision scale.

https://doi.org/10.1371/journal.pone.0236371.g005

transducer (DRMOD-I2C-R10B, B+B Thermo-Technik GmbH, Germany), and the flow rate of the extruded alginate is measured with a precision scale (DI-100, Denver Instrument, USA).

We then fit the zero-shear viscosity, $\tilde{\eta}_0$, the corner shear rate, $\dot{\gamma}_c$, and the power-law shear thinning exponent, α, of a 3-parameter Carreau-Yasuda fluid to match the measured flow rate versus pressure relationship. The viscosity-shear rate relationship is given by

$$\tilde{\eta}(\dot{\gamma}) = \tilde{\eta}_0 \left[1 + \left(\frac{\dot{\gamma}}{\dot{\gamma}_c}\right)^{\alpha}\right]^{-1} \quad , \tag{10}$$

which is derived from Eq (9) by omitting the infinite-shear viscosity ($\tilde{\eta}_\infty = 0$), and introducing the corner-shear rate $\dot{\gamma}_c = K^{-1}$ as well as the single exponent $\alpha = a_1 = a_2$. Fitting is performed using a Marquard-Levenberg least-squares method implemented in the Python library SciPy, where the squared difference between the measured and the computed flow rate is minimized for each pressure level. The flow rate is computed according to (S-64) with the printing parameters mentioned above and $N = 150$ interpolation intervals between shear rates of 10^{-6} s^{-1} to 10^{8} s^{-1}. Since the inner diameter of the printer cartridge is large compared to that of the nozzle, we neglect a possible pressure drop along the cartridge.

3.2 Results

When measured with a cone-plate rheometer, the viscosity of a 2.5% alginate solution displays a pronounced shear rate dependency (Fig 6a), which is well described by a 3-parameter CY model according to Eq (10). Specifically, at shear rates below the corner shear rate $\dot{\gamma}_c \approx 17.8\ s^{-1}$, the viscosity is approximately constant, with $\tilde{\eta}_0 \approx 7.9$ Pas. At shear rates above $\dot{\gamma}_c$, the viscosity decreases according to a power-law with exponent $\alpha \approx 0.74$.

When the same 2.5% alginate solution is extruded through a 28 mm long 551 μm diameter capillary, we find an over-proportional increase in flow rate with increasing pressure (Fig 6b). Specifically, a doubling in pressure causes an approximately 10-fold increase in flow rate. This experimentally measured flow rate versus pressure relationship is exactly predicted by our numerical solution (blue line in Fig 6b), adding further support to the validity of our algorithm.

If a rheometer is not available, the above procedure can be inverted to obtain the rheological properties of the bioink as follows: starting from a first guess of the CY parameters, the pressure versus flow rate is computed using our Python tool. Subsequently, the viscosity parameters are refined until the prediction matches with the experimental data as shown in Fig 6b. The parameters obtained from the flow-rate versus pressure data (red squares in Fig 6b) are $\tilde{\eta}_0 \approx 6.8$ Pas, $\dot{\gamma}_c \approx 27.9\ s^{-1}$, and $\alpha \approx 0.78$ and differ only slightly from the parameters extracted from the cone-plate rheometer measurements. Accordingly, also only a slight difference between both parameter sets is seen in the velocity, shear rate and viscosity profiles shown in Fig 7. Also visible in Fig 6b is an increasing deviation of the flow rate versus pressure prediction for the cone-plate rheometer from the measured data with increasing pressure. This is likely due to shear rheometers not being able to achieve the large shear rates that occur under realistic printing conditions, while the capillary rheometer method intrinsically accounts for that.

A specific advantage of this capillary rheometry approach is that the experiment can be performed with the very same bioink that is currently in the printing cartridge prior to the actual printing process. Since most bioprinters are pressure controlled, i.e. the bioink is extruded through a printing needle with a constant pressure, the highly non-linear increase of the flow rate with increasing pressure makes it difficult to find the optimal printing parameters and to

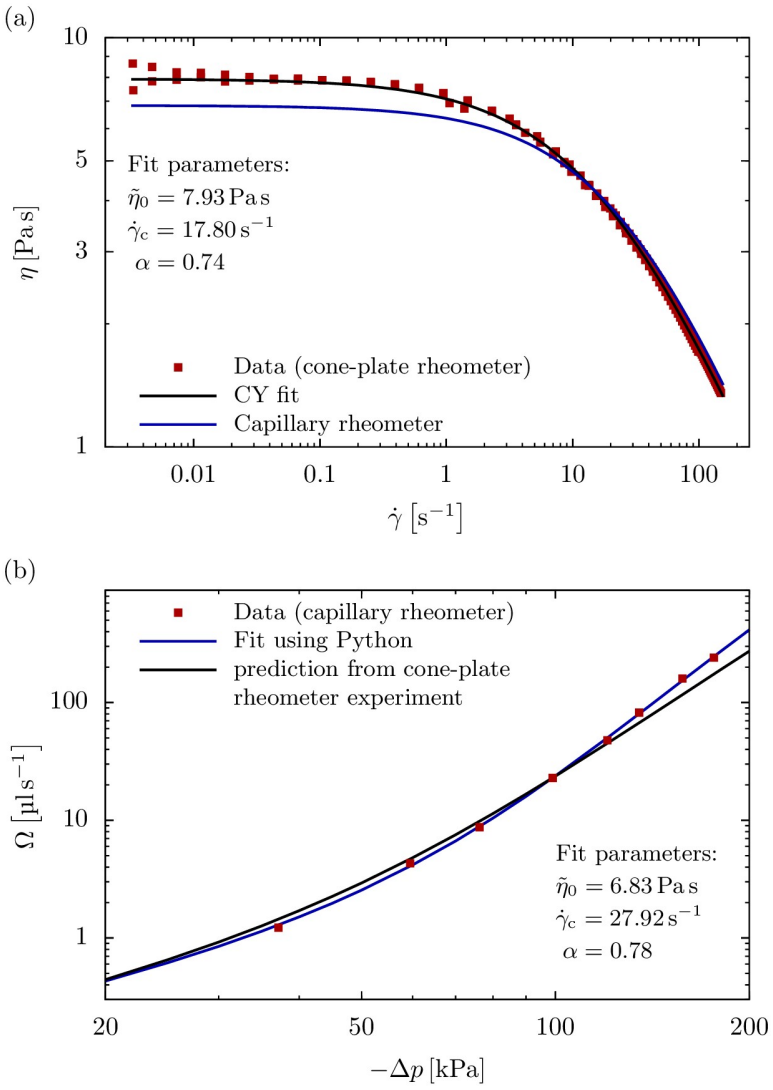

Fig 6. Comparison between capillary rheometer and cone-plate rheometer results. (a) Viscosity versus shear rate for a 2.5% alginate solution as measured with a cone-plate rheometer (data from 4 independent measurements, red squares) shows the pronounced shear thinning of a CY fluid that is well characterized by 3 fit parameters (black line) according to Eq (10). This shear thinning behavior can be predicted (blue line) from an independent capillary rheometry experiment using our Python tool. (b) Flow rate versus pressure relationship of the alginate solution when extruded through a 28 mm long 551 μm diameter capillary (red squares). This relationship follows our numerical solution using 3 fit parameters (blue line). The flow rate versus pressure relationship can similarly be predicted (black line) from the viscosity values obtained from an independent cone-plate rheometer experiment shown in the upper panel, showing significant deviations with increasing pressure.

https://doi.org/10.1371/journal.pone.0236371.g006

predict the material shear stresses during the printing process. Our algorithm solves both problems.

Conclusion

We presented a simple yet highly accurate algorithm to calculate the velocity and shear rate profiles for generalized Newtonian fluids, such as shear thinning bioinks, in cylindrical nozzles. For this, an arbitrary experimentally known viscosity-shear rate relation is split into a set

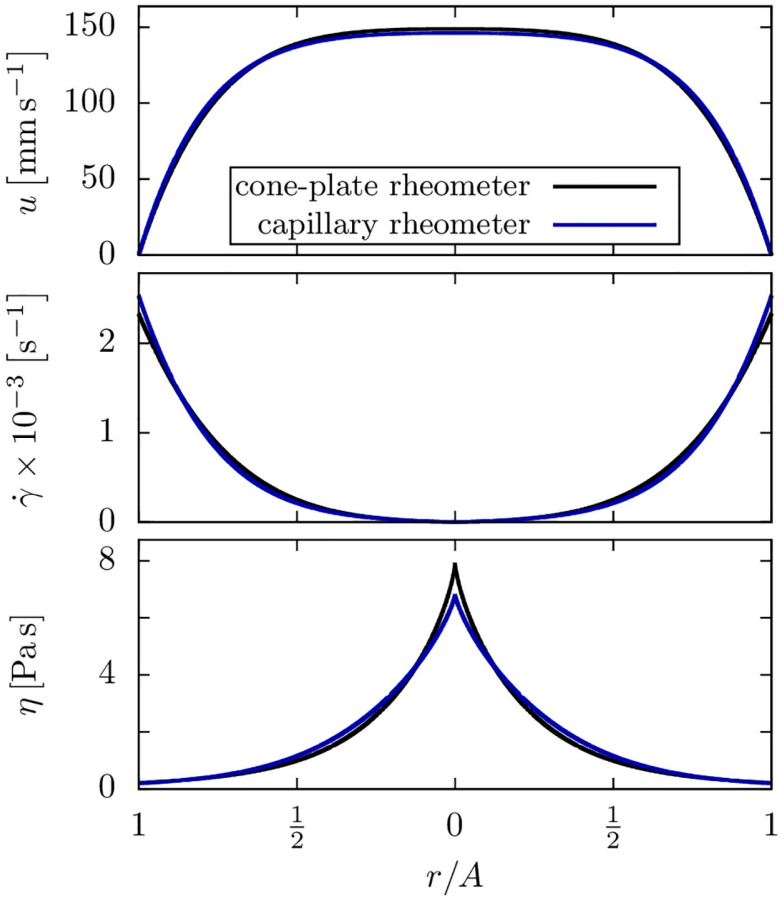

Fig 7. Alginate flow profile from capillary rheometer and cone-plate rheometer data. Flow profiles of 2.5% alginate hydrogel with a pressure difference of $\Delta p = -10^5$ Pa and $N = 150$. There is only a slight difference between the flow profiles calculated from the viscosity parameters obtained with a cone-plate rheometer (black line) and our capillary rheometer (blue line).

https://doi.org/10.1371/journal.pone.0236371.g007

of continuous intervals described by power-laws. This includes the possibility to predict velocity and shear stress profiles in pure as well as cell-laden bioinks. In each interval, an exact solution for the shear rate and velocity is computed and connected to neighboring intervals to obtain a continuous smooth profile over the entire nozzle diameter. For the shear stress, the linear radial dependency independent of the fluid rheology was confirmed. In addition, the total flow rate as well as the average viscosity, shear rate and shear stress are also found mathematically.

We implemented our method as an easy-to-use Python tool for calculating the velocity and shear rate profiles for a Carreau-Yasuda fluid. To validate this tool, we compared our predictions to a mathematically exact global solution and to Lattice Boltzmann simulations for realistic chitosan hydrogels under typical bioprinting conditions. In both cases, we found excellent agreement. We further measured the velocity profile of an alginate solution in a microfluidic channel and found good agreement with Lattice Boltzmann simulations.

An important experimental application of our theoretical method is capillary rheometry. Here, the flow rate versus pressure relationship for a given hydrogel is obtained using a standard bioprinter. This data can then be fit to our theoretical predictions yielding the

corresponding rheological parameters of the bioink. We illustrated this application for alginate and found good agreement with classical rheometer data.

Our method and the accompanying Python implementation provide a fast and simple tool to predict flow rates and shear stresses during bioprinting for a given bioink and thus will help to optimize printing parameters, especially for shear stress-sensitive living cells.

Supporting information

S1 File. Mathematical derivation, further experimental validation, and user's guide. The supplementary material for the manuscript contains a detailed mathematical derivation of the presented method and a simple model to estimate the force and deformation experienced by a cell in shear thinning capillary flow. We also include further experimental measurements for alginate 2% and 3% and chitosan 3% in square and rectangular microchannels, as well as the corresponding error calculations. A user's guide for the developed Python tool is provided.
(PDF)

S2 File. CYprofiles.py. File containing the implemented classes of our tool.
(PY)

S3 File. Tutorial.py. File with a basic usage example for the implemented classes.
(PY)

Acknowledgments

We thank Werner Schneider and Jia You for designing and building the capillary rheometer and for performing the measurements, Lena Fischer and Rainer Detsch for help with alginate preparation, Delf Kah, Alexander Winterl and Christoph Mark for help with the development of the bioprinter control software, and Ronny Reimann for the creating the experimental setup schematic. We gratefully acknowledge computing time provided by the SuperMUC system of the Leibniz Rechenzentrum, Garching, as well as by the Bavarian Polymer Institute (BPI). Christian Bächer acknowledges support by the study program "Biological Physics" of the Elite Network of Bavaria.

Author Contributions

Formal analysis: Sebastian J. Müller, Christian Bächer.

Funding acquisition: Dirk W. Schubert, Ben Fabry, Stephan Gekle.

Investigation: Elham Mirzahossein, Emil N. Iftekhar, Stefan Schrüfer.

Methodology: Sebastian J. Müller, Elham Mirzahossein, Emil N. Iftekhar.

Software: Sebastian J. Müller.

Supervision: Dirk W. Schubert, Ben Fabry, Stephan Gekle.

Writing – original draft: Sebastian J. Müller, Stephan Gekle.

Writing – review & editing: Sebastian J. Müller, Ben Fabry, Stephan Gekle.

References

1. Blaeser A, Duarte Campos DF, Puster U, Richtering W, Stevens MM, Fischer H. Controlling Shear Stress in 3D Bioprinting is a Key Factor to Balance Printing Resolution and Stem Cell Integrity. Advanced Healthcare Materials. 2015; 5(3):326–333. https://doi.org/10.1002/adhm.201500677 PMID: 26626828

2. Snyder J, Rin Son A, Hamid Q, Wang C, Lui Y, Sun W. Mesenchymal stem cell printing and process regulated cell properties. Biofabrication. 2015; 7(4):044106–17. https://doi.org/10.1088/1758-5090/7/4/044106 PMID: 26696405
3. Zhao Y, Li Y, Mao S, Sun W, Yao R. The influence of printing parameters on cell survival rate and printability in microextrusion-based 3D cell printing technology. Biofabrication. 2015; 7(4):045002–11. https://doi.org/10.1088/1758-5090/7/4/045002 PMID: 26523399
4. Paxton N, Smolan W, Böck T, Melchels F, Groll J, Jüngst T. Proposal to assess printability of bioinks for extrusion-based bioprinting and evaluation of rheological properties governing bioprintability. Biofabrication. 2017; 9(4):044107. https://doi.org/10.1088/1758-5090/aa8dd8 PMID: 28930091
5. Emmermacher J, Spura D, Cziommer J, Kilian D, Wollborn T, Fritsching U, et al. Engineering Considerations on Extrusion-Based Bioprinting: Interactions of Material Behavior, Mechanical Forces and Cells in the Printing Needle. Biofabrication. 2020; 12(2):025022. https://doi.org/10.1088/1758-5090/ab7553 PMID: 32050179
6. Malda J, Visser J, Melchels FP, Jüngst T, Hennink WE, Dhert WJA, et al. 25th Anniversary Article: Engineering Hydrogels for Biofabrication. Advanced Materials. 2013; 25(36):5011–5028. https://doi.org/10.1002/adma.201302042 PMID: 24038336
7. Zuidema JM, Rivet CJ, Gilbert RJ, Morrison FA. A protocol for rheological characterization of hydrogels for tissue engineering strategies. Journal of Biomedical Materials Research Part B: Applied Biomaterials. 2013; 102(5):1063–1073. https://doi.org/10.1002/jbm.b.33088
8. Tian XY, Li MG, Cao N, Li JW, Chen XB. Characterization of the flow behavior of alginate/hydroxyapatite mixtures for tissue scaffold fabrication. Biofabrication. 2009; 1(4):045005. https://doi.org/10.1088/1758-5082/1/4/045005 PMID: 20811114
9. Sarker B, Rompf J, Silva R, Lang N, Detsch R, Kaschta J, et al. Alginate-based hydrogels with improved adhesive properties for cell encapsulation. International Journal of Biological Macromolecules. 2015; 78:72–78. https://doi.org/10.1016/j.ijbiomac.2015.03.061 PMID: 25847839
10. Leppiniemi J, Lahtinen P, Paajanen A, Mahlberg R, Metsä-Kortelainen S, Pinomaa T, et al. 3D-Printable Bioactivated Nanocellulose–Alginate Hydrogels. ACS Applied Materials & Interfaces. 2017; 9(26):21959–21970. https://doi.org/10.1021/acsami.7b02756
11. Shi J, Wu B, Li S, Song J, Song B, Lu WF. Shear stress analysis and its effects on cell viability and cell proliferation in drop-on-demand bioprinting. Biomedical Physics & Engineering Express. 2018; 4(4):045028. https://doi.org/10.1088/2057-1976/aac946
12. Nair K, Gandhi M, Khalil S, Yan KC, Marcolongo M, Barbee K, et al. Characterization of cell viability during bioprinting processes. Biotechnology Journal. 2009; 4(8):1168–1177. https://doi.org/10.1002/biot.200900004 PMID: 19507149
13. Highley CB, Rodell CB, Burdick JA. Direct 3D Printing of Shear-Thinning Hydrogels into Self-Healing Hydrogels. Adv Mater. 2015; 27(34):5075–5079. https://doi.org/10.1002/adma.201501234 PMID: 26177925
14. Larsen BE, Bjørnstad J, Pettersen EO, Tønnesen HH, Melvik JE. Rheological characterization of an injectable alginate gel system. BMC Biotechnol. 2015; 15(1). https://doi.org/10.1186/s12896-015-0147-7
15. Hölzl K, Lin S, Tytgat L, Van Vlierberghe S, Gu L, Ovsianikov A. Bioink properties before, during and after 3D bioprinting. Biofabrication. 2016; 8(3):032002. https://doi.org/10.1088/1758-5090/8/3/032002 PMID: 27658612
16. Ouyang L, Yao R, Zhao Y, Sun W. Effect of bioink properties on printability and cell viability for 3D bioplotting of embryonic stem cells. Biofabrication. 2016; 8(3):035020–12. https://doi.org/10.1088/1758-5090/8/3/035020 PMID: 27634915
17. Jüngst T, Smolan W, Schacht K, Scheibel T, Groll J. Strategies and Molecular Design Criteria for 3D Printable Hydrogels. Chem Rev. 2016; 116(3):1496–1539. https://doi.org/10.1021/acs.chemrev.5b00303 PMID: 26492834
18. Jose RR, Rodriguez MJ, Dixon TA, Omenetto F, Kaplan DL. Evolution of Bioinks and Additive Manufacturing Technologies for 3D Bioprinting. ACS Biomater Sci Eng. 2016; 2(10):1662–1678. https://doi.org/10.1021/acsbiomaterials.6b00088
19. Thakur A, Jaiswal MK, Peak CW, Carrow JK, Gentry J, Dolatshahi-Pirouz A, et al. Injectable shear-thinning nanoengineered hydrogels for stem cell delivery. Nanoscale. 2016; 8(24):12362–12372. https://doi.org/10.1039/C6NR02299E PMID: 27270567
20. Markstedt K, Mantas A, Tournier I, Martínez Ávila H, Hägg D, Gatenholm P. 3D Bioprinting Human Chondrocytes with Nanocellulose–Alginate Bioink for Cartilage Tissue Engineering Applications. Biomacromolecules. 2015; 16(5):1489–1496. https://doi.org/10.1021/acs.biomac.5b00188 PMID: 25806996

21. Ning L, Betancourt N, Schreyer DJ, Chen X. Characterization of Cell Damage and Proliferative Ability during and after Bioprinting. ACS Biomaterials Science & Engineering. 2018; 4(11):3906–3918. https://doi.org/10.1021/acsbiomaterials.8b00714

22. Phillips TN, Roberts GW. Lattice Boltzmann models for non-Newtonian flows. IMA Journal of Applied Mathematics. 2011; 76(5):790–816. https://doi.org/10.1093/imamat/hxr003

23. Ostwald W. Ueber die rechnerische Darstellung des Strukturgebietes der Viskosität. Kolloid-Zeitschrift. 1929; 47(2):176–187. https://doi.org/10.1007/BF01496959

24. Blair GWS, Hening JC, Wagstaff A. The Flow of Cream through Narrow Glass Tubes. The Journal of Physical Chemistry. 1939; 43(7):853–864. https://doi.org/10.1021/j150394a004

25. Carreau PJ. Rheological Equations from Molecular Network Theories. Transactions of the Society of Rheology. 1972; 16(1):99–127. https://doi.org/10.1122/1.549276

26. Wu Q, Therriault D, Heuzey MC. Processing and Properties of Chitosan Inks for 3D Printing of Hydrogel Microstructures. ACS Biomaterials Science & Engineering. 2018; 4(7):2643–2652. https://doi.org/10.1021/acsbiomaterials.8b00415

27. Escudier MP, Gouldson IW, Pereira AS, Pinho FT, Poole RJ. On the reproducibility of the rheology of shear-thinning liquids. Journal of Non-Newtonian Fluid Mechanics. 2001; 97(2-3):99–124. https://doi.org/10.1016/S0377-0257(00)00178-6

28. Cruz DA, Coelho PM, Alves MA. A Simplified Method for Calculating Heat Transfer Coefficients and Friction Factors in Laminar Pipe Flow of Non-Newtonian Fluids. Journal of Heat Transfer. 2012; 134 (9):091703. https://doi.org/10.1115/1.4006288

29. Sochi T. Analytical solutions for the flow of Carreau and Cross fluids in circular pipes and thin slits. Rheologica Acta. 2015; 54(8):745–756. https://doi.org/10.1007/s00397-015-0863-x

30. Manojlovic V, Djonlagic J, Obradovic B, Nedovic V, Bugarski B. Investigations of Cell Immobilization in Alginate: Rheological and Electrostatic Extrusion Studies. Journal of Chemical Technology & Biotechnology. 2006; 81(4):505–510. https://doi.org/10.1002/jctb.1465

31. Batchelor GK. An Introduction to Fluid Dynamics. Cambridge: Cambridge University Press; 2000. Available from: http://ebooks.cambridge.org/ref/id/CBO9780511800955.

32. Oliphant TE. Python for Scientific Computing. Computing in Science & Engineering. 2007; 9(3):10–20. https://doi.org/10.1109/MCSE.2007.58

33. Limbach HJ, Arnold A, Mann BA, Holm C. ESPResSo—an extensible simulation package for research on soft matter systems. Computer Physics Communications. 2006; 174(9):704–727. https://doi.org/10.1016/j.cpc.2005.10.005

34. Roehm D, Arnold A. Lattice Boltzmann simulations on GPUs with ESPResSo. The European Physical Journal Special Topics. 2012; 210(1):89–100. https://doi.org/10.1140/epjst/e2012-01639-6

35. Sarker M, Chen XB. Modeling the Flow Behavior and Flow Rate of Medium Viscosity Alginate for Scaffold Fabrication With a Three-Dimensional Bioplotter. Journal of Manufacturing Science and Engineering. 2017; 139(8):081002. https://doi.org/10.1115/1.4036226

SUPPLEMENTARY MATERIAL FOR THE MANUSCRIPT

Flow and hydrodynamic shear stress inside a printing needle during biofabrication

Sebastian J. Müller[1], Elham Mirzahossein[2], Emil Iftekhar[2], Christian Bächer[1], Stefan Schrüfer[3], Dirk W. Schubert[3], Ben Fabry[2] and Stephan Gekle[1]

[1]Biofluid Simulation and Modeling, Universität Bayreuth, Germany
[2]Biophysics Group, Friedrich-Alexander Universität Erlangen-Nürnberg, Germany
[3]Polymer Physics and Processing, Friedrich-Alexander Universität Erlangen-Nürnberg, Germany
Authors to whom correspondence should be addressed:
sjmueller@uni-bayreuth.de, stephan.gekle@uni-bayreuth.de

S-1. Theory

Our algorithm starts from an experimentally known viscosity-shear rate relation $\eta(\dot{\gamma})$ and interpolates it by a series of power-law functions. This interpolation is subsequently used for writing down a similar series of Navier-Stokes equations which are solved first for the shear rate and then for the velocity profile.

S-1.1. Viscosity model

The viscosity-shear rate relationship of the bioink, or any other generalized Newtonian fluid, can be approximated by a continuous, piecewise function

$$\eta\left(\dot{\gamma}\right) = \begin{cases} K_0\dot{\gamma}^{n_0-1} & 0 \leq \dot{\gamma} < \dot{\Gamma}_0 \\ \vdots & \\ K_i\dot{\gamma}^{n_i-1} & \dot{\Gamma}_{i-1} \leq \dot{\gamma} < \dot{\Gamma}_i \\ \vdots & \\ K_N\dot{\gamma}^{n_N-1} & \dot{\Gamma}_{N-1} \leq \dot{\gamma} < \infty \end{cases}, \tag{S-1}$$

as depicted in figure 1a of the main text. In every interval the viscosity-shear rate relation is described by a power-law model with a consistency parameter K_i having the physical unit $\mathrm{Pa\,s^{n_i}}$, and a dimensionless exponent n_i, according to the literature [1–7]. We note that the shear rate can also be understood as dimensionless quantity, normalized to a constant shear rate of $1\,\mathrm{s}^{-1}$ without changing its numerical value. Doing so, the consistency parameter can be interpreted as a reference viscosity with the more meaningful physical unit Pa s.
The i^{th} interval is bounded by the shear rates $\dot{\Gamma}_{i-1}$ and $\dot{\Gamma}_i$. The condition

$$K_i\dot{\Gamma}_i^{n_i-1} = K_{i+1}\dot{\Gamma}_i^{n_{i+1}-1} \tag{S-2}$$

ensures the continuity of (S-1) across the interval boundary $\dot{\Gamma}_i$ $(i = 0, \ldots, N-1)$. Since real fluids usually exhibit Newtonian behavior for zero and infinite shear rates, we take

$$n_0 = n_N = 1 \tag{S-3}$$

for the power-law exponents in the first and last interval.
We note that instead of the power-law interpolation, a linear interpolation would also be possible. However, since most bioinks show power-law shear thinning over a wide range of shear rates, a power-law interpolation is computationally more efficient when logarithmically-spaced shear rate intervals are used, as shown in figure 1a.

S-1.2. Determination of K_i and n_i

Starting from an experimentally known viscosity-shear rate relation $\tilde{\eta}\left(\dot{\gamma}\right)$ which can be given either as raw rheological data or as a viscosity model with known parameters

(e.g. [8, 9]) such as the Carreau-Yasuda model, the consistency indices K_i and exponents n_i in each interpolation interval are determined as follows. The lowest and highest consistency indices are fixed by eq. (S-3) as

$$K_0 = \tilde{\eta}\left(\dot{\Gamma}_0\right) \quad \text{and} \quad K_N = \tilde{\eta}\left(\dot{\Gamma}_{N-1}\right) \quad . \tag{S-4}$$

Since rheological data often spans multiple decades, we choose an equidistant partitioning of the interval $[\dot{\Gamma}_0, \dot{\Gamma}_{N-1}]$ on a logarithmic scale, as shown in figure 1a. Given the bounds of this interval and the number of interpolated points, the intermediate shear rates are given by

$$\dot{\Gamma}_i = \dot{\Gamma}_0 \left(\frac{\dot{\Gamma}_{N-1}}{\dot{\Gamma}_0}\right)^{\frac{i}{N-1}} \quad . \tag{S-5}$$

The parameters of the interpolating power-law functions $\eta_i\left(\dot{\gamma}\right)$ are found by inserting the known viscosity values at the interval bounds. Thus, the following system of equations needs to be solved:

$$K_i \dot{\Gamma}_{i-1}^{n_i-1} = \tilde{\eta}\left(\dot{\Gamma}_{i-1}\right) \tag{S-6}$$

$$K_i \dot{\Gamma}_{i}^{n_i-1} = \tilde{\eta}\left(\dot{\Gamma}_{i}\right) \tag{S-7}$$

By division of the two equations, the power-law exponent is found to be

$$n_i = 1 + \log\left(\frac{\tilde{\eta}\left(\dot{\Gamma}_{i-1}\right)}{\tilde{\eta}\left(\dot{\Gamma}_{i}\right)}\right)\left(\log\left(\frac{\dot{\Gamma}_{i-1}}{\dot{\Gamma}_{i}}\right)\right)^{-1} \quad . \tag{S-8}$$

Multiplication of (S-6) by (S-7) gives an expression for the consistency index:

$$K_i = \sqrt{\tilde{\eta}\left(\dot{\Gamma}_{i-1}\right)\tilde{\eta}\left(\dot{\Gamma}_{i}\right)}\left(\dot{\Gamma}_{i-1}\dot{\Gamma}_{i}\right)^{\frac{1-n_i}{2}} \tag{S-9}$$

By inserting a functional form or raw data for $\tilde{\eta}\left(\dot{\gamma}\right)$ into (S-8) and (S-9) the interpolation can be performed in the entire range of shear rates.

S-1.3. Governing equations

The Navier-Stokes equations to determine the flow field $\vec{u}$ read

$$\varrho\left[\frac{\partial \vec{u}}{\partial t} + \left(\vec{u}\cdot\boldsymbol{\nabla}\right)\vec{u}\right] = -\boldsymbol{\nabla}p + \boldsymbol{\nabla}\cdot\left(\underline{\underline{\tau}}\right) + \vec{f} \quad , \tag{S-10}$$

with the fluid mass density ϱ, the pressure gradient $\boldsymbol{\nabla}p$, the viscous stress tensor $\underline{\underline{\tau}}$, and an external force term $\vec{f}$. The viscous stress tensor is related to the viscosity and the strain rate tensor $\underline{\underline{\varepsilon}}$ via

$$\underline{\underline{\tau}} = 2\eta\left(\dot{\gamma}\right)\underline{\underline{\varepsilon}} \quad , \tag{S-11}$$

where the strain rate tensor is defined as

$$\underline{\underline{\varepsilon}} = \tfrac{1}{2}\left[\boldsymbol{\nabla}\vec{u} + (\boldsymbol{\nabla}\vec{u})^{\mathsf{T}}\right] \quad . \tag{S-12}$$

Here, $\boldsymbol{\nabla}\vec{u}$ denotes the dyadic product of the gradient operator and the velocity vector and $(\boldsymbol{\nabla}\vec{u})^{\mathsf{T}}$ its transpose. The shear rate can be obtained as invariant of the strain rate tensor, i. e.

$$\dot{\gamma} = \sqrt{2\sum_{\alpha,\beta}\varepsilon_{\alpha\beta}\varepsilon_{\alpha\beta}} \quad . \tag{S-13}$$

For a purely Newtonian fluid, the viscosity in (S-11) would be a constant.

S-1.3.1. Flow conditions. Analogously to the well-known Poiseuille flow of a Newtonian fluid [10, pp. 180 ff.], we assume a stationary, laminar, and pressure driven flow, with the velocity having only an axial component depending on the radial position. We consider a cylindrical channel and neglect entrance and exit effects. For the following derivation, a cylindrical coordinate system with a radial component r, an azimuthal component ϕ, and an axial component z, is employed. In these coordinates, the flow conditions read:

$$\vec{f} = \vec{0} \tag{S-14}$$

$$\frac{\partial\vec{u}}{\partial t} = \vec{0} \tag{S-15}$$

$$\frac{\partial\vec{u}}{\partial z} = \vec{0} \tag{S-16}$$

$$\frac{\partial\vec{u}}{\partial\phi} = \vec{0} \tag{S-17}$$

$$\vec{u}\,(r,\phi,z) = u\vec{e}_z \tag{S-18}$$

S-1.3.2. Constant pressure gradient. For a purely Newtonan fluid, the flow conditions (S-14)-(S-18) imply a spatially constant pressure gradient throughout the entire channel. In the following, we prove that the same holds for an arbitrary generalized Newtonian fluid. The strain rate tensor in cylindrical coordinates reads:

$$\underline{\underline{\varepsilon}} = \tfrac{1}{2}\begin{pmatrix} \underbrace{2\partial_r u_r}_{(S-18)_{\underline{\underline{0}}}} & \underbrace{\partial_r u_\phi + \frac{1}{r}\partial_\phi u_r - \frac{1}{r}u_\phi}_{(S-17),(S-18)_{\underline{\underline{0}}}} & \underbrace{\partial_z u_r}_{(S-18)_{\underline{\underline{0}}}} + \partial_r u_z \\ - & \underbrace{2\partial_\phi u_\phi + 2\frac{1}{r}u_r}_{(S-17),(S-18)_{\underline{\underline{0}}}} & \underbrace{\frac{1}{r}\partial_\phi u_z + \partial_z u_\phi}_{(S-17)_{\underline{\underline{0}}}} \\ - & - & \underbrace{2\partial_z u_z}_{(S-16)_{\underline{\underline{0}}}} \end{pmatrix} \tag{S-19}$$

where the notation $\partial_x = \frac{\partial}{\partial x}$ denotes a partial spatial derivative with respect to the coordinate x. The "$-$" signs indicate the symmetric components of the tensor. The

underbraced terms vanish due to the flow conditions. Thus, the viscous stress tensor reduces to a single component,

$$\tau_{rz} = \tau_{zr} = \eta\left(\dot{\gamma}\right) \frac{\partial u_z}{\partial r} \quad . \tag{S-20}$$

The components of the NSE yield:

$$\frac{\partial p}{\partial r} = 0 \qquad (r-\text{component}) \tag{S-21}$$

$$\frac{\partial p}{\partial \phi} = 0 \qquad (\phi-\text{component}) \tag{S-22}$$

$$\frac{\partial p}{\partial z} = \frac{1}{r}\frac{\partial}{\partial r}\left(r\tau_{rz}\right) \qquad (z-\text{component}) \tag{S-23}$$

This shows that the pressure gradient has only a z-component. By applying the derivative ∂_z again on the remaining z-component of the NSE, we obtain:

$$\partial_z^2 p = \partial_z \left[\frac{1}{r}\partial_r \left(r\eta\left(\dot{\gamma}\right)\partial_r u\right)\right] \tag{S-24}$$

$$= \frac{1}{r}\partial_r \left[r\partial_z \left(\eta\left(\dot{\gamma}\right)\partial_r u\right)\right] \tag{S-25}$$

$$= \frac{1}{r}\partial_r \left(r\eta\left(\dot{\gamma}\right)\partial_r \underbrace{\partial_z u}_{\overset{(S-17)}{=}0} + r\partial_r u \underbrace{\partial_z \eta\left(\dot{\gamma}\right)}_{\overset{(S-17)}{=}0} \right) = 0 \tag{S-26}$$

which shows that the pressure gradient is indeed constant and allows us to define

$$G := \frac{\partial p}{\partial z} = \frac{\Delta p}{L} \quad , \tag{S-27}$$

where $\Delta p = p_L - p_0 < 0$ is the pressure difference along a channel segment of length L. Applying the flow conditions, the Navier-Stokes equations reduce to the ordinary differential equation (1):

$$G = \frac{1}{r}\frac{\partial}{\partial r}\left(r\eta\left(\dot{\gamma}\right)\frac{\partial u}{\partial r}\right) \tag{S-28}$$

This equation is however still highly non-linear due to the dependency of $\eta\left(\dot{\gamma}\right)$ on $\partial_r u$ via the shear rate $\dot{\gamma}$ (cf. (S-31), (4)).

S-1.3.3. Ansatz and boundary conditions. Similar to the piecewise viscosity model in (S-1), we decompose the axial velocity $u\left(r\right)$ into intervals:

$$u\left(r\right) = \begin{cases} u_0\left(r\right) & 0 \le r < R_0 \\ \vdots & \\ u_i\left(r\right) & R_{i-1} \le r < R_i \\ \vdots & \\ u_N\left(r\right) & R_{N-1} \le r < \infty \end{cases} \tag{S-29}$$

as illustrated in figure 1b. The essential difference between (S-1) and (S-29) is that the interval boundaries are determined by shear rates $\dot{\Gamma}_i$ for the former and by radial positions R_i for the latter. While the interval boundaries for the viscosity $\dot{\Gamma}_i$ are an input quantity (see section S-1.2), the radial boundaries are determined *a posteriori* from the shear rate profile by the condition

$$\dot{\gamma}\left(R_i\right) = \dot{\Gamma}_i \tag{S-30}$$

as will be shown in (S-42) below. The shear rate as a function of the radial position $\dot{\gamma}\left(r\right)$ is given by the first derivative of the velocity with respect to the radial position, i. e.

$$\dot{\gamma}\left(r\right) = -\frac{\partial u\left(r\right)}{\partial r} \quad , \tag{S-31}$$

and can also be written in the same piecewise manner:

$$\dot{\gamma}\left(r\right) = \begin{cases} \dot{\gamma}_0\left(r\right) & 0 \leq r < R_0 \\ \vdots & \\ \dot{\gamma}_i\left(r\right) & R_{i-1} \leq r < R_i \\ \vdots & \\ \dot{\gamma}_N\left(r\right) & R_{N-1} \leq r < \infty \end{cases} \tag{S-32}$$

As for classical Poiseuille flow, we assume the common case of the velocity monotonically decreasing with the radial position. According to (S-31), the shear rate is therefore always positive. For $u\left(r\right)$ to be continuously differentiable and finite at the channel center, the piecewise definitions of the velocity and the shear rate must be equal at the intermediate points, R_i, i. e.

$$u_i\left(R_i\right) = u_{i+1}\left(R_i\right) \tag{S-33}$$

and

$$\dot{\gamma}_i\left(R_i\right) = \dot{\gamma}_{i+1}\left(R_i\right) \quad . \tag{S-34}$$

The flow shall further fulfill a no-slip boundary condition at the cylindrical channel wall at $r = A$, i. e.

$$u\left(A\right) = 0 \quad . \tag{S-35}$$

To ensure the continuous differentiability of the axially symmetric flow field, the flow must have a maximum at the channel center, $r = 0$. Therefore, the shear rate has to vanish at this point:

$$\dot{\gamma}\left(0\right) = 0 \tag{S-36}$$

S-1.4. Solution to the shear rate profile

Inserting the ansatz (S-29) and (S-32) into the Navier-Stokes equation (S-28) yields the following system of equations, (3) and (4), where $i \in \{0, \ldots, N\}$ denotes the intervals as above:

$$G = \frac{1}{r}\frac{\partial}{\partial r}\left(-rK_i\dot{\gamma}_i\left(r\right)^{n_i}\right) \tag{S-37}$$

$$\dot{\gamma}_i\left(r\right) = -\frac{\partial u_i\left(r\right)}{\partial r} \quad . \tag{S-38}$$

The first equation (S-37), (3), can be rearranged and integrated once to obtain

$$\dot{\gamma}_i\left(r\right) = \left(-\frac{Gr}{2K_i} - \frac{c_i}{K_i r}\right)^{\frac{1}{n_i}} \quad , \tag{S-39}$$

where the c_i are a set of integration constants that are determined next using the continuity conditions (S-34) and the boundary condition (S-36).

S-1.4.1. Determination of the integration constants of the shear rate profile. The integration constants c_i can be shown to be zero using the complete induction proof described in the following. The base clause, (S-39) for $i = 0$ with the boundary condition (S-36) gives

$$\dot{\gamma}_0\left(0\right) = \lim_{r\to 0}\left(-\frac{Gr}{2K_0} - \frac{c_0}{K_0 r}\right)^{\frac{1}{n_0}} \stackrel{!}{=} 0 \quad , \tag{S-40}$$

which is only fulfilled if the integration constant vanishes, thus, $c_0 = 0$.
Assuming that $c_i = 0$, c_{i+1} can be determined using the continuity condition (S-34),

$$\dot{\gamma}_i\left(R_i\right) = \dot{\gamma}_{i+1}\left(R_i\right) = \dot{\Gamma}_i \quad , \tag{S-41}$$

where the $\dot{\Gamma}_i$ are given. The equality $\dot{\Gamma}_i = \dot{\gamma}_i\left(R_i\right)$ yields an expression for the radial position R_i of the interfacial point between $\dot{\gamma}_i\left(r\right)$ and $\dot{\gamma}_{i+1}\left(r\right)$,

$$R_i = -\frac{2K_i\dot{\Gamma}_i^{n_i}}{G} \quad , \tag{S-42}$$

that can be inserted into the second part of (S-41) using (S-39):

$$\dot{\Gamma}_i = \left(-\frac{GR_i}{2K_{i+1}} - \frac{c_{i+1}}{K_{i+1}R_i}\right)^{\frac{1}{n_{i+1}}} \tag{S-43}$$

$$= \left(\frac{K_i}{K_{i+1}}\dot{\Gamma}_i^{n_i} + \frac{c_{i+1}G}{2K_{i+1}K_i\dot{\Gamma}_i^{n_i}}\right)^{\frac{1}{n_{i+1}}} \tag{S-44}$$

Employing the continuity condition of the viscosity model (S-2) gives an expression for the ratio of the consistency parameters, i. e.

$$K_i\dot{\Gamma}_i^{n_i-1} = K_{i+1}\dot{\Gamma}_i^{n_{i+1}-1} \tag{S-45}$$

$$\frac{K_i}{K_{i+1}} = \dot{\Gamma}_i^{n_{i+1}-n_i} \quad . \tag{S-46}$$

Inserting (S-46) into (S-44) finally yields

$$\dot{\Gamma}_i = \left(\dot{\Gamma}_i^{n_{i+1}} + \frac{c_{i+1} G}{2 K_{i+1} K_i \dot{\Gamma}_i^{n_i}} \right)^{\frac{1}{n_{i+1}}} \quad , \tag{S-47}$$

which is equal only if $c_{i+1} = 0$ thus completing the proof.
With that, the final form for the shear rate profile in the i^{th} interval is obtained as (cf. (5)):

$$\dot{\gamma}_i (r) = \left(-\frac{G}{2K_i} r \right)^{\frac{1}{n_i}} \tag{S-48}$$

Note that this solution reduces to the simple power-law model solution if the index i is dropped.

S-1.5. Solution to the velocity profile

The velocity profile is obtained by inserting (S-48), (5), into the second part of the system of differential equations (S-38), (4), and integrating over r:

$$\frac{\partial u_i (r)}{\partial r} = - \left(-\frac{G}{2K_i} r \right)^{\frac{1}{n_i}} \tag{S-49}$$

$$u_i (r) = - \left(-\frac{G}{2K_i} \right)^{\frac{1}{n_i}} \frac{n_i}{n_i + 1} r^{1+\frac{1}{n_i}} + \tilde{c}_i \tag{S-50}$$

The integration constants $\tilde{c}_i$ are determined next using the no-slip boundary condition (S-35) and the continuity conditions for the velocity field (S-33).

S-1.5.1. Determination of the integration constants of the velocity profile. Since the number of intervals of the viscosity model N is independent of the choice of the flow parameters, G and A, and this choice uniquely determines the R_i via (S-42), the outer channel boundary R is not necessarily located in the last interval of the velocity ansatz function $u_N (r)$. Instead, the radius of the channel lies in the k^{th} interval, i. e.

$$R_{k-1} \leq A \leq R_k \quad , \tag{S-51}$$

where $0 < k \leq N$. Intervals with $i > k$ whose boundaries R_i lie beyond the channel radius A have no physical significance and are disregarded in the following. Consequently, the no-slip boundary condition applies to the k^{th} interval:

$$u_k (A) = - \left(-\frac{G}{2K_k} \right)^{\frac{1}{n_k}} \frac{n_k}{n_k + 1} A^{1+\frac{1}{n_k}} + \tilde{c}_k \stackrel{!}{=} 0 \tag{S-52}$$

The integration constant can therefore easily be found as

$$\tilde{c}_k = \left(-\frac{G}{2K_k} \right)^{\frac{1}{n_k}} \frac{n_k}{n_k + 1} A^{1+\frac{1}{n_k}} \quad . \tag{S-53}$$

For $i < k$, the continuity condition for the velocity field (S-33) can be written as

$$-\left(-\frac{G}{2K_i}\right)^{\frac{1}{n_i}} \frac{n_i}{n_i+1} R_i^{1+\frac{1}{n_i}} + \tilde{c}_i = -\left(-\frac{G}{2K_{i+1}}\right)^{\frac{1}{n_{i+1}}} \frac{n_{i+1}}{n_{i+1}+1} R_i^{1+\frac{1}{n_{i+1}}} + \tilde{c}_{i+1} \quad . \tag{S-54}$$

Assuming that $\tilde{c}_{i+1}$ is known and rearranging this equation for $\tilde{c}_i$ yields

$$\tilde{c}_i = \tilde{c}_{i+1} - R_i \left[\underbrace{\left(-\frac{G}{2K_{i+1}}\right)^{\frac{1}{n_{i+1}}} R_i^{\frac{1}{n_{i+1}}}}_{=\dot{\gamma}_{i+1}(R_i)\,=\,\dot{\Gamma}_i} \frac{n_{i+1}}{n_{i+1}+1} - \underbrace{\left(-\frac{G}{2K_i}\right)^{\frac{1}{n_i}} R_i^{\frac{1}{n_i}}}_{=\dot{\gamma}_i(R_i)\,=\,\dot{\Gamma}_i} \frac{n_i}{n_i+1} \right] \quad , \tag{S-55}$$

where the underbraced terms can be identified as the shear rates at the interfacial position which are equal by the continuity conditions (S-34). Hence,

$$\tilde{c}_i = \tilde{c}_{i+1} - R_i \dot{\Gamma}_i \left(\frac{n_{i+1}}{n_{i+1}+1} - \frac{n_i}{n_i+1} \right) \quad . \tag{S-56}$$

Finally, inserting the expression for the known outermost integration constant, $\tilde{c}_k$, the interior integration constants can be determined as

$$\tilde{c}_i = \tilde{c}_k - \sum_{j=i}^{k-1} R_j \dot{\Gamma}_j \left(\frac{n_{j+1}}{n_{j+1}+1} - \frac{n_j}{n_j+1} \right) \quad . \tag{S-57}$$

Combining (S-50), (S-53) and (S-57), the velocity profile in the i^{th} interval is given by (6):

$$\begin{aligned} u_i(r) = &-\left(-\frac{G}{2K_i}\right)^{\frac{1}{n_i}} \frac{n_i}{n_i+1} r^{1+\frac{1}{n_i}} + \left(-\frac{G}{2K_k}\right)^{\frac{1}{n_k}} \frac{n_k}{n_k+1} A^{1+\frac{1}{n_k}} \\ &- \sum_{j=i}^{k-1} R_j \dot{\Gamma}_j \left(\frac{n_{j+1}}{n_{j+1}+1} - \frac{n_j}{n_j+1} \right) \end{aligned} \tag{S-58}$$

S-1.6. Calculation of averages

In the following, we derive mathematical expressions for the flow rate as well as the average shear rate, viscosity, and shear stress. The flow rate or, equivalently, the average flow velocity determines the printing speed in 3D bioprinting processes. The average shear rate and shear stress can be used to estimate cell damage during printing [7, 11].

S-1.6.1. Average velocity and flow rate. The cross-sectional average of the velocity field is given by

$$\overline{u} = \frac{1}{\pi A^2} \int_0^{2\pi} \mathrm{d}\phi \int_0^A \mathrm{d}r\, r u(r) \quad . \tag{S-59}$$

The first integral can be evaluated and gives a factor 2π, the second integral is split into the intervals:

$$\overline{u} = \frac{2}{A^2}\left[\int_0^{R_0} \mathrm{d}r\, r u_0(r) + \sum_{i=1}^{k-1}\int_{R_{i-1}}^{R_i} \mathrm{d}r\, r u_i(r) + \int_{R_{k-1}}^{A} \mathrm{d}r\, r u_k(r)\right] \tag{S-60}$$

Abbreviating the prefactors in (S-50), i. e.

$$u_i(r) = a_i r^{1+\frac{1}{n_i}} + \tilde{c}_i \quad , \tag{S-61}$$

with

$$a_i = -\left(-\frac{G}{2K_i}\right)^{\frac{1}{n_i}} \frac{n_i}{n_i+1} \quad , \tag{S-62}$$

the average velocity is found to be:

$$\begin{aligned}\overline{u} = \frac{2}{A^2}\Bigg[&\frac{a_0}{3+\frac{1}{n_0}} R_0^{3+\frac{1}{n_0}} + \frac{\tilde{c}_0}{2} R_0^2 + \sum_{i=1}^{k-1} \frac{a_i}{3+\frac{1}{n_i}}\left(R_i^{3+\frac{1}{n_i}} - R_{i-1}^{3+\frac{1}{n_i}}\right) \\ &+ \sum_{i=1}^{k-1} \frac{\tilde{c}_i}{2}\left(R_i^2 - R_{i-1}^2\right) + \frac{a_k}{3+\frac{1}{n_k}}\left(A^{3+\frac{1}{n_k}} - R_{k-1}^{3+\frac{1}{n_k}}\right) + \frac{\tilde{c}_k}{2}\left(A^2 - R_{k-1}^2\right)\Bigg]\end{aligned} \tag{S-63}$$

The flow rate is given by

$$\Omega = \pi A^2 \overline{u} \quad . \tag{S-64}$$

S-1.6.2. Average shear rate. The same procedure as above can be applied to find the average shear rate. With (S-48) shortened to

$$\dot{\gamma}_i(r) = b_i r^{\frac{1}{n_i}} \quad , \tag{S-65}$$

the average shear rate is given by:

$$\overline{\dot{\gamma}} = \frac{2}{A^2}\left[\frac{b_0}{2+\frac{1}{n_0}} R_0^{2+\frac{1}{n_0}} + \sum_{i=1}^{k-1} \frac{b_i}{2+\frac{1}{n_i}}\left(R_i^{2+\frac{1}{n_i}} - R_{i-1}^{2+\frac{1}{n_i}}\right) + \frac{b_k}{2+\frac{1}{n_k}}\left(A^{2+\frac{1}{n_k}} - R_{k-1}^{2+\frac{1}{n_k}}\right)\right] \tag{S-66}$$

S-1.6.3. Average viscosity. The viscosity field, $\eta(r)$, is calculated by inserting the shear rate field from (S-48) into the power-law definitions of the respective interpolation interval in (S-1). Thus,

$$\eta_i(r) = K_i\left(\dot{\gamma}_i(r)\right)^{n_i-1} = K_i\left(-\frac{G}{2K_i} r\right)^{1-\frac{1}{n_i}} \quad , \tag{S-67}$$

which can be shortened to

$$\eta_i(r) = d_i r^{1-\frac{1}{n_i}} \quad . \tag{S-68}$$

Using the same procedure as above, the integral in the i^{th} interval yields

$$\int_{R_{i-1}}^{R_i} \mathrm{d}r\, r\eta_i(r) = \frac{d_i}{3-\frac{1}{n_i}} \left(R_i^{3-\frac{1}{n_i}} - R_{i-1}^{3-\frac{1}{n_i}} \right) \tag{S-69}$$

if $n_i \neq \frac{1}{3}$ and

$$\int_{R_{i-1}}^{R_i} \mathrm{d}r\, r\eta_i(r) = d_i \int_{R_{i-1}}^{R_i} \mathrm{d}r\, r^{-1} = d_i \ln\left(\frac{R_i}{R_{i-1}}\right) \tag{S-70}$$

if $n_i = \frac{1}{3}$. The average viscosity for our model is therefore given by

$$\overline{\eta} = \frac{2}{A^2} \left[\int_0^{R_0} \mathrm{d}r\, r\eta_0(r) + \sum_{i=1}^{k-1} \int_{R_{i-1}}^{R_i} \mathrm{d}r\, r\eta_i(r) + \int_{R_{k-1}}^{A} \mathrm{d}r\, r\eta_k(r) \right] \quad , \tag{S-71}$$

where the integrals are chosen as (S-69) or (S-70) according to n_i. ‡

S-1.6.4. Average shear stress. The radial profile of the shear stress is given as the product of the shear rate field (S-48) and the viscosity field. The latter is calculated by inserting the shear rate field from (S-48) into the power-law definitions of the respective interpolation interval in (S-1):

$$\eta_i(r) = K_i \left(\dot{\gamma}_i(r)\right)^{n_i - 1} \tag{S-72}$$

The shear stress profile is therefore obtained as

$$\begin{aligned} \sigma_i(r) &= \dot{\gamma}_i(r)\, \eta_i(r) = K_i \left(\dot{\gamma}_i(r)\right)^{n_i} \\ &= -\tfrac{1}{2} G r = \sigma(r) \quad , \end{aligned} \tag{S-73}$$

where the index i can be dropped since it is independent of the viscosity interpolation. This linear relationship of shear stress and radial position is well-known for power-law fluids [11]. Its average is found by simply solving one integral that yields:

$$\overline{\sigma} = \frac{2}{A^2} \int_0^A \mathrm{d}r\, r\sigma(r) = -\frac{GA}{3} \tag{S-74}$$

‡ Note that in the inner-most interval with R_0 as its right boundary the shear rate is always close to zero and thus the fluid is Newtonian with $n_0 = 1$ (see (S-3)) such that the mathematically undefined situation of (S-70) with $R_{i-1} = 0$ is excluded.

S-1.7. Global analytical solution for a simplified CY model

In order to validate the algorithm presented above according to the procedure described in section 2 of the manuscript, we calculate a global mathematical solution to the Navier-Stokes equation (S-28), (1), for a simplified Carreau-Yasuda model. In the following, we derive an analytical solution for the flow profiles of a CY model (cf. (9)) with the following simplification:

$$\begin{aligned} \eta_\infty &= 0 \\ a_1 = a_2 &= 1 \end{aligned} \tag{S-75}$$

The viscosity as a function of the shear rate is therefore given as (cf. (8))

$$\tilde{\eta}\left(\dot{\gamma}\right) = \frac{\eta_0}{1 + K\dot{\gamma}} \quad . \tag{S-76}$$

Using the same assumptions as in section S-1.3.1, the NSE yields:

$$G = \frac{1}{r}\frac{\partial}{\partial r}\left(-r\frac{\eta_0\dot{\gamma}}{1 + K\dot{\gamma}}\right) \tag{S-77}$$

After a first integration and rearrangement of the equations one obtains

$$\dot{\gamma}\left(r\right) = \frac{-\frac{Gr}{2} - \frac{c_1}{r}}{\eta_0 + \frac{KGr}{2} + \frac{Kc_1}{r}} \tag{S-78}$$

and application of boundary condition (S-36) determines the integration constant as $c_1 = 0$. Therefore, the shear rate profile is given as:

$$\dot{\gamma}\left(r\right) = \frac{-\frac{Gr}{2}}{\eta_0 + \frac{KGr}{2}} = -\frac{1}{\frac{2\eta_0}{Gr} + K} \tag{S-79}$$

Inserting this result into (S-38) and integrating the resulting equation gives the velocity profile:

$$\begin{aligned} u\left(r\right) &= -\int \mathrm{d}r\, \dot{\gamma}\left(r\right) \\ &= \frac{r}{K} - \frac{2\eta_0}{GK^2}\ln\left(\frac{2\eta_0}{G} + Kr\right) + c_2 \end{aligned} \tag{S-80}$$

The second integration is easily found by applying the no-slip boundary condition (S-35). Thus, the velocity profile is given by:

$$u\left(r\right) = \frac{r - A}{K} + \frac{2\eta_0}{GK^2}\ln\left(\frac{\frac{2\eta_0}{G} + KA}{\frac{2\eta_0}{G} + Kr}\right) \tag{S-81}$$

S-1.8. Estimate of force and deformation experienced by flowing cells

In this section, we provide a simple approach to estimate the force sensed by a cell and its resulting deformation during printing.
Both quantities depend on the radial position r at which the cell transitions through the channel. Considering, in a first approximation, the cell as a sphere with radius R_c, the shear force acting on it is given by the surface integral of the shear stress over the sphere. Due to the linearity of the shear stress with the radial position, and as long the cell is small compared to the channel, the force is obtained as the product of the surface area and the shear stress at the radial position of the sphere center, as detailed next.
With the shear stress given in (S-73), the shear force acting on the cell is obtained as:

$$\begin{aligned} F_z &= \int_0^{2\pi}\int_0^{\pi} \sigma\left(R_{\text{surface}}\right) R_c^2 \sin\theta \,\mathrm{d}\theta \,\mathrm{d}\phi = 2\pi R_c^2 \int_0^{\pi} \sigma\left(r + R_c\cos\theta\right)\sin\theta \,\mathrm{d}\theta \\ &= 2\pi R_c^2 \left(-\frac{G}{2}\right)\left[\underbrace{\int_0^{\pi} r\sin\theta\,\mathrm{d}\theta}_{=2r} + \underbrace{\int_0^{\pi} R_c\cos\theta\sin\theta\,\mathrm{d}\theta}_{=0}\right] = 4\pi R_c^2\left(-\frac{G}{2}r\right) \\ &= A_{\text{cell}}\cdot\sigma\left(r\right) \end{aligned} \tag{S-82}$$

The result is depicted in figure S-1a.
Another critical quantity is the cell deformation, which can be approximated using the shear stress and the mechanical properties of the cell. As a rough estimate, we assume the cell to behave linearly elastic with the stress–strain relationship given as

$$\varepsilon\left(r\right) = \frac{\sigma\left(r\right)}{E} \quad , \tag{S-83}$$

where the strain ε quantifies the relative stretching of the cell. The Young's modulus E is chosen as 1 kPa to 10 kPa to cover the typical range of stiffness for cells [13]. This leads to significant deformations as shown in figure S-1b which reiterates the importance of hydrodynamic shear forces in bioprinting.

Figure S-1. (a) The force F acting on cells as radial function according to (S-82). (b) The strain according to (S-83) as a deformation measure for a linear elastic cell. The corresponding flow profile is shown in fig. 3. We note that the assumption of linear elasticity predicts relatively large deformations, which would not be the case for a more realistic, strain-hardening behavior.

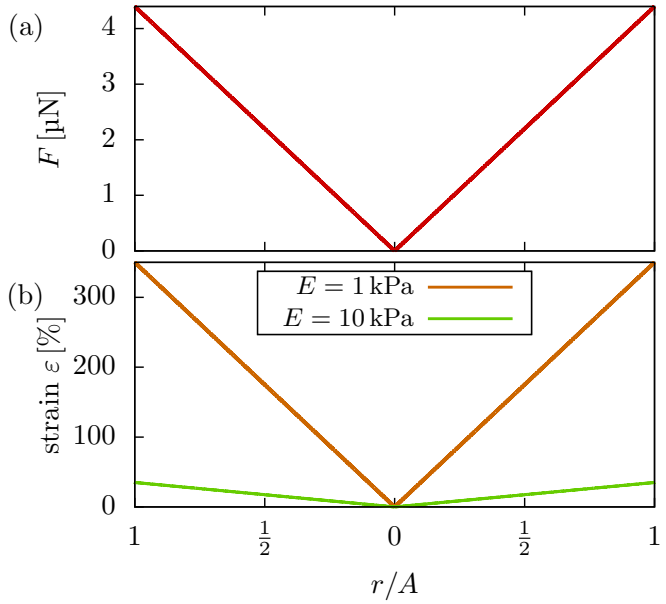

S-1.9. Inclusion of wall-slip effects

Wall-slip effects are sometimes reported, especially for fluids exhibiting non-Newtonian behavior [12] or highly hydrophobic channel coatings. The general approach to include a velocity slip at a wall is to allow for a finite tangential velocity at this point or, equivalently, to shift (in the calculations) the channel wall further outwards by a distance known as the slip length. It is thus straightforward to incorporate slip effects into our calculations if the slip length is known.
Alternatively, if the slip velocity next to the wall is known instead of the slip length, simply shifting upwards the computed no-slip velocity profile by a constant value represents a very good approximation. The shear rate would stay unchanged, and likewise the viscosity and the shear stress. Therefore, the inclusion of slip effects in our algorithm would be unproblematic.

S-2. Additional experimental validation of the algorithm

S-2.1. Additional experiments

In this section, we provide more validation to our algorithm with experimental measurements. Using the same approach as detailed in 2.3 of the manuscript, we performed velocity profile measurements of 2 % alginate at 100, 200, and 300 kPa, of 3 % alginate at 300, 400, and 500 kPa, and 3 % chitosan at 300, and 400 kPa. These measurements as well as the velocity profiles calculated using our Lattice Boltzmann method are depicted in figure S-2, showing good agreement. Since the pressure drop in the connectors and tubings is unknown but depends on the rheology of the hydrogel, we assume a constant pressure drop before the microchannel of 21 % for 2 % alginate, 10 % for 3 % alginate, and 23 % for 3 % chitosan, respectively. Additionally, we measured the flow profile of 3 % alginate in a rectangular microchannel with 1000 µm × 200 µm cross section. Due to limitations of the field of view of the microscope, less than one half of the channel could be focused during the measurements. In figure S-3, the mirrored experimentally measured velocity profile is shown in comparison to our Lattice Boltzmann calculations. Due to connectors and tubing with a diameter of approximately the size of the microchannel, the pressure drop of 48 % is reasonable.

S-2.2. Error quantification

In the following, we present an error calculation for the different flow experiments. First, we calculate an averaged velocity profile for the measurements as well as our calculations by averaging the data in a given d-interval. For the square channel, we choose a bin width of $d_{\mathrm{bin}} = 7.31\,\mu\mathrm{m}$ (corresponding to $N_{\mathrm{bins}} = 26$ bins in the range of $d = -95\,\mu\mathrm{m}$ to 95 µm), for the rectangular channel $d_{\mathrm{bin}} = 16.3\,\mu\mathrm{m}$ (corresponding to $N_{\mathrm{bins}} = 26$ bins

Figure S-2. Experimentally measured velocity profiles in a 190 µm × 190 µm microchannel in comparison to numerical results using the Lattice Boltzmann method. (a, c, e) 2 % alginate at 100, 200, and 300 kPa. (b, d, f) 3 % alginate at 300, 400, and 500 kPa. (g, h) 3 % chitosan at 300 and 400 kPa.

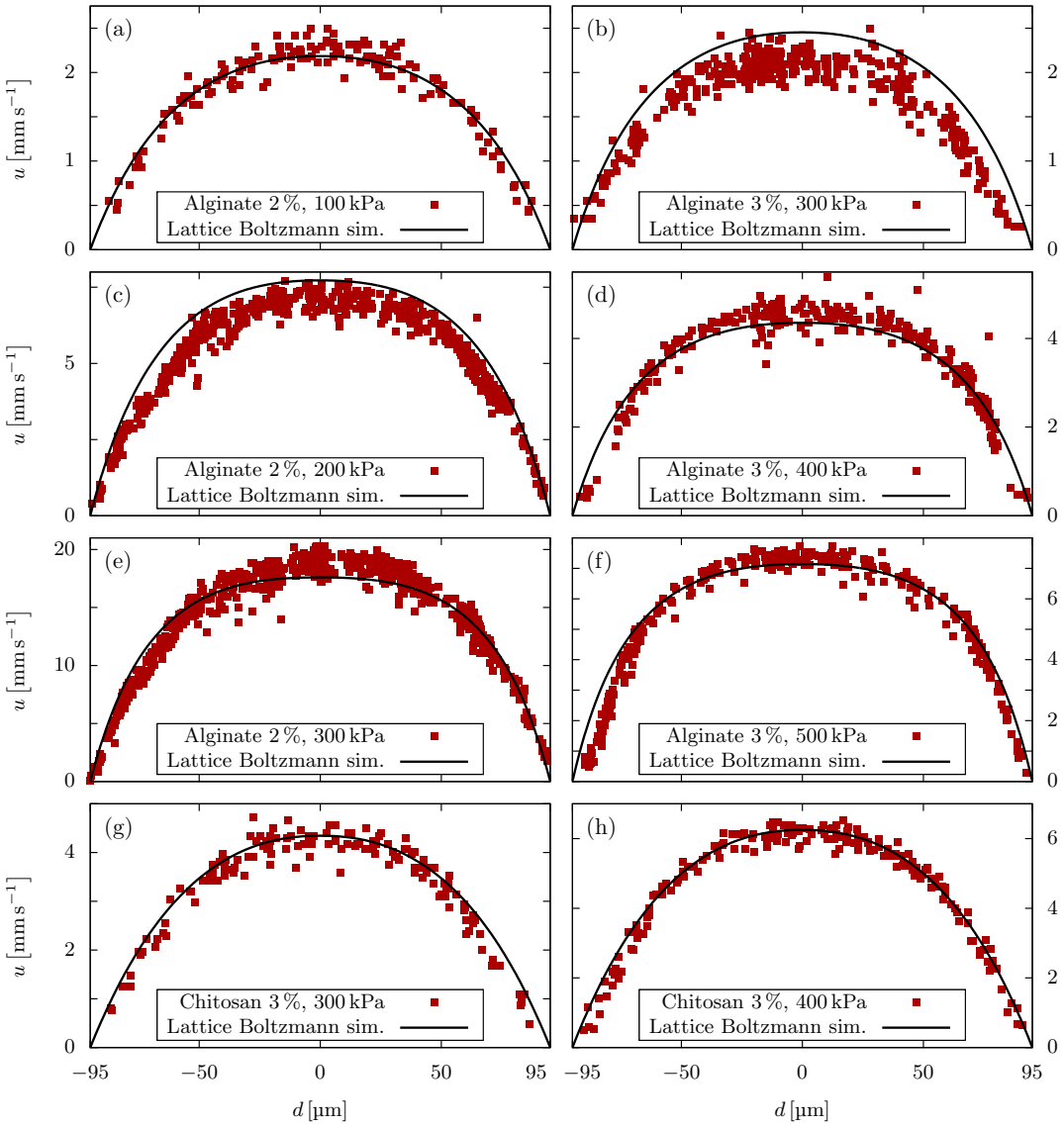

in the range of $d = 75\,\mu\text{m}$ to $500\,\mu\text{m}$). The average velocity in each bin is computed by

$$\overline{u}_i = \frac{1}{N_i} \sum_{k=1}^{N_i} u_k \quad , \tag{S-84}$$

Figure S-3. Experimentally measured velocity profiles of 3 % alginate at 400 and 500 kPa in a 1 mm × 200 µm microchannel in comparison to numerical results using the Lattice Boltzmann method. The experimental data is mirrored with respect to the channel center.

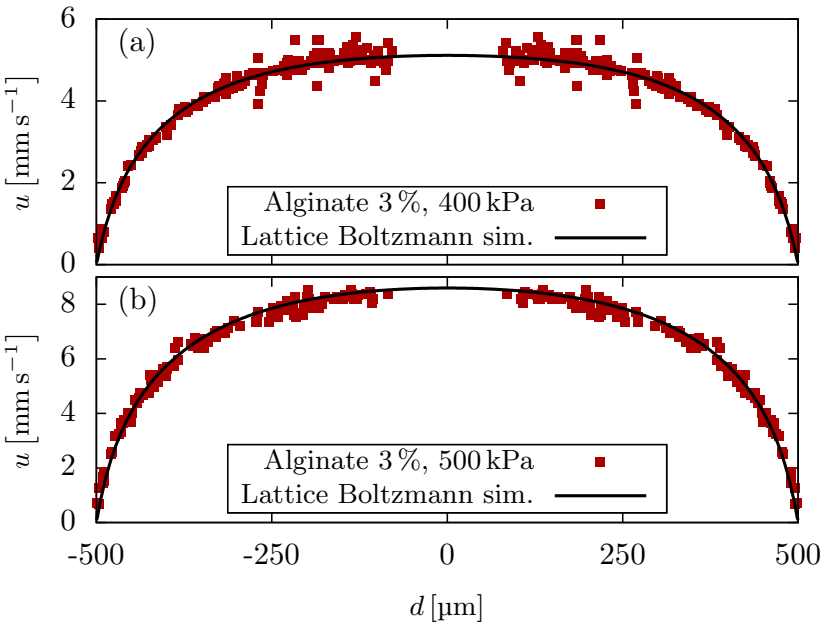

where N_i is the number of data points in the i-th bin. Using this approach, we additionally calculate the standard deviation of the data from the average value as

$$\sigma_{u,i} = \left(\frac{1}{N_i - 1} \sum_{k=1}^{N_i} (u_k - \overline{u}_i)^2 \right)^{\frac{1}{2}} \quad . \tag{S-85}$$

Using the averaged profiles, we calculate the relative error between measurement and Lattice Boltzmann computation as:

$$\epsilon = \left(\frac{1}{N_{\text{bins}}} \sum_{k=1}^{N_{\text{bins}}} \frac{\left(\overline{u}_k^{\text{Exp}} - \overline{u}_k^{\text{LB}} \right)^2}{\left(\overline{u}_{\text{max}}^{\text{LB}} \right)^2} \right)^{\frac{1}{2}} \tag{S-86}$$

The averaged profiles with a range of $\pm\sigma_{u,i}$ are shown in figure S-4 for the square microchannel and in figure S-5 for the rectangular microchannel, where we find relative errors in the range of $\epsilon = 3.3\,\%$ to $13.5\,\%$, and $\epsilon = 2\,\%$, respectively.

Figure S-4. Averaged profiles from figure S-2. The gray area indicates the range of one standard deviation from the mean curve. ϵ gives the relative error calculated according to (S-86).

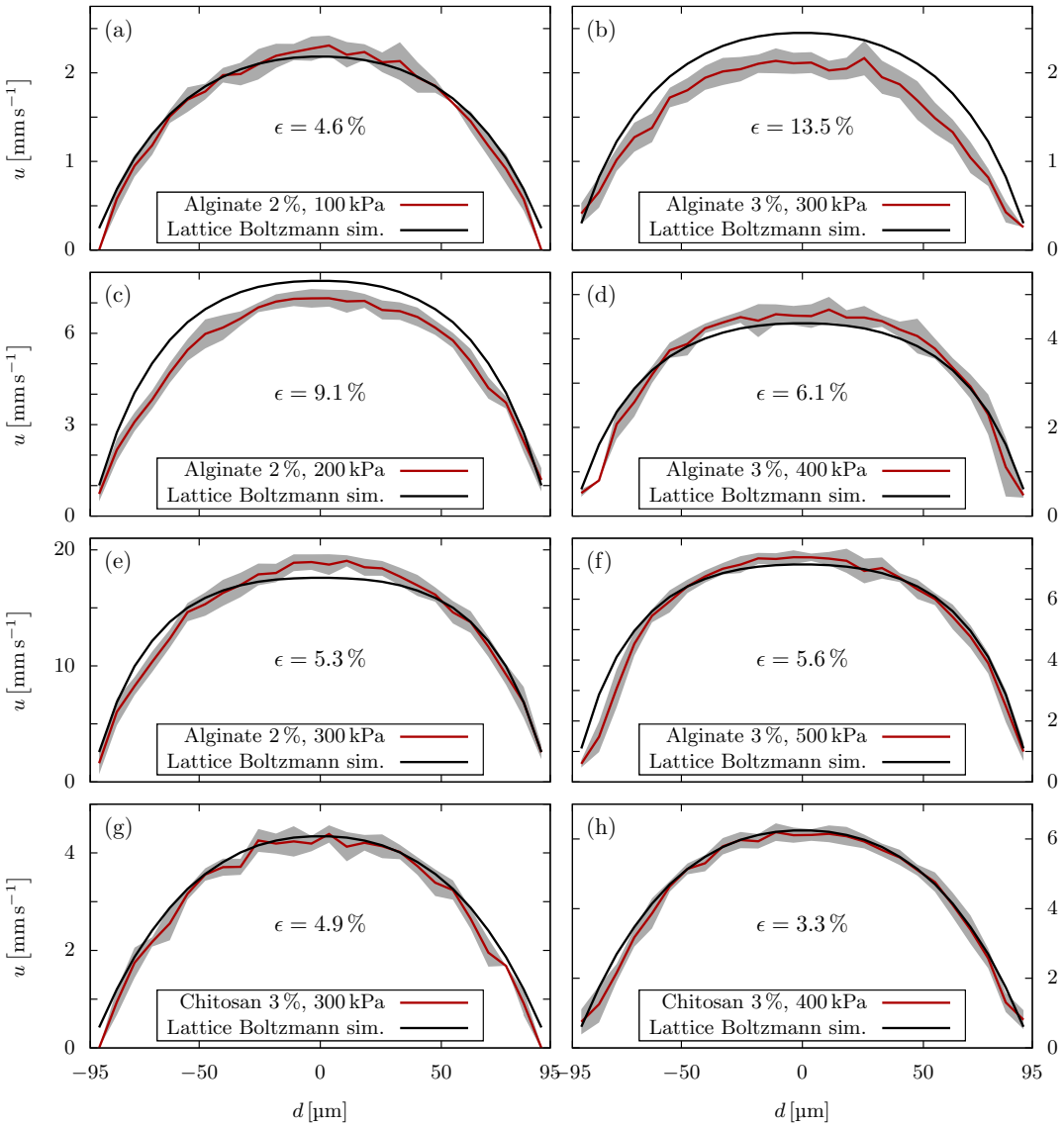

Figure S-5. Averaged profiles from figure S-3. The gray area indicates the range of one standard deviation from the mean curve. ϵ gives the relative error calculated according to (S-86).

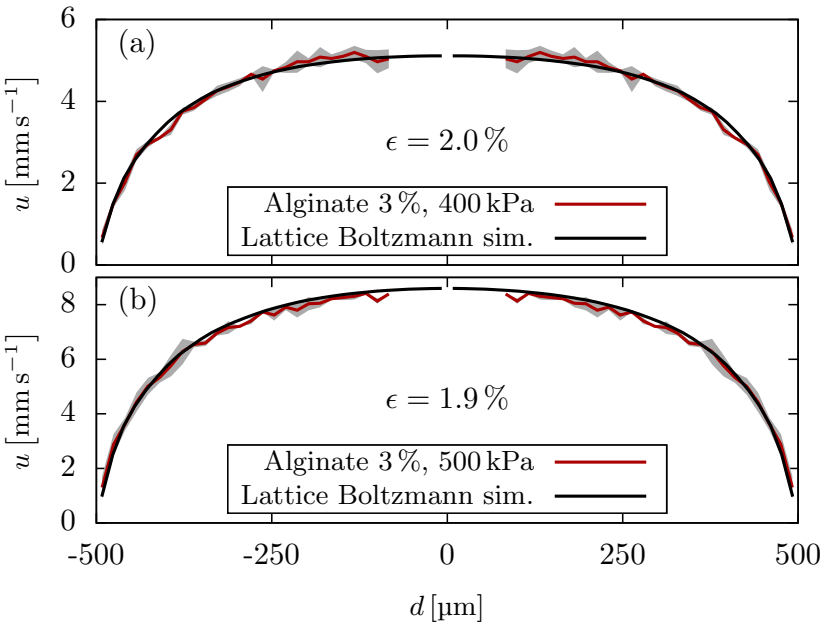

S-3. Computational procedure and user guide

This section describes the structure and usage of the Python classes, found in the Supplementary Material, that implement the presented algorithm for the Carreau-Yasuda model. The first part gives an overview of the four implemented Python classes. The second part provides a short user guide explaining how to use the classes for flow profile calculations. Note that their usage requires a Python (version 2 or 3) installation [14, 15]. The use of a Python IDE, e. g. Spyder [16], Thonny [17] or PyCharm [18], is optional but can be advantageous. The coloring in the code examples is the following: `blue` denotes classes, `green` denotes variables, and `gray` means a comment.
For the Carreau-Yasuda model [19] the viscosity is given by

$$\tilde{\eta}\left(\dot{\gamma}\right) = \tilde{\eta}_\infty + \frac{\tilde{\eta}_0 - \tilde{\eta}_\infty}{\left[1 + \left(K\dot{\gamma}\right)^{a_1}\right]^{\frac{a_2}{a_1}}} \quad , \tag{S-87}$$

where $\tilde{\eta}_0$ and $\tilde{\eta}_\infty$ are the viscosities in the limit of zero and infinite shear rates and K is a time constant with the unit s. Its inverse, $K^{-1} = \dot{\gamma}_c$, is sometimes referred to as *corner shear rate* and determines the transition to the zero-shear Newtonian plateau. The exponents a_1 and a_2 determine the shape of the transition between the zero-shear Newtonian plateau and the power-law region as well as the power-law behavior.

S-3.1. Overview of Python classes

The tool uses four classes that hold the input parameters, perform the calculations and save or plot output data. They can be found in the file `CYprofiles.py`. The four classes are:

(i) `Analytical_Viscosity()`: instances of this class hold the parameters of the Carreau-Yasuda model and can calculate the viscosity for a given shear rate according to (S-87).

(ii) `Interpolation()`: instances of this class perform the interpolation of a given `Analytical_Viscosity()` in a provided range of shear rates using the partitioning described in section S-1.2.

(iii) `Printing_Parameters()`: instances of this class hold the printing parameters, i.e. the nozzle radius and the pressure gradient or the flow rate.

(iv) `Profiles()`: instances of this class perform the calculation of the velocity, shear rate, and viscosity profile for given `Interpolation()` and `Printing_Parameters()` according to the presented algorithm. If a flow rate is provided, the corresponding pressure gradient is calculated iteratively to match the given flow rate.

S-3.2. User guide

This section is meant to serve as an explanatory tutorial for our Python tool. It will cover the two main steps necessary for calculating a flow profile: the viscosity

interpolation according to section S-1.2 and the profile calculation according to the presented algorithm. The following code examples can be found in the file `tutorial.py`.

Step 1 - Performing the interpolation Starting point for the viscosity interpolation is the Carreau-Yasuda model. After fitting rheological data, the values of its parameters in (S-87) are known. The `Analytical_Viscosity()` is then initialized by:

```
# initialize variables
eta0     =  1.0e2    ≙  η̃_0      [Pa s]
etainf   =  1.0e-3   ≙  η̃_∞      [Pa s]
K        =  1.0e-3   ≙  K        [s]
a1       =  0.3      ≙  a_1
a2       =  0.9      ≙  a_2

# initialize Analytical_Viscosity instance
analytical = Analytical_Viscosity( eta0=eta0, etainf=etainf,K=K,a1=a1,a2=a2 )
```

To perform the interpolation, the range of shear rates to interpolate and the number of (power-law) intervals is required:

```
# initialize variables
gamma0      =  1.0e-6   ≙  Γ̇_0       [s^-1]
gammaN      =  1.0e6    ≙  Γ̇_{N-1}   [s^-1]
Ninterpol   =  100      ≙  N − 1

# initialize Interpolation instance
interpol= Interpolation(gamma0=gamma0, gammaN=gammaN,
  Ninterpol=Ninterpol, analytical=analytical)
```

The calculation is then simply performed by executing

```
interpol.calculate_interpolation()
```

and the interpolation can be checked by plotting the calculated data via

```
interpol.plot_interpolation()
```

.

To save the viscosity interpolation, one can use

```
interpol.save_interpolation(file)
```

to save the data in viscosity-shear rate format and

```
interpol.save_interpolation_parameters(file)
```

to save the power-law parameters for all intervals in a file.

Step 2 - Calculating the flow profile Once the interpolation is completed, the next step is the definition of the printing parameters, i. e. the channel radius and the pressure gradient. This is done by:

```
# initialize variables
rchannel   =  1.0e-4  ≙  A   [m]
pgrad      =  -1.0e7  ≙  G   [Pa m^-1]

# initialize Printing_Parameters instance
printparams = Printing_Parameters(
  pressureGradient=pgrad, channelRadius=rchannel)
```

To calculate the radial profiles for the velocity (in $\mathrm{m\,s^{-1}}$), the shear rate (in $\mathrm{s^{-1}}$), and the viscosity (in $\mathrm{Pa\,s}$), the `Profiles()` class is initialized with printing parameters and an interpolation by

```
# initialize Profiles instance
fluidprofiles = Profiles(
  interpolation=interpol, printingParameters=printparams)
```

Finally, the calculation is performed by executing

```
fluidprofiles.calculate_profiles()
```

and the data can be plotted using the following methods:

```
fluidprofiles.plot_velocity()
fluidprofiles.plot_shearrate()
fluidprofiles.plot_shearstress()
fluidprofiles.plot_viscosity()
```

The data for all calculated fields is saved to a file with

```
fluidprofiles.save_profiles(file)
```

and

```
fluidprofiles.save_averages(file)
```

for the averaged quantities, respectively.
In the case of an imposed flow rate, i. e. if the pressure gradient is unknown, our tool automatically computes the corresponding pressure gradient necessary for the profile calculation. To do so, solely the initialization of the printing parameters changes as follows:

```
# initialize variables
rchannel   =  1.0e-4  ≙  A   [m]
flowrate   =  1.0e-9  ≙  Ω   [m^3 s^-1]
```

```
# initialize Printing_Parameters instance
printparams = Printing_Parameters(
  flowrate=flowrate, channelRadius=rchannel)
```

S-4. Lattice Boltzmann algorithm for generalized Newtonian fluids

This section briefly summarizes the Lattice Boltzmann method and the extension we added to the open-source package ESPResSo [20]. For an introduction into the Lattice Boltzmann method we refer the interested reader to the book by Krüger et al.[21]. The Lattice Boltzmann equation for the multiple relaxation time scheme used in ESPResSo reads:

$$f_i\left(\vec{x}+\vec{c}_i\Delta t, t+\Delta t\right) - f_i\left(\vec{x},t\right) = \sum_{j=0}^{18} \left(\underline{\underline{M}}^{-1}\underline{\underline{\omega}}\,\underline{\underline{M}}\right)_{ij}\left(f_j\left(\vec{x},t\right) - f_i^{\mathrm{eq}}\left(\vec{x},t\right)\right) \tag{S-88}$$

It describes the collision and streaming of the population distribution f_i $(i = 0, \ldots, 18)$ during one time step Δt. Here, $\vec{c}_i$ are the discretized lattice velocities, $\underline{\underline{M}}$ denotes transformation matrix that maps the populations onto moment space, $\underline{\underline{\omega}}$ is the diagonal relaxation frequency matrix, and f_i^{eq} denote the equilibrium population distributions. The relaxation frequency for the shear moments ω_{S} is related to the dynamic viscosity of the fluid via [22]

$$\eta = \varrho c_s^2\left(\frac{1}{\omega_{\mathrm{S}}} - \tfrac{1}{2}\right)\Delta t \quad , \tag{S-89}$$

with the fluid mass density ϱ and the lattice speed of sound c_s. The calculation of the viscosity according to the rheological model requires the local shear rate at each lattice node. Chai *et al* [22] showed that the local strain rate tensor can be obtained from the populations by

$$\varepsilon_{\alpha\beta} = -\frac{1}{2\varrho c_s^2\Delta t}\sum_{i,j=0}^{18}\left[\left(\vec{c}_i\right)_\alpha\left(\vec{c}_i\right)_\beta\left(\underline{\underline{M}}^{-1}\underline{\underline{\omega M}}\right)_{ij}\left(f_j\left(\vec{x},t\right) - f_i^{\mathrm{eq}}\left(\vec{x},t\right)\right)\right] \quad . \tag{S-90}$$

The shear rate is then obtained as invariant of the strain rate tensor according to (S-13). From the local shear rate, the viscosity according to the rheological model and the local relaxation time according to (S-89) are computed at each lattice node and updated in every time step.

In order to ensure simulation stability, we choose the time step globally according to Krüger *et al* [21, p. 273] as

$$\Delta t = c_s^2\left(\tau - \tfrac{1}{2}\right)\frac{\Delta x^2}{\nu^\star} = \frac{\Delta x^2}{6\nu^\star} \quad , \tag{S-91}$$

with $c_s^2 = \frac{1}{3}$, a global relaxation parameter $\tau = 1$, and a reference kinematic viscosity $\nu^\star$. The latter is provided, for instance, by the upper Newtonian viscosity plateau of

the corresponding CY model.
At the boundary of the cylindrical channel a bounce-back algorithm is applied to realize a no-slip boundary condition. The flow is driven by a pressure gradient along the z-direction, which is realized as external force density in the algorithm.

References

[1] Blaeser A, Duarte Campos D F, Puster U, Richtering W, Stevens M M and Fischer H 2015 *Advanced Healthcare Materials* **5** 326–333 ISSN 2192-2640

[2] Fu T, Carrier O, Funfschilling D, Ma Y and Li H Z 2016 *Chemical Engineering & Technology* **39** 987–992 ISSN 09307516 URL http://doi.wiley.com/10.1002/ceat.201500620

[3] Fyrippi I, Owen I and Escudier M 2004 *Flow Measurement and Instrumentation* **15** 131–138 ISSN 0955-5986

[4] Ning L, Betancourt N, Schreyer D J and Chen X 2018 *ACS Biomaterials Science & Engineering* **4** 3906–3918 ISSN 2373-9878, 2373-9878 URL http://pubs.acs.org/doi/10.1021/acsbiomaterials.8b00714

[5] Ruschak K J and Weinstein S J 2014 *Polymer Engineering & Science* **54** 2301–2309 ISSN 00323888 URL http://doi.wiley.com/10.1002/pen.23782

[6] Tian X Y, Li M G, Cao N, Li J W and Chen X B 2009 *Biofabrication* **1** 045005 ISSN 1758-5082

[7] Snyder J, Rin Son A, Hamid Q, Wang C, Lui Y and Sun W 2015 *Biofabrication* **7** 044106–17

[8] Escudier M, Gouldson I, Pereira A, Pinho F and Poole R 2001 *Journal of Non-Newtonian Fluid Mechanics* **97** 99–124 ISSN 03770257 URL http://linkinghub.elsevier.com/retrieve/pii/S0377025700001786

[9] Wu Q, Therriault D and Heuzey M C 2018 *ACS Biomaterials Science & Engineering* **4** 2643–2652 ISSN 2373-9878, 2373-9878 URL http://pubs.acs.org/doi/10.1021/acsbiomaterials.8b00415

[10] Batchelor G K 2000 *An Introduction to Fluid Dynamics* (Cambridge: Cambridge University Press) ISBN 978-0-511-80095-5 URL http://ebooks.cambridge.org/ref/id/CBO9780511800955

[11] Paxton N, Smolan W, Böck T, Melchels F, Groll J and Jüngst T 2017 *Biofabrication* **9** 044107 ISSN 1758-5090

[12] Sarker M and Chen X B 2017 *Journal of Manufacturing Science and Engineering* **139** 081002 ISSN 1087-1357, 1528-8935

[13] Yokokura T, Nakashima Y, Yonemoto Y, Hikichi Y and Nakanishi Y 2017 *International Journal of Engineering Science* **114** 41–48 ISSN 00207225

[14] Oliphant T E 2007 *Computing in Science & Engineering* **9** 10–20 ISSN 1521-9615

[15] 2019 Welcome to Python.org URL https://www.python.org/

[16] 2019 Spyder Website URL https://www.spyder-ide.org/

[17] 2019 Thonny, Python IDE for beginners URL https://thonny.org/

[18] 2019 PyCharm: the Python IDE for Professional Developers by JetBrains URL https://www.jetbrains.com/pycharm/

[19] Carreau P J 1972 *Transactions of the Society of Rheology* **16** 99–127 ISSN 0038-0032 URL http://sor.scitation.org/doi/10.1122/1.549276

[20] Limbach H, Arnold A, Mann B and Holm C 2006 *Computer Physics Communications* **174** 704–727 ISSN 00104655 URL https://linkinghub.elsevier.com/retrieve/pii/S001046550500576X

[21] Krüger T, Kusumaatmaja H, Kuzmin A, Shardt O, Silva G and Viggen E M 2017 *The Lattice Boltzmann Method* Graduate Texts in Physics (Cham: Springer International Publishing) ISBN 978-3-319-44647-9 978-3-319-44649-3 URL http://link.springer.com/10.1007/978-3-319-44649-3

[22] Chai Z, Shi B, Guo Z and Rong F 2011 *Journal of Non-Newtonian Fluid Mechanics* **166** 332–342 ISSN 03770257 URL https://linkinghub.elsevier.com/retrieve/pii/S0377025711000073

Publication 2

A hyperelastic model for simulating cells in flow

S. J. Müller, F. Weigl, C. Bezold, C. Bächer,
K. Albrecht, and S. Gekle

Biomechanics and Modeling in Mechanobiology **20**, 2021

DOI: 10.1007/s10237-020-01397-2

Biomechanics and Modeling in Mechanobiology (2021) 20:509–520
https://doi.org/10.1007/s10237-020-01397-2

ORIGINAL PAPER

A hyperelastic model for simulating cells in flow

Sebastian J. Müller[1] · Franziska Weigl[2] · Carina Bezold[1] · Christian Bächer[1] · Krystyna Albrecht[2] · Stephan Gekle[1]

Received: 12 February 2020 / Accepted: 14 October 2020 / Published online: 20 November 2020

Abstract
In the emerging field of 3D bioprinting, cell damage due to large deformations is considered a main cause for cell death and loss of functionality inside the printed construct. Those deformations, in turn, strongly depend on the mechano-elastic response of the cell to the hydrodynamic stresses experienced during printing. In this work, we present a numerical model to simulate the deformation of biological cells in arbitrary three-dimensional flows. We consider cells as an elastic continuum according to the hyperelastic Mooney–Rivlin model. We then employ force calculations on a tetrahedralized volume mesh. To calibrate our model, we perform a series of FluidFM® compression experiments with REF52 cells demonstrating that all three parameters of the Mooney–Rivlin model are required for a good description of the experimental data at very large deformations up to 80%. In addition, we validate the model by comparing to previous AFM experiments on bovine endothelial cells and artificial hydrogel particles. To investigate cell deformation in flow, we incorporate our model into Lattice Boltzmann simulations via an Immersed-Boundary algorithm. In linear shear flows, our model shows excellent agreement with analytical calculations and previous simulation data.

Keywords Hyperelasticity · Cell deformation · Mooney–Rivlin · Atomic force microscopy · Shear flow · Lattice-Boltzmann

1 Introduction

The dynamic behavior of flowing cells is central to the functioning of organisms and forms the base for a variety of biomedical applications. Technological systems that make use of the elastic behavior of cells are, for example, cell sorting (Shen et al. 2019), real-time deformability cytometry (Otto et al. 2015; Fregin et al. 2019) or probing techniques for cytoskeletal mechanics (Kollmannsberger and Fabry 2011; Gonzalez-Cruz et al. 2012; Huber et al. 2013; Bongiorno et al. 2014; Fischer-Friedrich et al. 2014; Lange et al. 2015; Fischer-Friedrich et al. 2016; Nyberg et al. 2017; Lange et al. 2017; Kubitschke et al. 2017; Jaiswal et al. 2017; Mulla et al. 2019). In most, but not all, of these applications, cell deformations typically remain rather small. A specific example where large deformations become important is 3D bioprinting. Bioprinting is a technology which, analogously to common 3D printing, pushes a suspension of cells in highly viscous hydrogels—so-called bioink—through a fine nozzle to create three-dimensional tissue structures. A major challenge in this process lies in the control of large cell deformations and cell damage during printing. Those deformations arise from hydrodynamic stresses in the printer nozzle and ultimately affect the viability and functionality of the cells in the printed construct (Snyder et al. 2015; Blaeser et al. 2015; Zhao et al. 2015; Paxton et al. 2017; Müller et al. 2020). How exactly these hydrodynamic forces correlate with cell deformation, however, strongly depends on the elastic behavior of the cell and its interaction with the flowing liquid. Theoretical and computational modeling efforts in this area have thus far been restricted to pure fluid simulations without actually incorporating the cells (Khalil and Sun 2007; Aguado et al. 2012; Blaeser et al. 2015) or

Electronic supplementary material The online version of this article (https://doi.org/10.1007/s10237-020-01397-2) contains supplementary material, which is available to authorized users.

✉ Sebastian J. Müller
sjmueller@uni-bayreuth.de

Stephan Gekle
stephan.gekle@uni-bayreuth.de

[1] Theoretical Physics VI, Biofluid Simulation and Modeling, University of Bayreuth, Universitätsstraße 30, Bayreuth 95440, Germany

[2] Department of Functional Materials in Medicine and Dentistry and Bavarian Polymer Institute (BPI), University of Würzburg, Pleicherwall 2, Würzburg 97070, Germany

simple 2D geometries (Tirella et al. 2011; Li et al. 2015). The complexity of cell mechanics and the diversity of possible applications make theoretical modeling of cell mechanics in flow a challenge which, to start with, requires reliable experimental data for large cell deformations.

The most appropriate tool to measure cellular response at large deformations is atomic force microscopy (AFM) (Lulevich et al. 2003; Lulevich et al. 2006; Ladjal et al. 2009; Kiss 2011; Fischer-Friedrich et al. 2014; Hecht et al. 2015; Ghaemi et al. 2016; Sancho et al. 2017; Efremov et al. 2017; Ladjal et al. 2018; Chim et al. 2018). AFM cantilevers with pyramidal tips, colloidal probes, or flat geometries are used to indent or compress cells. Therefore, a common approach to characterize the elasticity of cells utilizes the Hertzian theory, which describes the contact between two linear elastic solids [(Johnson 2003), p. 90–104], but is limited to the range of small deformations (Dintwa et al. 2008). Experimental measurements with medium-to-large deformations typically show significant deviations from the Hertz prediction, e.g., for cells or hydrogel particles (Neubauer et al. 2019). Instead of linear elasticity, a suitable description of cell mechanics for bioprinting applications requires more advanced hyperelastic material properties. While for simple anucleate fluid-filled cells such as, e.g., red blood cells, theoretical models abound (Freund 2014; Závodszky et al. 2017; Mauer et al. 2018; Guckenberger et al. 2018; Kotsalos et al. 2019), the availability of models for cells including a complex cytoskeleton is rather limited. In axisymmetric geometries, Caille et al. (2002) and Mokbel et al. (2017) used an axisymmetric finite element model with neo-Hookean hyperelasticity to model AFM and microchannel experiments on biological cells. In shear flow, approximate analytical treatments are possible (Roscoe 1967; Gao and Hu 2009; Gao et al. 2011; Gao et al. 2012). Computationally, Gao and Hu (2009) carried out 2D simulations while in 3D Lykov et al. (2017) utilized a DPD technique based on a bead-spring model. Furthermore, Villone et al. (2014, 2015) presented an arbitrary Lagrangian-Eulerian approach for elastic particles in viscoelastic fluids. Finally, Rosti et al. (2018) and Saadat et al. (2018) considered viscoelastic and neo-Hookean finite element models, respectively, in shear flow.

In this work, we introduce and calibrate a computational model for fully three-dimensional simulations of cells in arbitrary flows. Our approach uses a Lattice-Boltzmann solver for the fluid and a direct force formulation for the elastic equations. In contrast to earlier works (Caille et al. 2002; Gao et al. 2011; Mokbel et al. 2017; Rosti et al. 2018; Saadat et al. 2018), our model uses a three-parameter Mooney–Rivlin elastic energy functional. To demonstrate the need for this more complex elastic model, we carry out extensive FluidFM® indentation experiments for REF52 (rat embryonic fibroblast) cells at large deformation up to 80% (Alexandrova et al. 2008). In addition, our model compares favorably with previous AFM experiments on bovine endothelial cells (Caille et al. 2002) as well as artificial hydrogel particles (Neubauer et al. 2019). Our model provides a much more realistic force-deformation behavior compared to the small-deformation Hertz approximation, but is still simple and fast enough to allow the simulation of dense cell suspensions in reasonable time. Particularly, our approach is less computationally demanding than conventional finite-element methods which usually require large matrix operations. Furthermore, it is easily extensible and allows, e.g., the inclusion of a cell nucleus by the choice of different elastic moduli for different parts of the volume.

We finally present simulations of our cell model in different flow scenarios using an Immersed-Boundary algorithm to couple our model with Lattice Boltzmann fluid calculations. In a plane Couette (linear shear) flow, we investigate the shear stress dependency of single cell deformation, which we compare to the average cell deformation in suspensions with higher volume fractions and show that our results in the neo-Hookean limit are in accordance with earlier elastic cell models (Gao et al. 2011; Rosti et al. 2018; Saadat et al. 2018).

2 Theory

In general, hyperelastic models are used to describe materials that respond elastically to large deformations [(Bower 2010), p. 93]. Many cell types can be subjected to large reversible shape changes. This section provides a brief overview of the hyperelastic Mooney–Rivlin model implemented in this work.

The displacement of a point is given by

$$u_i = y_i - x_i\,, \tag{1}$$

where x_i ($i = 1, 2, 3$) refers to the undeformed configuration (material frame) and y_i to the deformed coordinates (spatial frame). We define the deformation gradient tensor and its inverse as [(Bower 2010), p. 14, 18]

$$\mathsf{F}_{ij} = \frac{\partial y_i}{\partial x_j} = \frac{\partial u_i}{\partial x_j} + \delta_{ij} \quad \text{and} \quad \mathsf{F}^{-1}_{ij} = \frac{\partial x_i}{\partial y_j}\,. \tag{2}$$

Together with the right Cauchy-Green deformation tensor, $\mathsf{C} = \mathsf{F}^{\mathsf{T}}\mathsf{F}$ (material description), we can define the following invariants which are needed for the strain energy density calculation below:

$$J = \det \mathsf{F} \tag{3}$$

$$I = T_{\mathsf{C}} J^{-2/3} \tag{4}$$

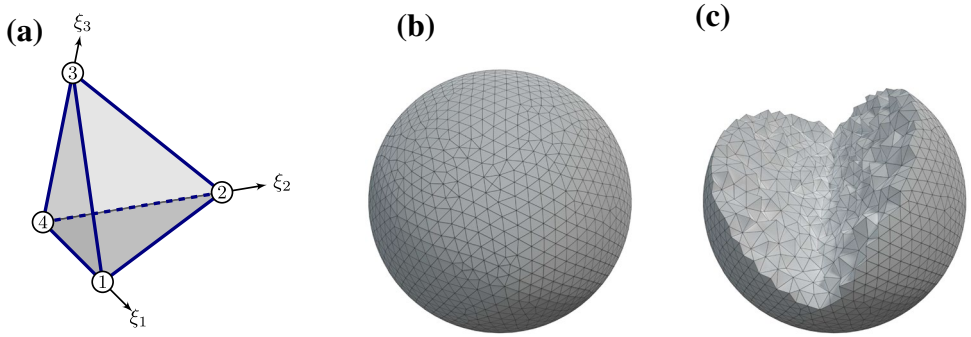

Fig. 1 **a** The four noded tetrahedron as mesh element within a local dimensionless coordinate system $\{\xi_1, \xi_2, \xi_3\}$. **b** The spherical cell model with its triangulated surface. **c** Its inner tetrahedralized mesh

$$K = \tfrac{1}{2}\left(T_{\mathsf{C}}^2 - T_{\mathsf{C}^2}\right) J^{-4/3} \tag{5}$$

Here,

$$T_{\mathsf{C}} = \operatorname{tr}\mathsf{C} \quad \text{and} \quad T_{\mathsf{C}^2} = \operatorname{tr}\left(\mathsf{C}^2\right) \tag{6}$$

are the trace of the right Cauchy-Green deformation tensor and its square, respectively. The nonlinear strain energy density of the Mooney–Rivlin model is given by (Mooney 1940; Rivlin 1948)

$$U = \left[\frac{\mu_1}{2}(I-3) + \frac{\mu_2}{2}(K-3) + \frac{\kappa}{2}(J-1)^2\right], \tag{7}$$

where μ_1, μ_2, and κ are material properties. They correspond—for consistency with linear elasticity in the range of small deformations—to the shear modulus $\mu = \mu_1 + \mu_2$ and bulk modulus κ of the material and are therefore related to the Young's modulus E and the Poisson ratio ν via [(Bower 2010), p. 74]

$$\mu = \frac{E}{2(1+\nu)} \quad \text{and} \quad \kappa = \frac{E}{3(1-2\nu)}. \tag{8}$$

Through the choice $\mu_2 = 0$ in (7), we recover the simpler and frequently used (Gao et al. 2011; Saadat et al. 2018) neo-Hookean strain energy density:

$$U_{\mathrm{NH}} = \left[\frac{\mu}{2}(I-3) + \frac{\kappa}{2}(J-1)^2\right] \tag{9}$$

As we show later, this can be a sufficient description for some cell types. To control the strength of the second term and quickly switch between neo-Hookean and Mooney–Rivlin strain energy density calculation, we introduce a factor $w \in [0,1]$ and set

$$\mu_1 = w\mu \quad \text{and} \quad \mu_2 = (1-w)\mu \tag{10}$$

such that $w = 1$, which equals setting $\mu_2 = 0$ in (7), corresponds to the purely neo-Hookean description in (9), while $w < 1$ increases the influence of the μ_2-term and thus leads to a more pronounced strain hardening as shown in figure S-6 of the Supporting Information.

3 Tetrahedralized cell model

In this section, we apply the hyperelastic theory of Sect. 2 to a tetrahedralized mesh as shown in Fig. 1.

3.1 Calculation of elastic forces

We consider a mesh consisting of tetrahedral elements as depicted in Fig. 1. The superscript α refers to the four vertices of the tetrahedron. The elastic force acting on vertex α in direction i is obtained from (7) by differentiating the strain energy density U with respect to the vertex displacement as

$$f_i^\alpha = -V_0 \frac{\partial U}{\partial u_i^\alpha}, \tag{11}$$

where V_0 is the reference volume of the tetrahedron. In contrast to Saadat et al. (2018), the numerical calculation of the force in our model does not rely on the integration of the stress tensor, but on a differentiation where the calculation of all resulting terms involves only simple arithmetics. Applying the chain rule for differentiation yields:

$$\begin{aligned} f_i^\alpha = -V_0 \Bigg[& \left(\frac{\partial U}{\partial I}\frac{\partial I}{\partial T_{\mathsf{C}}} + \frac{\partial U}{\partial K}\frac{\partial K}{\partial T_{\mathsf{C}}}\right)\frac{\partial T_{\mathsf{C}}}{\partial \mathsf{F}_{kl}} \\ & + \left(\frac{\partial U}{\partial I}\frac{\partial I}{\partial J} + \frac{\partial U}{\partial K}\frac{\partial K}{\partial J} + \frac{\partial U}{\partial J}\right)\frac{\partial J}{\partial \mathsf{F}_{kl}} \\ & + \frac{\partial U}{\partial K}\frac{\partial K}{\partial T_{\mathsf{C}^2}}\frac{\partial T_{\mathsf{C}^2}}{\partial \mathsf{F}_{kl}}\Bigg]\frac{\partial \mathsf{F}_{kl}}{\partial u_i^\alpha} \end{aligned} \tag{12}$$

The evaluation of (12) requires the calculation of the deformation gradient tensor F, which is achieved by linear interpolation of the coordinates and displacements inside each tetrahedral mesh element as detailed in the next section. We note that our elastic force calculation is purely local making it straightforward to employ different elastic models in different regions of the cell and/or to combine it with elastic shell models. This flexibility can be used to describe, e.g., the cell nucleus (Caille et al. 2002) or an actin cortex (Bächer and Gekle 2019) surrounding the cell interior.

3.2 Interpolation of the displacement field

Following standard methods, e.g., Bower (2010), we start by interpolating a point x_i inside a single tetrahedron using the vertex positions x_i^α ($\alpha = 1, 2, 3, 4$). The interpolation uses an inscribed, dimensionless coordinate system, denoted by (ξ_1, ξ_2, ξ_3) with $0 \leq \xi_i \leq 1$[1], as depicted in Fig. 1a. One vertex defines the origin while the remaining three indicate the coordinate axes. A set of shape functions, i.e., interpolation functions, $N^\alpha(\xi_1, \xi_2, \xi_3)$ is employed to interpolate positions inside the tetrahedron volume. An arbitrary point x_i inside the element is interpolated as

$$x_i = \sum_{\alpha=1}^{4} N^\alpha(\xi_1, \xi_2, \xi_3) x_i^\alpha \,, \tag{13}$$

where the shape functions are defined as [(Bower 2010), p. 483]:

$$N^1(\xi_1, \xi_2, \xi_3) = \xi_1 \tag{14}$$

$$N^2(\xi_1, \xi_2, \xi_3) = \xi_2 \tag{15}$$

$$N^3(\xi_1, \xi_2, \xi_3) = \xi_3 \tag{16}$$

$$N^4(\xi_1, \xi_2, \xi_3) = 1 - \xi_1 - \xi_2 - \xi_3 \tag{17}$$

According to (1), the displacement of vertex α in i-direction is given by

$$u_i^\alpha = y_i^\alpha - x_i^\alpha \,. \tag{18}$$

Therefore similar to (13), the displacement at an arbitrary point in the volume can also be expressed in terms of the shape functions and the vertex displacements as

$$u_i = \sum_{\alpha=1}^{4} N^\alpha(\xi_1, \xi_2, \xi_3) u_i^\alpha \,. \tag{19}$$

The calculation of the deformation gradient tensor according to (2) requires the spatial derivative of the displacement:

$$\mathsf{F}_{ij} - \delta_{ij} = \frac{\partial u_i}{\partial x_j} = \frac{\partial u_i}{\partial \xi_k} \frac{\partial \xi_k}{\partial x_j} = \mathsf{A}_{ik} \mathsf{B}_{kj} \tag{20}$$

By inserting (19) into (20) and evaluating the shape functions, the components of the matrix A are easily determined to be the difference of the displacements between the origin (vertex 4) and the remaining vertices 1, 2 and 3:

$$\mathsf{A}_{ik} = u_i^k - u_i^4 \tag{21}$$

Note that due to the linear interpolation A_{ik} is constant inside a given tetrahedron. The matrix $\mathsf{B} = \mathsf{J}^{-1}$ is the inverse of the Jacobian matrix, obtained similarly to (21) as

$$\mathsf{J}_{ik} = \frac{\partial x_i}{\partial \xi_k} = x_i^k - x_i^4 \,. \tag{22}$$

Since x_i refers to the reference coordinates, the calculation of the matrices J and B has to be performed only once at the beginning of a simulation. With the interpolation of the displacement in each tetrahedron, we can write all derivatives occurring in (12), as listed in the following:

$$\begin{aligned}
\frac{\partial U}{\partial I} &= \frac{\mu_1}{2} & \frac{\partial I}{\partial T_\mathsf{C}} &= J^{-\frac{2}{3}} \\
\frac{\partial U}{\partial K} &= \frac{\mu_2}{2} & \frac{\partial K}{\partial T_\mathsf{C}} &= T_\mathsf{C} J^{-\frac{4}{3}} \\
\frac{\partial T_\mathsf{C}}{\partial \mathsf{F}_{il}} &= 2\mathsf{F}_{il} & \frac{\partial I}{\partial J} &= -\frac{2}{3} T_\mathsf{C} J^{-\frac{5}{3}} \\
\frac{\partial K}{\partial J} &= -\frac{2}{3}\left(T_\mathsf{C}^2 - T_{\mathsf{C}^2}\right) J^{-\frac{7}{3}} & \frac{\partial U}{\partial J} &= \kappa(J-1) \\
\frac{\partial J}{\partial \mathsf{F}_{il}} &= J\mathsf{F}_{li}^{-1} & \frac{\partial K}{\partial T_{\mathsf{C}^2}} &= -\frac{1}{2} J^{-\frac{4}{3}} \\
\frac{\partial T_{\mathsf{C}^2}}{\partial \mathsf{F}_{il}} &= 4\mathsf{F}_{ik}\mathsf{C}_{kl} & \frac{\partial \mathsf{F}_{kl}}{\partial u_i^\alpha} &= \delta_{ki}\mathsf{B}_{ml}\left(\delta_{m\alpha} - \delta_{4\alpha}\right)
\end{aligned}$$

3.3 Taylor deformation parameter

As a measure for the cell deformation, we use the Taylor deformation parameter (Ramanujan and Pozrikidis 1998; Clausen and Aidun 2010; Guckenberger et al. 2016; Saadat et al. 2018)

$$D = \frac{a_3 - a_1}{a_3 + a_1} \,, \tag{23}$$

[1] (Bower 2010), p. 481, 483] erroneously states a range of $-1 \leq \xi_i \leq 1$ for the tetrahedral element.

where a_1 and a_3 are, respectively, the minor and major semi-axis of an ellipsoid corresponding to the inertia tensor of the cell. The Taylor deformation is a good measure for approximately elliptic cell deformations, as they occur in shear flow (cf. Sect. 6).

To calculate D, first the components of the inertia tensor

$$\Theta_{ij} = \int_V x_k x_k \delta_{ij} - x_i x_j \mathrm{d}V\,, \tag{24}$$

where $\mathbf{x}$ is a vector inside the volume V, are calculated using our discretized cell with N_{tet} tetrahedra as

$$\Theta_{ij} = \sum_{l=1}^{N_{\text{tet}}} V_l \left(r_k^l r_k^l \delta_{ij} - r_i^l r_j^l \right). \tag{25}$$

The vector $\mathbf{r}^l$ denotes the center of mass of the l^{th} tetrahedron and V_l is its current volume. The eigenvalues $\theta_1 > \theta_2 > \theta_3$ of Θ can be used to fit the semi axes $a_1 < a_2 < a_3$ of the corresponding ellipsoid:

$$\begin{aligned} a_1 &= \frac{5}{2M}\left(-\theta_1 + \theta_2 + \theta_3\right) \\ a_2 &= \frac{5}{2M}\left(\theta_1 - \theta_2 + \theta_3\right) \\ a_3 &= \frac{5}{2M}\left(\theta_1 + \theta_2 - \theta_3\right) \end{aligned} \tag{26}$$

The prefactor contains the mass M of the ellipsoid (considering uniform mass density) and drops out in the calculation of D.

4 Comparison of the numerical model to FluidFM® measurements on REF52 cells

In this section, we validate compression simulations of our cell model with FluidFM® compression experiments of REF52 cells stably expressing paxillin-YFP (Alexandrova et al. 2008). These experiments provide as an output the required force to produce a certain deformation of the cell, which can be directly compared to our model. We start with a detailed description of the experiments and show the suitability of our model to describe the elastic behavior of REF52 cells afterwards.

4.1 FluidFM® indentation measurements

We perform a series of compression measurements of REF52 cells with a Flex FPM (Nanosurf GmbH, Germany) system that combines the AFM with the FluidFM® technology (Cytosurge AG, Switzerland). In contrast to conventional AFM techniques, FluidFM® uses flat cantilevers that possess a microchannel connected to a pressure system. By applying a suction pressure, cells can be aspirated and retained at the aperture of the cantilever's tip. A more detailed description of the setup and its functionality is already reported in Sancho et al. (2017). All experiments are based on a cantilever with an aperture of 8 μm diameter and a nominal spring constant of 2Nm^{-1}. In order to measure the cellular deformation, a cell was sucked onto the tip and compressed between the cantilever and the substrate until a setpoint of 100nN was reached. Immediately before the experiment, the cells were detached by using Accutase (Sigma Aldrich) and were therefore in suspension at the time of indentation. In this way, it can be ensured that only a single cell is deformed during each measurement.

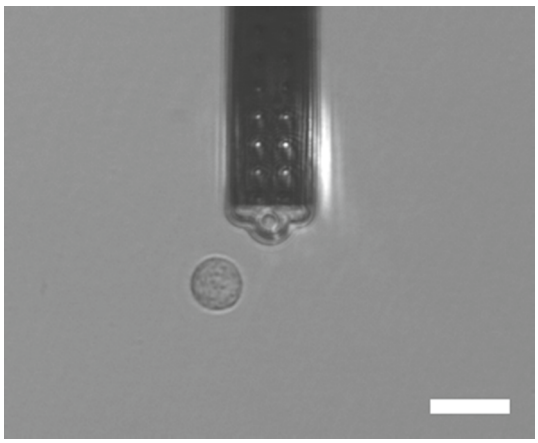

Fig. 2 Example micrograph showing the FluidFM® cantilever and a cell viewed from the top. Scale bar is 30μm

An example micrograph of the experiment before compression is shown in Fig. 2. Analogously to AFM, primary data in form of cantilever position (in m) and deflection (in V) has to be converted to force and deformation through the deflection sensitivity (in m V^{-1}) and the cantilevers' spring constant. The cellular deformation further requires the determination of the contact point, which we choose as the cantilever position where the measured force starts to increase. The undeformed cell size is obtained as mean from a horizontal and vertical diameter measurement using the software imageJ.

4.2 Simulation setup

The experimental setup of the previous section is easily transferred and implemented for our cell model: The undeformed spherical cell rests on a fixed plate while a second plate approaches from above to compress the cell as depicted in Fig. 3a and b. In Sect. 5.2, we will also use a slightly modified version where a sphere indents the cell as shown

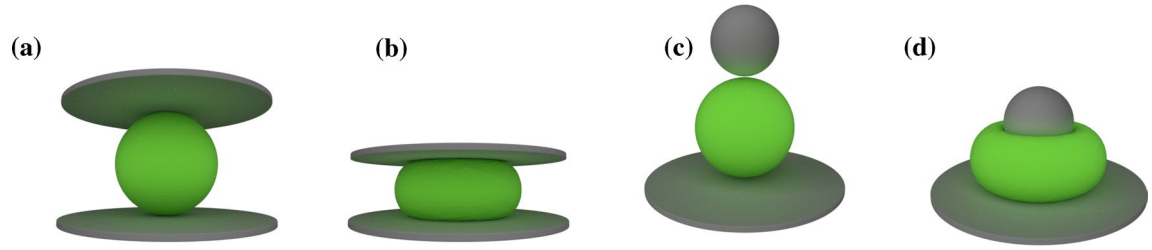

Fig. 3 **a** and **b** Cell compression simulations: The cell is compressed between a lower, resting, and an upper, moving, plate. **c** and **d** Colloidal probe cell indentation simulations: The cell rests on a plate, while being indented with a sphere

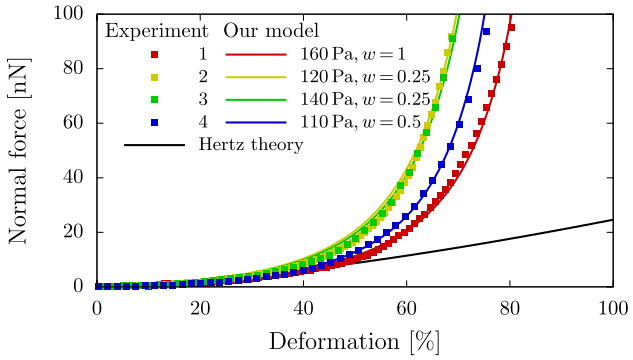

Fig. 4 Our numerical model in comparison to our FluidFM® measurements on REF52 cells. The labels give the two fit parameters E and w. We find Young's moduli in the range of 110Pa to 160Pa. The Hertz theory is shown for a Young's modulus of 180Pa

in Fig. 3c and d. A repulsive force prevents the cell vertices from penetrating the plates or the spherical indenter. The elastic restoring forces (cf. Sect. 3) acting against this imposed compression are transmitted throughout the whole mesh, deforming the cell.

We use meshes consisting of 2000 to 5000 vertices and about 10000 to 30000 tetrahedra to build up a spherical structure. More details of the mesh and its generation (Sect. S-2.4) as well as the algorithm (Sect. S-3) are provided in the SI.

4.3 Results

In our FluidFM® experiment series with REF52 cells, the cell radii lie between 7.1μm and 10.4μm with an overall average of 8.6±0.7μm. In Fig. 4, we depict the force as function of the non-dimensionalized deformation, i.e., the absolute compression divided by the cell diameter. The experimental data curves share general characteristics: The force increases slowly in the range of small deformations up to roughly 40%, while a rapidly increasing force is observed for larger deformations. Although the variation of the cell radius in the different measurements is already taken into account in the deformation, the point of the force upturn differs significantly which indicates a certain variability in the elastic parameters of the individual cells.

We use the compression simulation setup as detailed in Sect. 4.2 to calculate force-deformation curves of our cell model. The Poisson ratio is chosen as $\nu = 0.48$. In section S-2.7 of the Supporting Information, we show that variations of ν do not strongly affect the results. A best fit approach is used to determine the Young's modulus and the ratio of shear moduli w and leads to very good agreement between model prediction and experimental data as shown in Fig. 4 as well as section S-1 of the SI. While the general range of force values is controlled using the Young's modulus, the Mooney–Rivlin ratio w especially defines the point of the force upturn. We find Young's moduli in the range 110Pa to 160Pa and $w = 0.25$, 0.5, and 1. For very small deformations, our hyperelastic model produces the same results as would be expected from a linear elastic model according to the Hertz theory. See the SI (section S-2.5) for further details on the calculation of the force-deformation according to the Hertzian theory. For large deformations, the force rapidly increases due to its nonlinear character, showing strain-hardening behavior and huge deviations from the Hertz theory. Overall, we find an excellent match between simulation and our FluidFM® measurements with REF52 cells.

5 Comparison of our numerical model to other micromechanical setups

In this section, we compare our simulations to axisymmetric calculations using the commercial software Abaqus and validate our cell model with further experimental data for bovine endothelial cells from (Caille et al. 2002) and very recent data for hydrogel particles from (Neubauer et al. 2019).

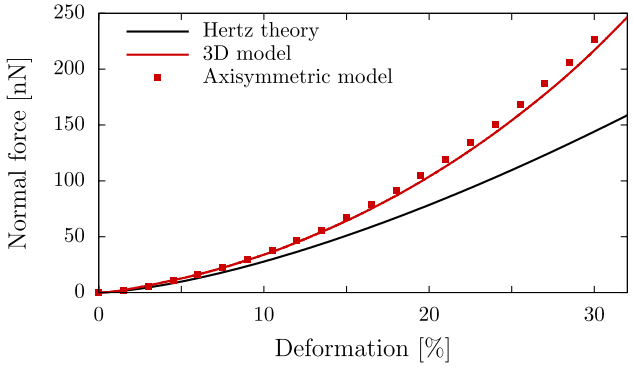

Fig. 5 Comparison of force-deformation curves obtained from our model (red line) with the linear elastic Hertz theory (black line) and the two-dimensional simulation with Abaqus (red squares), showing good agreement between our three-dimensional and the axisymmetric model

5.1 Validation with axisymmetric simulations

To validate our model numerically, we compare our simulated force—deformation curves to calculations using the commercial software Abaqus (Smith 2009) (version 6.14).

In Abaqus, we use a rotationally symmetric setup consisting of a two-dimensional semicircle, which is compressed between two planes, similar to our simulation setup in Sect. 4.2 and the finite element model utilized in (Caille et al. 2002). The semicircle has a radius $r = 15\mu m$, a Young's modulus of $E = 2.25kPa$ and a Poisson ratio of $\nu = 0.48$. We choose a triangular mesh and the built-in implementation of the hyperelastic neo-Hookean model. In Fig. 5, we see very good agreement between the results of the two different numerical methods.

5.2 Validation with AFM experiments

To compare with the AFM experiments of Caille et al. (2002), we simulate a cell with radius 15μm using the setup of Sect. 4.2. For the hydrogel particle indentation (Neubauer et al. 2019) we use the setup depicted in Fig. 3c and d with a particle radius of 40μm and a radius of the colloidal probe of 26.5μm. The Poisson ratio is chosen as 0.48 in all simulations and the Young's modulus is determined using a best fit to the experimental data points. Since the neo-Hookean description appears to be sufficient for these data sets, we further set $w = 1$.

In Fig. 6a, we show the experimental data for suspended, round, bovine endothelial cells of five separate measurements from (Caille et al. 2002) together with the prediction of the Hertz theory for a Young's modulus of 1000Pa. Fitting our data with Young's moduli in the range

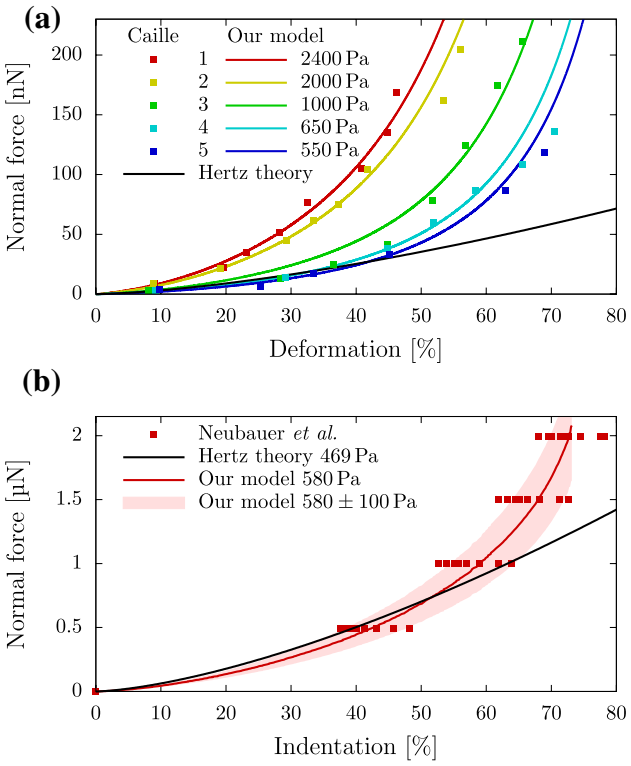

Fig. 6 **a** Our numerical model in comparison to experimental measurements of bovine endothelial cells from (Caille et al. 2002). The black line depicts the prediction of the Hertz theory for a Young's modulus of 1000Pa. **b** Our numerical model in comparison to experimental measurements of hydrogel particles from (Neubauer et al. 2019). The indicated range corresponds to the experimentally found range of ± 100Pa for the Young's modulus according to the depicted Hertz model

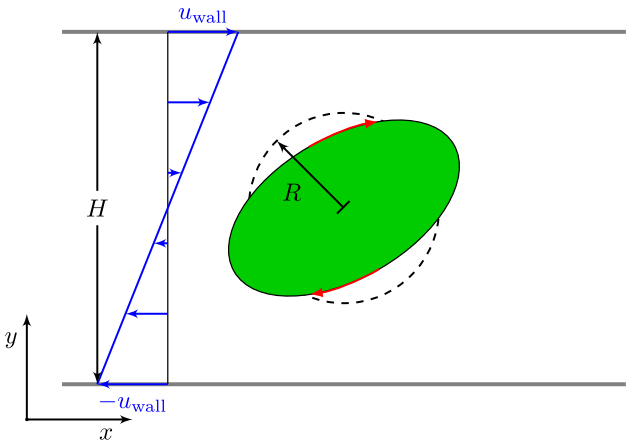

Fig. 7 Schematic of the single cell in shear flow. The cell sits in the center of the box and shows an approximately elliptic deformation as well as tank-treading, i.e., a rotation of the membrane around the steady shape in the *x*-*y*-plane

of 550Pa to 2400Pa, we find good agreement between our calculations and the experimental data. We note that Caille et al. (2002) observed similarly good agreement for their axisymmetric incompressible neo-Hookean FEM simulations which, however, cannot be coupled to external flows in contrast to the approach presented here. The same procedure is applied to the colloidal probe indentation data of hydrogel particles from (Neubauer et al. 2019), showing in Fig. 6b the experimental data and the prediction of the Hertz theory from (Neubauer et al. 2019). We find excellent agreement between our model calculations for Young's moduli in the range of 580 ± 100Pa and the experimental data. For both systems, Fig. 6 shows large deviations between the Hertzian theory and the experimental data for medium-to-large deformations. Our model provides a significant improvement in this range.

6 Application in shear flow

We now apply our model to study the behavior of cells in a plane Couette (linear shear) flow setup and compare the steady cell deformation to other numerical and analytical cell models of Gao et al. (2011), Rosti et al. (2018) and Saadat et al. (2018). A sketch of the simulation setup is shown in Fig. 7. For simplicity, we choose $w = 1$ to reduce the Mooney–Rivlin description (7) to two free parameters μ and κ (or E and ν), obtaining a compressible neo-Hookean form. We use the Lattice Boltzmann implementation of the open source software package ESPResSo (Limbach et al. 2006; Roehm and Arnold 2012). Coupling between fluid and cell is achieved via the immersed-boundary algorithm (Devendran and Peskin 2012; Saadat et al. 2018) which we implemented into ESPResSo (Bächer et al. 2017; Bächer and Gekle 2019). We note here that, in contrast to Saadat et al. (2018), we do not subtract the fluid stress within the particle interior. This leads to a small viscous response of the cell material in addition to its elasticity. To obtain (approximately) the limit of a purely elastic particle, we exploit a recently developed method by Lehmann et al. (2020) to discriminate between the cell interior and exterior during the simulation. Using this technique, we can tune the ratio between inner and outer viscosity λ with $\lambda \to 0$ representing a purely elastic particle. For simplicity, we will nevertheless set $\lambda = 1$ in the following, except where otherwise noted. Details of the method are provided in the SI (section S-4.1). As measure for the deformation, we investigate the Taylor parameter D (23) of our initially spherical cell model in shear flow at different shear rates $\dot{\gamma}$.

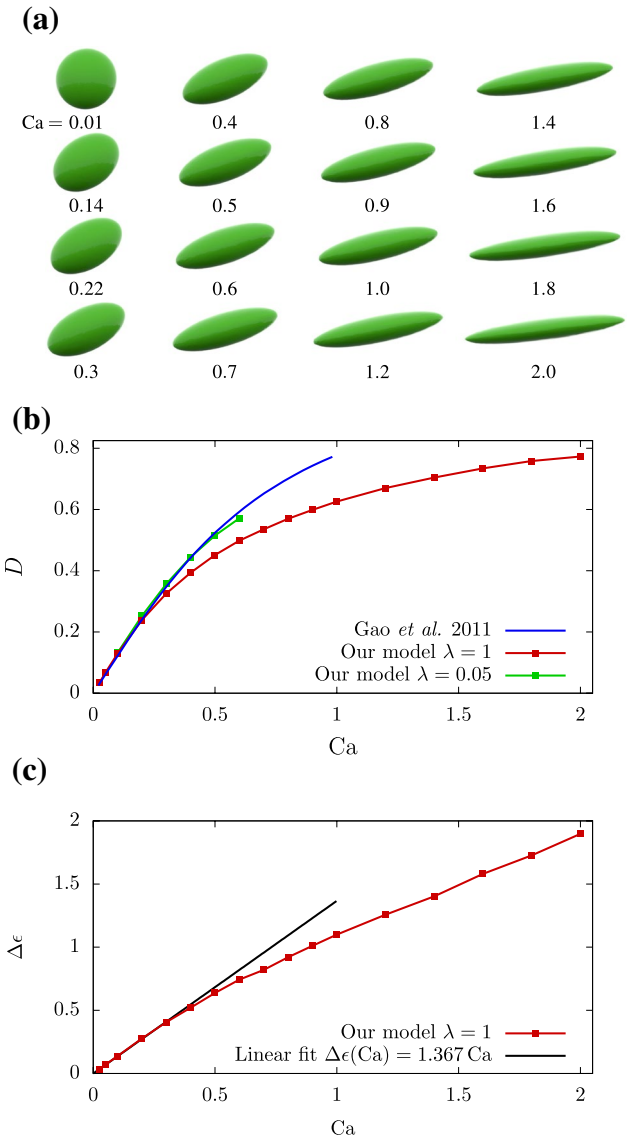

Fig. 8 **a** Converged shapes of a single cell in a $10 \times 15 \times 5$ ($x \times y \times z$) simulation box (in units of the cell radius) with a shear flow in x-direction as function of the capillary number Ca. **b** Comparison of our model predictions for a single cell in shear flow to the analytical 3D calculations in Fig. 7 of Gao et al. (2011) in the range of $\mathrm{Ca} \in [0.01, 2.0]$. **c** The relative stretch $\Delta\epsilon$ of our cell model as function of the capillary number Ca. A linear behavior is found for small capillary numbers up to $\mathrm{Ca} = 0.3$, while increasing stress is required for larger deformations due to the strain-hardening quality of the neo-Hookean model. Lines are a guide to the eye

6.1 Single cell simulation

The first simulation setup, a single cell in infinite shear flow, is realized by choosing a simulation box of the dimensions $10 \times 15 \times 5$ ($x \times y \times z$) in units of the cell radius. The infinite shear flow is approximated by applying a tangential velocity u_{wall} on the x-z-planes at $y = 0$ in negative and at $y = 15$ in positive x-direction, as depicted in Fig. 7. The tangential

wall velocity is calculated using the distance H of the parallel planes and the constant shear rate $\dot{\gamma}$ via

$$u_{\text{wall}} = \tfrac{1}{2} H\dot{\gamma} \,. \tag{27}$$

The box is periodic in x and z. A single cell is placed at the center of the simulation box corresponding to a volume fraction of $\phi = 0.0003$. We choose the following parameters: fluid mass density $\varrho = 10^3 kgm^{-3}$, dynamic viscosity $\eta = 10^{-3}$Pas, and shear rate $\dot{\gamma} = 4s^{-1}$. The capillary number is defined by (Gao and Hu 2009)

$$\text{Ca} = \frac{\eta\dot{\gamma}}{\mu} \,, \tag{28}$$

and is used to set the shear modulus μ of our cell relative to the fluid shear stress $\eta\dot{\gamma}$. Simulation snapshots of the steady-state deformation of a single cell in shear flow are depicted in dependency of the capillary number in Fig. 8a. We compare the Taylor deformation parameter D to previous approximate analytical calculations of Gao et al. (2011) for a three-dimensional elastic solid in infinite shear flow in Fig. 8b and see reasonable agreement for our standard case of $\lambda = 1$. Reducing the inner viscosity by setting $\lambda = 0.05$, i.e., close to the limit of a purely elastic solid, the agreement is nearly perfect. Finally, we demonstrate that the elastic particle exhibits a tank-treading motion in section S-4.2.

A possibly even more intuitive way to measure cell deformation is the net strain of the cell which we define as

$$\Delta\epsilon = \frac{\left(d_{\max} - d_{\text{ref}}\right)}{d_{\text{ref}}} \,. \tag{29}$$

It describes the relative stretching of the cell using the maximum elongation $d_{\max}$, i.e., the maximum distance of two cell vertices, and its reference diameter $d_{\text{ref}} = 2R$. A strain of $\Delta\epsilon = 1$ thus corresponds to an elongation of the cell by an additional 100% of its original size. In Fig. 8c, we depict the $\Delta\epsilon$ as function of Ca. For small capillary numbers, i.e., small shear stresses, a linear stress-strain dependency is observed. Above Ca ≈ 0.3, the strain-hardening, nonlinear behavior of the neo-Hookean model can be seen. By stretching the cell up to 280% of its initial size, this plot demonstrates again the capability of our model to smoothly treat large deformations.

6.2 Multiple cell simulations

The second simulation setup, implemented to investigate the multiple particle aspect of our model, consists of 4 (8) cells in a $5 \times 8 \times 4$ simulation box (in units of the cell radius), corresponding to a volume fraction of $\phi = 0.11$ ($\phi = 0.22$) occupied by cells. The cells are inserted at random initial positions in the box and the flow parameters are the same as in the first setup (cf. Sect. 6.1).

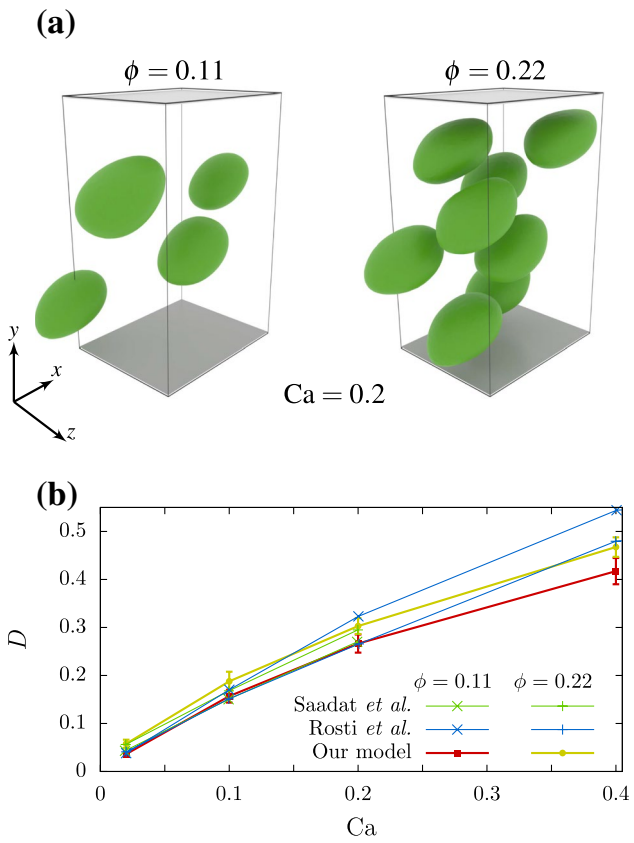

Fig. 9 **a** Multiple cells in a $5 \times 8 \times 4$ ($x \times y \times z$) simulation box (in units of the cell radius) with a confined shear flow in x-direction for a capillary number of Ca $= 0.2$ and 4 cells corresponding to a volume fraction of $\phi = 0.11$, and 8 cells corresponding to $\phi = 0.22$. **b** Averaged deformation of multiple cell simulations with $\phi = 0.11$ and $\phi = 0.22$ in comparison to data from Fig. 3 of Rosti et al. (2018) and Fig. 13 of Saadat et al. (2018)

Figure 9a shows simulation snapshots of the cells in suspensions with volume fraction $\phi = 0.11$ and $\phi = 0.22$ for Ca $= 0.2$. The Taylor deformation of the suspensions, depicted in Fig. 9b, is calculated as an average over all cells and over time after an initial transient timespan. We find good agreement when comparing the averaged cell deformation in suspension with Rosti et al. (2018), Saadat et al. (2018).

7 Conclusion

We presented a simple but accurate numerical model for cells and other microscopic particles for the use in computational fluid-particle dynamics simulations.

The elastic behavior of the cells is modeled by applying Mooney–Rivlin strain energy calculations on a uniformly tetrahedralized spherical mesh. We performed a

series of FluidFM® compression experiments with REF52 cells as an example for cells used in bioprinting processes and found excellent agreement between our numerical model and the measurements if all three parameters of the Mooney–Rivlin model are used. In addition, we showed that the model compares very favorably to force versus deformation data from previous AFM compression experiments on bovine endothelial cells (Caille et al. 2002) as well as colloidal probe AFM indentation of artificial hydrogel particles (Neubauer et al. 2019). At large deformations, a clear improvement compared to Hertzian contact theory has been observed.

By coupling our model to Lattice Boltzmann fluid calculations via the Immersed-Boundary method, the cell deformation in linear shear flow as function of the capillary number was found in good agreement with analytical calculations by Gao et al. (2011) on isolated cells as well as previous simulations of neo-Hookean and viscoelastic solids (Rosti et al. 2018; Saadat et al. 2018) at various volume fractions.

The presented method together with the precise determination of model parameters by FluidFM® /AFM experiments may provide an improved set of tools to predict cell deformation— and ultimately cell viability—in strong hydrodynamic flows as occurring, e.g., in bioprinting applications.

Acknowledgements Funded by the Deutsche Forschungsgemeinschaft (DFG, German Research Foundation)—Project number 326998133—TRR 225 "Biofabrication" (subproject B07). We gratefully acknowledge computing time provided by the SuperMUC system of the Leibniz Rechenzentrum, Garching. We further acknowledge support through the computational resources provided by the Bavarian Polymer Institute. Christian Bächer thanks the Studienstiftung des deutschen Volkes for financial support and acknowledges support by the study program "Biological Physics" of the Elite Network of Bavaria. Furthermore, we thank the laboratory of professor Alexander Bershadsky at Weizmann Insitute of Science in Isreal for providing the REF52 cells stably expressing paxillin-YFP.

Funding Open Access funding enabled and organized by Projekt DEAL.

Compliance with ethical standards

Conflicts of interest The authors declare that they have no conflict of interest.

References

Aguado BA, Mulyasasmita W, Su J, Lampe KJ, Heilshorn SC (2012) Improving viability of stem cells during syringe needle flow through the design of hydrogel cell carriers. Tissue Eng Part A 18(7–8):806–815

Alexandrova AY, Arnold K, Schaub S, Vasiliev JM, Meister JJ, Bershadsky AD, Verkhovsky AB (2008) Comparative dynamics of retrograde actin flow and focal adhesions: formation of nascent adhesions triggers transition from fast to slow flow. PLoS ONE 3(9):e3234. https://doi.org/10.1371/journal.pone.0003234

Bächer C, Gekle S (2019) Computational modeling of active deformable membranes embedded in three-dimensional flows. Phys Rev E 99(6):062418. https://doi.org/10.1103/PhysRevE.99.062418

Bächer C, Schrack L, Gekle S (2017) Clustering of microscopic particles in constricted blood flow. Phys Rev Fluids 2(1):013102

Blaeser A, Duarte Campos DF, Puster U, Richtering W, Stevens MM, Fischer H (2015) Controlling shear stress in 3D bioprinting is a key factor to balance printing resolution and stem cell integrity. Adv Healthcare Mater 5(3):326–333. https://doi.org/10.1002/adhm.201500677

Bongiorno T, Kazlow J, Mezencev R, Griffiths S, Olivares-Navarrete R, McDonald JF, Schwartz Z, Boyan BD, McDevitt TC, Sulchek T (2014) Mechanical stiffness as an improved single-cell indicator of osteoblastic human mesenchymal stem cell differentiation. J Biomech 47(9):2197–2204

Bower AF (2010) Applied Mechanics of Solids. CRC Press, Boca Raton

Caille N, Thoumine O, Tardy Y, Meister JJ (2002) Contribution of the nucleus to the mechanical properties of endothelial cells. J Biomech 35(2):177–187. https://doi.org/10.1016/S0021-9290(01)00201-9

Chim YH, Mason LM, Rath N, Olson MF, Tassieri M, Yin H (2018) A one-step procedure to probe the viscoelastic properties of cells by atomic force microscopy. Sci Rep 8(1):1–12

Clausen JR, Aidun CK (2010) Capsule dynamics and rheology in shear flow: particle pressure and normal stress. Phys Fluids 22(12):123302. https://doi.org/10.1063/1.3483207

Devendran D, Peskin CS (2012) An immersed boundary energy-based method for incompressible viscoelasticity. J Comput Phys 231(14):4613–4642

Dintwa E, Tijskens E, Ramon H (2008) On the accuracy of the Hertz model to describe the normal contact of soft elastic spheres. Granular Matter 10(3):209–221. https://doi.org/10.1007/s10035-007-0078-7

Efremov YM, Wang WH, Hardy SD, Geahlen RL, Raman A (2017) Measuring nanoscale viscoelastic parameters of cells directly from AFM force-displacement curves. Sci Rep 7(1):1541–14

Fischer-Friedrich E, Hyman AA, Jülicher F, Müller DJ, Helenius J (2014) Quantification of surface tension and internal pressure generated by single mitotic cells. Sci Rep 4:6213. https://doi.org/10.1038/srep06213

Fischer-Friedrich E, Toyoda Y, Cattin CJ, Müller DJ, Hyman AA, Jülicher F (2016) Rheology of the active cell cortex in mitosis. Biophys J 111(3):589–600. https://doi.org/10.1016/j.bpj.2016.06.008

Fregin B, Czerwinski F, Biedenweg D, Girardo S, Gross S, Aurich K, Otto O (2019) High-throughput single-cell rheology in complex samples by dynamic real-time deformability cytometry. Nat Commun 10(1):415. https://doi.org/10.1038/s41467-019-08370-3

Freund JB (2014) Numerical Simulation of Flowing Blood Cells. Annu Rev Fluid Mech 46(1):67–95

Gao T, Hu HH (2009) Deformation of elastic particles in viscous shear flow. J Comput Phys 228(6):2132–2151. https://doi.org/10.1016/j.jcp.2008.11.029

Gao T, Hu HH, Castañeda PP (2011) Rheology of a suspension of elastic particles in a viscous shear flow. J Fluid Mech 687:209–237

Gao T, Hu HH, Castañeda PP (2012) Shape dynamics and rheology of soft elastic particles in a shear flow. Phys Rev Lett 108(5):058302–4

Ghaemi A, Philipp A, Bauer A, Last K, Fery A, Gekle S (2016) Mechanical behaviour of micro-capsules and their rupture under compression. Chem Eng Sci 142(C):236–243. https://doi.org/10.1016/j.ces.2015.11.002

Gonzalez-Cruz RD, Fonseca VC, Darling EM (2012) Cellular mechanical properties reflect the differentiation potential of adipose-derived mesenchymal stem cells. Proc Nat Acad Sci (USA) 109(24):E1523–E1529

Guckenberger A, Schraml MP, Chen PG, Leonetti M, Gekle S (2016) On the bending algorithms for soft objects in flows. Comput Phys Commun 207:1–23. https://doi.org/10.1016/j.cpc.2016.04.018

Guckenberger A, Kihm A, John T, Wagner C, Gekle S (2018) Numerical-experimental observation of shape bistability of red blood cells flowing in a microchannel. Soft Matter 14(11):2032–2043. https://doi.org/10.1039/C7SM02272G

Hecht FM, Rheinlaender J, Schierbaum N, Goldmann WH, Fabry B, Schäffer TE (2015) Imaging viscoelastic properties of live cells by AFM: power-law rheology on the nanoscale. Soft Matter 11(23):4584–4591

Huber F, Schnau J, Rönicke S, Rauch P, Müller K, Fütterer C, Käs J (2013) Emergent complexity of the cytoskeleton: from single filaments to tissue. Adv Phys 62(1):1–112

Jaiswal D, Cowley N, Bian Z, Zheng G, Claffey KP, Hoshino K (2017) Stiffness analysis of 3D spheroids using microtweezers. PLoS One 12(11):e0188346

Johnson KL (2003) Contact mechanics, 9th edn. Cambridge University Press, Cambridge

Khalil S, Sun W (2007) Biopolymer deposition for freeform fabrication of hydrogel tissue constructs. Mater Sci Eng: C 27(3):469–478

Kiss R (2011) Elasticity of human embryonic stem cells as determined by atomic force microscopy. J Biomech Eng 133(10):101009. https://doi.org/10.1115/1.4005286

Kollmannsberger P, Fabry B (2011) Linear and nonlinear rheology of living cells. Ann Rev Mater Res 41(1):75–97. https://doi.org/10.1146/annurev-matsci-062910-100351

Kotsalos C, Latt J, Chopard B (2019) Bridging the computational gap between mesoscopic and continuum modeling of red blood cells for fully resolved blood flow. J Comput Phys 398:108905

Kubitschke H, Schnauss J, Nnetu KD, Warmt E, Stange R, Kaes J (2017) Actin and microtubule networks contribute differently to cell response for small and large strains. New J Phys 19(9):093003–13

Ladjal H, Hanus JL, Pillarisetti A, Keefer C, Ferreira A, Desai JP (2009) Atomic force microscopy-based single-cell indentation: Experimentation and finite element simulation. In: 2009 IEEE/RSJ International Conference on Intelligent Robots and Systems, IEEE, St. Louis, MO, USA, pp 1326–1332, 10.1109/IROS.2009.5354351

Ladjal H, Hanus JL, Pillarisetti A, Keefer C, Ferreira A, Desai JP (2018) Atomic force microscopy-based single-cell indentation: Experimentation and finite element simulation. In: 2009 IEEE/RSJ International Conference on Intelligent Robots and Systems (IROS 2009), IEEE, pp 1326–1332

Lange JR, Steinwachs J, Kolb T, Lautscham LA, Harder I, Whyte G, Fabry B (2015) Microconstriction arrays for high-throughput quantitative measurements of cell mechanical properties. Biophys J 109(1):26–34

Lange JR, Metzner C, Richter S, Schneider W, Spermann M, Kolb T, Whyte G, Fabry B (2017) Unbiased high-precision cell mechanical measurements with microconstrictions. Biophys J 112(7):1472–1480

Lehmann M, Müller SJ, Gekle S (2020) Efficient viscosity contrast calculation for blood flow simulations using the lattice Boltzmann method. Int J Numer Meth Fluids 92:1463– 1477. https://doi.org/10.1002/fld.4835

Li M, Tian X, Kozinski JA, Chen X, Hwang DK (2015) Modeling mechanical cell damage in the bioprinting process employing a conical needle. J Mech Med Biol 15(05):1550073–15

Limbach H, Arnold A, Mann B, Holm C (2006) ESPResSo—an extensible simulation package for research on soft matter systems. Comp Phys Commun 174(9):704–727. https://doi.org/10.1016/j.cpc.2005.10.005

Lulevich V, Zink T, Chen HY, Liu FT, Gy Liu (2006) Cell mechanics using atomic force microscopy-based single-cell compression. Langmuir 22(19):8151–8155. https://doi.org/10.1021/la060561p

Lulevich VV, Radtchenko IL, Sukhorukov GB, Vinogradova OI (2003) Deformation properties of nonadhesive polyelectrolyte microcapsules studied with the atomic force microscope. J Phys Chem B 107(12):2735–2740. https://doi.org/10.1021/jp026927y

Lykov K, Nematbakhsh Y, Shang M, Lim CT, Pivkin IV (2017) Probing eukaryotic cell mechanics via mesoscopic simulations. PLoS Comput Biol 13(9):e1005726–22

Mauer J, Mendez S, Lanotte L, Nicoud F, Abkarian M, Gompper G, Fedosov DA (2018) Flow-induced transitions of red blood cell shapes under shear. Phys Rev Lett 121(11):118103

Mokbel M, Mokbel D, Mietke A, Träber N, Girardo S, Otto O, Guck J, Aland S (2017) Numerical simulation of real-time deformability cytometry to extract cell mechanical properties. ACS Biomater Sci Eng 3(11):2962–2973

Mooney M (1940) A theory of large elastic deformation. J Appl Phys 11(9):582–592. https://doi.org/10.1063/1.1712836

Mulla Y, MacKintosh FC, Koenderink GH (2019) Origin of Slow Stress Relaxation in the Cytoskeleton. Phys Rev Lett 122(21):218102

Müller SJ, Mirzahossein E, Iftekhar EN, Bächer C, Schrüfer S, Schubert DW, Fabry B, Gekle S (2020) Flow and hydrodynamic shear stress inside a printing needle during biofabrication. PLOS ONE 15(7):e0236371. https://doi.org/10.1371/journal.pone.0236371

Neubauer JW, Hauck N, Männel MJ, Seuss M, Fery A, Thiele J (2019) Mechanoresponsive hydrogel particles as a platform for three-dimensional force sensing. ACS Appl Mater Interfaces 11(29):26307–26313. https://doi.org/10.1021/acsami.9b04312

Nyberg KD, Hu KH, Kleinman SH, Khismatullin DB, Butte MJ, Rowat AC (2017) Quantitative deformability cytometry: rapid, calibrated measurements of cell mechanical properties. Biophys J 113(7):1574–1584

Otto O, Rosendahl P, Mietke A, Golfier S, Herold C, Klaue D, Girardo S, Pagliara S, Ekpenyong A, Jacobi A, Wobus M, Töpfner N, Keyser UF, Mansfeld J, Fischer-Friedrich E, Guck J (2015) Real-time deformability cytometry: on-the-fly cell mechanical phenotyping. Nat Methods 12(3):199–202. https://doi.org/10.1038/nmeth.3281

Paxton N, Smolan W, Böck T, Melchels F, Groll J, Jungst T (2017) Proposal to assess printability of bioinks for extrusion-based bioprinting and evaluation of rheological properties governing bioprintability. Biofabrication 9(4):044107. https://doi.org/10.1088/1758-5090/aa8dd8

Ramanujan S, Pozrikidis C (1998) Deformation of liquid capsules enclosed by elastic membranes in simple shear flow: large deformations and the effect of fluid viscosities. J Fluid Mech 361:117–143. https://doi.org/10.1017/S0022112098008714

Rivlin RS (1948) Large elastic deformations of isotropic materials. I. fundamental concepts. Philos Trans R Soc A: Math Phys Eng Sci 240(822):459–490. https://doi.org/10.1098/rsta.1948.0002

Roehm D, Arnold A (2012) Lattice Boltzmann simulations on GPUs with ESPResSo. Euro Phys J Spec Top 210(1):89–100. https://doi.org/10.1140/epjst/e2012-01639-6

Roscoe R (1967) On the rheology of a suspension of viscoelastic spheres in a viscous liquid. J Fluid Mech 28(02):273–21

Rosti ME, Brandt L, Mitra D (2018) Rheology of suspensions of viscoelastic spheres: Deformability as an effective volume fraction. Phys Rev Fluids 3(1):012301. https://doi.org/10.1103/PhysRevFluids.3.012301

Saadat A, Guido CJ, Iaccarino G, Shaqfeh ESG (2018) Immersed-finite-element method for deformable particle suspensions in viscous and viscoelastic media. Phys Rev E 98(6):063316. https://doi.org/10.1103/PhysRevE.98.063316

Sancho A, Vandersmissen I, Craps S, Luttun A, Groll J (2017) A new strategy to measure intercellular adhesion forces in mature cell-cell contacts. Sci Rep 7(1):46152–14

Shen Y, Yalikun Y, Tanaka Y (2019) Recent advances in microfluidic cell sorting systems. Sensors Actuators B: Chem 282:268–281. https://doi.org/10.1016/j.snb.2018.11.025

Smith M (2009) ABAQUS/Standard User's Manual, Version 6.9. Dassault Systèmes Simulia Corp, United States

Snyder J, Rin Son A, Hamid Q, Wang C, Lui Y, Sun W (2015) Mesenchymal stem cell printing and process regulated cell properties. Biofabrication 7(4):044106. https://doi.org/10.1088/1758-5090/7/4/044106

Tirella A, Vozzi F, Vozzi G, Ahluwalia A (2011) PAM2 (Piston Assisted Microsyringe): a new rapid prototyping technique for biofabrication of cell incorporated scaffolds. Tiss Eng Part C: Methods 17(2):229–237

Villone MM, Hulsen MA, Anderson PD, Maffettone PL (2014) Simulations of deformable systems in fluids under shear flow using an arbitrary Lagrangian Eulerian technique. Comp Fluids 90(C):88–100

Villone MM, D'Avino G, Hulsen MA, Maffettone PL (2015) Dynamics of prolate spheroidal elastic particles in confined shear flow. Phys Rev E 92(6):062303

Závodszky G, van Rooij B, Azizi V, Hoekstra A (2017) Cellular level in-silico modeling of blood rheology with an improved material model for red blood cells. Front Physiol 8:061006–14

Zhao Y, Li Y, Mao S, Sun W, Yao R (2015) The influence of printing parameters on cell survival rate and printability in microextrusion-based 3D cell printing technology. Biofabrication 7(4):045002. https://doi.org/10.1088/1758-5090/7/4/045002

SUPPLEMENTARY MATERIAL FOR THE MANUSCRIPT

A hyperelastic model for simulating cells in flow

Sebastian J. Müller[1], Franziska Weigl[2], Carina Bezold[1], Christian Bächer[1], Krystyna Albrecht[2], and Stephan Gekle[1]

[1]Theoretical Physics VI, Biofluid Simulation and Modeling, University of Bayreuth, Universitätsstraße 30 Germany,
[2]Department of Functional Materials in Medicine and Dentistry and Bavarian Polymer Institute (BPI), University of Würzburg, Pleicherwall 2, 97070 Würzburg, Germany
Author to whom correspondence should be addressed:
stephan.gekle@uni-bayreuth.de

S-1 Supplementary Material for the cell experiments

Additional force-deformation curves for our FluidFM® measurements on REF52 cells are shown in figure S-1. Compared to the curves depicted in the manuscript in figure 4, these measurements show an earlier upturn of the force. Thus, our model overestimates the force necessary for a small deformation of the cell and slightly underestimates the force for larger deformations. Nevertheless, all measurements fit in the simulated range of $E = 220 \pm 100\,\mathrm{Pa}$ for $w = 0.25$ and an averaged cell radius of $8.6(7)\,\mu\mathrm{m}$, as figure S-1 shows. The cell radii and Young's moduli for all measurements are listed in table S-1.

Table S-1 Measured cell radii R and fitted Young's moduli E and w for our FluidFM® experiments.

Number	1	2	3	4	5	6	7	8	9
R [µm]	7.1	9.2	8.3	8.0	9.5	9.1	8.4	9.4	8.3
E [Pa]	160	190	220	170	210	290	210	220	125
w	1	0.25	0.25	0.5	0.25	0.25	0.25	0.25	0.25

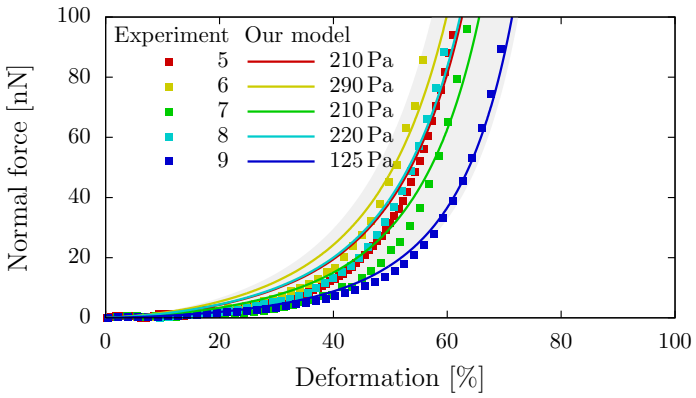

Fig. S-1 Our numerical model in comparison to our FluidFM® measurements on REF52 cells. The ratio of the shear moduli is chosen as $w = 0.25$ for all curves. The gray area shows the simulation of a cell with an averaged cell radius of $8.6(7)\,\mu\mathrm{m}$ and Young's modulus range $220 \pm 100\,\mathrm{Pa}$.

S-2 Supporting Information for the numerical model

S-2.1 Convergence of single cell deformation in shear flow

The temporal development of the deformation D of a single cell in a Couette flow can be seen in figure S-2. Starting from a spherical shape ($D = 0$), the cell experiences a shape change during an initial transient timespan, after which it assumes a steady shape. For capillary numbers $\mathrm{Ca} > 0.2$, we first find an overrelaxation of the deformation before it converges towards a constant value.

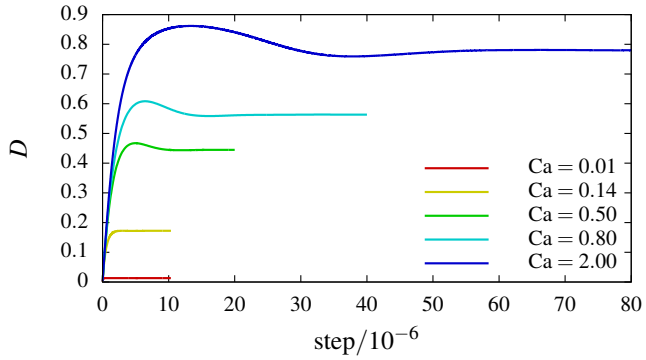

Fig. S-2 Single cell deformation in Couette flow for different capillary numbers. After an initial transient timespan, the deformation converges to a constant value.

S-2.2 Reduction of the system resolution

In figure S-3 we show that a system with reduced cell resolution (from $R_{\mathrm{Cell}} = 10$ to $R_{\mathrm{Cell}} = 6$ grid cells) and a smaller simulation box (from $100 \times 150 \times 100$ to $60 \times 90 \times 30$ grid cells) produces the same deformation versus capillary number behavior as the system with higher resolution.

S-2.3 Translational and rotational invariance of the force calculation

As a very direct test for the correct behavior of our model, we consider a single tetrahedron and examine the behavior of the volume and the elastic force for an initially applied translation, rotation and stretching. In figure S-4a, the behavior of the volume under these deformations is shown over the first time steps. While the volume remains constant under pure translation, pure rotation, and a combination of both, it quickly relaxes towards its reference value after an initial stretch is applied. The same behavior is observed for the elastic force acting on one tetrahedron vertex, in figure S-4b.

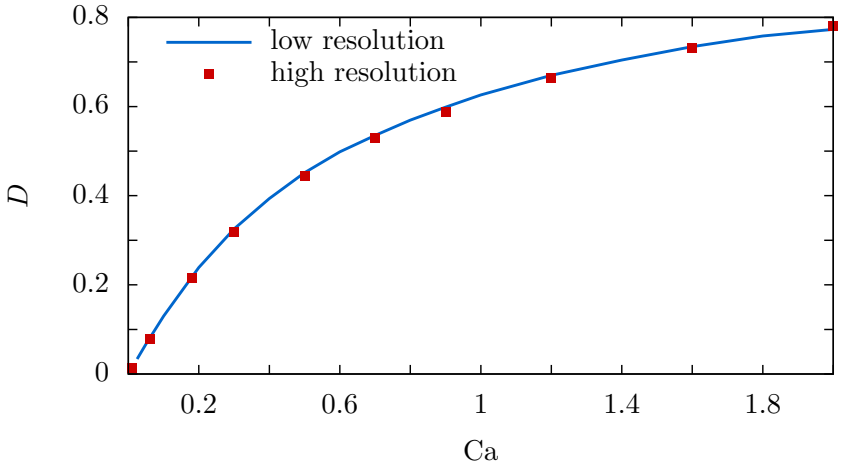

Fig. S-3 Taylor deformation as function of the capillary number for two different cell and channel resolutions. The large system ($R_{\text{Cell}} = 10$, box: $100 \times 150 \times 100$ grid cells) produces the same outcome as the down-scaled system ($R_{\text{Cell}} = 6$, box: $60 \times 90 \times 30$ grid cells).

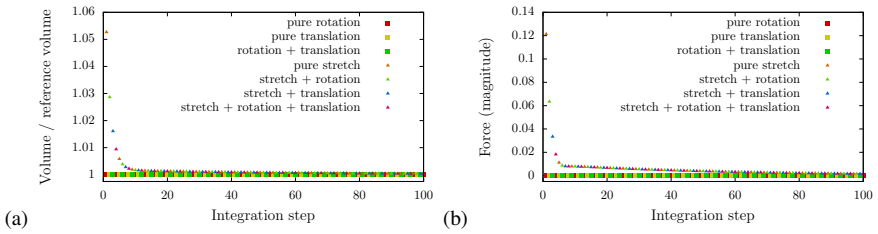

Fig. S-4 The behavior of (a) the volume and (b) the elastic force on a single vertex of a tetrahedron after an initial rotation, translation or stretching.

S-2.4 Mesh generation and mesh independence

The tetrahedral mesh of our spheroid is generated using the software gmsh (version 4.3.0) [1]. The Frontal2D meshing algorithm produced a mesh with highest uniformity considering edge length, triangle area and tetrahedron volume distribution. Nevertheless, all other available meshing algorithms produce likewise uniform meshes, with one exception being the Frontal3D algorithm, as listed in table S-2. We demand the uniformity of the mesh to increase the accuracy of our coupled Immersed-Boundary Lattice Boltzmann simulations. Figure S-5 shows the force-deformation curves for meshes with increasing number of tetrahedra, which are converged and thus prove sufficient sampling of the volume mesh.

Table S-2 Statistics of meshes created using different built-in algorithms of Gmsh [1]. Listed are edge length L, triangle area A, and tetrahedron volume V providing average, standard deviation, minimum and maximum value for each mesh.

Algorithm	Frontal2D	MeshAdapt	Delaunay2D	Delaunay3D	Frontal3D
$\bar{L}$	1.252	1.362	1.292	1.362	1.484
σ_L	0.243	0.301	0.299	0.301	0.530
L_{min}	0.616	0.588	0.592	0.588	0.510
L_{max}	2.138	2.345	2.462	2.345	3.622
$\bar{A}$	0.348	0.422	0.382	0.422	0.565
σ_A	0.377	0.473	0.436	0.473	0.837
A_{min}	0.218	0.228	0.192	0.228	0.204
A_{max}	1.577	1.851	1.709	1.851	4.444
$\bar{V}$	0.218	0.291	0.252	0.291	0.473
σ_V	0.078	0.121	0.112	0.121	0.405
V_{min}	0.049	0.051	0.043	0.051	0.049
V_{max}	0.600	0.881	0.840	0.881	2.353

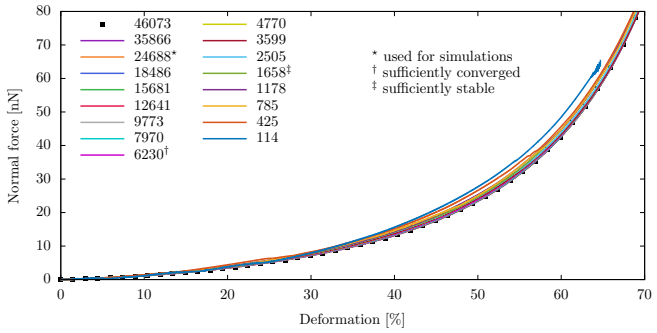

Fig. S-5 Force-deformation behavior of meshes with increasing number of tetrahedra. Meshes with $N \geq 1658$ tetrahedra are stable in the investigated range of deformation. Above 6230 tetrahedra, all meshes produce the same converged output. The following parameters were used: cell radius $R = 7.5\,\mu\text{m}$, Young's modulus $E = 300\,\text{Pa}$, and Poisson ratio $\nu = 0.48$.

S-2.5 Hertz theory

Although originally designed for the contact between two linear elastic spheres, the Hertz theory can be applied to the contact between a linear elastic sphere and a flat plate [2]. The general assumptions for the Hertz-theory are the following [3, p. 91-92]:

- frictionless, smooth contact surfaces
- contact area small compared to sphere dimension
- homogeneous, isotropic and linear elastic material

S-2.5.1 Sphere-sphere contact

The following quantities are necessary to describe the normal contact of two elastic spheres. The radii R_1 and R_2 of the spheres define the effective radius of curvature R

of the bodies by

$$\frac{1}{R} = \frac{1}{R_1} + \frac{1}{R_2} \quad . \tag{S-1}$$

Through their Young's moduli and the Poisson ratios, E_1, E_2 and ν_1, ν_2, the effective stiffness K is defined as:

$$\frac{1}{K} = \frac{1-\nu_1^2}{E_1} + \frac{1-\nu_2^2}{E_2} \tag{S-2}$$

The displacement δ, which measures the distance that the sphere centers approach each other due to a normal force N acting on each sphere, can be expressed in terms of the above parameters [2]:

$$\delta = \left(\frac{9N^2}{16RK^2} \right)^{\frac{1}{3}} \tag{S-3}$$

Therefore, the force–displacement relation according to the Hertzian theory for a sphere-sphere contact is given by

$$N(\delta) = \frac{4}{3} K R^{\frac{1}{2}} \delta^{\frac{3}{2}} \quad . \tag{S-4}$$

S-2.5.2 Sphere-plane contact

The analytical solution for the force–displacement relation according to the Hertzian theory for the contact of a linear elastic sphere with a rigid plane can be obtained from (S-4) by applying the following modifications: the plane has no curvature, thus $R_2 \to \infty$ and (S-1) simply yields $R = R_1$. Since the plane is assumed rigid, i. e. $E_2 \gg E_1$, (S-2) reduces to $K = \frac{E_1}{1-\nu_1^2}$. In this case, N is the force acting on the sphere and δ is the distance between the center of the sphere and the plane.

S-2.6 Influence of the Mooney-Rivlin ratio w

To clarify the influence of w, we plot in figure S-6 the force versus deformation behavior of our cell model for different values of w. With decreasing w, i. e. decreasing μ_1 while increasing μ_2, the strain hardening effect clearly increases and the upturn of the force curve begins at lower deformations. This is due to μ_2 scaling the term in the strain energy density that is quadratic with the deformation (cf. equations (4) and (5) of the manuscript).

S-2.7 Influence of the Poisson ratio ν

In figure S-7 we demonstrate that variations of the Poisson ratio ν within the range of an approximately incompressible material do not notably influence the force-deformation curves.

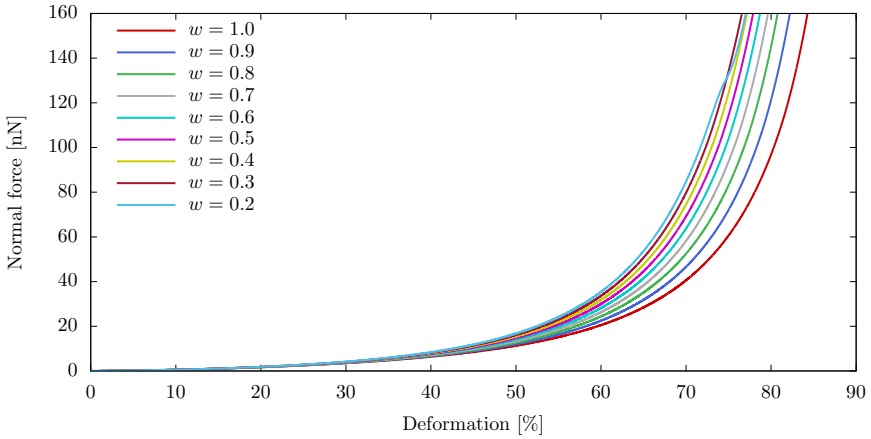

Fig. S-6 Variation of w: The lower w (the lower μ_1 compared to μ_2), the stronger the non-linear upturn of the force becomes. The curve with $w = 1$ corresponds to the one in Fig. 4 of the manuscript with a Young's modulus of $E = 160\,\text{Pa}$.

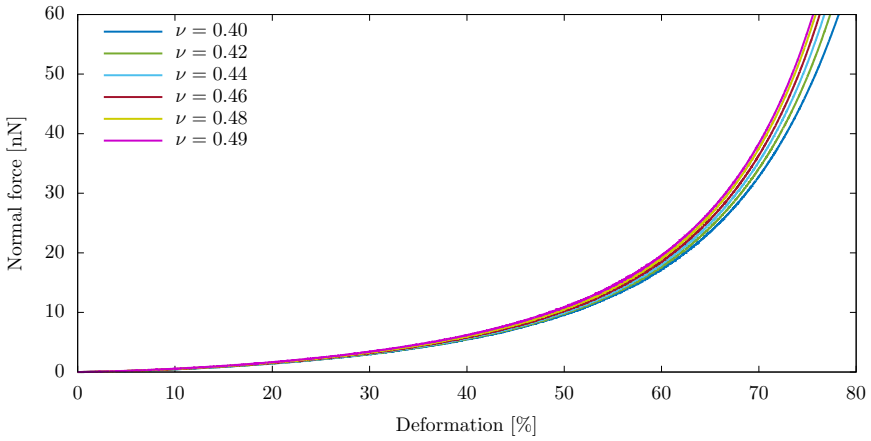

Fig. S-7 Force versus deformation curves for different Poisson ratios ν. The following parameters were used: cell radius $R = 7.5\,\mu\text{m}$ and Young's modulus $E = 300\,\text{Pa}$.

S-3 Compression and indentation simulations

After initialization, each time step of our overdamped relaxation simulation consists of the following two steps: the movement of the upper wall to compress – or the sphere to indent – the cell and the integration of the equation of motion of the cell vertices,

$$\dot{\mathbf{y}}^{\alpha} = \gamma^{-1}(\mathbf{f}^{\alpha} + \mathbf{f}^{\alpha}_{\text{probe}}) \quad . \tag{S-5}$$

The vertex velocity $\dot{\mathbf{y}}^{\alpha}$ is obtained from the elastic restoring forces ($\mathbf{f}^{\alpha}$ (12) and the probe repulsion $\mathbf{f}^{\alpha}_{\text{probe}}$), considering a friction factor γ. Since here we are only looking at a sequence of equilibrium states, the value of γ is irrelevant for the resulting force-deformation curves and only influences the performance and stability of the simulations. The equation of motion is integrated using a fourth order Runge-Kutta algorithm. The repulsive cell-probe interaction, preventing the cell vertices from penetrating the plates or the indenter, has the form

$$\mathbf{f}_{\text{probe}}(d) = \frac{c_{\text{F}}}{d^2}\mathbf{n} \quad , \tag{S-6}$$

with the cell-probe distance d and a proportionality factor c_{F}. The force points normal to the probe, resulting in a compression between two plates and a radial displacement away from the indenter. Physically, this corresponds to a free-slip boundary condition which does not restrict tangential motions of the cell along the probe.

S-4 Flow simulations with Lattice Boltzmann

S-4.1 Method

This section briefly summarizes the Lattice Boltzmann method implemented in the open-source package ESPResSo [4]. For an introduction into the Lattice Boltzmann method we refer the interested reader to the book by Krüger et al. [5]. The Lattice Boltzmann equation for the multiple relaxation time scheme used in ESPResSo reads:

$$f_i(\mathbf{x}+\mathbf{c}_i\Delta t, t+\Delta t) - f_i(\mathbf{x},t) = \sum_{j=0}^{18} \left(\mathsf{M}^{-1}\omega\,\mathsf{M}\right)_{ij} \left(f_j(\mathbf{x},t) - f_j^{\mathrm{eq}}(\mathbf{x},t)\right) \qquad \text{(S-7)}$$

It describes the collision and streaming of the population distribution f_i ($i = 0,\ldots,18$) during one time step Δt. Here, $\mathbf{c}_i$ are the discretized lattice velocities, M denotes transformation matrix that maps the populations onto moment space, ω is the diagonal relaxation frequency matrix, and f_i^{eq} denote the equilibrium population distributions. The relaxation frequency for the shear moments ω_{S} is related to the dynamic viscosity of the fluid via [6]

$$\eta = \rho c_s^2 \left(\frac{1}{\omega_{\mathrm{S}}} - \tfrac{1}{2}\right)\Delta t \quad , \qquad \text{(S-8)}$$

with the fluid mass density ρ and the lattice speed of sound c_s. In order to ensure simulation stability, we choose the time step globally according to Krüger *et al.*[5, p. 273] as

$$\Delta t = c_s^2\left(\tau - \tfrac{1}{2}\right)\frac{\Delta x^2}{\nu}\tilde{t} = \frac{\Delta x^2}{6\nu}\tilde{t} \quad , \qquad \text{(S-9)}$$

with $c_s^2 = \frac{1}{3}$, a global relaxation parameter $\tau = 1$, the kinematic viscosity ν, and an additional factor $\tilde{t}$ in the range 1–2 to manually tune the time step.
We further introduce a scaling factor r by which we divide both the viscosity and the Young's modulus. According to eq. (S-9), this leads to a larger time step and thus to a speed-up of the simulations. At the same time it leaves the important Capillary number unchanged and only increases the Reynolds number, which nevertheless remains $\ll 1$. The parameter r thus does not affect the physics of the simulation which we have carefully checked by a number of test runs with $r = 1$.
At the boundaries of the channel a bounce-back algorithm is applied to realize a no-slip boundary condition. For the plane Couette setup, the bounce-back algorithm additionally allows for a fixed tangential velocity component.
We use a combined CPU/GPU implementation which enables the calculation of the flow field on the GPU, while the calculation of the cell motion is done in parallel on multiple (4 to 20) CPUs. In lattice units, our simulation box for the single cell in shear flow setup (cf. section 6.1) has the dimensions $60 \times 90 \times 30$ ($x \times y \times z$), for the multiple cell simulation (cf. section 6.2) it is $50 \times 80 \times 40$. The dynamic viscosity, chosen as $\nu = 1$ in simulation units, determines the time step in our simulations as $\Delta t = \frac{1}{3}$ with $\tilde{t} = 2$.

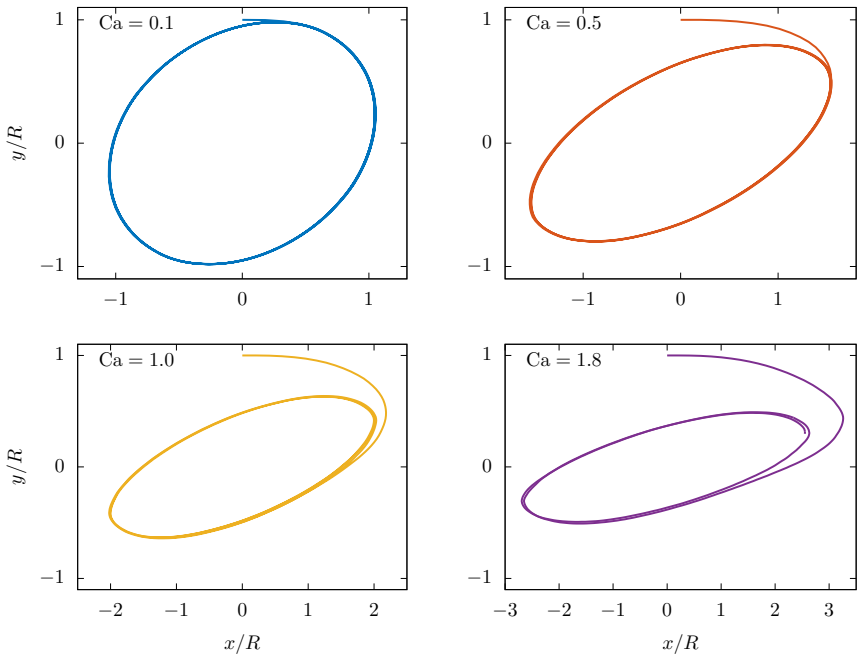

Fig. S-8 The trajectory of a surface node (here: starting at $y = R$ and $x, z = 0$) for different capillary numbers traces the ellipsoidal contour of the deformed particle. The non-elliptical part of the trajectory in the upper-right corner represents the approach from the initially spherical to the final shape.

S-4.2 Tank-treading motion

Figure S-8 shows the trajectories of selected vertices on the outer surface of the particle for different capillary numbers. They describe an ellipsoidal motion tracing the outer contour of the deformed particle thus demonstrating that in our simulations the particle exhibits tank-treading.

References

1. C. Geuzaine, J.F. Remacle, International Journal for Numerical Methods in Engineering **79**(11), 1309 (2009). DOI 10.1002/nme.2579
2. E. Dintwa, E. Tijskens, H. Ramon, Granular Matter **10**(3), 209 (2008). DOI 10.1007/s10035-007-0078-7
3. K.L. Johnson, *Contact Mechanics*, 9th edn. (Cambridge Univ. Press, Cambridge, 2003). OCLC: 250004367
4. H. Limbach, A. Arnold, B. Mann, C. Holm, Computer Physics Communications **174**(9), 704 (2006). DOI 10.1016/j.cpc.2005.10.005
5. T. Krüger, H. Kusumaatmaja, A. Kuzmin, O. Shardt, G. Silva, E.M. Viggen, *The Lattice Boltzmann Method*. Graduate Texts in Physics (Springer International Publishing, Cham, 2017). DOI 10.1007/978-3-319-44649-3

6. Z. Chai, B. Shi, Z. Guo, F. Rong, Journal of Non-Newtonian Fluid Mechanics **166**(5-6), 332 (2011). DOI 10.1016/j.jnnfm.2011.01.002

Publication 3

Predicting cell stress and strain during extrusion 3D bioprinting

S. J. Müller, B. Fabry, and S. Gekle

Submitted, 2022

Preprint DOI: 10.1101/2022.09.28.509836

-

Predicting cell stress and strain during extrusion bioprinting

Sebastian J. Müller,[1] Ben Fabry,[2] and Stephan Gekle[1]

[1] *Biofluid Simulation and Modeling, Theoretische Physik VI, Universität Bayreuth, 95440 Bayreuth, Germany*

[2] *Department of Physics, Friedrich-Alexander University Erlangen-Nürnberg, 91054 Erlangen, Germany*

(Dated: January 8, 2023)

Bioprinting of living cells can cause major shape deformations, which may severely affect cell survival and functionality. While the shear stresses occurring during cell flow through the printer nozzle have been quantified to some extent, the extensional stresses occurring as cells leave the nozzle into the free printing strand have been mostly ignored. Here we use Lattice-Boltzmann simulations together with a finite-element based cell model to study cell deformation at the nozzle exit. Our simulation results are in good qualitative agreement with experimental microscopy images. We show that for cells flowing in the center of the nozzle extensional stresses can be significant, while for cells flowing off-center their deformation is dominated by the shear flow inside the nozzle. From the results of these simulations, we develop two simple methods that only require the printing parameters (nozzle diameter, flow rate, bioink rheology) to (i) accurately predict the maximum cell stress occurring during the 3D bioprinting process and (ii) approximately predict the cell strains caused by the elongational flow at the nozzle exit.

I. INTRODUCTION

The aim of 3D bioprinting is to transfer the well-established techniques of conventional 3D printing to the fabrication of functional, living tissues. The material to be printed typically consists of a chemically complex hydrogel, termed the bioink, in which living cells are suspended. This technology promises to become a major breakthrough, e.g. for cancer studies or – in the long run – organ replacements [1–5]. A key obstacle, however, remains to ensure the survival and functionality of cells during and after the fabrication process. Possible causes for cell damage are numerous, but can be broadly classified into insufficient bio-compatibility and mechanical damage. The former arises from direct interaction between the cell and the surrounding bioink and has been intensively studied [6–13].

Mechanical damage, by contrast, arises from hydrodynamic stresses as the cell passes from the reservoir through the printing nozzle, transitions into the printing strand, and finally comes to rest in the printed construct. It has been shown that even after optimizing biological and chemical conditions [14], such hydrodynamic stresses remain a crucial source of cell damage and death [15–25]. Understanding these mechanical stress response processes is notoriously difficult as they result from an interplay between the complex rheology of the bioink, which is typically shear thinning [26–29], and the even more complex viscoelastic response of the cell itself [30–39]. Despite these difficulties, certain progress towards reliable theoretical estimates of the cell stress inside printing needles has been achieved [15, 18, 40]. As a starting point, the fluid shear stress profiles within printing nozzles have been computed theoretically [17, 21, 41]. Some experimental studies correlated such stress calculations with cell viability or functionality [15, 22, 40, 42–47]. These studies, however, investigated hydrodynamic stresses only up to the end of the printing nozzle. At the transition from the nozzle exit into the free strand, the flow profile transitions rapidly from a Poiseuille-like profile in the nozzle to a plug flow profile inside the free bioink strand. This transition is accompanied by sizable radial flows whose effect on cell deformation and therefore cell damage has so far not been experimentally or theoretically quantified.

In this work, we start with fully three-dimensional Lattice Boltzmann calculations for the flow profile of shear thinning fluids [41] at the exit of a printing nozzle. To investigate cell stress and strains inside and during exit from the printing nozzle, we then employ our recently developed hyperelastic cell model [30] which includes explicit two-way coupling between bioink and cellular mechanics, and show its qualitative match with experimental micrographs taken during the printing process. From these investigations, we finally develop simple methods to predict the cell stress and strains occurring during bioprinting processes, and specifically during nozzle exit, by only using the printing parameters, i. e., the nozzle diameter, the bioink rheology, and the volumetric flow rate, as input quantities. For this, we combine the classical theories of Jeffery [48] and Roscoe [49] with our semi-analytical flow computations of shear thinning bioinks in capillaries [41].

II. METHODS AND SETUP

A. Flow dynamics: Lattice-Boltzmann simulations

In our simulations, we employ a fully three-dimensional fluid dynamics solver. We use the implementation of the Lattice Boltzmann method [50] provided by the software

package ESPResSo [51, 52], which we extended with algorithms to allow for the simulation of free-slip surfaces [53] and shear thinning fluids [41]. Using an immersed-boundary algorithm [32, 54–56], we couple our cell model (section II C) to the flow.

B. Bioink rheology

The shear thinning rheology is considered an essential material property for bioinks, as it serves two purposes: first, the large viscosity of the material at rest provides the necessary mechanical stability of the printed construct itself. Second, the shear thinning properties allow the material to be printed at significantly lower pressure — considering the same printing speed —, thus reducing the overall hydrodynamic stresses acting on cells inside the nozzle.
We describe the viscosity as function of the rate of strain $|\dot{S}|$ according to a three-parameter simplified Carreau-Yasuda model, also known as Cross model [41, 57]:

$$\eta\left(|\dot{S}|\right) = \frac{\eta_0}{1 + \left(K|\dot{S}|\right)^{\alpha}} \tag{1}$$

Here, η_0 is the zero-shear viscosity and the exponent α characterizes the shear thinning strength of the bioink, with $\alpha = 0$ for a Newtonian fluid, and $\alpha > 0$ for a shear thinning fluid. The inverse of the time constant, K^{-1}, defines the rate of strain at which the viscosity is equal to $\eta_0/2$. $|\dot{S}|$ is calculated as the contraction of the rate of strain tensor $\dot{S}$ via

$$|\dot{S}| = \sqrt{2\dot{S}_{ij}\dot{S}_{ij}} \tag{2}$$

with the tensor elements

$$\dot{S}_{ij} = \frac{1}{2}\left(\frac{\partial u_i}{\partial x_j} + \frac{\partial u_j}{\partial x_i}\right). \tag{3}$$

The diagonal elements of $\dot{S}$ are the rates of elongation of the fluid along the coordinate axes, and the off-diagonal elements are the respective shear rates. We choose $\eta_0 = 10\,\mathrm{Pa\,s}$ and $K = 0.05\,\mathrm{s}$ for the zero-shear viscosity and the time constant, respectively. This parameter choice roughly resembles the values obtained for 2.5 % alginate hydrogels [26, 41, 58] which is a widely used bioink material, although other materials can exhibit similar shear-thinning properties. In order to investigate the influence of the shear thinning strength in our calculations, we pick six different values for α between 0 and 1 with $\alpha = 0.75$ [41] corresponding to the said alginate solution. The viscosity as function of the shear rate is depicted in figure 1(a). For an idealized, i.e. infinitely long, cylindrical nozzle, the velocity profile and the fluid stress σ_f can be computed according to [41][59] as shown in figure 1(b and c) with the pressure adjusted so as to ensure the same flow rate for each α. In our previous study [41], we introduced this method to calculate

FIG. 1. (a) Viscosity as function of the shear rate for the six different degrees of shear thinning ($\alpha = 0$, 0.15, 0.3, 0.45, 0.6,and 0.75). Squares indicate the maximum shear rate in the nozzle channel under the flow conditions used in our simulations (cf. section II D). (b) Corresponding velocity profiles for an average velocity of $5\,\mathrm{mm\,s^{-1}}$ inside the cylindrical printing nozzle. With increasing shear thinning strength, the velocity profile flattens at the center. (c) Corresponding fluid stress profiles. Stresses are linear with the radial position, and the maximum fluid stress decreases significantly with increasing α at constant flow rate.

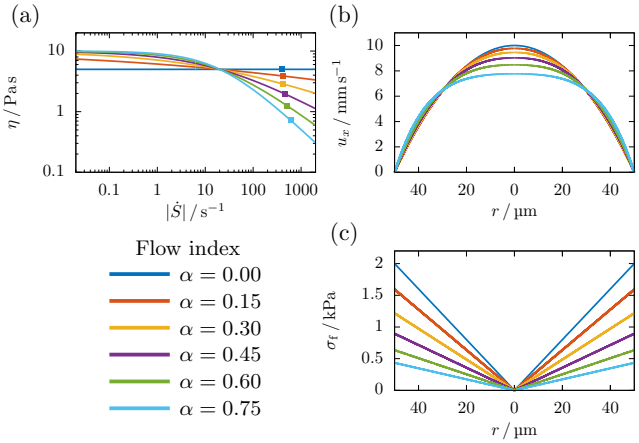

the velocity, shear rate, viscosity, and shear stress, profiles for an inelastic shear thinning fluid in a cylindrical nozzle. The central assumptions — a laminar, uni-axial, pressure driven, flow — are usually applicable for the description of bioink extrusion. In the following, we define the fluid stress as:

$$\sigma_\mathrm{f} = \eta\left(|\dot{S}|\right)|\dot{S}| \tag{4}$$

We note that, if a constant extrusion pressure was used for calculation, the fluid stress profile in figure 1(c) would be the same regardless of α [41].

C. Cell elasticity

1. *Hyperelastic cell model*

Our cell is modeled as hyperelastic continuum, with a sphere as equilibrium configuration. We provide extensive validation of the model in a previous publication [30]. This includes AFM and FluidFM® measurements on biological cells and hydrogel particles as well as comparison to analytical theories [38, 49] and previous numerical simulations in shear flow [32, 60].
As a hyperelastic model, we employ the neo-Hookean material model. This model is strain-hardening for compressive strain, e.g. in AFM experiments, but also for shear strains as occurring mainly in microfluidic experiments.

Its strain energy density is computed via [61, p. 100]

$$U = \frac{\mu}{2}(I-1) + \frac{\kappa}{2}(J-1)^2\,, \tag{5}$$

where $J = \det(F)$ is the determinant of the deformation gradient tensor $F_{ij} = \frac{\partial x_i}{\partial y_j}$ [61, p. 14, 18], with the undeformed and deformed vertex coordinates x_i and y_i, respectively. $I = J^{-2/3}\,\mathrm{tr}(F^\intercal F)$ denotes the second invariant of F. As elastic parameters we choose a shear modulus of $\mu = 1000\,\mathrm{Pa}$ and a Poisson ratio of $\nu = 0.48$. A simulation series with $\mu = 500\,\mathrm{Pa}$ is included in section S-9 of the Supplementary Material. The Poisson ratio near 0.5 provides sufficient incompressibility of the cell, while the shear modulus lies in the range typically found for mammalian stem cells [62]. In consistency with linear elasticity for small deformations, the shear and bulk modulus relate to the Young's modulus and Poisson ratio via

$$\mu = \frac{E}{2(1+\nu)} \quad \text{and} \quad \kappa = \frac{E}{3(1-2\nu)}\,. \tag{6}$$

The cell radius is chosen as $R_\mathrm{c} = 8\,\mu\mathrm{m}$ (6 in simulation units), and the mesh consists of 9376 tetrahedra.

In our numerical method, the interior of the cell is filled with the same fluid as the outside fluid. Together with the Neo-Hookean elasticity, this leads to an effectively viscoelastic cell response [30].

2. *Force calculation and flow coupling*

For numerical simulations, the spherical volume is uniformly tetrahedralized using the meshing software Gmsh [63]. The elastic forces acting on each vertex of one tetrahedron are obtained via differentiation of the strain energy density (5) with respect to the relative vertex displacement,

$$f_i = -V_0 \frac{\partial U}{\partial u_i}\,, \tag{7}$$

where V_0 denotes the reference volume of the tetrahedron and $u_i = y_i - x_i$. This approach is explained in detail in section 3.1 in [30].

The coupling between the cell model and the bioink is realized using an immersed-boundary algorithm [64, 65]. After computation of the cell vertex forces, they are transmitted into the fluid via extrapolation from the moving Lagrangian cell mesh onto the static Eulerian Lattice Boltzmann grid. The two-way coupling is completed through advecting the cell vertices with the local interpolated fluid velocity.

3. *Cell stress calculations*

In addition to the elastic forces, we are able to obtain the internal stress distribution inside our cell model. We compute the Cauchy stress tensor in each tetrahedron from the strain energy density and the deformation gradient tensor according to Bower [61, p. 97] as:

$$\sigma_{ij} = J^{-1} F_{ik} \frac{\partial U}{\partial F_{jk}} \tag{8}$$

For the neo-Hookean model in (5), this becomes

$$\sigma_{ij} = \frac{\mu}{J^{5/3}}\left(B_{ij} - \frac{1}{3}B_{kk}\delta_{ij}\right) + \kappa(J-1)\delta_{ij}\,, \tag{9}$$

where $B = FF^\intercal$ denotes the left Cauchy-Green deformation tensor.

In order to obtain a simple scalar observable to quantify the cell stress, we start from the local von Mises stress in each tetrahedron. The von Mises stress is an invariant of the Cauchy stress tensor and commonly used in plasticity theory to predict yielding of materials under multiaxial loading conditions through construction of a fictitious uniaxial loading. Using the principal stresses, i. e., the eigenvalues σ_1, σ_2, and σ_3, of the Cauchy stress tensor (9), we calculate [61, p. 48]

$$\sigma_\mathrm{vM} = \sqrt{\frac{1}{2}\Big[(\sigma_1-\sigma_2)^2 + (\sigma_2-\sigma_3)^2 + (\sigma_3-\sigma_1)^2\Big]}. \tag{10}$$

An alternative equivalent formulation to (10) is the contraction of the deviator of the Cauchy stress tensor $\sigma^\mathrm{dev}_{ij} = \sigma_{ij} - \frac{1}{3}\sigma_{kk}$. It reads:

$$\sigma_\mathrm{vM} = \sqrt{\frac{3}{2}\sigma^\mathrm{dev}_{ij}\sigma^\mathrm{dev}_{ij}}. \tag{11}$$

The total cell stress σ_vM is then computed by averaging the local von Mises stress over all tetrahedra in the cell model weighted by the undeformed volume of each tetrahedron.

4. *Validation of the cell stress calculation*

We validate our cell stress calculations using a linear shear flow setup: the simulation box with dimensions $10 \times 15 \times 5$ ($x \times y \times z$ in units of R_c) is bounded by two planes at $y = 0$ and $y = 15R_\mathrm{c}$, moving with a tangential velocity in $\pm x$-direction. This creates a linearly increasing velocity across the gap and thus a constant shear rate $\dot\gamma$ in the box. The shear rate is varied to achieve a range of fluid stresses up to 1.5 kPa, while the fluid viscosity ($\alpha = 0$) and the cell's shear modulus remain constant. In non-dimensional terms, this range corresponds to capillary numbers $\mathrm{Ca} = \frac{\sigma_\mathrm{f}}{\mu}$ between 0 and 1.5.

During the simulation, the initially spherical cell traverses through a series of ellipsoidal deformations before reaching a stationary state, at which the whole cell volume performs a tank-treading motion, i. e., the cell vertices rotate around the fixed ellipsoidal cell shape. In

FIG. 2. Comparison of the cell stress predicted by Roscoe [49] and the average cell stress of our model in shear flow. Insets show the stationary, tank-treading shape of the simulated cell at fluid stresses corresponding to Ca = 0.2, 0.6, and 1.2.

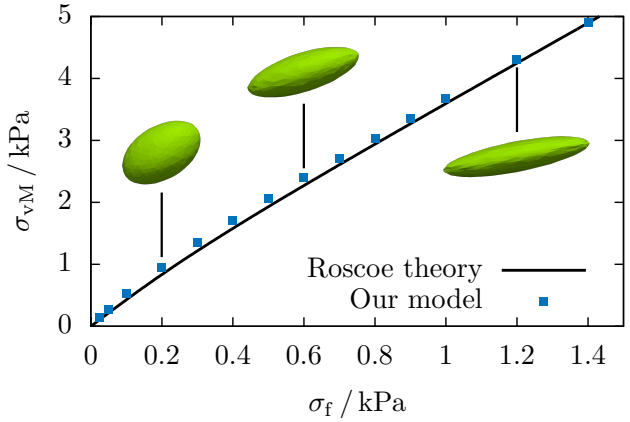

figure 2, we compare the elastic cell stress in the stationary state calculated by (10) to the analytical calculations of Roscoe [49] (detailed in section S-4) and find excellent agreement for a realistic range of fluid stresses.

In addition to the elastic stress, we compute the viscous contribution resulting from the fluid motion enclosed by the cell volume. This quantity is extracted from the Lattice-Boltzmann strain rate tensor field [41, 66] inside the cell using our method from [67] and averaging over the cell volume. In figure S-2 we show that the agreement of the numerically obtained viscous cell stress with Roscoe theory is equally good as for the elastic component.

We note that cell and fluid stress in figure 2 are time-independent and stationary. We further dissect their relation in detail in section III A.

D. Bioprinting simulations

The two essential parts of the bioprinting process are (i) the flow inside the nozzle channel and (ii) the flow transition at the nozzle exit. Both situations will be studied separately in this work.

1. *Nozzle channel*

We model the nozzle channel using a periodic cylindrical no-slip channel with a radius of $R = 50\,\mu\text{m}$ and length of 133 µm (37.5 and 100 in simulation units), as depicted in the left dashed box in figure 3. The shear thinning fluid dynamics are solved by the Lattice-Boltzmann method as described in section II A. No-slip boundary conditions are imposed at the channel wall. The flow is driven by a pressure gradient G along the nozzle axis. To compare the different bioinks detailed in section II B, we consider a fixed average velocity of $5\,\text{mm}\,\text{s}^{-1}$ (volumetric flow rate $\Omega = 3.93 \times 10^{-11}\,\text{m}^3\,\text{s}^{-1} \approx 141\,\mu\text{l}\,\text{h}^{-1}$). The corresponding pressure gradient is different for each α and is obtained according to [41]. Our input parameters as well as averaged and maximum quantities of the nozzle channel flow are listed in table I. We note that compared to common flow cytometry setups [31, 35], the channel radius in typical bioprinting applications is significantly larger, thus allowing cells to flow off-centered. To account for this, a single spherical cell is inserted at different radial starting positions of 0, $1.5\,R_c$, $3\,R_c$, and $4.5\,R_c$, as shown in figure 3.

2. *Nozzle exit*

The geometry of our simulations at the nozzle exit is depicted by the right dashed box in figure 3, the flow dynamics are again solved by the Lattice-Boltzmann method. The free bioink strand of length 933 µm (700 in simulation units) behind the nozzle exit is assumed to have the same radius as the inner radius of the nozzle channel, with free-slip boundary conditions applied at the fluid surface, which result in a plug motion of the bioink. This way we neglect the small extension of the bioink strand at the nozzle exit known as Barus effect or die swell [68]. Equal flow conditions as inside the nozzle channel are achieved by applying the average velocity of $5\,\text{mm}\,\text{s}^{-1}$ as normal velocity at the circular inflow and outflow planes, instead of a constant pressure gradient as used in the nozzle channel setup. We insert a single cell at different radial positions as explained above. The starting configuration of the cell is taken from the corresponding simulation of the nozzle channel setup, i. e., the cell is inserted in a deformed state close to the nozzle exit, as shown in the first frames in figure 9.

FIG. 3. Schematic of the bioprinter setup: the nozzle channel is bounded by a cylindrical wall and periodic in x-direction. Single cells are inserted at different radial offsets. The nozzle exit consists of the transition from the no-slip nozzle channel to the free bioink strand. Cells are initialized in a deformed state close to the transition.

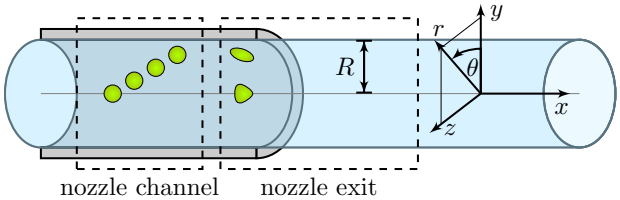

TABLE I. Flow parameters of our bioprinter setup with a nozzle radius of 50 µm and an average velocity of 5 mm s^{-1}.

α	G	$\sigma_\mathrm{f}^\mathrm{max}$	$\sigma_\mathrm{f}^\mathrm{avg}$	u_x^max	$\lvert\dot{S}\rvert^\mathrm{max}$	$\lvert\dot{S}\rvert^\mathrm{avg}$
–	Pa m^{-1}	kPa	kPa	mm s^{-1}	s^{-1}	s^{-1}
0.00	8.00×10^7	2.00	1.33	10.0	400	267
0.15	6.37×10^7	1.59	1.06	9.77	410	265
0.30	4.87×10^7	1.22	0.81	9.45	426	262
0.45	3.58×10^7	0.89	0.60	9.03	454	257
0.60	2.54×10^7	0.63	0.42	8.47	502	251
0.75	1.74×10^7	0.44	0.29	7.77	604	242

III. RESULTS

A. Dissecting the notion of "cell stress"

In many situations, it has become a common approach to invoke the term "cell stress" and to equate it directly to the fluid stress, i. e., the viscosity multiplied by the local shear rate at the cell position. Here, we show that this simple approach, while being correct in its order of magnitude, hides a good amount of the more complex features of intracellular stress. To illustrate this, we apply the theory of Roscoe [49] for a cell in linear shear flow, which accurately describes cell behavior in our numerical simulations (see section II C 4) and in microchannel experiments [69], provided that the cell does not flow in the channel center where the shear rate approaches zero.

Inside a flowing cell, two qualitatively different kinds of stress arise. The first kind are viscous stresses that are caused by frictional motion (i. e. tank-treading) of the cell interior. The second kind are elastic stresses that are caused by the deformation (e. g. shearing and stretching) of the cell. The magnitude of the former are governed by the cell's internal viscosity, while the latter are set by its elastic moduli. We note that, in principle, both a cell's viscosity and its elasticity can be non-homogeneous, i. e., they vary spatially throughout the cell, and anisotropic, i. e., they depend on direction, e. g., due to alignment of certain cytoskeletal elements. Here and in most other situations, these more complicated effects are neglected, and the cell is considered a homogeneous, isotropic viscoelastic medium. Furthermore, as shown in [49] for a cell in pure shear flow, stability requires that viscous and elastic cellular stresses do not vary between different locations inside the cell. Their value can be calculated from Roscoe theory as detailed in the Supporting Information (eqs. (S-43) and (S-48)).

We start with the limiting case of low shear rates corresponding to small capillary numbers $\mathrm{Ca} = \frac{\sigma_f}{\mu} \to 0$. In this limit, fluid stresses are not sufficient to cause significant cell deformation, and the cell essentially remains spherical. Indeed, the classical calculation for a rigid sphere in shear flow detailed in section S-6 of the Supporting Information yields a surprisingly accurate description of this limit. The cell rotates as a rigid body, which implies the absence of internal frictional motions

FIG. 4. Components of the cell stress tensor σ_{ij} normalized by the undisturbed fluid stress σ_f across multiple orders of magnitude of the Capillary number computed using the Roscoe theory. Elastic stresses are shown in blue, viscous stresses are shown in purple. Components not appearing in the figure remain zero throughout. The directions 1, 2, 3 refer to a body-fixed coordinate system as indicated by the insets.

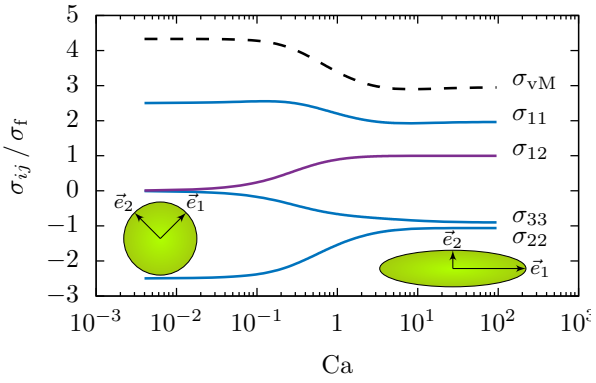

and thus leads to a vanishing viscous cell stress as shown by the purple curve in figure 4. Similarly, elastic stresses in the vorticity direction vanish as shown by the σ_{33} component in figure 4. A positive stress appears in a direction inclined by 45° with respect to the flow direction (σ_{11}), with a corresponding negative stress in the perpendicular direction. Their magnitude is precisely 5/2 times the undisturbed fluid stress σ_f, which exactly corresponds to the situation of the rigid sphere as shown in section S-6.

In the opposite limit of high shear rates ($\mathrm{Ca} \to \infty$), the situation becomes more involved. In agreement with our numerical simulations shown in figure 2, the cell becomes strongly elongated and aligned in flow direction. Due to the persisting tank-treading motion, internal viscous stresses do not disappear. Instead, the flatness of the cell shape minimizes the cell's disturbing influence on the surrounding fluid flow, and indeed the cell's internal viscous stress now becomes equal to the undisturbed fluid stress, as can be seen by the purple curve in figure 4. Maintaining the flattened cell shape, however, in addition requires elastic stresses. As shown by the blue curve in figure 4, all three elastic stress components arise with their ratios being $\sigma_{11} : \sigma_{22} : \sigma_{33} = 2 : -1 : -1$. The positive stress in flow direction, σ_{11} is balanced by negative stresses in the two other directions. These ratios can easily be understood by the analogy with a uniaxially stretched beam as detailed in section S-7 of the Supporting Information.

Despite this complexity, it may be helpful in many situations to have at hand a single measure to quantify "cell stress". Such a measure can be provided by the elastic von Mises stress σ_vM given in (11) which we include as the black dashed line in figure 4. The ratio $\sigma_\mathrm{vM}/\sigma_\mathrm{f}$ transitions from $\frac{5}{2}\sqrt{3}$ at low to 3 at high Ca. In the intermediate range, the proportionality factor is situated between these two limits. As can also be deduced from

figure 2, the relation between σ_{vM} and σ_f changes the most in the range of $0.1 < Ca < 1$, while otherwise an approximately linear dependency emerges.

From the results of this subsection, we conclude that the common approach of equating (undisturbed) fluid stress to "cell stress" can be a reasonable approximation for low and high Capillary numbers.

B. Cell flowing inside the nozzle channel

Using our setup described in section II D 1, we investigate the cell behavior and the cell's internal stress distribution during the flow inside the nozzle. Depending on the initial radial position, we observe two modes of deformation of the cell:
(i) A cell flowing along the axis of the nozzle channel assumes an axisymmetric bullet-like shape, as can be seen in figure 5(a) and (b) for a Newtonian and a highly shear thinning bioink, respectively. In both cases, the radial dependency of the internal cell stress is highly non-homogeneous and resembles the linearly increasing fluid stress of the undisturbed liquid (cf. figure 1(c)), since the cell's surface has to balance higher fluid shear stresses for increasing r in the stationary state. However, the magnitude of the stress and likewise the cell deformation decrease significantly when the shear thinning index α is increased at the same volumetric flow rate. This finding may explain earlier experimental observations in which more shear thinning bioinks were found to increase cell survival in bioprinting [22, 44] when the pressure was reduced to ensure equal flow rates for all conditions.
(ii) A cell flowing off-center deforms into an approximately ellipsoidal shape exhibiting tank-treading motion. Due to the curvature of the flow, the cell migrates towards the channel center (sometimes referred to as margination), where it eventually assumes the bullet-like shape discussed in the previous paragraph. A sequence of simulation snapshots for a cell flowing in the Newtonian bioink is shown in figure 5(c), where the internal stress distribution of the off-centered cells can be observed. Figure 6(a) shows the corresponding development of the radial position over time starting from an offset of 36 µm. With increasing shear thinning strength, i. e., decreasing pressure gradient, the cell takes longer to migrate towards the channel center.
In figure 6(b) the same situation is studied for a constant pressure gradient. We find that here the migration speed of the cell becomes independent of the shear thinning properties of the bioink and thus conclude that cell migration is determined predominantly by the applied pressure gradient and not the flow speed. This finding can be understood since the stress, and thus the forces, that the cell feels are directly determined by the local fluid stress. Therefore, when printing bioinks with different rheology at the same printing pressure, the radial cell distribution will not change. When printing bioinks with increasing shear thinning strength at the same flow rate, by contrast, fewer cells will migrate to the center of the nozzle.
The ellipsoidal cell shape during the migration allows us to compare the cell stress to the prediction of the Roscoe theory [49] detailed in section II C 4. In figure 6(c) we plot the development of the cell stress in a Newtonian bioink when cells are initially placed at different offsets from the nozzle center. Due to the migration of the cells towards the channel center, the local fluid stress experienced by a given cell decreases monotonically over time. In order to directly compare with the prediction of Roscoe theory, which assumes a constant fluid shear stress, we choose this local fluid stress as abscissa. Cells start at offsets of 12 µm, 24 µm and 36 µm corresponding to initial fluid stresses of $\sigma_f \approx 0.5$ kPa, 1.0 kPa, and 1.5 kPa, respectively. The initial shape is undeformed and thus $\sigma_{vM} = 0$ for $t = 0$. The cell first experiences a transient of large stresses and quickly relaxes towards the cell stress predicted by Roscoe where the curved flow is locally approximated as a pure shear flow, as indicated by the square symbols. Due to the migration towards the channel center, the cell stress decreases with time and radial position. The curves of all initial radial offsets perfectly agree with the prediction of the Roscoe theory, as long as the cell's radial position is larger than R_c. When the cell is close to the channel center, the local shear flow approximation becomes invalid, thus causing deviations from the theoretical prediction.
A similar plot is provided for shear thinning bioinks in figure 6(d) where the stress of cells starting at offset $4.5R_c$ for different α is compared with Roscoe theory. We again find excellent agreement with the Roscoe theory independent of the shear thinning strength. This finding may seem surprising at first, as the theory of Roscoe is designed for purely Newtonian fluids surrounding the cell, but stays valid for shear thinning bioinks as well. This demonstrates that the key property determining cell motion is indeed not the shear rate, but rather the shear stress. The plots for the remaining cell offsets and bioinks are included in the SI (cf. figure S-3).

C. Analysis of the flow field at the nozzle exit

In this section, we investigate the influence of the shear thinning rheology of the bioinks introduced in section II B on the undisturbed (cell free) flow field at the nozzle exit, where the transition from nozzle channel to the free bioink strand causes additional radial flows. We use the second setup described in section II D, without a cell, and run the calculations until the flow becomes stationary.
In figure 7(a) and (b), we show x-y-slices of the velocity profiles for the axial and radial velocity, respectively, at different values of the shear thinning parameter α. From top to bottom, the shear thinning strength of the fluid increases, while the flow rate is kept constant. The axial velocity component in figure 7(a) shows the same trend for increasing α as seen in figure 1(b): the flow de-

FIG. 5. Internal stress distribution for a cell flowing at the center of the nozzle channel in (a) a Newtonian fluid and (b) a strongly shear thinning fluid. (c) Internal stress distribution and radial migration of an off-centered cell towards the axis of the nozzle channel in a Newtonian bioink. The bottom labels give the axial distance traveled during the time given by the top labels.

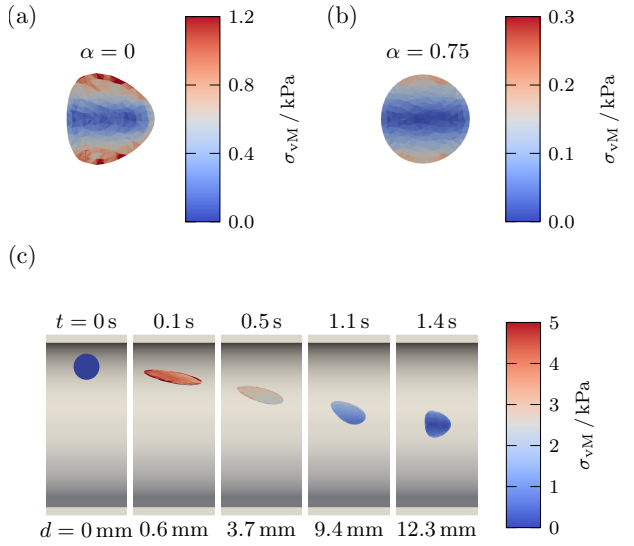

velops a central plateau inside the nozzle channel which at the nozzle exit transitions into the plug flow inside the bioink strand. Indeed, as shown in figure 7(c), the ratio $u_x^{\max}/u_x^{\text{avg}}$ between the maximum velocity inside the nozzle channel and the average velocity assumes the Poiseuille value of 2 at $\alpha = 0$ and decreases towards the plug-flow value of 1 for increasing shear thinning strength.

The second column, figure 7(b), shows the corresponding radial flow components. Due to the radial symmetry, they vanish at the center and increase towards the boundary, showing a drop-like shape with its tip pointing to the position of the nozzle orifice, where the boundary conditions change. The radial flow components decrease with increasing α, since the fluid has to be displaced less due to smaller axial velocity difference across the transition. Figure 7(d) quantifies this observation by comparison of the maximum radial flow velocity at the exit with the average axial flow. Combining the axial and radial flows, streamlines are computed in order to visualize the fluid motion in the stationary state. As can be seen in the overlaying lines in figure 7(a) and (b), the streamlines show very similar elongational behavior for all α at the nozzle exit due to the simultaneous decrease of the axial and the radial flow component. They are, however, not exactly equal, since the maximum axial and radial velocities scale slightly differently with α. Finally, comparing the ratio of axial and radial velocities, we find that the maximum radial flow velocity is always about 10 % of the maximum axial flow velocity, roughly independent of α.

FIG. 6. Radial migration r (center-of-mass) of a cell starting near the nozzle wall for different shear thinning strengths (see (d) for color labels) with (a) constant flow rate and (b) constant pressure gradient ($G = 1.14 \times 10^7\,\text{Pa}\,\text{m}^{-1}$). For constant G, the migration speed is almost independent of α. (c,d) Cell stress as function of the local fluid stress compared to the Roscoe theory (black line). Due to the radial migration of the cell, the cell experiences a continuous change of the local fluid stress over time. (c) The cell starting at different offsets (from right to left: $4.5R_c$, $3R_c$, and $1.5R_c$) in the Newtonian fluid. The duration of the deformation from the spherical reference shape to the approximately elliptical shape is given by the points. (d) Cells starting at offset $4.5R_c$ for bioinks with increasing shear thinning strength in comparison with the Roscoe theory. For details, see text.

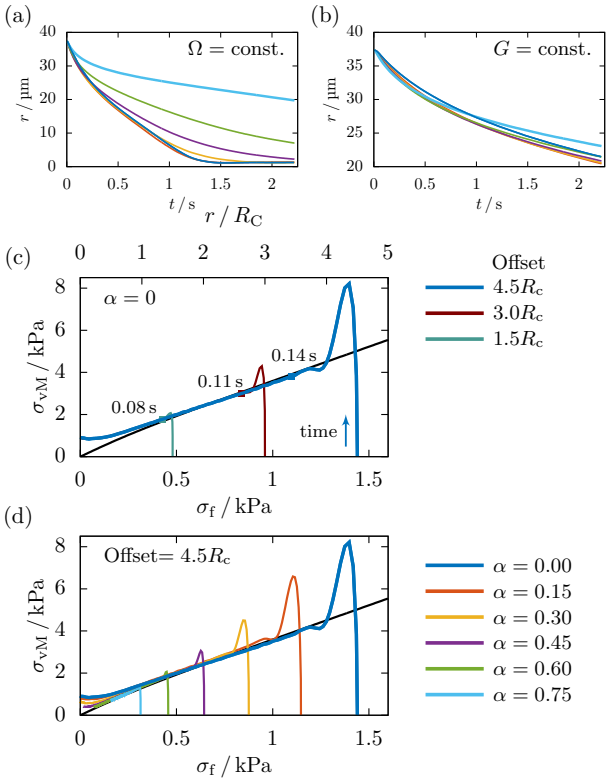

The fluid stress along the axial direction for different offsets is shown in figure 8 for $\alpha = 0$ and $\alpha = 0.75$. In addition to the total fluid stress, we plot the shear and elongational component separately. To do so, we first decompose the rate of strain tensor into the shear and elongational components

$$\dot{S}_{ij} = \dot{S}_{ij}^{\text{shear}} + \dot{S}_{ij}^{\text{elong}}\,, \tag{12}$$

where $\dot{S}^{\text{elong}}$ is a diagonal tensor and $\dot{S}^{\text{shear}}$ contains only off-diagonal elements. Using this decomposition — further details can be found in section S-3 —, we can define the shear and elongational components of the fluid stress as

$$\sigma_{\text{f}}^{\text{shear}} := \eta\Big(|\dot{S}|\Big)\sqrt{4\dot{S}_{xr}^2} \tag{13}$$

FIG. 7. x-y-slices of the flow at the nozzle exit for increasingly shear thinning fluids: (a) axial velocity component and (b) radial velocity component with streamlines as overlay. (c) The ratio of maximum axial velocity inside the nozzle to the average flow velocity as function of the shear thinning strength α. (d) The ratio of maximum radial velocity after the nozzle exit to the average flow velocity as function of α.

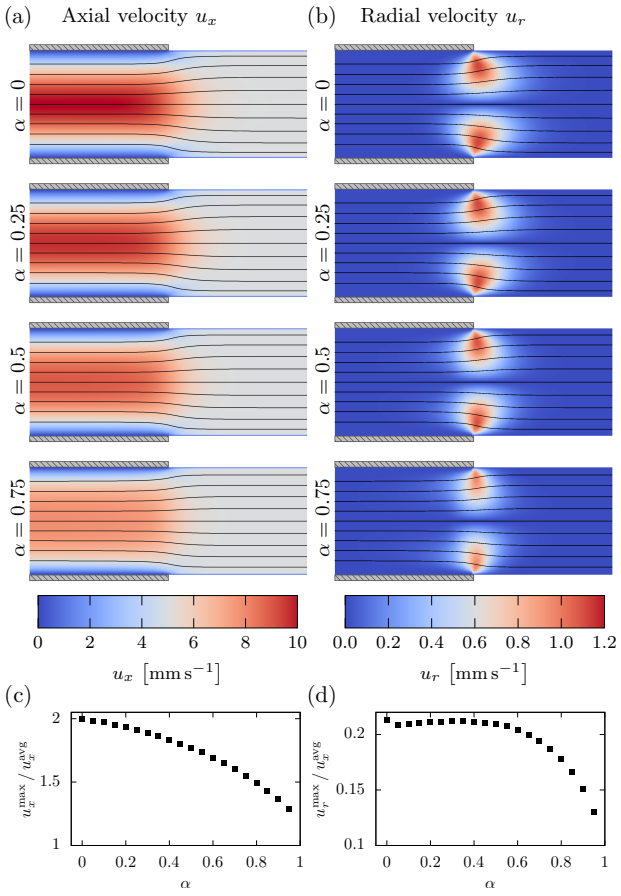

and

$$\sigma_{\mathrm{f}}^{\mathrm{elong}} := \eta\Big(|\dot{S}|\Big)\sqrt{2(\dot{S}_{xx}^2 + \dot{S}_{rr}^2 + \dot{S}_{\theta\theta}^2)}\,. \qquad (14)$$

Note that $\dot{S}_{x\theta} = \dot{S}_{r\theta} = 0$, since no azimuthal flow components are present, but that nevertheless $\dot{S}_{\theta\theta} \neq 0$ as detailed in section S-3. Thus, the total fluid stress is obtained from (13) and (14) via:

$$\sigma_{\mathrm{f}} = \sqrt{\left(\sigma_{\mathrm{f}}^{\mathrm{shear}}\right)^2 + \left(\sigma_{\mathrm{f}}^{\mathrm{elong}}\right)^2} \qquad (15)$$

Along the channel center (cf. figure 8(a) and (e)), all shear components of the stress vanish, leaving only the elongational ones, which show a clear peak at the exit. Considering the symmetry, this peak is caused solely by the axial flow deceleration.
With increasing radial offset from the center, as can be seen in figure 8(b-d and f-h) for offsets $1.5R_{\mathrm{c}}$, $3.0R_{\mathrm{c}}$, and

FIG. 8. Decomposition of the fluid stress in shear (13) and elongational component (14) at the nozzle exit for the (a-d) Newtonian fluid and (e-h) the highly shear thinning bioink with $\alpha = 0.75$. x denotes the axial distance from the nozzle orifice.

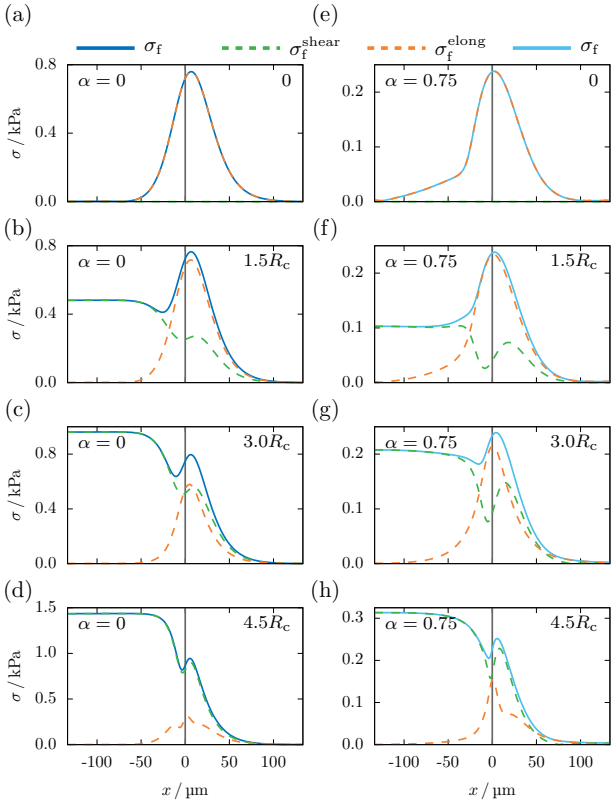

$4.5R_{\mathrm{c}}$, the influence of the shear components increases significantly. It can also be seen that the peak of the fluid stress is not only determined by the elongational flow components, but also partly by the shear component $\dot{S}_{xr} = \frac{1}{2}\left(\frac{\partial u_x}{\partial r} + \frac{\partial u_r}{\partial x}\right)$. This is further discussed in section S-2 in the SI. The radial offset at which the shear stress inside the nozzle channel exceeds the magnitude of the fluid stress peak depends on the shear thinning strength of the bioink: when comparing figure 8(c) and (g), the stress peak for the Newtonian fluid is already smaller than the fluid stress inside the nozzle channel, while for $\alpha = 0.75$ it is still higher. When selecting shear thinning bioinks in bioprinting, it is thus important to keep in mind that the relative significance of the radial flows at the nozzle exit, both elongational and corresponding shear components, increases when a stronger shear thinning bioink is used.

D. Cell flowing through the nozzle exit

In this section, we investigate the influence of the flow transition on cells passing the exit of the printer nozzle using our computer simulations and actual micrographs

of cells flowing through a real 3D bioprinter nozzle. As discussed in section III C, elongational flow components on a short length scale ($\approx 2R$) occur at the nozzle exit. These act in different ways on the cell, depending on its radial position when passing the transition:

1. *Centered cell*

Flowing along the center of the channel, the cell experiences symmetric flow conditions also when passing through the nozzle exit. The deceleration in flow direction leads to an axial compression, while the radial flow stretches the cell in radial direction, leading to an oblate deformation of the cell. As can be seen in the simulation snapshots in figure 9(a) and (b) for the centered flowing cell, its stress uniformly increases inside the whole cell volume during this elongational deformation. After the transition, the cell quickly relaxes towards its spherical equilibrium shape inside the bioink strand.

Next, we assess the cellular stress resulting from the various flow regimes and ink properties which may affect cell survival and health. As can be seen in figure 10(a), an increase in the shear thinning strength of the bioink leads to a decreasing cell stress inside the nozzle channel, as expected from the experimentally observed increased cell survival in more shear thinning bioinks [22, 44]. In contrast to these beneficial effects of shear thinning inside the nozzle, we find that the importance of the elongational stress peak at the nozzle exit notably increases relative to the stress inside the nozzle when α is increased: for the Newtonian case (dark blue line figure 10(a)), cell stress increases by approximately 50% from 0.9 kPa to 1.3 kPa during the transition, while for the most shear-thinning bioink (light blue line) it increases six-fold from 0.1 kPa to 0.6 kPa.
Besides cell stresses, an important measure to assess cell damage is cell strain, see e. g. [14]. Due to the symmetry at the channel center, we define an axial strain $\alpha_1 := l_x/(2R_c)$ and a radial strain $\alpha_2 := l_r/(2R_c)$, as the maximum elongation of the cell in the considered direction divided by the cell's reference diameter. As shown in figure 11, the behavior of these cell strains is similar to that of the cell stresses in the paragraph above. Independent of the shear thinning exponent α, the axial strain α_1 of the cell's bullet shape inside the nozzle channel is almost negligible, and only a clear peak in deformation is observed when passing the nozzle exit. The radial strain α_2, on the other hand, already starts with a significant difference from the equilibrium shape. A cell suspended in a highly shear thinning bioink flowing at the nozzle center therefore experiences only the elongational flow right at the nozzle exit, while remaining almost undeformed otherwise.

2. *Off-centered cell*

We now observe a cell flowing near the nozzle wall Here, the elongational flow at the nozzle exit is combined with shear components inside the nozzle. When passing the transition, the cell is pushed in radial direction leading to a non-ellipsoidal change in shape, before it relaxes towards the equilibrium shape in the bioink strand. An overall decrease of the cell stress when passing through the transition can be observed in the simulation snapshots for the off-centered flowing cell in figure 9(a) and (b). Compared to centered cells in figure 10(a), the importance of elongational relative to shear stress decreases for off-centered cells as shown in figure 10(b)-(d). Indeed, for off-centered cells, the relaxation from the shear-dominated axial flow inside the nozzle channel to the stress-free plug flow in the bioink strand is the most significant effect.
We determine this relaxation time scale τ for every simulation by fitting an exponentially decaying function to the cell stress versus time data (see SI figure S-8). Figure 10(e) shows the obtained relaxation times for all cell offsets as function of α. We find that the relaxation time increases with increasing shear thinning strength α when keeping η_0 constant. This is caused by the larger viscosity of the bioinks with higher α for low rates of strain (cf. figure 1), resulting in a higher resistance of the fluid against the cell shape relaxation. Similar to our observations of the fluid stress at the nozzle exit in section III C, we find in figure 10(a to d) that the cell stress peak at the nozzle exit becomes more significant compared to the cell stress inside the nozzle channel when the cell is closer to the center and for stronger shear thinning fluids.

3. *Microscopy experiments*

To verify our numerical predictions, we image with a high speed camera a bioink strand with cells flowing out of a printing nozzle into a larger reservoir of water. Details of this imaging setup are included in the SI (cf. section S-1). With the objective focused at the tip of the nozzle (inner radius 100 µm), the micrograph in figure 9(c) shows cells suspended in a strand of 2 % alginate bioink during extrusion at a flow rate of 10 µl s^{-1}. As can be seen in the marked areas in figure 9(c), cells flowing close to the center exhibit a radially elongated change of shape, while cells flowing near the nozzle wall show an axial elongation. In accordance with our simulations, we observe the cells in the experiment relaxing towards their spherical stress-free shape shortly after the nozzle exit.

E. Prediction of elongational stress, cell stress and cell strain during bioprinting

The methods employed in sections III B, III C, and III D lead to accurate predictions for important param-

FIG. 9. Internal cell stress distribution of cells flowing at different offsets through the nozzle exit in (a) the Newtonian fluid and (b) the shear thinning bioink with $\alpha = 0.75$. (c) Experimental image of cells exiting a 100 µm radius nozzle in 2 % alginate bioink. Left green boxes indicate radially/axially elongated cells flowing in/off-center, respectively. Right green box indicates a cell after relaxation back to equilibrium. Movies of both simulation and experiment can be found in the supplementary material.

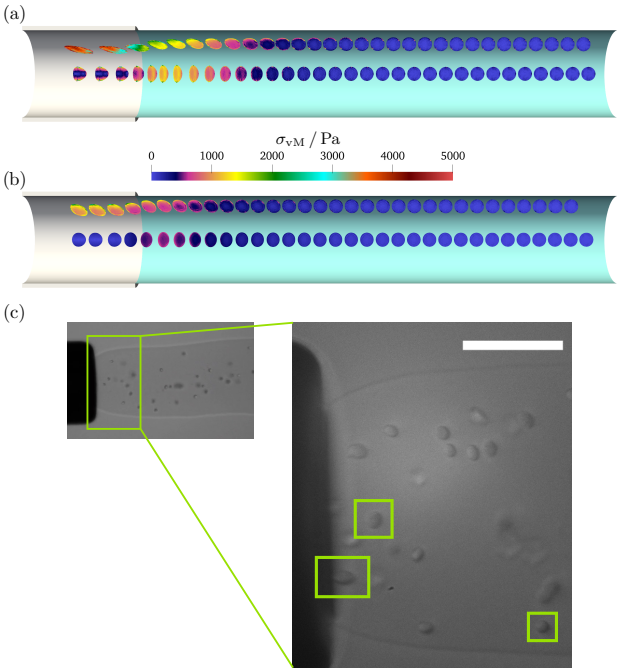

FIG. 10. Change of the cell stress when passing through the nozzle exit and flowing in the free bioink strand for increasingly shear thinning bioinks. From (a) to (d), the data is given for the initial cell's radial offsets 0, $1.5R_c$, $3R_c$, and $4.5R_c$. (e) Relaxation times τ of the cell stress when flowing in the free bioink strand as function of α and the initial radial cell offset.

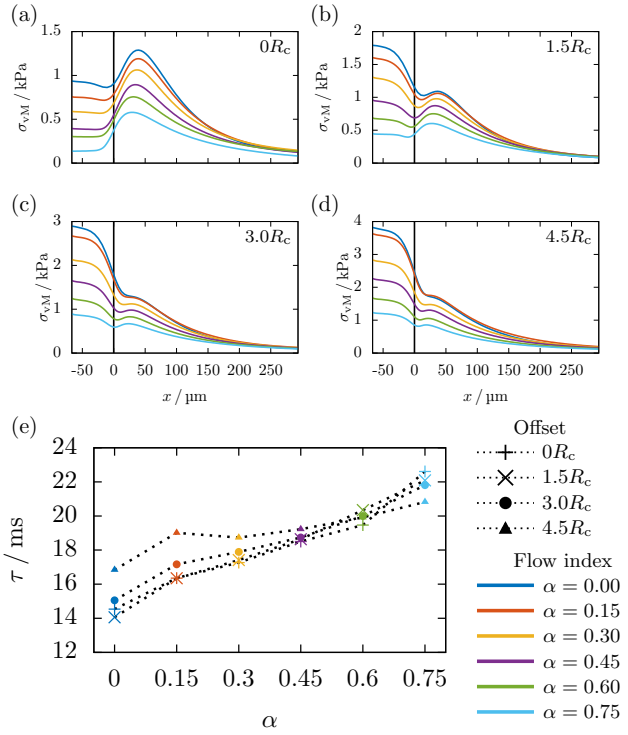

eters such as cell strain or stress, but require numerical simulations with specialized software. As a practical tool, we develop in the following a simpler yet still accurate method to predict important cell quantities from the printing parameters only.

1. *Elongational fluid stress at the nozzle exit*

To quantify the importance of elongational effects, we define the average elongational fluid stress $\bar{\sigma}_f^{elong}$ which we obtain by averaging σ_f^{elong} from the simulations along the nozzle axis in an interval of $\mp R$ around the peak seen in figure 8(a) and (e). In figure 12 we plot $\bar{\sigma}_f^{elong}$ as function of the shear thinning strength of the fluid. As would be expected from the decreasing pressure gradient, the elongational stress monotonously decreases with α. In order to obliviate the need for full numerical simulations of the entire flow field in practice, we now show that a good estimate for $\bar{\sigma}_f^{elong}$ can be obtained by using a much simpler method for flow field computations [41].

For this, we assume that the length of the transition is equal to the nozzle diameter $2R$, as can be verified by comparing with figure 7(a) and (b) and figure 8(a) and (e). Starting from the velocity profile of [41], the change in axial velocity along this length then gives the approximate elongation rate at the nozzle exit:

FIG. 11. Cell strain for a cell flowing in the center (a) α_1 in x-direction and (b) α_2 in r-direction at the nozzle exit for the different bioinks. The colors correspond to the flow index as in figure 10.

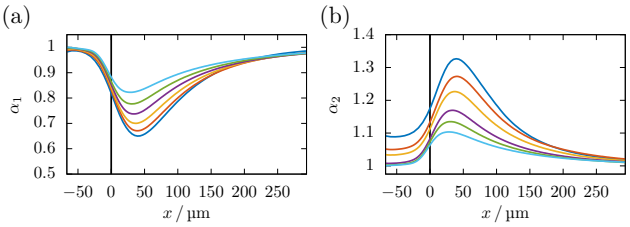

$$\dot{\varepsilon} \approx \frac{u_x^{max} - u_x^{avg}}{2R} \tag{16}$$

Next, we calculate the stress assuming elongational flow conditions, i. e., $\dot{S}_{xx} = -2\dot{S}_{rr} = -2\dot{S}_{\theta\theta} = -\dot{\varepsilon}$, via

$$\bar{\sigma}_f^{elong} = \eta\left(\sqrt{3}\dot{\varepsilon}\right)\sqrt{3}\dot{\varepsilon} \tag{17}$$

which is derived in the SI (cf. section S-3). This approximated average elongational stress is in very good agreement with the full numerical simulation of the nozzle exit, as shown in figure 12.
We use this approximation to further estimate the elongational cell strain and stress for centered flowing cells at the nozzle exit in the next section.

2. *Cell stress and strain for centered cells*

We proceed with an estimation of the maximum stress and strain experienced by cells while flowing inside the nozzle as well as during their transition into the free strand at the nozzle exit.

Starting with the latter, we focus on cells flowing at or close to the nozzle center where (as we have shown in figure 8(a), (b), (e), and (f) above) elongational stresses are the most significant fluid stress contribution. The theories of Jeffery and Roscoe [48, 49] contain a solution for the cell strains α_1 and α_2 in a stationary elongational flow (cf. section S-4 B). It reads

$$\frac{2}{\sqrt{3}}\frac{\bar{\sigma}_{\mathrm{f}}^{\mathrm{elong}}}{\mu} = \left(\alpha_1^2 - \frac{1}{\alpha_1}\right)\int_0^\infty \frac{\lambda\,\mathrm{d}\lambda}{\left(\frac{1}{\alpha_1}+\lambda\right)^2(\alpha_1^2+\lambda)^{\frac{3}{2}}} \tag{18}$$

and can be solved numerically for α_1 as function of the elongational fluid stress and the cell's shear modulus. The other cell strains are $\alpha_2 = \alpha_3 = \alpha_1^{-1/2}$ due to symmetry. Using the elongation rate from (17) as input value, we compare the theoretical values with the data obtained from the full numerical simulations in figure 13(a). We note that the theory slightly, but consistently, overestimates cell strains. Indeed, since the elongational flow is experienced by the cell for only a short time span while the theory assumes a stationary elongational flow, this overestimation is to be expected. Interestingly, and in line with what has already been observed in figure 6, Roscoe theory yields surprisingly accurate predictions even for highly shear thinning inks. We again attribute this to the central role of stresses, instead of flow rates, for the cell deformation process in printing nozzles when these are large compared to the radius of the cell. With our approximation consistently over-estimating the simulated results, it can be considered as practical upper limit for predicting cell survival.

As a consequence of the stationarity condition assumed by Roscoe theory, it would predict unrealistically large cell strains in the case of printing velocities higher than the 0.5mm/s used in this work. In reality, however, the flow through the nozzle exit is highly transient and the stationary state is never attained. To assess nevertheless the effect of printing speed, we perform additional simulations for cell flowing centered through the nozzle at $1\,\mathrm{cm\,s^{-1}}$ to $10\,\mathrm{cm\,s^{-1}}$ average extrusion velocity, in order to cover the typical range of 3D bioprinting speeds. Figure 14(a) shows the resulting peak cell strains at the exit from full numerical simulations in comparison to our estimate for 0.5mm/s in figure 13(a). It is apparent that a variation of more than one order of magnitude in flow velocity does hardly affect the cell strains, since the higher velocities significantly decrease the time span during which the high elongational stresses are acting on the cell. Hence, the printing speed does practically not affect the elongational strains occurring during printing.

Based on this estimate for cell strain, we proceed to estimate the corresponding cell stress for centered cells. For this, the fluid elongational stress from (17) is fed into the elongational Roscoe theory given by eqs. (18) and (S-52). The result is in good agreement with the full numerical simulations as shown in figure 13(b) for centered cells (green line).

3. *Cell stress and strain for off-centered cells*

For off-centered cells, we have shown in figure 10(d) that shear components inside the nozzle are an important contribution to the overall cell stress, especially inside less shear thinning bioinks, where they substantially exceed the stress caused by elongational flows at the nozzle exit. We next estimate this overall maximum cell strain and stress.

Due to their almost ellipsoidal shape, we choose as strain measure for the off-centered flowing cells now the ellipsoid's major and minor semi-axis α_1' and α_2', which are obtained through computing the equivalent ellipsoid from the deformed cell's inertia tensor, as detailed in [30].

Starting from the fluid shear stress obtained from our earlier work [41], we employ the shear part of Roscoe theory in (S-45) and (S-47) and plot the resulting stresses and strains for cells starting at $1.5R_\mathrm{c}$, $3R_\mathrm{c}$, and $4.5R_\mathrm{c}$ in figure 13(c,d). Again, we observe very good agreement with the simulations from section III D(ii).

Upon increasing the average flow velocity by more than one order of magnitude in figure 14(b), we find that cells flowing at maximum radial offset in Newtonian bioinks are not able to attain a stable state while flowing inside the nozzle channel. However, this limitation is solely a result of the large viscosity of the hypothetical Newtonian fluid, and would not affect a real printing process. With increasing shear thinning strength, as shown in figure 14(b), a stable cell shape can be achieved also for high flow velocities of $10\,\mathrm{cm\,s^{-1}}$. The maximum cell strains are accurately predicted by Roscoe theory.

IV. CONCLUSION

In this work, we investigated the cell stress and strain and the bioink flow behavior during a 3D bioprinting extrusion process using Lattice-Boltzmann numerical simulations together with corresponding qualitative experiments. The two scenarios considered were the flow inside the nozzle channel as well as at the nozzle exit,

FIG. 12. The average elongational stress $\bar{\sigma}_f^{elong}$ across the nozzle exit from figure 8(a and e) can be estimated from (17).

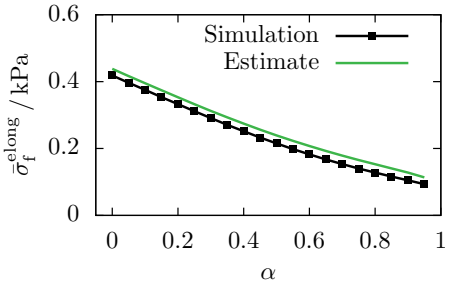

FIG. 13. (a) The peak strain and (b) cell stress for centered flowing cells at the transition can be approximated using our estimate of the average elongational fluid stress from (17) and the Jeffery and Roscoe theories for a cell in an elongational flow from section S-4 B. For off-centered cells, our flow calculations inside the nozzle channel and the theory of Roscoe for a cell in shear flow.

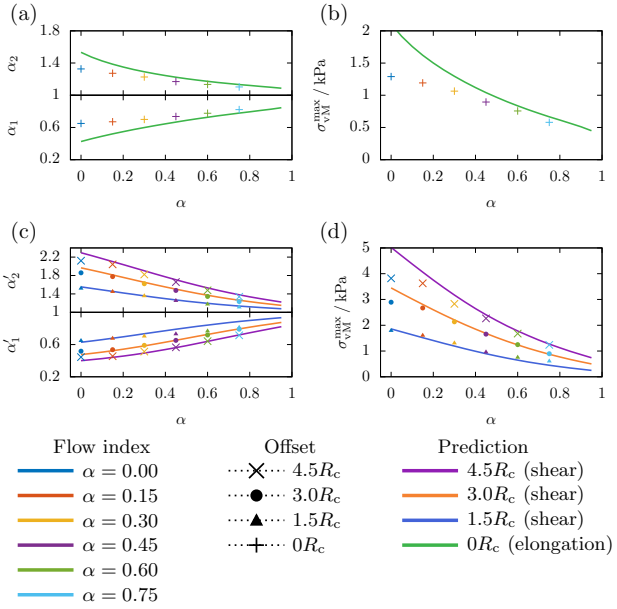

where the flow transitions into the free bioink strand.

During the first stage of the printing process while cells are flowing inside the printing nozzle, our simulations showed a bullet-like deformation for cells in the center of the channel and an ellipsoidal shape for cells flowing off-center. The latter can be understood on the basis of the classical theory of Roscoe [49] which relates cell stress to the local fluid stress. Interestingly, our simulations demonstrate that these relations hold even in realistic shear thinning bioinks, even though they were originally designed for Newtonian fluids only. The radially inward-directed migration of the cell due to the shear forces was also found to be independent of

FIG. 14. (a) Peak elongational cell strain for centered flowing cells passing the transition for an average extrusion velocity of $1\,\mathrm{cm\,s^{-1}}$, $2\,\mathrm{cm\,s^{-1}}$, $5\,\mathrm{cm\,s^{-1}}$, and $10\,\mathrm{cm\,s^{-1}}$ in comparison to the data of figure 13(a) for $5\,\mathrm{mm\,s^{-1}}$. (b) Maximum cell strain for cells flowing off-centered at $4.5\,R_c$ for increasing velocities is in accordance with the prediction of the Roscoe theory.

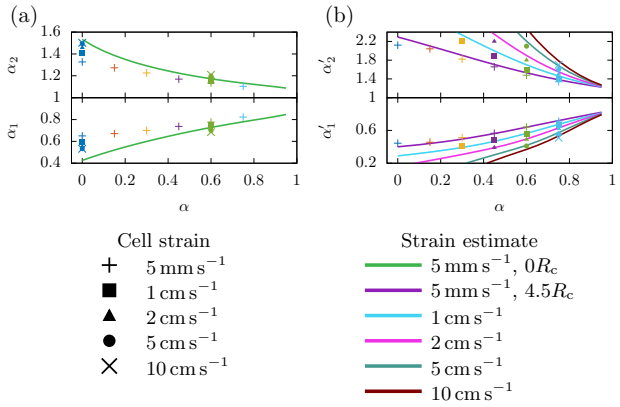

the shear thinning strength and solely dependent on the printing pressure. We show that, when bioprinting at constant flow rate (or velocity), the shear thinning properties reduce the overall cell stress and strain significantly, while this will not be the case for printing processes performed at constant printing pressure.

In the second stage, cells transition into the free printing strand as they exit the printer nozzle. During this transition, cells are exposed to an elongational flow pattern. While a radial deformation also occurs for cells flowing off-center, we find that the shear deformations dominate in this case. For cells in the channel center, however, this flow causes notable radial stretch of the cells as predicted by our numerical simulations, in qualitative agreement with experimental microscopy images. We show that this effect becomes particularly relevant for cells flowing in highly shear thinning bioinks, as the shear deformation inside the nozzle can virtually be eliminated, while the radial elongation inevitably takes place (figure 10a). In addition, we find that the elongational cell strain is practically independent of the extrusion velocity of the bioink, since the faster velocity balances the high elongational stress by reducing the application time. The relaxation times of the elongated cells even increase with the shear thinning strength, thus prolonging the time that they remain under strain with potentially harmful side effects (figure 10e).

Using our numerical simulation techniques as a starting point together with the velocity profiles derived in our earlier work [41], we finally developed simple estimates for cell stress and/or cell strain for centered as well as off-centered cells.

ACKNOWLEDGMENTS

We thank Nico Schwarm for preparing the cell/alginate sample and help with the imaging experiment. Funded by the Deutsche Forschungsgemeinschaft (DFG, German Research Foundation) — Project number 326998133 — TRR 225 "Biofabrication" (subprojects B07 and A01). We gratefully acknowledge computing time provided by the SuperMUC system of the Leibniz Rechenzentrum, Garching. We further acknowledge support through the computational resources provided by the Bavarian Polymer Institute.

[1] W. Sun, B. Starly, A. C. Daly, J. A. Burdick, J. Groll, G. Skeldon, W. Shu, Y. Sakai, M. Shinohara, M. Nishikawa, J. Jang, D.-W. Cho, M. Nie, S. Takeuchi, S. Ostrovidov, A. Khademhosseini, R. D. Kamm, V. Mironov, L. Moroni, and I. T. Ozbolat, Biofabrication **12**, 022002 (2020).

[2] R. W. Barrs, J. Jia, S. E. Silver, M. Yost, and Y. Mei, Chemical Reviews **120**, 10887 (2020).

[3] R. Levato, T. Jungst, R. G. Scheuring, T. Blunk, J. Groll, and J. Malda, Advanced Materials **32**, 1906423 (2020).

[4] J. Groll, T. Boland, T. Blunk, J. A. Burdick, D.-W. Cho, P. D. Dalton, B. Derby, G. Forgacs, Q. Li, V. A. Mironov, L. Moroni, M. Nakamura, W. Shu, S. Takeuchi, G. Vozzi, T. B. F. Woodfield, T. Xu, J. J. Yoo, and J. Malda, Biofabrication **8**, 013001 (2016).

[5] J. Malda, J. Visser, F. P. Melchels, T. Jüngst, W. E. Hennink, W. J. A. Dhert, J. Groll, and D. W. Hutmacher, Advanced Materials **25**, 5011 (2013).

[6] T. Böck, V. Schill, M. Krähnke, A. F. Steinert, J. Tessmar, T. Blunk, and J. Groll, Macromolecular Bioscience **18**, 1700390 (2018).

[7] T. U. Esser, K. Roshanbinfar, and F. B. Engel, Expert Opinion on Biological Therapy **19**, 105 (2019).

[8] J. Hauptstein, T. Böck, M. Bartolf-Kopp, L. Forster, P. Stahlhut, A. Nadernezhad, G. Blahetek, A. Zernecke-Madsen, R. Detsch, T. Jüngst, J. Groll, J. Teßmar, and T. Blunk, Advanced Healthcare Materials **9**, 2000737 (2020).

[9] I. A. D. Mancini, S. Schmidt, H. Brommer, B. Pouran, S. Schäfer, J. Tessmar, A. Mensinga, M. H. P. van Rijen, J. Groll, T. Blunk, R. Levato, J. Malda, and P. R. van Weeren, Biofabrication **12**, 035028 (2020).

[10] C. Mueller, M. Trujillo-Miranda, M. Maier, D. E. Heath, A. J. O'Connor, and S. Salehi, Advanced Materials Interfaces **8**, 2001167 (2021).

[11] K. Roshanbinfar, L. Vogt, B. Greber, S. Diecke, A. R. Boccaccini, T. Scheibel, and F. B. Engel, Advanced Functional Materials **28**, 1803951 (2018).

[12] S. Schmidt, F. Abinzano, A. Mensinga, J. Teßmar, J. Groll, J. Malda, R. Levato, and T. Blunk, International Journal of Molecular Sciences **21**, 7071 (2020).

[13] A. Weizel, T. Distler, D. Schneidereit, O. Friedrich, L. Bräuer, F. Paulsen, R. Detsch, A. Boccaccini, S. Budday, and H. Seitz, Acta Biomaterialia **118**, 113 (2020).

[14] L. Fischer, M. Nosratlo, K. Hast, E. Karakaya, N. Ströhlein, T. U. Esser, R. Gerum, S. Richter, F. Engel, R. Detsch, B. Fabry, and I. Thievessen, Biofabrication **14**, 045005 (2022).

[15] S. Han, C. M. Kim, S. Jin, and T. Y. Kim, Biofabrication **13**, 035048 (2021).

[16] G. Poologasundarampillai, A. Haweet, S. N. Jayash, G. Morgan, J. E. Moore, and A. Candeo, Bioprinting **23**, e00144 (2021).

[17] J. Emmermacher, D. Spura, J. Cziommer, D. Kilian, T. Wollborn, U. Fritsching, J. Steingroewer, T. Walther, M. Gelinsky, and A. Lode, Biofabrication **12**, 025022 (2020).

[18] S. Boularaoui, G. Al Hussein, K. A. Khan, N. Christoforou, and C. Stefanini, Bioprinting **20**, e00093 (2020).

[19] F. Ruther, T. Distler, A. R. Boccaccini, and R. Detsch, Journal of Materials Science: Materials in Medicine **30**, 8 (2019).

[20] J. Shi, B. Wu, S. Li, J. Song, B. Song, and W. F. Lu, Biomedical Physics & Engineering Express **4**, 045028 (2018).

[21] N. Paxton, W. Smolan, T. Böck, F. Melchels, J. Groll, and T. Jungst, Biofabrication **9**, 044107 (2017).

[22] L. Ouyang, R. Yao, Y. Zhao, and W. Sun, Biofabrication **8**, 035020 (2016).

[23] A. Blaeser, D. F. Duarte Campos, U. Puster, W. Richtering, M. M. Stevens, and H. Fischer, Advanced Healthcare Materials **5**, 326 (2015).

[24] J. Snyder, A. Rin Son, Q. Hamid, C. Wang, Y. Lui, and W. Sun, Biofabrication **7**, 044106 (2015).

[25] Y. Zhao, Y. Li, S. Mao, W. Sun, and R. Yao, Biofabrication **7**, 045002 (2015).

[26] J. Hazur, R. Detsch, E. Karakaya, J. Kaschta, J. Teßmar, D. Schneidereit, O. Friedrich, D. W. Schubert, and A. R. Boccaccini, Biofabrication **12**, 045004 (2020).

[27] C. Hu, L. Hahn, M. Yang, A. Altmann, P. Stahlhut, J. Groll, and R. Luxenhofer, Journal of Materials Science **56**, 691 (2021).

[28] A. Nadernezhad, L. Forster, F. Netti, L. Adler-Abramovich, J. Teßmar, and J. Groll, Polymer Journal **52**, 1007 (2020).

[29] M. Weis, J. Shan, M. Kuhlmann, T. Jungst, J. Tessmar, and J. Groll, Gels **4**, 82 (2018).

[30] S. J. Müller, F. Weigl, C. Bezold, C. Bächer, K. Albrecht, and S. Gekle, Biomechanics and Modeling in Mechanobiology 10.1007/s10237-020-01397-2 (2020).

[31] B. Fregin, F. Czerwinski, D. Biedenweg, S. Girardo, S. Gross, K. Aurich, and O. Otto, Nature Communications **10**, 415 (2019).

[32] A. Saadat, C. J. Guido, G. Iaccarino, and E. S. G. Shaqfeh, Physical Review E **98**, 063316 (2018).

[33] M. Mokbel, D. Mokbel, A. Mietke, N. Träber, S. Girardo, O. Otto, J. Guck, and S. Aland, ACS Biomaterials Science & Engineering **3**, 2962 (2017).

[34] A. Mietke, O. Otto, S. Girardo, P. Rosendahl, A. Taubenberger, S. Golfier, E. Ulbricht, S. Aland, J. Guck, and E. Fischer-Friedrich, Biophysical Journal **109**, 2023 (2015).

[35] O. Otto, P. Rosendahl, A. Mietke, S. Golfier, C. Herold, D. Klaue, S. Girardo, S. Pagliara, A. Ekpenyong, A. Ja-

cobi, M. Wobus, N. Töpfner, U. F. Keyser, J. Mansfeld, E. Fischer-Friedrich, and J. Guck, Nature Methods **12**, 199 (2015).
[36] F. Huber, J. Schnauß, S. Rönicke, P. Rauch, K. Müller, C. Fütterer, and J. Käs, Advances in Physics **62**, 1 (2013).
[37] M. L. Rodriguez, P. J. McGarry, and N. J. Sniadecki, Applied Mechanics Reviews **65**, 060801 (2013).
[38] T. Gao, H. H. Hu, and P. P. Castañeda, Journal of Fluid Mechanics **687**, 209 (2011).
[39] P. Kollmannsberger and B. Fabry, Annual Review of Materials Research **41**, 75 (2011).
[40] L. Ning, N. Betancourt, D. J. Schreyer, and X. Chen, ACS Biomaterials Science & Engineering **4**, 3906 (2018).
[41] S. J. Müller, E. Mirzahossein, E. N. Iftekhar, C. Bächer, S. Schrüfer, D. W. Schubert, B. Fabry, and S. Gekle, PLOS ONE **15**, e0236371 (2020).
[42] L. Lemarié, A. Anandan, E. Petiot, C. Marquette, and E.-J. Courtial, Bioprinting **21**, e00119 (2021).
[43] K. Fakhruddin, M. S. A. Hamzah, and S. I. A. Razak, IOP Conference Series: Materials Science and Engineering **440**, 012042 (2018).
[44] T. Billiet, E. Gevaert, T. De Schryver, M. Cornelissen, and P. Dubruel, Biomaterials **35**, 49 (2014).
[45] Y. B. Bae, H. K. Jang, T. H. Shin, G. Phukan, T. T. Tran, G. Lee, W. R. Hwang, and J. M. Kim, Lab on a Chip **16**, 96 (2016).
[46] K. Nair, M. Gandhi, S. Khalil, K. C. Yan, M. Marcolongo, K. Barbee, and W. Sun, Biotechnology Journal **4**, 1168 (2009).
[47] R. Chang, J. Nam, and W. Sun, Tissue Engineering Part A **14**, 41 (2008).
[48] G. B. Jeffery, Proceedings of the Royal Society of London. Series A, Containing Papers of a Mathematical and Physical Character **102**, 161 (1922).
[49] R. Roscoe, Journal of Fluid Mechanics **28**, 273 (1967).
[50] T. Krüger, H. Kusumaatmaja, A. Kuzmin, O. Shardt, G. Silva, and E. M. Viggen, The Lattice Boltzmann Method, Graduate Texts in Physics (Springer International Publishing, Cham, 2017).
[51] H. Limbach, A. Arnold, B. Mann, and C. Holm, Computer Physics Communications **174**, 704 (2006).
[52] D. Roehm and A. Arnold, The European Physical Journal Special Topics **210**, 89 (2012).
[53] M. Schlenk, E. Hofmann, S. Seibt, S. Rosenfeldt, L. Schrack, M. Drechsler, A. Rothkirch, W. Ohm, J. Breu, S. Gekle, and S. Förster, Langmuir **34**, 4843 (2018).
[54] D. Devendran and C. S. Peskin, Journal of Computational Physics **231**, 4613 (2012).
[55] C. Bächer, L. Schrack, and S. Gekle, Physical Review Fluids **2**, 013102 (2017).
[56] C. Bächer and S. Gekle, Physical Review E **99**, 062418 (2019).
[57] M. M. Cross, Journal of Colloid Science **20**, 417 (1965).
[58] V. Manojlovic, J. Djonlagic, B. Obradovic, V. Nedovic, and B. Bugarski, Journal of Chemical Technology & Biotechnology **81**, 505 (2006).
[59] Or using our web tool under `https://bio.physik.fau.de/flow_webpage/flow.html`.
[60] M. E. Rosti, L. Brandt, and D. Mitra, Physical Review Fluids **3**, 012301 (2018).
[61] A. F. Bower, Applied Mechanics of Solids (CRC Press, Boca Raton, 2010).
[62] R. Kiss, Journal of Biomechanical Engineering **133**, 101009 (2011).
[63] C. Geuzaine and J.-F. Remacle, International Journal for Numerical Methods in Engineering **79**, 1309 (2009).
[64] R. Mittal and G. Iaccarino, Annual Review of Fluid Mechanics **37**, 239 (2005).
[65] C. S. Peskin, Acta Numerica **11**, 479 (2002).
[66] Z. Chai, B. Shi, Z. Guo, and F. Rong, Journal of Non-Newtonian Fluid Mechanics **166**, 332 (2011).
[67] M. Lehmann, S. J. Müller, and S. Gekle, International Journal for Numerical Methods in Fluids 10.1002/fld.4835 (2020).
[68] P. Fisch, M. Holub, and M. Zenobi-Wong, Biofabrication **13**, 015012 (2021).
[69] R. Gerum, E. Mirzahossein, M. Eroles, J. Elsterer, A. Mainka, A. Bauer, S. Sonntag, A. Winterl, J. Bartl, L. Fischer, S. Abuhattum, R. Goswami, S. Girardo, J. Guck, S. Schrüfer, N. Ströhlein, M. Nosratlo, H. Herrmann, D. Schultheis, F. Rico, S. J. Müller, S. Gekle, and B. Fabry, eLife **11**, e78823 (2022).

Supplementary Information

Predicting cell stress and strain during extrusion 3D bioprinting

Sebastian J. Müller[1], Ben Fabry[2], and Stephan Gekle[1]

[1] Biofluid Simulation and Modeling, Theoretische Physik VI, Universität Bayreuth, 95440 Bayreuth, Germany (www.gekle.physik.uni-bayreuth.de)

[2] Department of Physics, Friedrich-Alexander University Erlangen-Nürnberg, 91054 Erlangen, Germany

S-1. BIOPRINTER IMAGING SETUP

MDA-MB-231 breast carcinoma cells were suspended in a 2 % alginate-DMEM solution (sodium alginate PH176, batch nr. 4503283839, JRS Pharma GmbH, Rosenberg, Germany) at a concentration of $10^6 \frac{\text{cells}}{\text{ml}}$. The cell-alginate suspension was then extruded through a stainless steel needle with an inner diameter of 200 µm and a length of 12.7 mm (Nordson EFD, East Providence, USA) at a constant flow rate of $10\,\mu\text{l}\,\text{s}^{-1}$ using a volume-controlled 3-D printer [1]. The needle was dipped into a transparent plastic cuvette (rotilabo, Roth, Germany) filled with PBS solution. The cells were imaged through a non-infinity corrected 10× 0.25 NA objective (Zeiss, Germany) and a lens-less 150 mm tube (Thorlabs, Germany) using a CMOS camera (acA720-520um, Basler, Germany) at an exposure time of 30 µs and a frame rate of 100 Hz.

FIG. S-1. Decomposition of the shear component of the strain rate tensor for (a) the Newtonian fluid and (b) the bioink with $\alpha = 0.75$. In both cases, the local peak of the rate of strain is due to the radial shear component $\frac{\partial u_r}{\partial x}$, while the axial shear decreases monotonously.

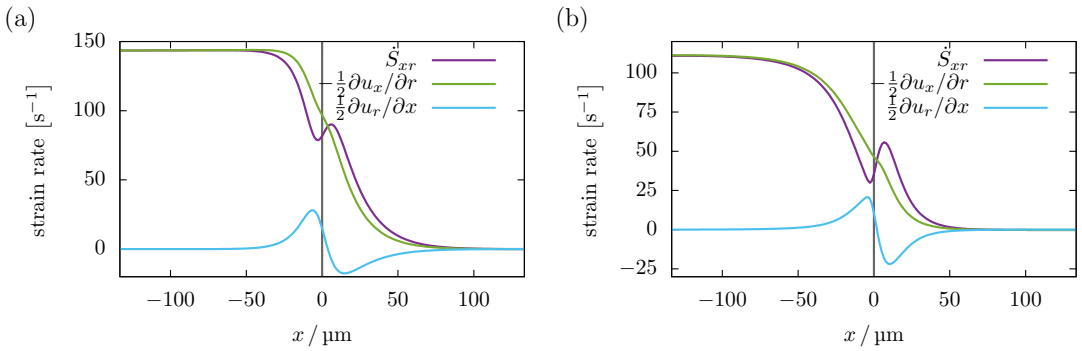

S-2. FLUID SHEAR STRESS AT THE NOZZLE EXIT

As shown in figure 7 of the manuscript, the total fluid shear stress σ_f along the axial direction always has a local or global peak right after the nozzle exit. When considering the flow close to the channel axis, this peak is clearly a result of the elongational flow at the nozzle exit. Moving closer to the wall, the influence of the elongational components decreases, however, the peak is still present and part of the shear components of the flow. In figure S-1 we decompose the strain rate tensor element $\dot{S}_{xr} = \frac{1}{2}\left(\frac{\partial u_x}{\partial r} + \frac{\partial u_r}{\partial x}\right)$ into its axial and radial shear component. While the axial strain rate $\frac{\partial u_x}{\partial r}$ monotonously decreases along the nozzle exit, the radial strain rate $\frac{\partial u_r}{\partial x}$ increases, changes its sign, and relaxes to zero again due to the localized radial flows at the nozzle exit.

S-3. FLUID STRESS TENSOR DECOMPOSITION

The components of the rate of strain tensor in a cylindrical coordinate system are given by:

$$\dot{S}_{xx} = \frac{\partial u_x}{\partial x} \tag{S-1}$$

$$\dot{S}_{xr} = \dot{S}_{rx} = \tfrac{1}{2}\left(\frac{\partial u_r}{\partial x} + \frac{\partial u_x}{\partial r}\right) \tag{S-2}$$

$$\dot{S}_{rr} = \frac{\partial u_r}{\partial r} \tag{S-3}$$

$$\dot{S}_{x\theta} = \dot{S}_{\theta x} = \tfrac{1}{2}\left(\frac{\partial u_\theta}{\partial x} + \frac{1}{r}\frac{\partial u_x}{\partial \theta}\right) \tag{S-4}$$

$$\dot{S}_{r\theta} = \dot{S}_{\theta r} = \tfrac{1}{2}\left(\frac{1}{r}\frac{\partial u_r}{\partial \theta} - \frac{u_\theta}{r} + \frac{\partial u_\theta}{\partial r}\right) \tag{S-5}$$

$$\dot{S}_{\theta\theta} = \frac{1}{r}\left(\frac{\partial u_\theta}{\partial \theta} + u_r\right) \tag{S-6}$$

For the present axisymmetric situation, this simplifies to

$$\dot{S}_{ij} = \dot{S}_{ij}^{\text{shear}} + \dot{S}_{ij}^{\text{elong}}\,, \tag{S-7}$$

$$\dot{S}^{\text{shear}} = \begin{pmatrix} 0 & \frac{1}{2}\left(\frac{\partial u_r}{\partial x} + \frac{\partial u_x}{\partial r}\right) & 0 \\ \frac{1}{2}\left(\frac{\partial u_r}{\partial x} + \frac{\partial u_x}{\partial r}\right) & 0 & 0 \\ 0 & 0 & 0 \end{pmatrix}, \tag{S-8}$$

$$\dot{S}^{\text{elong}} = \begin{pmatrix} \frac{\partial u_x}{\partial x} & 0 & 0 \\ 0 & \frac{\partial u_r}{\partial r} & 0 \\ 0 & 0 & \frac{u_r}{r} \end{pmatrix}. \tag{S-9}$$

We can thus compute the scalar shear rate

$$\left|\dot{S}^{\text{shear}}\right| = \sqrt{2\dot{S}_{ij}^{\text{shear}}\dot{S}_{ij}^{\text{shear}}} = \sqrt{4\dot{S}_{xr}^2} \tag{S-10}$$

$$= \left|\frac{\partial u_r}{\partial x} + \frac{\partial u_x}{\partial r}\right| \tag{S-11}$$

and the scalar elongation rate

$$\left|\dot{S}^{\text{elong}}\right| = \sqrt{2\dot{S}_{ij}^{\text{elong}}\dot{S}_{ij}^{\text{elong}}} \tag{S-12}$$

$$= \sqrt{2(\dot{S}_{xx}^2 + \dot{S}_{rr}^2 + \dot{S}_{\theta\theta}^2)} \tag{S-13}$$

$$= \sqrt{2\left(\frac{\partial u_x}{\partial x}\right)^2 + 2\left(\frac{\partial u_r}{\partial r}\right)^2 + 2\left(\frac{u_r}{r}\right)^2}\,, \tag{S-14}$$

and the rate of strain

$$\left|\dot{S}\right| = \sqrt{\left|\dot{S}^{\text{shear}}\right|^2 + \left|\dot{S}^{\text{elong}}\right|^2}\,. \tag{S-15}$$

Using the shear and elongation rates, we define the fluid's scalar shear and elongational stress via

$$\sigma_{\text{f}}^{\text{shear}} := \eta\Big(|\dot{S}|\Big)\left|\dot{S}^{\text{shear}}\right| \tag{S-16}$$

and

$$\sigma_{\text{f}}^{\text{elong}} := \eta\Big(|\dot{S}|\Big)\left|\dot{S}^{\text{elong}}\right|\,. \tag{S-17}$$

The total fluid stress is thus obtained as:

$$\sigma_{\text{f}} = \eta\Big(|\dot{S}|\Big)|\dot{S}| = \sqrt{\left(\sigma_{\text{f}}^{\text{shear}}\right)^2 + \left(\sigma_{\text{f}}^{\text{elong}}\right)^2} \tag{S-18}$$

When assuming a perfect elongational flow, i. e., $u_x = -\dot{\varepsilon}x$, $u_r = \frac{1}{2}\dot{\varepsilon}r$, and $u_\theta = 0$, the fluids rate of strain is given via

$$|\dot{S}| = \left|\dot{S}_{ij}^{\text{elong}}\right| = \sqrt{2\dot{\varepsilon}^2 + 2\left(\tfrac{1}{2}\dot{\varepsilon}\right)^2 + 2\left(\tfrac{1}{2}\dot{\varepsilon}\right)^2} = \sqrt{3}\dot{\varepsilon} \tag{S-19}$$

and thus follows the fluid stress as:

$$\sigma_{\text{f}} = \sigma_{\text{f}}^{\text{elong}} = \eta\Big(\sqrt{3}\dot{\varepsilon}\Big)\sqrt{3}\dot{\varepsilon} \tag{S-20}$$

S-4. JEFFERY AND ROSCOE THEORY

An analytical theory describing the deformation and stresses of a cell embedded in a linear flow was proposed by Roscoe [2], based on the work of Jeffery [3]. For convenience, we briefly summarize their theoretical approach and the application of the theory for cells in a shear and an elongational flow scenario in this section.

Jeffery [3] originally solved the problem of the motion of a rigid ellipsoidal particle in a linear flow, i. e., the undisturbed fluid velocity can be written as (using the notation of Roscoe [2])

$$v_i' = e_{ij}'^{(1)} x_j - \zeta_{ij}' x_j \,, \tag{S-21}$$

where the fluid's rate of strain and vorticity are defined by

$$e_{ij}'^{(1)} = \frac{1}{2}\left(\frac{\partial v_i'}{\partial x_j} + \frac{\partial v_j'}{\partial x_i}\right) \quad \text{and} \quad \zeta_{ij}' = \frac{1}{2}\left(\frac{\partial v_i'}{\partial x_j} - \frac{\partial v_j'}{\partial x_i}\right). \tag{S-22}$$

Jeffery [3] derived the fluid stress acting on the surface of a rigid ellipsoidal particle as

$$p_{ij}' = -p_\mathrm{h}\delta_{ij} + \eta_0 A_{ij} \,, \tag{S-23}$$

with an arbitrary hydrostatic pressure p_h and a deviatoric tensor A_{ij}. Roscoe [2] notes that the deviatoric stress can further be divided into two parts,

$$p_{ij}' = -p_\mathrm{h}\delta_{ij} + 2\eta_0 e_{ij}'^{(1)} + \eta_0\left(A_{ij} - 2e_{ij}'^{(1)}\right), \tag{S-24}$$

one due to the undisturbed flow from (S-21) and one due to the disturbance of the flow induced by the particle presence. The components A_{ij} in a coordinate system coinciding with the ellipsoid axes can be calculated via (remaining components by cyclic change of indices):

$$A_{11} = \frac{4}{3}\frac{2g_1'' e_{11}'^{(1)} - g_2'' e_{22}'^{(1)} - g_3'' e_{33}'^{(1)}}{g_2'' g_3'' + g_3'' g_1'' + g_1'' g_2''} \tag{S-25}$$

$$A_{12} = \frac{g_1 e_{12}'^{(1)} - \alpha_2^2 g_3' \zeta_{12}'}{2g_3'(\alpha_1^2 g_1 + \alpha 2^2 g_2)} \tag{S-26}$$

g_i, g_i', and g_i'' are integrals of the type

$$g_1 = \int_0^\infty \frac{\mathrm{d}\lambda}{(\alpha_1^2+\lambda)\Delta} \tag{S-27}$$

$$g_1' = \int_0^\infty \frac{\mathrm{d}\lambda}{(\alpha_2^2+\lambda)(\alpha_3^2+\lambda)\Delta} = \frac{g_3-g_2}{\alpha_2^2-\alpha_3^2} \tag{S-28}$$

$$g_1'' = \int_0^\infty \frac{\lambda\,\mathrm{d}\lambda}{(\alpha_2^2+\lambda)(\alpha_3^2+\lambda)\Delta} = \frac{\alpha_2^2 g_2-\alpha_3^2 g_3}{\alpha_2^2-\alpha_3^2}\,, \tag{S-29}$$

where $\Delta = \sqrt{(\alpha_1^2+\lambda)(\alpha_2^2+\lambda)(\alpha_3^2+\lambda)}$.

Equation (S-23) can directly be employed to compute the stresses acting on a rigid ellipsoid suspended in the undisturbed flow given by (S-21), e. g., a cell inside an elongational flow, as detailed in section S-4 B. Roscoe [2] extended the theory of Jeffery [3] to compute the stresses acting on a non-rigid ellipsoid with moving boundaries, i. e., tank-treading motion. The ellipsoid's surface motion is assumed to be linear — similar to (S-21) — given by

$$v_i = \bar{e}_{ij}^{(1)} x_j - \bar{\zeta}_{ij} x_j\,, \tag{S-30}$$

with $\bar{e}_{ij}^{(1)}$ and $\bar{\zeta}_{ij}$ denoting respectively the average rate of strain and vorticity inside the particle, which are always equal to their values at the particle surface [2]. The velocity disturbance $\Delta v_i' = v_i - v_i'$ at the particle surface induced by the surface motion of the non-rigid particle is equal to the velocity disturbance of a rigid particle in an undisturbed flow given by

$$v_i'' = v_i' - v_i\,. \tag{S-31}$$

Therefore, (S-24) can be employed to compute the fluid stresses for a non-rigid particle with a moving boundary by simply computing the stress contribution due to the disturbance using the equivalent undisturbed flow (S-31), while keeping the contribution due to the actual undisturbed flow (S-21). Thus:

$$p_{ij}' = -p_\mathrm{h}\delta_{ij} + 2\eta_0 e_{ij}'^{(1)} + \eta_0\Big(A_{ij}' - 2\Big(e_{ij}'^{(1)} - \bar{e}_{ij}^{(1)}\Big)\Big) \tag{S-32}$$

$$= -p_\mathrm{h}\delta_{ij} + \eta_0\Big(A_{ij}' + 2\bar{e}_{ij}^{(1)}\Big) \tag{S-33}$$

Here, the tensor A_{ij}' is computed for an undisturbed flow of the form given in (S-31) instead of (S-21).

A. Cell stress and strain in shear flow

Roscoe [2] applies (S-32) to compute the motion of a tank-treading ellipsoidal particle in a linear shear flow. The coordinates of a material point of the particle starting at position $(\tilde{x}_1, \tilde{x}_2, \tilde{x}_3)$ following an elliptical trajectory are given by

$$x_1 = \alpha_1(\tilde{x}_1 \cos(\nu t) - \tilde{x}_2 \sin(\nu t)) \tag{S-34}$$

$$x_2 = \alpha_2(\tilde{x}_1 \sin(\nu t) + \tilde{x}_2 \cos(\nu t)) \tag{S-35}$$

$$x_3 = \alpha_3 \tilde{x}_3 \,, \tag{S-36}$$

where x_1, x_2, and x_3, align with the ellipsoid's semi-axes, thus yielding the surface velocity:

$$v_1 = -\frac{\alpha_1}{\alpha_2} \nu x_2 \tag{S-37}$$

$$v_2 = \frac{\alpha_2}{\alpha_1} \nu x_1 \tag{S-38}$$

$$v_3 = 0 \tag{S-39}$$

The surface velocity defines the rate of strain and vorticity from (S-30). A linear shear flow — commonly described in the global coordinate system as $v_1' = \kappa x_2$, $v_2' = v_3' = 0$ with a shear rate κ — written in terms of a coordinate system aligned with the ellipsoid's semi-axes through rotation by an angle θ is given by

$$v_1' = \kappa\big(x_1 \sin\theta \cos\theta + x_2 \cos^2(\theta)\big) \tag{S-40}$$

$$v_2' = -\kappa\big(x_1 \sin^2(\theta) + x_2 \sin\theta \cos\theta\big) \tag{S-41}$$

$$v_3' = 0 \,. \tag{S-42}$$

From that, the undisturbed fluid's rate of strain and vorticity from (S-21), and, together with (S-30), the fluid stress at the particle surface from (S-32) can be computed.
In a stationary state, the fluid stress must be balanced by the cell stress at the particle surface. As mentioned in section III-A of the manuscript, the cell stress consists of an elastic and a viscous part. For the triaxial ellipsoidal deformation described in (S-34), the elastic stress at the particle surface can be computed from (9) assuming an incompressible cell ($J = 1$). With the corresponding deformation gradient tensor given by $F_{ij} = \alpha_i \delta_{ij}$, the non-zero diagonal elements of the Cauchy stress are then found as

$$\sigma_{11} = \frac{\mu}{3}\big(2\alpha_1^2 - \alpha_2^2 - \alpha_3^2\big) \,, \tag{S-43}$$

with similar expressions for σ_{22} and σ_{33} obtained by cyclic change of indices. The obtained system of two equations of the stress balance is solved by considering only the differences of the principal stresses, which eliminates the hydrostatic pressure:

$$p'_{11} - p'_{22} = \sigma_{11} - \sigma_{22} \tag{S-44}$$

$$\Leftrightarrow 2\eta_0\kappa\sin(2\theta)\frac{g''_1 + g''_2}{g''_2 g''_3 + g''_3 g''_1 + g''_1 g''_2} = \mu\left(\alpha_1^2 - \alpha_2^2\right) \tag{S-45}$$

$$p'_{11} + p'_{22} - 2p'_{33} = \sigma_{11} + \sigma_{22} - 2\sigma_{33} \tag{S-46}$$

$$\Leftrightarrow 2\eta_0\kappa\sin(2\theta)\frac{g''_1 - g''_2}{g''_2 g''_3 + g''_3 g''_1 + g''_1 g''_2} = \mu\left(\alpha_1^2 + \alpha_2^2 - \frac{2}{\alpha_1^2\alpha_2^2}\right) \tag{S-47}$$

Note that $\alpha_3 = \frac{1}{\alpha_1\alpha_2}$ due to the assumed incompressibility. The viscous contribution of the cell stress can be computed directly from its internal fluid motion (S-37)–(S-39) as:

$$\sigma_{12} = \sigma_{21} = 2\eta_1 e'^{(1)}_{12} = -\eta_1\nu\frac{\alpha_1^2 - \alpha_2^2}{\alpha_1\alpha_2} \tag{S-48}$$

Through numerical solution of these equations one obtains the cell stresses and strains as well as the tank-treading frequency as function of the undisturbed fluid's shear rate κ (cf. Roscoe[2, eq.(80),(41)]).

To compare it with the Roscoe theory, we numerically assess the viscous shear stress inside the cell from our simulations by extracting the Lattice-Boltzmann strain rate tensor field inside the cell. For that, we first compute the symmetric strain rate tensor components from the Latte Boltzmann populations of the current and previous time step using the method from [4]. Then, we mask the strain rate tensor field using a flag grid that distinguishes the interior and exterior of the cell, which we track using our method from [6]. The viscous cell stress is obtained by averaging the off-diagonal component of the strain rate tensor field. In figure S-2 we show how the resulting viscous component of the cell stress as function of the cell's shear modulus in a linear shear flow of constant strain rate $|\dot{S}| = 100\,\mathrm{s}^{-1}$. For low μ — i. e., for soft cells — the shear stress inside the cells asymptotically approaches the viscous shear stress of the surrounding undisturbed fluid, as it is increasingly stretched and hence more aligned with the flow. Very stiff cells, on the other hand, will remain their undeformed spherical shape. It can be seen that the transition between these two limits in large parts happens in the stiffness range of biological cells at around 100 Pa to 10 kPa.

FIG. S-2. Viscous shear stress σ_{12} inside the cell as function of the cell stiffness in a shear flow with $|\dot{S}| = 100\,\mathrm{s}^{-1}$. The straight line indicates the viscous fluid stress of the surrounding undisturbed flow field.

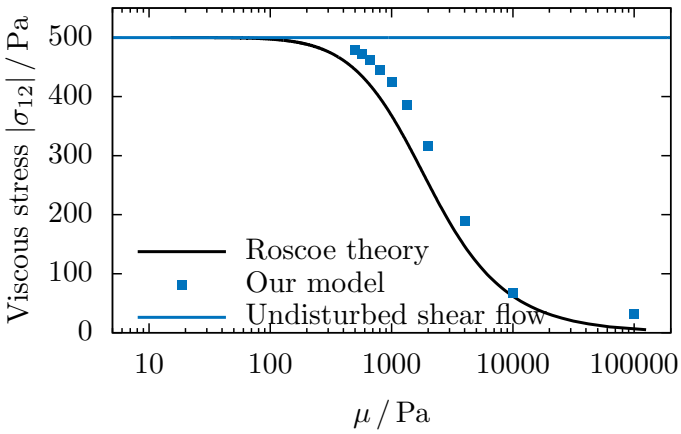

B. Cell stress and strain in elongational flow

Roscoe [2] applies (S-23) to compute the steady state deformation and stresses of an ellipsoid in an elongational flow, where the undisturbed velocity is given by

$$v_1' = \xi x_1 \tag{S-49}$$

$$v_2' = -\frac{1}{2}\xi x_2 \tag{S-50}$$

$$v_3' = -\frac{1}{2}\xi x_3\,, \tag{S-51}$$

with the elongational rate ξ. From this, the rate of strain and vorticity in (S-21) and the deviatoric tensor A_{ij} are calculated. Since the ellipsoid's boundary has no motion, $v_i = 0$. Due to the symmetry of the flow and the incompressibility, $\alpha_2 = \alpha_3 = \alpha_1^{-1/2}$ applies to the ellipsoid. The fluid's normal stress differences from (S-23) are then set to balance the surface stresses of the triaxially elongated particle:

$$p_{11}' - p_{22}' = \sigma_{11} - \sigma_{22} \tag{S-52}$$

$$2\eta_0 \frac{\xi}{g_2''} = \mu\left(\alpha_1^2 - \frac{1}{\alpha_1}\right) \tag{S-53}$$

The numerical solution of this equation yields the cell stresses and strains as function of the undisturbed fluid's elongational rate ξ. We note that due to the stationarity condition a stable solution can not be found for very high elongational rates.

S-5. APPLICABILITY OF ROSCOE THEORY FOR SHEAR THINNING BIOINKS

In figure 5(c and d) of the manuscript we show the cell stress as function of the fluid stress for different cell starting positions in the channel in a Newtonian bioink and for the maximum radial offset for increasing shear thinning strength. Figure S-3 shows additional data curves for all investigated bioinks, i. e., data similar to figure 5(c) for different α. In Addition to the fluid stress on the lower x-axis, the upper x-axis gives the radial position of the cell in units of the cell radius.

As mentioned in section III A of the manuscript, the key property determining cell motion is the shear stress. To underline this, we plot in figure S-4 the cell stress data from figure 5(d), but with respect to the rate of strain instead of the shear stress. Due to the similar velocities, the range of the $|\dot{S}|$-axis is similar for all flow indices. Therefore — instead of collapsing onto a master curve as in figure 5(d) — the curves fan out, suggesting a weaker dependency of the cell stress on the shear rate for increasingly shear thinning bioinks. This, however, is slightly misleading, since it neglects the change in viscosity of the surrounding liquid.

In section III E we find that the influence of higher extrusion velocities on the elongational cell strain is almost negligible. However, this does obviously not apply to the shear conditions inside the nozzle channel, as a higher pressure gradient is necessary to produce larger flow velocities. In figure S-5 below, we show data similar to that of figure 5(c and d), for a cell starting at the largest radial offset in a bioink with $\alpha = 0.6$ for average extrusion velocities of $1\,\mathrm{cm\,s^{-1}}$, $2\,\mathrm{cm\,s^{-1}}$, and $5\,\mathrm{cm\,s^{-1}}$, demonstrating the validity of the Roscoe theory also for higher velocities.

FIG. S-3. The cell stress inside the nozzle channel as function of the local shear stress for all used bioinks, as in figure 5(c). The upper x-axis gives the radial position of the cell in units of the cell radius.

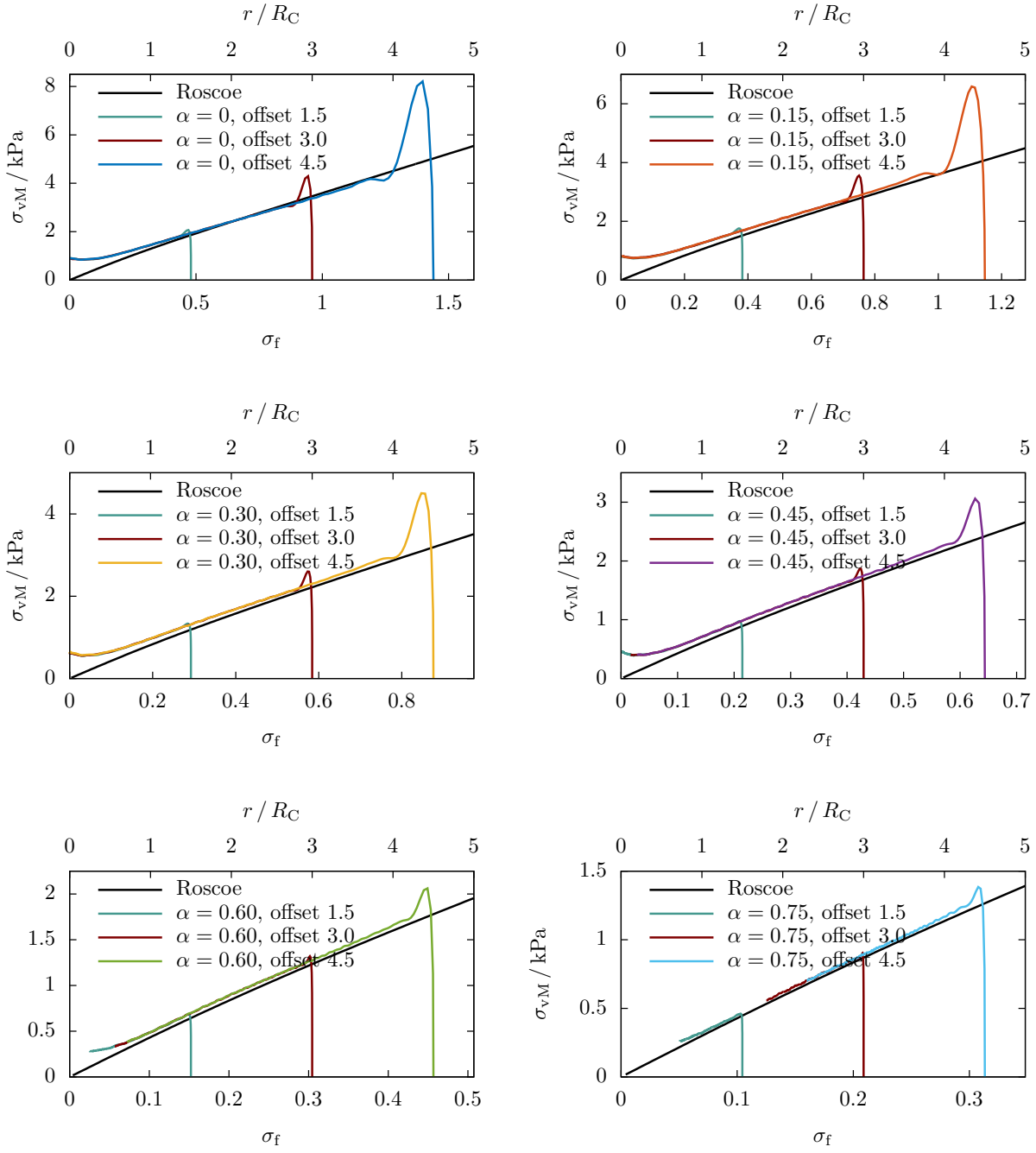

FIG. S-4. Data from figure 5(d), but plotted versus the local rate of strain $|\dot{S}|$ of the fluid. Due to the constant average velocity, the shear rates experienced by the cells are of similar magnitude.

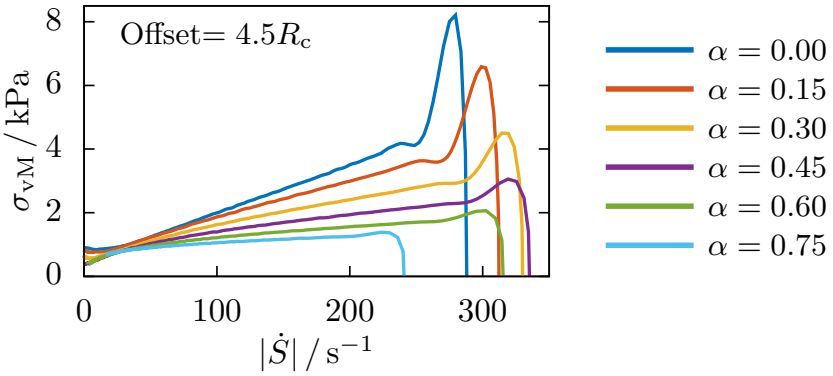

FIG. S-5. The cell stress as function of the fluid stress (similar to figure 5(d) for a cell starting at the largest radial offset in a bioink with $\alpha = 0.6$ for average extrusion velocities of $1\,\mathrm{cm\,s^{-1}}$, $2\,\mathrm{cm\,s^{-1}}$, and $5\,\mathrm{cm\,s^{-1}}$, demonstrating the validity of the Roscoe theory also for higher velocities.)

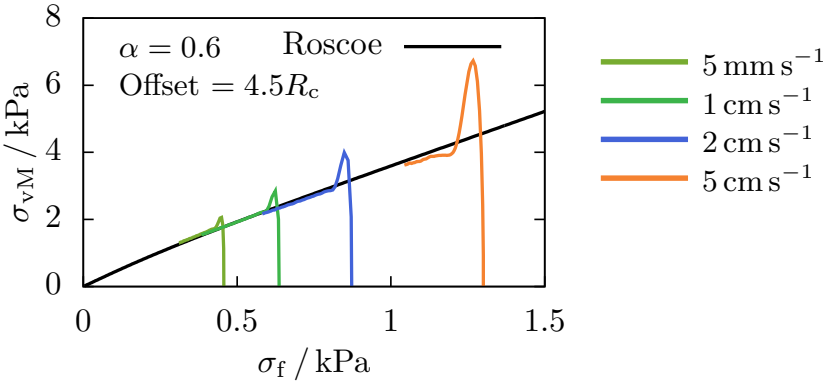

S-6. RIGID SPHERE IN FLOW

To compute the additional stress caused by a rigid sphere in pure shear flow, we start from the strain rate tensor (S-22) of the undisturbed flow. As usual, for a shear rate κ, this is given by

$$\underline{e}'^{(1)} = \frac{1}{2}\begin{pmatrix} 0 & \kappa & 0 \\ \kappa & 0 & 0 \\ 0 & 0 & 0 \end{pmatrix} \tag{S-54}$$

The sphere is neutrally buouyant as well as force- and torque-free. We then compute the so-called stresslet (see, e. g., [7, eq. (2.32)]) which embodies the additional stress in the fluid due to the presence of the sphere

$$\begin{aligned} \underline{S} &= \frac{20}{3}\pi\eta_0 R_\mathrm{c}^3 \underline{e}'^{(1)} \\ &= \frac{20}{6}\pi\eta_0 R_\mathrm{c}^3 \kappa \begin{pmatrix} 0 & 1 & 0 \\ 1 & 0 & 0 \\ 0 & 0 & 0 \end{pmatrix} \end{aligned} \tag{S-55}$$

This quantity is normalized by the shear stress of the undisturbed fluid integrated over the sphere volume

$$S_\mathrm{f} = \frac{4}{3}\pi R_\mathrm{c}^3 \eta_0 \kappa \tag{S-56}$$

thus leading to the dimensionless stresslet

$$\begin{aligned} \underline{S}^* &= \frac{\underline{S}}{S_\mathrm{f}} \\ &= \frac{5}{2}\begin{pmatrix} 0 & 1 & 0 \\ 1 & 0 & 0 \\ 0 & 0 & 0 \end{pmatrix}. \end{aligned} \tag{S-57}$$

(S-57) is given in the laboratory system. To express it in the body-fixed coordinate system of the cell, we require a rotation by 45° (cf. left inset in figure 4) given by the matrix

$$\underline{M}_{45} = \frac{\sqrt{2}}{2}\begin{pmatrix} 1 & -1 & 0 \\ 1 & 1 & 0 \\ 0 & 0 & 1 \end{pmatrix}. \tag{S-58}$$

The final result is

$$\begin{aligned} \underline{S}^*_{\mathrm{rot}} &= \underline{M}_{45}\, \underline{S}^*\, \underline{M}^{\mathrm{T}}_{45} \\ &= \frac{5}{2} \begin{pmatrix} -1 & 0 & 0 \\ 0 & 1 & 0 \\ 0 & 0 & 0 \end{pmatrix} \end{aligned} \tag{S-59}$$

thus furnishing an explanation for the cell stress at low flow rates in figure 4.

S-7. UNIAXIAL STRETCHING OF AN ELASTIC BEAM

In the limit of high Capillary numbers, the elastic components of the cell stress tensor approximately develop according to the ratio $\sigma_{11} : \sigma_{22} : \sigma_{33} = 2 : -1 : -1$. This ratio is equivalent to what would be expected from the uniaxial extension of an elastic beam, as briefly outlined in the following. The uniaxial stretching with a factor $\alpha_1 = a$ in x_1-direction of an isotropic, incompressible material results in $\alpha_2 = \alpha_3 = \frac{1}{\sqrt{a}}$ for the remaining principal stretches. The left Cauchy-Green deformation tensor is hence given by $B = \mathrm{diag}\left(a^2, \frac{1}{a}, \frac{1}{a}\right)$, which can be inserted into (S-43) of the manuscript in order to obtain the stress components as:

$$\sigma_{11} = \frac{2}{3}\mu\left(a^2 - \frac{1}{a}\right) \tag{S-60}$$

$$\sigma_{22} = \sigma_{33} = -\frac{1}{3}\mu\left(a^2 - \frac{1}{a}\right) \tag{S-61}$$

S-8. STRESS RELAXATION INSIDE THE BIOINK STRAND

In figure S-6 we show the individual fits of the cell stress relaxation times τ from figure 9(e) of the manuscript. As a fit function we use an exponential decay of the form

$$\sigma_{\mathrm{vM}}(t) = \sigma_{\mathrm{vM}}^{\mathrm{arb.offset}} + \sigma_{\mathrm{vM}}^{(0)} \exp\left(-\frac{t - t_0}{\tau}\right), \tag{S-62}$$

where $\sigma_{\mathrm{vM}}^{(0)}$ denotes the cell stress at t_0 (indicated by the gray area), and $\sigma_{\mathrm{vM}}^{\mathrm{arb.offset}}$ is an arbitrary small offset. At t_0, the cell passes the transition (i. e.$x = 0$).

When the cell relaxes in a quiescent fluid, i. e., when we disable any imposed flow or external pressure, the relaxation times of the cell decrease slightly. This is shown in figure S-7, where we compare the relaxation times of cells inside quiescent fluid to those of cells passing through the nozzle exit into the bioink strand (cf.figure 9(e))

FIG. S-6. Relaxation time fit of the cell stress in the bioink strand using an exponentially decaying function. The fit excludes they gray shaded area.

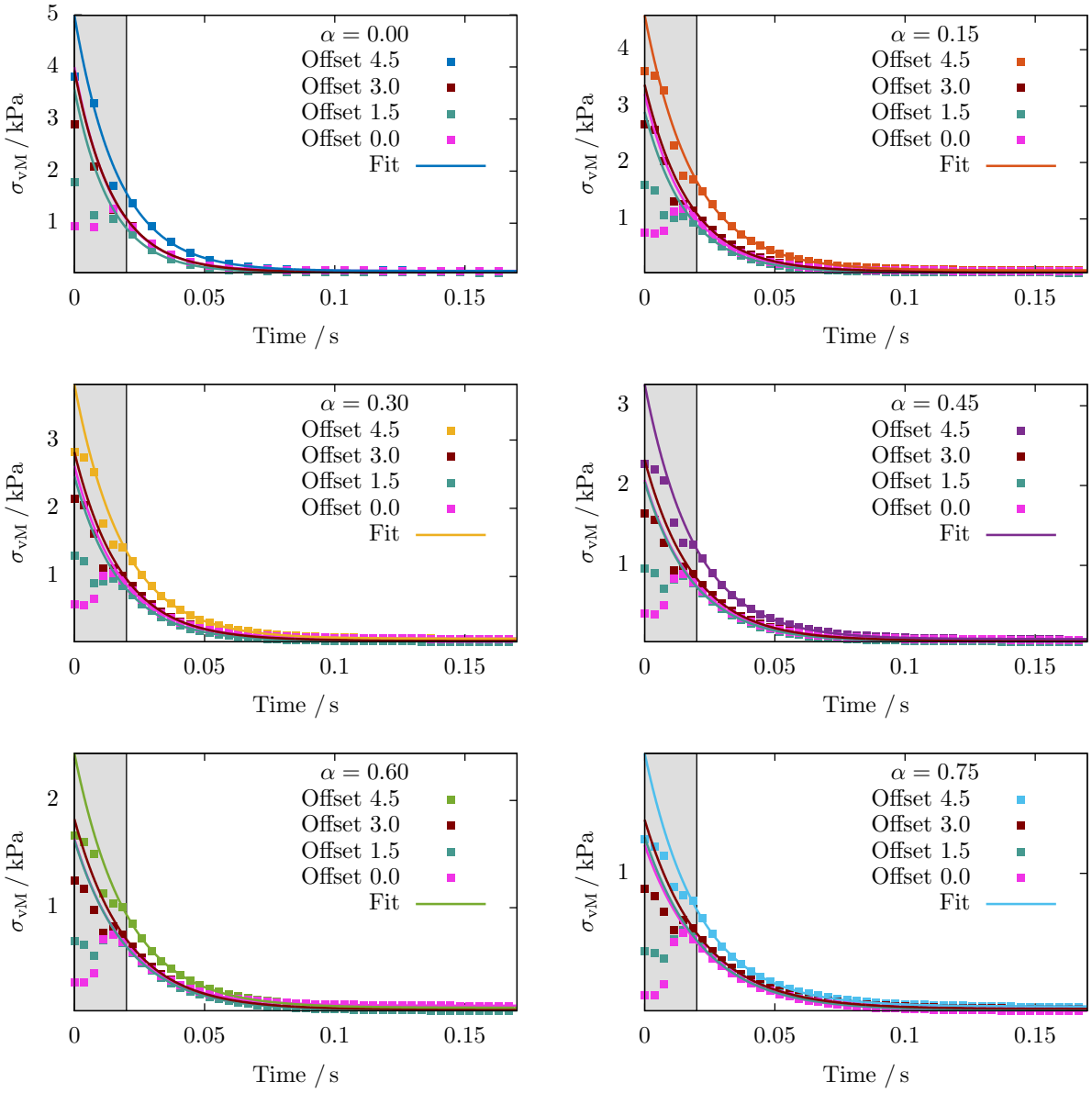

FIG. S-7. Relaxation times of cells suspended in quiescent liquid (solid lines), compared to the data in figure 9(e) (dotted lines).

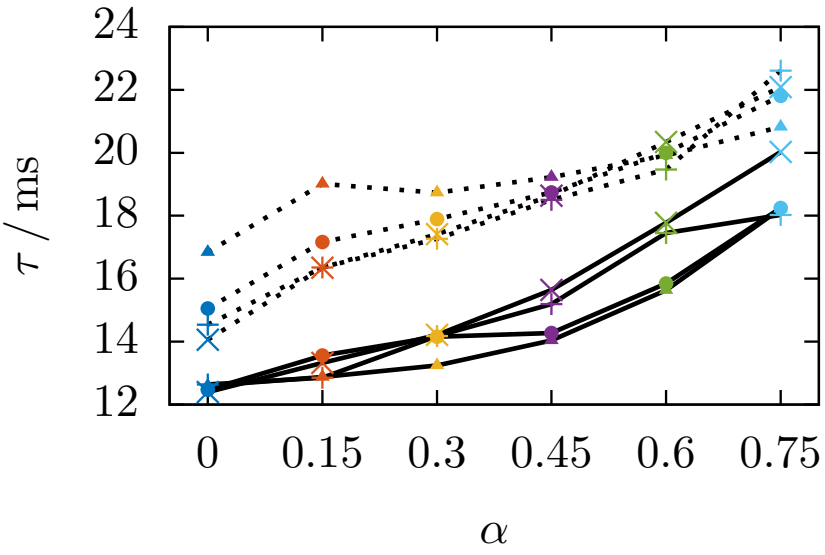

S-9. CELL STIFFNESS VARIATION

All simulations in the manuscript were performed using a cell with a fixed shear modulus. We plot in figure S-8 the results of figure 9 and figure 10 (gray lines) together with the same data of a softer cell with a shear modulus of $\mu = 500\,\mathrm{Pa}$.

The maximum cell stress in figure S-8(a) to (e), i. e., the peak right after the exit as well as the magnitude inside the nozzle channel before the exit, are approximately half of the value obtained for the stiffer cell. This is due to the stress calculation in (9), where the shear modulus scales the influence of the deformation. Additionally, the cell strain peaks in figure S-8(f) and (g) are of similar order. An inverse scaling with the stiffness is observed for the stress relaxation time τ in figure S-8(e), showing values about twice as large for the soft cell compared to the stiff one.

FIG. S-8. Influence of the cell stiffness: (a) to (e) data from figure 9 and (f, g) data from figure 10 for a softer cell with $\mu = 500\,\mathrm{Pa}$.

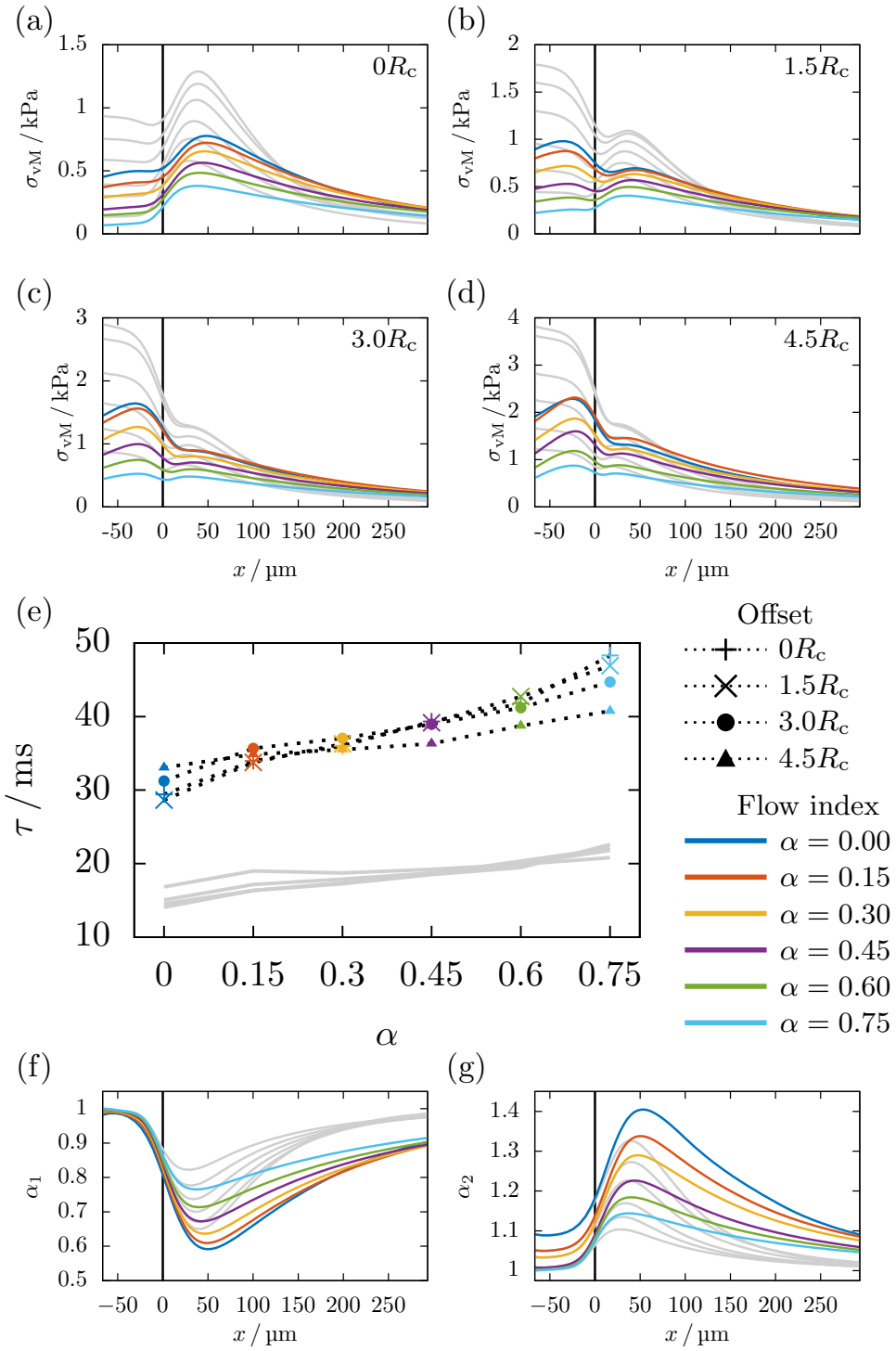

FIG. S-9. Estimated elongational stress at the nozzle exit for a bioink with shear thinning exponent $\alpha = 0.6$ in differently sized nozzles and with (a) variable extrusion speed u_{avg}, or (b) different flow rate Ω or (c) different printing pressures.

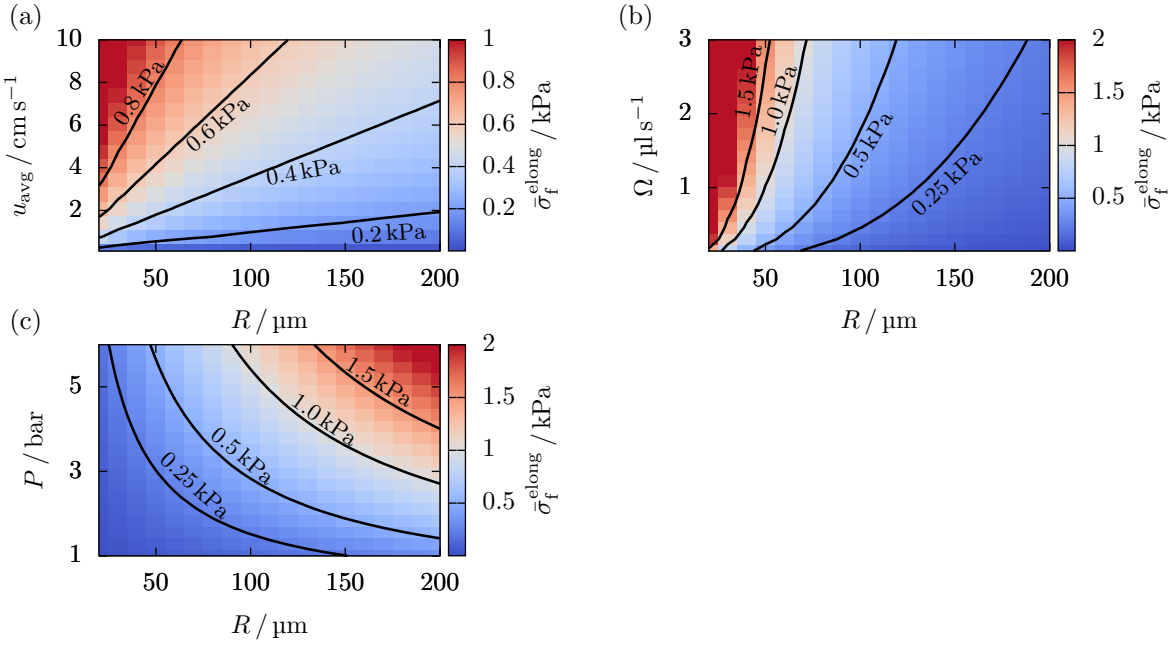

S-10. ELONGATIONAL FLOW ESTIMATE

To compute the average elongational stress $\bar{\sigma}_{\mathrm{f}}^{\mathrm{elong}}$ acting on cells right at the nozzle exit, we start by calculating the maximum and average flow velocity of our bioink using our tool from [5], as in figure 1(b). From equations (15) and (16) we then obtain $\bar{\sigma}_{\mathrm{f}}^{\mathrm{elong}}$ as a function of the average extrusion velocity u_{avg} and the nozzle radius R. The result is shown in figure S-9, using the same parameter space as in figure 13 of the manuscript.

[1] M. Kahl, M. Gertig, P. Hoyer, O. Friedrich, and D. F. Gilbert, Frontiers in Bioengineering and Biotechnology **7**, 184 (2019).

[2] R. Roscoe, Journal of Fluid Mechanics **28**, 273 (1967).

[3] G. B. Jeffery, Proceedings of the Royal Society of London. Series A, Containing Papers of a Mathematical and Physical Character **102**, 161 (1922).

[4] Z. Chai, B. Shi, Z. Guo, and F. Rong, Journal of Non-Newtonian Fluid Mechanics **166**, 332 (2011).

[5] S. J. Müller, E. Mirzahossein, E. N. Iftekhar, C. Bächer, S. Schrüfer, D. W. Schubert, B. Fabry, and S. Gekle, PLOS ONE **15**, e0236371 (2020).

[6] M. Lehmann, S. J. Müller, and S. Gekle, International Journal for Numerical Methods in Fluids 10.1002/fld.4835 (2020).

[7] E. Guazzelli, J. F. Morris, and S. Pic, *A physical introduction to suspension dynamics*, Cambridge texts in applied mathematics (Cambridge University Press, Cambridge ; New York, 2012).

Publication 4

A mechanically homogeneous equivalent of real cells

S. Wohlrab*, S. J. Müller*, and S. Gekle

Draft, 2022

A mechanically homogeneous equivalent of real cells

Sebastian Wohlrab* · **Sebastian J. Müller*** · **Stephan Gekle**

Abstract Biological cells are built up from many different constituents of varying size and stiffness which contribute to the cell's mechanical properties and whose presence influences the behavior of the cell in flow or under compression. However, assuming a homogeneous cell interior remains a common simplification in experimental mechanical characterization techniques as well as large scale computer simulations. In this study, we propose a homogeneous equivalent to inhomogeneously constituted cells and provide systematic proof of the validity of this simplification. We investigate numerically a hyperelastic cell with an explicitly heterogeneous interior under compression and in flow, mimicking respectively common atomic force microscopy and microfluidic characterization techniques. We find that our homogeneous equivalent cell with a volume averaged elastic modulus reproduces quantitatively the behavior of its inhomogeneous counterpart, and that this equality is independent of the stiffness or spatial distribution of the heterogeneity.

1 Introduction

Approximating biological cells as homogeneously elastic bodies is a highly common assumption employed in experimental micromechanical characterization techniques and large-scale computer simulations of physiological flows.
However, the different constituents of the cell, e. g., the cortex, membrane, and nucleus, all have different mechanical properties [1–4]. Atomic force microscopy has successfully been used to characterize the mechanical properties of whole cells [5–13], capsules [14], or the cell nucleus [15]. The effect of the nucleus on AFM based measurements has partially been studied [16], however, in the range of small deformations which allow an comparison with the Hertz theory. Other micromechanical evaluation techniques include the flow through confined microchannels [3, 3, 17–21, 21], or the flow through larger channels [22]. The characterization in flow typically allows for a much higher throughput than the AFM-based techniques. An important conceptual difference between these two methods is that, while a certain deformation is imposed on the cell and its responding force is measured during compression, certain fluid forces are imposed and the cell reacts with a corresponding deformation when suspended in flowing liquid. A practical difference is that flow-based methods typically characterize the cell as a whole, whereas AFM-based techniques can precisely probe the cell's constituents [15]. From a numerical point of view, a resource-efficient application of the computational methods commonly requires a set of simplifications. Numerical cells models exist in very complex forms [23] to explicitly study their isolated dynamics. In large-scale simulations like physiological flows require them, a common approach is to assume cells with a homogeneously elastic interior [24, 25]. And while the similarity between several numerical investigations and the corresponding experimental measurements suggest the validity of this simplification, there exists so far no proof that the assumption should be correct for large cell deformations as well.
In this work, we systematically proof the possibility to substitute any inhomogeneously constituted cell with a simple homogeneous cell with an effective elasticity. For that, we first construct a well-defined inhomogeneous cell with an inclusion, e. g., a nucleus, of variable stiffness (Young's modulus or shear modulus), size, and position. In addition, we build an inhomogeneous cell with a spatially random stiffness distribution. From the volume averaged mean of the constituents' Young's moduli we define an effective Young's modulus of a homogeneous equivalent cell. We perform AFM compression simulations as well as microflu-

Sebastian Wohlrab* · Sebastian J. Müller* · Stephan Gekle
Theoretical Physics VI, Biofluid Simulation and Modeling, University of Bayreuth, 95440 Bayreuth, Germany
E-mail: stephan.gekle@uni-bayreuth.de
*: Sebastian Wohlrab and Sebastian J. Müller contributed equally.

idic shear flow and pipe flow computations of our three cell models. We find excellent agreement of the resulting force versus deformation behavior in compression and the strain versus fluid forces behavior in flow. Through variation of stiffness, size, position, and shape, of the inhomogeneity we show that neither of these factors have a drastic impact on the cell's mechanical behavior. Any kind of intracellular mechanical diversity can hence be effectively described using our proposed homogeneous equivalent cell.

2 Methods and setup

2.1 Inhomogeneous cell with nucleus

As model for a well-defined inhomogeneous cell, we use a cell with a stiffer nucleus inside. We model the nucleate cell as a sphere of radius R which contains a spherical inclusion of radius R_n inside the cell volume, as shown in figure 1(a). It is labeled "Nucleus" in the plot. We tetrahedralize both volumes and apply the neo-Hookean strain energy computations from [13] in both parts. Properties of the whole cell are denoted without subscript, properties of the nucleus and the cytoskeleton by the subscripts "n" and "c", respectively. The Poisson's ratio is $\nu = 0.48$ in all simulations, which ensures sufficient incompressibility while maintaining numerical stability. To parametrize the stiffness we choose the Young's moduli E_n and E_c of the inhomogeneity and the shell, respectively.
For our systematic analysis, we further define the stiffness ratio and the size ratio

$$\gamma = \frac{E_\mathrm{n}}{E_\mathrm{c}} \quad \text{and} \quad \lambda = \frac{R_\mathrm{n}}{R}\,, \tag{1}$$

with $\gamma > 1$ describing an inhomogeneity stiffer than the rest of the cell and $0 < \lambda < 1$. An additional offset d of the inhomogeneity from the cell's geometrical center is given in units of the cell radius. Through variation of the control parameters γ, λ, and d, any kind of spherical inclusion into the cell volume is covered. We discuss the effect of an ellipsoidal inhomogeneity in the last paragraph of section 3.1.
As a reference configuration, from which variations of the control parameters start, we choose $\gamma = 2$, $\lambda = \frac{1}{2}$, and $d = 0$.

2.2 Random inhomogeneous cell model

In addition to the well-defined inhomogeneous system of section 2.1, we create a random inhomogeneous cell by randomly assigning a stiffness ratio $\gamma_i \in [1, 10]$ to every of the N_tet individual tetrahedra of the mesh, as shown in figure 1(a). It is labeled "Random" in the plot.

2.3 Homogeneous equivalent cell model

We construct a simplified but equivalent description of the inhomogeneous cell model from section 2.1, shown in figure 1(a). It is labeled "Homogeneous" in the plot. The same hyperelastic computations are performed on a tetrahedralized, initially spherical, mesh. Instead of the spatially inhomogeneous stiffness distribution, however, a single parameter is computed by volume weighted averaging the constituents. The effective Young's modulus of our equivalent cell model is defined as:

$$E_\mathrm{eff} = \frac{1}{V}(V_\mathrm{c}E_\mathrm{c} + V_\mathrm{n}E_\mathrm{n}) = \left[1 + (\gamma - 1)\lambda^3\right]E_\mathrm{c} \tag{2}$$

to substitute the inhomogeneous cell with nucleus. Analogously for our random inhomogeneous cell model, the effective Young's modulus is computed as

$$E_\mathrm{eff} = \frac{1}{V}\sum_{i=1}^{N_\mathrm{tet}} V_i E_\mathrm{c}\gamma_i = E_\mathrm{c}\gamma_\mathrm{eff}\,, \tag{3}$$

from the volumes V_i and the Young's moduli $E_i = \gamma_i E_\mathrm{c}$ of the N_tet individual tetrahedra. In our setup, the volume averaged stiffness ratio is $\gamma_\mathrm{eff} \approx 5.5$.

2.4 Cell simulations under compression

We create a compression scenario similar to mechanical characterization techniques of cells via atomic force microscopy by compressing our model between an upper, moving, and a lower, resting, plate using the algorithm from [13]. From our quasistatic simulation we obtain the normal force F exerted by the upper plate onto the cell, which causes a deformation as shown in figure 1(b). We define the deformation parameter δ as the relative compression, i. e., the plate-plate distance divided by the cell diameter. We perform our simulations up to very large deformations of $\delta = 75\,\%$ for parameters $\gamma \in \{0, 2, 10, 20\}$ and $\lambda \in \{0.1, 0.2, \ldots, 0.9\}$, as well as for our random inhomogeneous cell. We then perform another set of simulations with our homogeneous equivalent cell with the effective Young's modulus from (2) and (3).

2.5 Cell simulations in shear flow

As a first flow scenario we use a linear shear flow, where our initially spherical deforms into an ellipsoidal body that undergoes a tank-treading motion. To do so, we couple our hyperelastic tetrahedralized mesh to a Lattice Boltzmann flow simulation [26–28] via an immersed-boundary algorithm [29, 30], using the same procedure as in [13, 31].

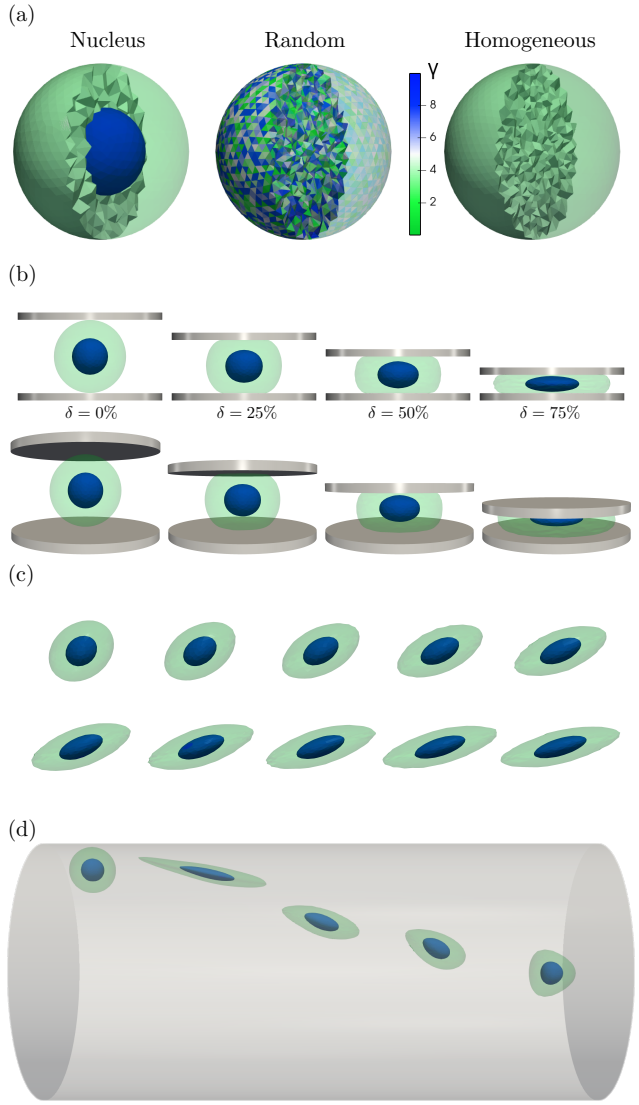

Fig. 1 (a) Definitions of our inhomogeneous cells and their homogeneous equivalent showing the stiffness ratio of the individual tetrahedra. (b) Our inhomogeneous cell under compression at different values of the deformation δ. (c) The stationary cell shape of a cell with a centered inhomogeneity in linear shear flow with increasing capillary number Ca. (d) Our inhomogeneous cell flowing through a cylindrical capillary migrates towards the symmetry axes while maintaining an ellipsoidal shape. At the center, it assumes a bullet-like shape.

Since the cell assumes an ellipsoidal shape, we choose the Taylor deformation parameter [13, 25]

$$D = \frac{a-b}{a+b} \tag{4}$$

with the ellipsoids major and minor semi-axis, respectively a and b, as our measure for the cell deformation. In analogy to the normal force introduced in section 2.4, the strength of the shear flow is best characterized using the dimensionless shear rate, or capillary number

$$\mathrm{Ca} = \frac{\eta\dot{\gamma}}{\mu_\mathrm{c}} = 2(1+\nu)\frac{\eta\dot{\gamma}}{E_\mathrm{c}}, \tag{5}$$

where η denotes the surrounding fluid's dynamic viscosity and $\dot{\gamma} = \frac{\partial u_x}{\partial y}$ the constant velocity gradient. Commonly, the shear modulus μ is used as stiffness parameter for this definition. It relates to the Young's modulus of the previous section via the Poisson's as $E = 2(1+\nu)\mu$. Hence, the stiffness ratios γ and γ_eff have the identical value when defined analogously to (1) and (3) via the shear moduli of the nucleus and the cytoskeleton, respectively μ_n and μ_c.
In figure 1(c), we show the stationary shape of our inhomogeneous cell at various Ca. In addition to the ellipsoidal deformation of the entire shape, we find that the centered inhomogeneity, too, deforms into an ellipsoidal manner. However, its isolated deformation is visibly less pronounced. We perform our simulations for $\gamma \in \{0,2,10,20\}$ and $d \in \{0,0.45\}$, and with our random inhomogeneous cell. Using the effective shear modulus μ_eff in (5), we compare the inhomogeneous cells' behavior with the master curve describing the homogeneous equivalent cell.

2.6 Cell simulations in capillary flow

In our second flow scenario, we place the initially spherical cell inside a cylindrical pipe with radius R_ch, where an axial pressure gradient G drives the Poiseuille flow [32]. Here, we need to distinguish two important cases, as illustrated in figure 1(d): (i) When placed off-centered the cell will assume an approximately ellipsoidal shape according to the local shear rate. Recently, it has been shown experimentally [22] and numerically [31], that a local shear flow approximation is valid for microfluidic and pipe flow applications, given that cells flow off-centered. The local Capillary number as function of the radial position r is given by

$$\mathrm{Ca}(r) = \frac{G}{2\mu_\mathrm{c}}\frac{r}{R_\mathrm{ch}} \tag{6}$$

Due to the fluid's shear stress, however, the cell continuously migrates from its starting point towards the center where the local shear flow approximation becomes insufficient.
(ii) At the channel axes the cell assumes a bullet-like shape due to the symmetrical flow conditions, as shown in figure 1(d). This shape can be characterized by its strain in axial and radial direction, which we define as the maximum elongation in the respective direction divided by the cells reference diameter:

$$\varepsilon_x := \frac{l_x}{2R} \quad \text{and} \quad \varepsilon_r := \frac{l_r}{2R} \tag{7}$$

We perform our simulations for $\gamma \in \{0,2,10\}$ and with the random inhomogeneous cell and compare the results to those of the homogeneous equivalent cell.

3 Results

3.1 Cells under compression

We first place a spherical nucleus with $\lambda = \frac{1}{2}$ at the center of the cell and perform the compression simulations. When increasing the stiffness ratio γ at a constant size of the nucleus under compression, we find that — as expected — the force needed to compress the whole cell to a certain deformation δ increases. This is shown in figure 2, where we plot the dimensionless force $F/(E_c R^2)$ versus the deformation for our inhomogeneous cells with nucleus. It is normalized using the Young's modulus of the shell E_c and hence identical for all simulations with different γ. In the same manner, we plot in figure 2 the data obtained from the simulations performed with the corresponding homogeneous equivalent cells as lines. We find that, even for a nucleus 20 times stiffer than the cytoskeleton, the deviation from the homogeneous equivalent cell are not significant. Interestingly, our data for $\gamma = 10$ matches perfectly with its homogeneous equivalent with $E_{\text{eff}} = 2.125 E_c$, whereas the differences for other values of γ deviate in different directions. While for $1 < \gamma < 10$, the inhomogeneous cell exhibits stronger strain hardening than the homogeneous equivalent cell, for $\gamma > 10$ the strain hardening is instead decreasing.

This deviation can be visualized in a more quantitative way when the force is non-dimensionalized using the corresponding effective Young's modulus (2), giving

$$F^* = \frac{F}{E_{\text{eff}} R^2}\,, \tag{8}$$

which is shown in figure 3(a). Due to this non-dimensionalization, all data curves describing homogeneous cells collapse onto one master curve. The data of the inhomogeneous cells then deviates from this master curve in different directions, which indicates the quality of the homogeneous equivalent description. It is apparent that the variation of γ does not lead to a consistent deviation from the homogeneous description, but instead changes in different directions. This is visualized in the inset of figure 3(a), where data for additional values of γ is plotted.

We now vary the size of the inhomogeneity at constant stiffness $\gamma = 2$ between the two limiting cases that describe homogeneous cells, namely $\lambda = 0$ (all softer shell) and $\lambda = 1$. In figure 3(b), the resulting normalized force (8) versus deformation curves show little deviation, and they always lie between the curves for $\gamma = 1$ and $\gamma = 2$ from figure 2. The inset of figure 3(b) shows the increase and decrease of the deviation from the homogeneous cases, with a maximum value at around $\lambda \approx 0.7$. Note that this value is close to, yet differs, from the value $\lambda = 2^{-\frac{1}{3}} \approx 0.79$ obtained for equal volumes of shell and inhomogeneity.

Next, we move the inhomogeneity ($\gamma = 2$ and $\lambda = \frac{1}{2}$) away from the center and very close to the cell surface, i. e., $d = 0.45$. As illustrated in figure 4(a), we denote with x the direction parallel to the plates and with y the perpendicular direction. We deduce the insignificance of the position of the inhomogeneity from the force versus deformation curves in figure 4(a), where all data points overlap exactly.

Finally, we alter the shape of the nucleus and replace the centered spherical inclusion with an ellipsoid of equal volume with semi-axes $a \approx 0.8R$, $b = c \approx 0.4R$. We choose again the parallel (x) and perpendicular (y) alignment of the major semi-axis, which we compare to the centered spherical inclusion ($\lambda = \frac{1}{2}$) denoted with ref, as shown in figure 4(b). The resulting force versus deformation curves for ($\gamma = 2$) in figure 4(b) underline that a variation of the inhomogeneity's shape effectively does not affect the compression behavior of a cell.

We then perform the same simulation with our random inhomogeneous cell model from figure 1(a). The force versus deformation behavior in figure 2 and figure 3(a) excellently matches with its homogeneous equivalent cell.

This section shows that, for compression scenarios, a heterogeneous cell can in practice be replaced with a homogeneous equivalent cell with a volume averaged Young's modulus, since neither the stiffness difference nor the size, the position, or the shape, of the inhomogeneity have a significant impact on the force necessary to produce a certain cell deformation.

Fig. 2 The force versus deformation behavior of our proposed homogeneous equivalent cell compared to inhomogeneous cells with stiffer nucleus and our random inhomogeneous cell. Increasing the stiffness of the nucleus increases the overall force necessary to compress the cell.

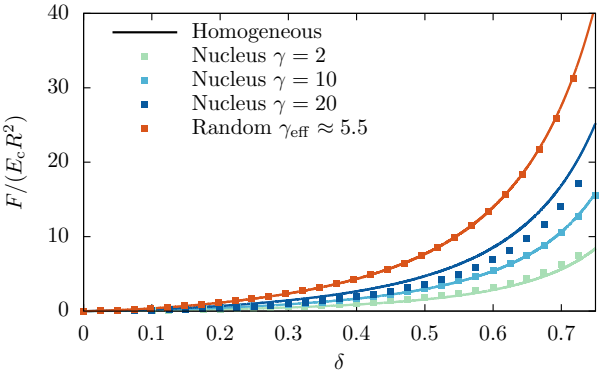

3.2 Cells in linear shear flow

For our investigations of cells in flow, we start by putting our initially spherical inhomogeneous cell ($\gamma = 2$, $\lambda = \frac{1}{2}$, and $d = 0$) in a linear shear flow with shear rate $\dot{\gamma}$. After a transient time span its shape becomes stationary (cf. figure 1(c)), and the cell undergoes a continuous tank-treading

Fig. 3 (a) The quality of the homogeneous equivalent can be visualized using the normalized force F^* (8). (b) Variation of the volume ratio λ (1). The insets show a close-up view revealing that parameter variations of γ and λ do not affect the quality in a consistent manner.

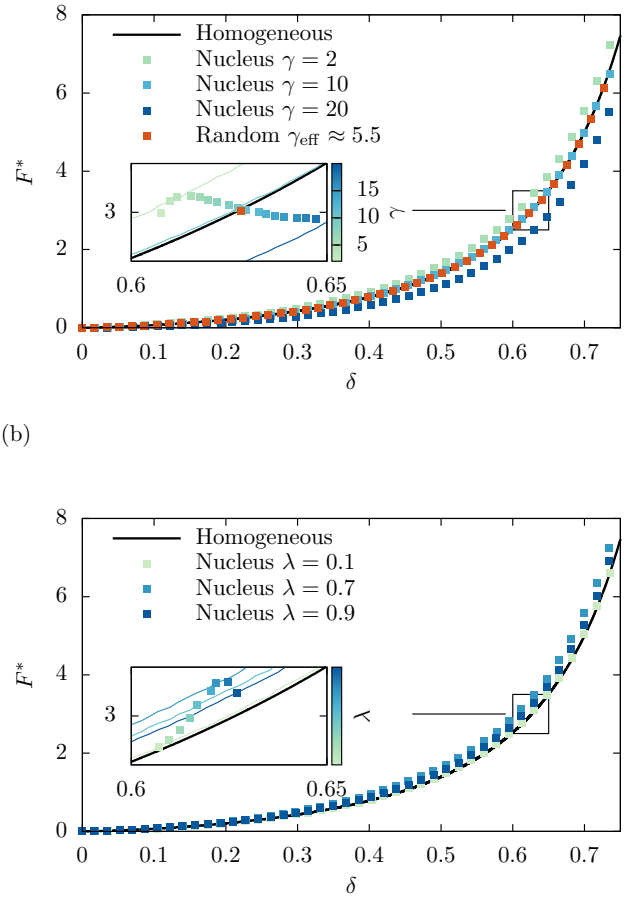

Fig. 4 (a) Variation of the position of the nucleus along two independent axes slightly increases the accuracy of the homogeneous description. (b) A nucleus with ellipsoidal shape (but same volume) comes without notable effect on the force versus deformation behavior independent of the orientation.

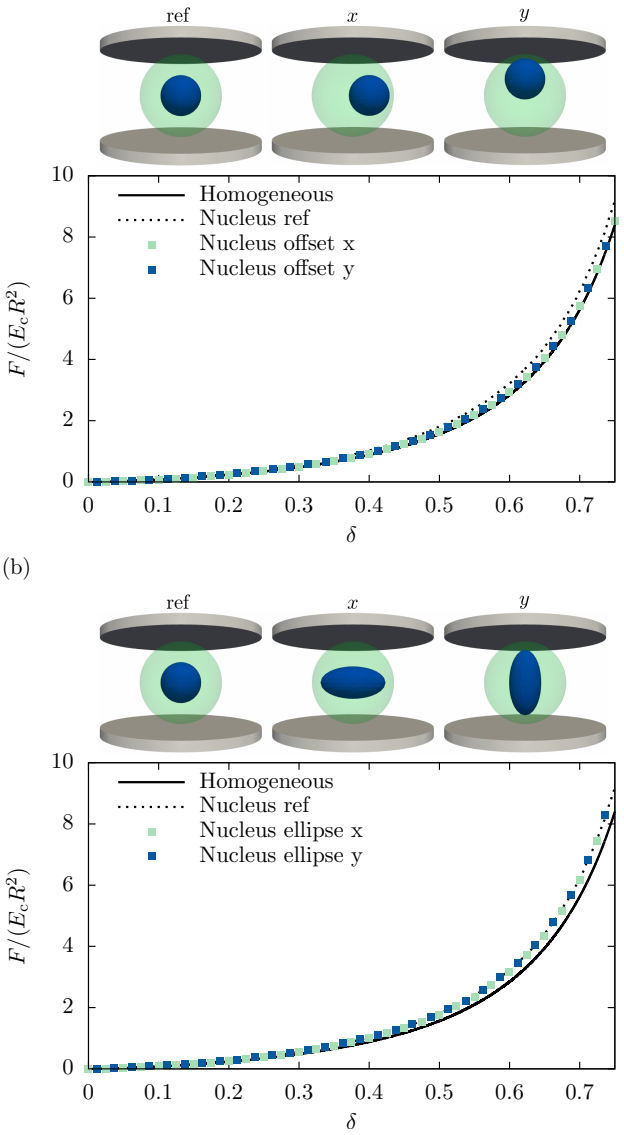

motion. We find in figure 5(a) excellent agreement between our nucleate cell and its homogeneous equivalent cell, when plotting the stationary value of D obtained from the simulation with $\gamma = 2$ as a function of the Capillary number (5). In accordance with the compression simulations of figure 2(a), we find that the inhomogeneous cell with nucleus at a stiffness ratio $\gamma = 2$ yields a slightly lower deformation than its homogeneous equivalent. Similarly in figure 5(b), we depict additionally the results for $\gamma = 5$ and 10. In comparison with the respective homogeneous equivalent cell, we find that only low deformations yield inaccurate results, which is to be expected from previous studies [16]. In that range, the data approaches the results as they would be obtained from a homogeneous cell with μ_c throughout. Analogously to our observation in the compression setup in figure 2(a), the data for $\gamma = 10$ is surprisingly accurate for large deformation. An excellent agreement is found when comparing our random inhomogeneous cell model to its homogeneous equivalent in figure 5(c).

A significant influence on the dynamic behavior is found when the stiffer nucleus is not centered in the cell. Our cell with nucleus at $d_{\parallel} = 0.45$ is show in figure 6(a). A series of snapshots depicts the tank-treading motion of the entire cell, where the nucleus produces a bump at the cell surface, which periodically moves along. This behavior is also reflected in the time development of the Taylor deformation (4), as shown in figure 6(b) (dashed lines), where D is plotted as function of the dimensionless time $t\dot{\gamma}$. If instead the nucleus in placed perpendicular to the shear plane at $d_{\perp} = 0.45$, the same stationary behavior as for a centered

Fig. 5 (a) Taylor deformation D as function of the Capillary number of our inhomogeneous cell with $\gamma = 2$ in linear shear flow (squares) and during its migration in a pipe flow (lines) compared to that of its homogeneous equivalent cell. (b) Taylor deformation of the nucleate cell for different γ. (c) Data as in (a) for the random inhomogeneous cell.

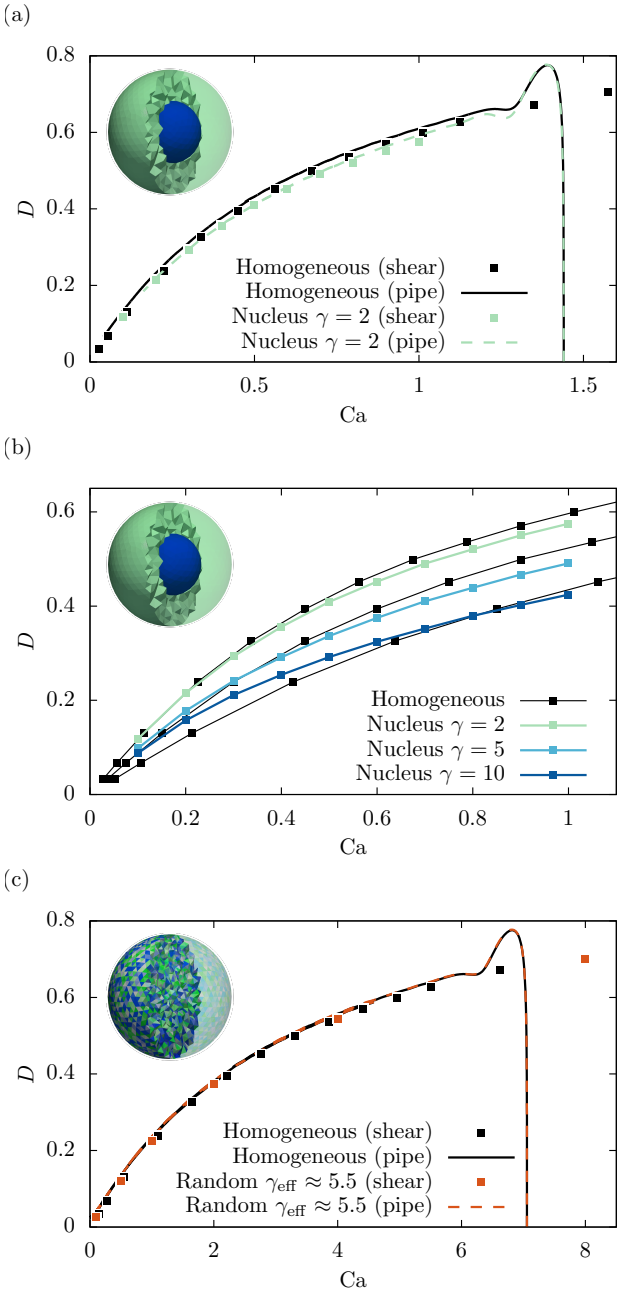

nucleus is obtained (solid lines). The time average of the deformation in this state is shown in figure 6(c) for both nucleus offsets as well as the corresponding homogeneous equivalent cell. It becomes clear that the time-averaged deformation of the cell with off-centered nucleus is perfectly covered by our homogeneous description.

Fig. 6 (a) Time series snapshots for the inhomogeneous cell with nucleus displaced parallel to the shear plane. Due to the rotation of the cellular material, the bump produced by the inhomogeneity travels around the cell. (b) Time development of the Taylor deformation parameter D for an inhomogeneous cell with the nucleus displaced parallel to the shear plane oscillating around that for a displacement perpendicular to the shear plane. (c) Average D of the cell with off-centered nucleus compared to the data of figure 5(a).

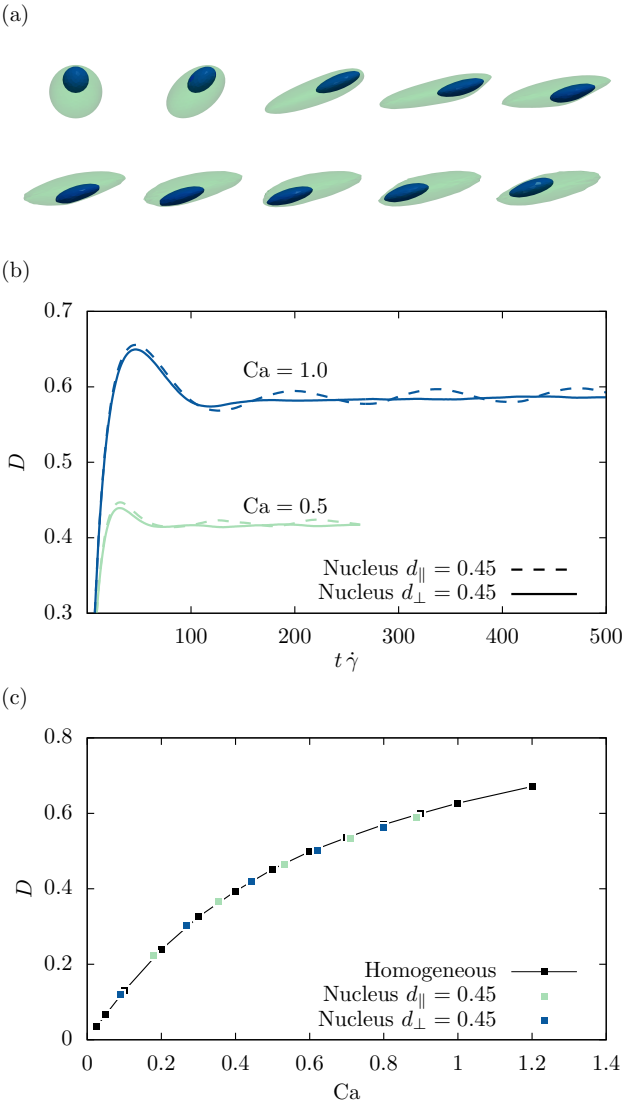

3.3 Cell in capillary flow

The two major differences between the pressure driven flow through a pipe or microchannel and the simple shear flow scenario are (i) the non-linearity of the velocity profile and (ii) the symmetry conditions at the channel axis. We plot in figure 5(a) the Taylor deformation of our inhomogeneous cell ($\gamma = 2$, $\lambda = \frac{1}{2}$, and $d = 0$) when put near the wall inside the pipe. Reading the solid line from right to left, we see an initial transient deformation time span, during which the cell deforms into an ellipsoid, which is followed by the cell

migrating radially inwards through monotonously decreasing local shear rates, and hence, local Ca. We find excellent agreement between our nucleate cell and its homogeneous equivalent cell, as expected from our results in section 3.2. This result stays valid also for the data of the random inhomogeneous cell in figure 5(c), which is in excellent agreement with that of its homogeneous equivalent.

When the cell flows at the center of the channel, it assumes a stationary bullet-like shape as depicted in figure 7(a) for our inhomogeneous cell with $\gamma = 2$ and 10, as overlay over its homogeneous equivalent. Visible, these two shapes agree perfectly with each other, even though the cytoskeleton in contact with the surrounding fluid is 2.125 times softer for the inhomogeneous cell. As for a quantitative analysis, the axial and radial strains, ε_x and ε_r, assume a stationary value after a short time span. We depict the time average of these stationary values for our inhomogeneous cell with nucleus, our random inhomogeneous cell, and their respective homogeneous equivalent in figure 7(b). It becomes apparent that the radial strain of nucleate cell shows an increasing deviation from its homogeneous equivalent, while the axial strain remains accurate. In contrast to the decreasing radial strain of the homogeneous equivalent cell, which is simply explained by its larger stiffness, the radial strain of the nucleate cell remains almost unchanged. This can be understood the following way: On the one hand, the soft cytoskeleton of the nucleate cells has the same stiffness throughout all simulations. Since all simulations are performed using the same flow conditions, a similar stress is acting on the cell surface and the cytoskeleton. The stiffer nucleus, on the other hand, is centered inside the cell and located on the symmetry axis of the channel, where the fluid stress vanishes [32]. We can therefore assume a weaker influence of the nucleus in this scenario as compared to the off-centered flow, in which the nucleus itself was subjected to large stresses. This observation is underlined by our investigation of the random inhomogeneous cell, which shows excellent agreement with its homogeneous equivalent in figure 7(b). Thus, we conclude that our proposed homogeneous equivalent description is still valid in capillary flow.

Fig. 7 (a) Snapshots of the inhomogeneous cell with nucleus and its homogeneous equivalent when flowing at the center of the pipe for $\gamma = 2$ and 10. The gray area shows a slice of the homogeneous equivalent cell while the green/blue overlay depicts the inhomogeneous cell with nucleus. (b) The stationary axial ($\varepsilon_x < 1$) and radial strains ($\varepsilon_r > 1$) of our inhomogeneous cells as function of the stiffness ratio γ in comparison to those of the homogeneous equivalent cell. Error bars denote the standard deviation.

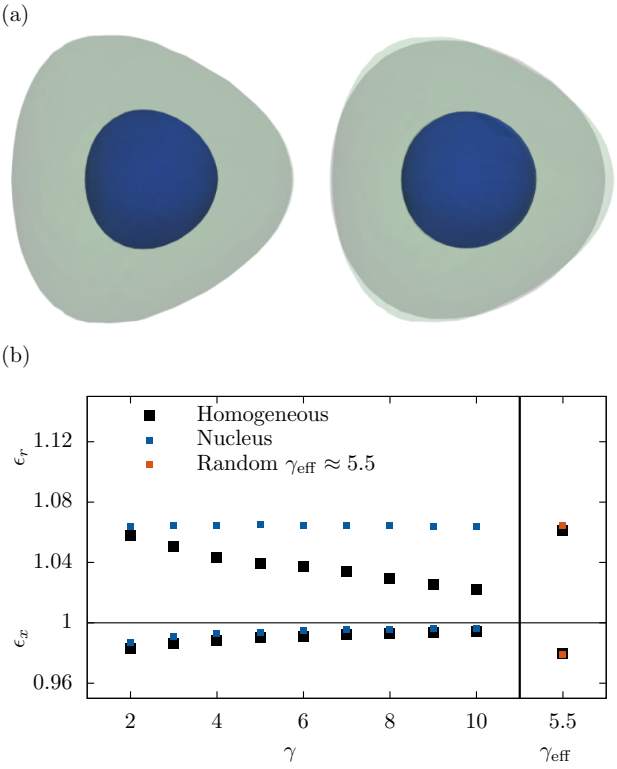

4 Conclusion

In this work, we presented systematic proof of the possibility to substitute any inhomogeneously constituted cell with a simple homogeneous equivalent cell by means of a volume averaged effective elasticity.

We constructed three numerical cell models, a homogeneous one, one including a well-defined inhomogeneity, and a random inhomogeneous cell. All models showed the same force versus imposed deformation behavior under AFM-like compression. In shear and pipe flow simulations, we found that an inhomogeneity can have an impact on the dynamic time evolution of the cell's shape. However, no difference in the stationary behavior was observed and the average strain as function of the fluid forces agrees exactly.

Our proposed homogeneous equivalent hence stays valid under different loading scenarios and is independent of the shape, size, stiffness, or distribution, of the cell's internal heterogeneity.

Acknowledgements

Funded by the Deutsche Forschungsgemeinschaft (DFG, German Research Foundation) — Project number 326998133 — TRR 225 "Biofabrication" (subprojects B07 and A01). We gratefully acknowledge computing time provided by the SuperMUC system of the Leibniz Rechenzentrum, Garching. We further acknowledge support through the computational resources provided by the Bavarian Polymer Institute.

References

1. A. Cordes, H. Witt, A. Gallemí-Pérez, B. Brückner, F. Grimm, M. Vache, T. Oswald, J. Bodenschatz, D. Flormann, F. Lautenschläger, M. Tarantola, A. Janshoff, Physical Review Letters **125**(6), 068101 (2020). DOI 10.1103/PhysRevLett.125.068101
2. D. Zhelev, D. Needham, R. Hochmuth, Biophysical Journal **67**(2), 696 (1994). DOI 10.1016/S0006-3495(94)80529-6
3. J.R. Lange, C. Metzner, S. Richter, W. Schneider, M. Spermann, T. Kolb, G. Whyte, B. Fabry, Biophysical Journal **112**(7), 1472 (2017). DOI 10.1016/j.bpj.2017.02.018
4. A. Mietke, O. Otto, S. Girardo, P. Rosendahl, A. Taubenberger, S. Golfier, E. Ulbricht, S. Aland, J. Guck, E. Fischer-Friedrich, Biophysical Journal **109**(10), 2023 (2015). DOI 10.1016/j.bpj.2015.09.006
5. E. Fischer-Friedrich, A.A. Hyman, F. Jülicher, D.J. Müller, J. Helenius, Scientific Reports **4**(1), 6213 (2015). DOI 10.1038/srep06213
6. N. Guz, M. Dokukin, V. Kalaparthi, I. Sokolov, Biophysical Journal **107**(3), 564 (2014). DOI 10.1016/j.bpj.2014.06.033
7. V. Lulevich, T. Zink, H.Y. Chen, F.T. Liu, G.y. Liu, Langmuir **22**(19), 8151 (2006). DOI 10.1021/la060561p
8. V.V. Lulevich, I.L. Radtchenko, G.B. Sukhorukov, O.I. Vinogradova, The Journal of Physical Chemistry B **107**(12), 2735 (2003). DOI 10.1021/jp026927y
9. H. Ladjal, J.L. Hanus, A. Pillarisetti, C. Keefer, A. Ferreira, J.P. Desai, in 2009 IEEE/RSJ International Conference on Intelligent Robots and Systems (IEEE, St. Louis, MO, USA, 2009), pp. 1326–1332. DOI 10.1109/IROS.2009.5354351
10. R. Kiss, Journal of Biomechanical Engineering **133**(10), 101009 (2011). DOI 10.1115/1.4005286
11. F.M. Hecht, J. Rheinlaender, N. Schierbaum, W.H. Goldmann, B. Fabry, T.E. Schäffer, Soft Matter **11**(23), 4584 (2015). DOI 10.1039/C4SM02718C
12. A. Sancho, I. Vandersmissen, S. Craps, A. Luttun, J. Groll, Scientific Reports **7**(1), 46152 (2017). DOI 10.1038/srep46152
13. S.J. Müller, F. Weigl, C. Bezold, A. Sancho, C. Bächer, K. Albrecht, S. Gekle, Biomechanics and Modeling in Mechanobiology **20**(2), 509 (2021). DOI 10.1007/s10237-020-01397-2
14. A. Ghaemi, A. Philipp, A. Bauer, K. Last, A. Fery, S. Gekle, Chemical Engineering Science **142**, 236 (2016). DOI 10.1016/j.ces.2015.11.002
15. N. Caille, O. Thoumine, Y. Tardy, J.J. Meister, Journal of Biomechanics **35**(2), 177 (2002)
16. G. Cao, J. Sui, S. Sun, Biomechanics and Modeling in Mechanobiology **12**(1), 55 (2013). DOI 10.1007/s10237-012-0381-z
17. M. Urbanska, H.E. Muñoz, J. Shaw Bagnall, O. Otto, S.R. Manalis, D. Di Carlo, J. Guck, Nature Methods **17**(6), 587 (2020). DOI 10.1038/s41592-020-0818-8
18. O. Otto, P. Rosendahl, A. Mietke, S. Golfier, C. Herold, D. Klaue, S. Girardo, S. Pagliara, A. Ekpenyong, A. Jacobi, M. Wobus, N. Töpfner, U.F. Keyser, J. Mansfeld, E. Fischer-Friedrich, J. Guck, Nature Methods **12**(3), 199 (2015). DOI 10.1038/nmeth.3281
19. B. Fregin, F. Czerwinski, D. Biedenweg, S. Girardo, S. Gross, K. Aurich, O. Otto, Nature Communications **10**(1), 415 (2019). DOI 10.1038/s41467-019-08370-3
20. A.C. Rowat, D.E. Jaalouk, M. Zwerger, W. Ung, I.A. Eydelnant, D.E. Olins, A.L. Olins, H. Herrmann, D.A. Weitz, J. Lammerding, Journal of Biological Chemistry **288**(12), 8610 (2013). DOI 10.1074/jbc.M112.441535
21. J.R. Lange, J. Steinwachs, T. Kolb, L.A. Lautscham, I. Harder, G. Whyte, B. Fabry, Biophysical Journal **109**(1), 26 (2015). DOI 10.1016/j.bpj.2015.05.029
22. R. Gerum, E. Mirzahossein, M. Eroles, J. Elsterer, A. Mainka, A. Bauer, S. Sonntag, A. Winterl, J. Bartl, L. Fischer, S. Abuhattum, R. Goswami, S. Girardo, J. Guck, S. Schrüfer, N. Ströhlein, M. Nosratlo, H. Herrmann, D. Schultheis, F. Rico, S. Müller, S. Gekle, B. Fabry, Viscoelastic properties of suspended cells measured with shear flow deformation cytometry. Preprint, Biophysics (2022). DOI 10.1101/2022.01.11.475843
23. K. Lykov, Y. Nematbakhsh, M. Shang, C.T. Lim, I.V. Pivkin, PLOS Computational Biology **13**(9), e1005726 (2017). DOI 10.1371/journal.pcbi.1005726
24. M.E. Rosti, L. Brandt, D. Mitra, Physical Review Fluids **3**(1), 012301 (2018). DOI 10.1103/PhysRevFluids.3.012301
25. A. Saadat, C.J. Guido, G. Iaccarino, E.S.G. Shaqfeh, Physical Review E **98**(6), 063316 (2018). DOI 10.1103/PhysRevE.98.063316
26. T. Krüger, H. Kusumaatmaja, A. Kuzmin, O. Shardt, G. Silva, E.M. Viggen, The Lattice Boltzmann Method. Graduate Texts in Physics (Springer International Publishing, Cham, 2017). DOI 10.1007/978-3-319-44649-3
27. D. Roehm, A. Arnold, The European Physical Journal Special Topics **210**(1), 89 (2012). DOI 10.1140/epjst/e2012-01639-6
28. H. Limbach, A. Arnold, B. Mann, C. Holm, Computer Physics Communications **174**(9), 704 (2006). DOI 10.1016/j.cpc.2005.10.005
29. M. Schlenk, E. Hofmann, S. Seibt, S. Rosenfeldt, L. Schrack, M. Drechsler, A. Rothkirch, W. Ohm, J. Breu, S. Gekle, S. Förster, Langmuir **34**(16), 4843

(2018). DOI 10.1021/acs.langmuir.8b00062

30. C. Bächer, L. Schrack, S. Gekle, Physical Review Fluids **2**(1), 013102 (2017). DOI 10.1103/PhysRevFluids.2.013102
31. S.J. Müller, B. Fabry, S. Gekle, bioRxiv (2022). DOI 10.1101/2022.09.28.509836
32. S.J. Müller, E. Mirzahossein, E.N. Iftekhar, C. Bächer, S. Schrüfer, D.W. Schubert, B. Fabry, S. Gekle, PLOS ONE **15**(7), e0236371 (2020). DOI 10.1371/journal.pone.0236371

Acknowledgments

First and foremost, I would like to thank my supervisor Prof. Dr. Stephan Gekle for his constant support during this thesis. He has always been open for discussions, provided support when needed, and let me work creatively when I wanted. I am very thankful for the time I spent in his research group, the knowledge I gained, and the people I met.

My gratitude goes to Claudia Brandt for taking care of all sorts of administrative matters and for shielding me from bureaucracy, and to Markus Hilt for his dedication to keeping the IT system running.

I would also like to thank all former and current members of our research group for the time and work together, especially Gabriel for sharing very pleasant office time, Sanwardhini for the lunch breaks and the weekly cake, Axel for the coffee talks, and Christian for fruitful discussions.

The SFB TRR 225 Biofabrication provided a great framework for the interdisciplinary collaborations of this thesis, and I am thankful for the good time and discussions I had during the regular meetings at Kloster Banz.

At last, I would like to thank my family, my parents, my brothers, and my sister, for their support during my life.

Eidesstattliche Versicherung

Hiermit versichere ich an Eides statt, dass ich die vorliegende Arbeit selbstständig verfasst und keine anderen als die von mir angegebenen Quellen und Hilfsmittel benutzt habe.

Weiterhin erkläre ich, dass ich Hilfe von gewerblichen Promotionsberatern bzw. Promotionsvermittlern oder ähnlichen Dienstleistern weder bisher in Anspruch genommen habe noch künftig in Anspruch nehmen werde.

Zusätzlich erkläre ich hiermit, dass ich keinerlei frühere Promotionsversuche unternommen habe.

Hiermit erkläre ich mich einverstanden, dass die elektronische Fassung der Dissertation unter Wahrung meiner Urheberrechte und des Datenschutzes einer gesonderten Überprüfung unterzogen werden kann.

Des Weiteren erkläre ich mich einverstanden, dass bei Verdacht wissenschaftlichen Fehlverhaltens Ermittlungen durch universitätsinterne Organe der wissenschaftlichen Selbstkontrolle stattfinden können.

Bayreuth, den 14. Februar 2023 Sebastian Johannes Müller